THE UNIVERSITY OF CHICAGO

SELF-ASSEMBLY OF COLLOIDAL NANOCRYSTALS:

SURFACE LIGANDS PROMOTE THE FORMATION OF UNEXPECTED SUPERLATTICES

A DISSERTATION SUBMITTED TO

THE FACULTY OF THE DIVISION OF THE PHYSICAL SCIENCES

IN CANDIDACY FOR THE DEGREE OF

DOCTOR OF PHILOSOPHY

DEPARTMENT OF CHEMISTRY

BY

MICHAEL ADAM BOLES

CHICAGO, ILLINOIS

JUNE 2016

Table of Contents

CHAPTER EIGHT

List of Figures

CHAPTER FOUR

Self-assembly of tetrahedral CdSe nanocrystals: effective patchiness via anisotropic steric interaction

CHAPTER FIVE

Structural characterization of spherical nanocrystal superlattices

CHAPTER SIX

Many-body effects in nanocrystal superlattices: departure from sphere packing explains stability of binary phases

CHAPTER SEVEN

PbS nanocrystal surface passivation drives binary phase behavior

CHAPTER EIGHT

Conclusion and outlook

List of Tables

Acknowledgements

I wish to thank my advisor, Professor Dmitri Talapin, for his guidance, patience, and encouragement throughout my graduate studies. It was a privilege to witness his energy, dedication, and enthusiasm for science. I also thank the other members of my thesis committee, Professor Philippe Guyot-Sionnest and Professor Heinrich Jaeger, for their thoughtful advice during the preparation of my thesis.

I have been fortunate to work with many talented and helpful people during my time at the University of Chicago. When I arrived in the summer of 2010, Dr. Maryna Bodnarchuk and Dr. Sara Rupich were particularly supportive introducing me to the experimental culture of the Talapin Laboratory. For their guidance I also owe a special thanks to Prof. Sandrine Ithurria-Lhullier, Prof. Matthew Panthani, Prof. Angshuman Nag, Dr. Maria Ibañéz, Prof. Jaeyoung Jang, and Dr. Chunxing She. In addition, I thank my colleagues J. Matthew Kurley, Dr. Dmitriy Dolzhnikov, Dr. Hao Zhang, Dmitry Baranov, Fernando Castro, Dr. Chengyang Jiang, Dr. Wenyong Liu, Igor Fedin, Patrick Cunningham, Vishwas Srivastava, Eric Janke, Margaret Hudson, Stephanie Diaz, João Batista Souza Junior, and Daniel Haubold.

I am also grateful to my undergraduate research advisor, Professor Tomas Baer, for introducing me to the world of science. His guidance in Chapel Hill and during my exchange year in Berlin, Germany paved the way to my PhD in Chicago. Similarly, I owe deep thanks to Professors Helmut Schwarz, Regine von Klitzing, and Michael Gradzielski for engaging and supporting me during my studies at the Technical University of Berlin.

The research outlined in this thesis has made use of many departmental facilities. For assistance with microscopy on countless occasions I particularly thank Dr. Jotham Austin, Prof.

Robert Josephs, and Dr. Yimei Chen. In addition, I am grateful to Dr. Antoni Jurkiewicz for his help with NMR and to Dr. Chang-Jin Qin for help with FT-IR spectroscopy. I also thank Dr. Byeongdu Lee for his assistance with x-ray scattering measurements at the Advanced Photon Source at Argonne National Laboratories. Finally, I wish to recognize Dr. Melinda Moore, Dr. Vera Dragisich, and Tanya Shpigel for their assistance with obligations outside of research.

My enjoyment of the beautiful city that is Chicago would have been curbed without those whom I call friends within and outside the department. Particular appreciation goes to Dr. James Payne, J. Matthew Kurley, Dr. Faraaz Khan, Sakari Ikäläinen, Maximiliano Colussi, Dr. Sebastian Eiser, Sarah Junker, Emily Nicholls, Dr. Dmitriy Dolzhnikov, Dr. Landon Durak, Allison Gardener, Ken Ellis, Jeff Montgomery, James Mitchell, Dr. Nathan La Porte, Leah Handel, Dr. Anthony Martinez, Dr. Noumaan Shamsi, Dr. Song Liu, and Wayne Lau.

Finally, I owe my parents, Ross and Elizabeth, and my sister, Katharine, my sincerest gratitude for a lifetime of love and support. To her husband, Will, and their children Benjamin and Paige, I thank you for the happiness you brought our family. To my fiancée, Julie, I am eternally grateful for your patience, courage, and inspiration.

Abstract

The advent and refinement of chemical techniques to produce uniform collections of colloidal nanocrystals in recent years has made accessible a wide range of nanocrystal materials, shapes, and sizes, offering a fertile testbed for developing an understanding of nanoscale crystallization. Elucidating the role of nanocrystal surfaces in promoting self-assembly of superlattice phases unanticipated by hard-shape packing models has been the focus of my graduate work. Chapter One provides a practical overview of the experimental approaches to prepare and characterize colloidal nanocrystals and self-assembled nanocrystal superlattices. Chapter Two discusses colloidal nanocrystal surfaces including atomic composition, chemical reactivity, and influence over electronic structure. Chapter Three provides an overview of nanocrystal self-assembly including interparticle potentials and predicted phase behavior for hard and soft shapes. Chapter Four describes the preparation of tetrahedrally-shaped CdSe nanocrystals and their self-assembly into an unexpected superlattice structure. Chapter Five presents a selection of electron microscopy images of superlattices comprised of nearly spherical nanocrystals. Chapter Six describes the application of image analysis techniques to elucidate ligand shell deformability of spherical nanocrystals and resulting implications for entropy-driven crystallization of soft objects. Chapter Seven analyzes the role of PbS surface ligand desorption in determining binary phase behavior with Au nanocrystals. Chapter Eight describes the implications of the ideas presented in this thesis, places them in the context of recent work by others in the field, and offers an outlook towards promising directions for future research. Together, the ideas contained herein aim to provide the conceptual foundation necessary to exploit nanocrystal self-assembly for the rational design of next-generation functional solids.

1. Preparation and characterization of colloidal nanocrystals and nanocrystal superlattices

1.1. Introduction: nanocrystals and nanocrystal superlattices

Nanocrystals (NCs) are fragments of semiconductor, metal, or dielectric crystals protected by a layer of surface-bound molecules (ligands) and dispersible in solution. A couple decades of research has revealed that precursor decomposition in the presence of organic surfactants is an effective approach to prepare size- and shape-uniform NCs.[1] By adjusting synthetic parameters (e.g., precursors, surfactants, reaction temperature and time) crystalline, monodisperse particles have been synthesized in a variety of shapes and sizes.[2] In addition, post-preparative improvements in homogeneity made possible by size-selective precipitation,[3] digestive ripening,[4] and chromatography[5] techniques further facilitate access to a uniform collection of particles.

Synthesis in organic media typically leaves a layer of hydrocarbon chains installed on the NC surface (Figure 1.1, center). The set of ligands forms a capping layer that saturates dangling bonds, screens the particle from its environment, and controls nucleation and growth kinetics during synthesis. This layer resembles the organic-inorganic interfaces formed by self-assembled surfactant monolayers adsorbed on planar crystalline surfaces[6] exemplified by the well-studied system of monolayers of thiols on gold.[7] Ligand exchange reactions extend the versatility of NC materials by allowing replacement of ligands optimized for synthesis with application-targeted species including organic or inorganic ions,[8] clusters,[9] and polymers.[10] Ligands also influence the optical and electronic properties of NCs, and provide steric or electrostatic stabilization of the colloidal state required for NC synthesis, processing, and some applications.

An ensemble of colloidal NCs can be encouraged to self-assemble into an ordered superlattice (Figure 1.1, right) by, for example, evaporation of carrier solvent. The complex phase behavior observed for even the simplest (e.g., spherical) building blocks, contributed in part by the non-additivity of nanoscale interparticle interactions,[11] has presented an intriguing puzzle to those working in the field. More practically, the flexibility of superlattice composition and structure suggests that controlled NC self-assembly could be an important enabler of next-generation materials design. Furthermore, while top-down techniques (e.g., electron beam lithography, dip-pen nanolithography[12]) for nanoscale patterning require elaborate facilities and permit only successive iterations of two-dimensional structure design, NC synthesis and self-assembly is carried out with comparatively basic equipment and enables production of complex, three-dimensional patterns of arbitrary functional materials in a single step, often with sub-nanometer precision.

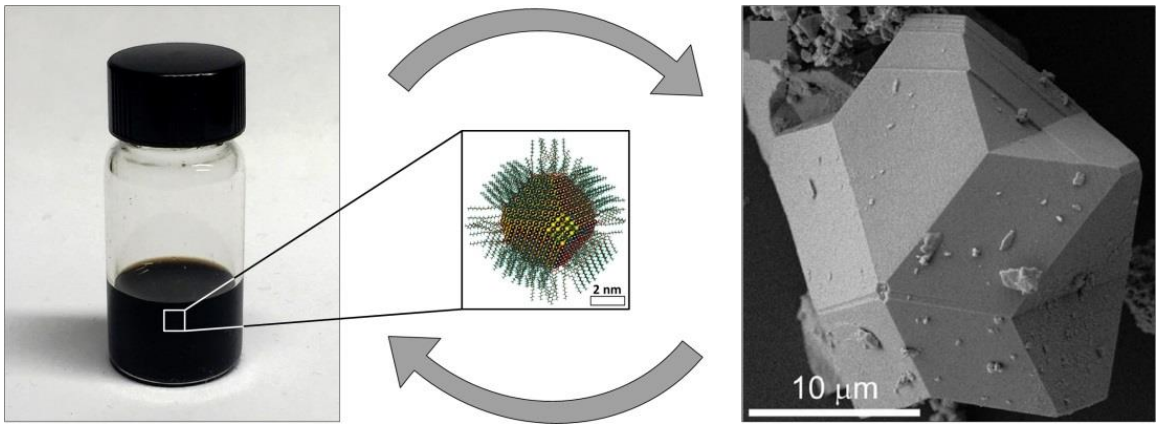

Figure 1.1. Self-assembly of colloidal nanocrystals. Individual nanocrystal building blocks prepared by colloidal chemistry techniques (left) are integrated into ordered arrays, or superlattices (right), without external direction, by the process of self-assembly. Since they are held together by weak (non-covalent) forces, superlattices may be redissolved back into constituent building blocks upon exposure to solvent. Shown here: 7nm-diameter PbS nanocrystals capped with oleic acid surface ligands self-assemble into a close-packed superlattice array. Adapted from refs.[13,14]

1.2. Synthesis of colloidal nanocrystals

Colloidal NCs may be prepared by decomposition of molecular precursors in the presence of surface-binding ligands. For example, lead sulfide (PbS) NCs may be synthesized by reacting lead acetate and hydrogen sulfide in the presence of oleic acid.[15] Heating the reaction mixture (typically between 100°C and 350°C) facilitates transformation of precursors into active species, or monomers. These monomers are subsequently converted into NCs in two steps (Figure 1.2): first, they form small inorganic clusters, or nuclei. The largest of these nuclei then grow into inorganic crystallites with dimensions on the order of several nanometers.[16] In addition to assisting with monomer conversion, the heated reaction mixture provides thermal energy necessary for rearrangement of core atoms during growth and resulting crystallinity of the inorganic core.

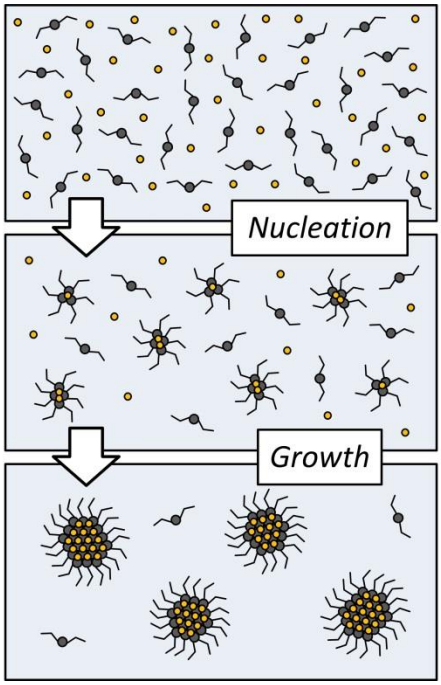

Figure 1.2. Colloidal synthesis of inorganic nanocrystals. Supersaturation of molecular precursors (top) leads to a burst of nucleation, creating small clusters (middle) serving as seeds for nanocrystal growth. While the smallest nuclei redissolve, the largest ones collect additional monomers from solution and grow into crystallites containing hundreds to thousands of atoms.

The crude synthesis mixture may be purified by repeated cycles of NC precipitation and redispersal. Using solvent-nonsolvent mixtures (e.g., hexane-ethanol) in conjunction with centrifugation, the unreacted precursors and high-boiling organics may be removed in the supernatant while the purified NCs are collected in the sediment. Furthermore, gradual addition of nonsolvent precipitates the largest NCs first, enabling post-synthetic narrowing of NC size distributions required for NC self-assembly. Hydrocarbon-capped NCs can typically be stored for years as colloidal solutions in solvents like toluene, octane, or chloroform.

1.3. Characterization of nanocrystals

A suite of spectroscopic, scattering, and imaging techniques may be used to characterize NCs.[17] These methods provide complementary pieces of information that can be divided into the following components (i) size and shape of the inorganic core, (ii) chemical bonds between the NC core and surface ligands, (iii) the composition and structure of ligand molecules, and (iv) effective properties of the whole capping layer such as effective thickness, density, and dielectric constant (Figure 1.3a).

1.3.1. Techniques to probe nanocrystal inorganic cores

Electronic transitions within the core of semiconductor NCs can be probed using light in the ultraviolet, visible, or near-infrared (UV-Vis-NIR) spectral range (Figure 1.3b). Such measurements may be used to obtain ensemble-level information on NC core size and size distribution. In addition, information on core size and shape may be obtained with imaging techniques such as transmission electron microscopy (TEM) or scanning electron microscopy (SEM). A key advantage of this technique is the ability to examine NCs at the single-particle level, revealing aspects of these systems otherwise hidden in ensemble averages. In some cases, TEM allows imaging atomic lattice planes of the NC inorganic core (Figure 1.3c, inset).

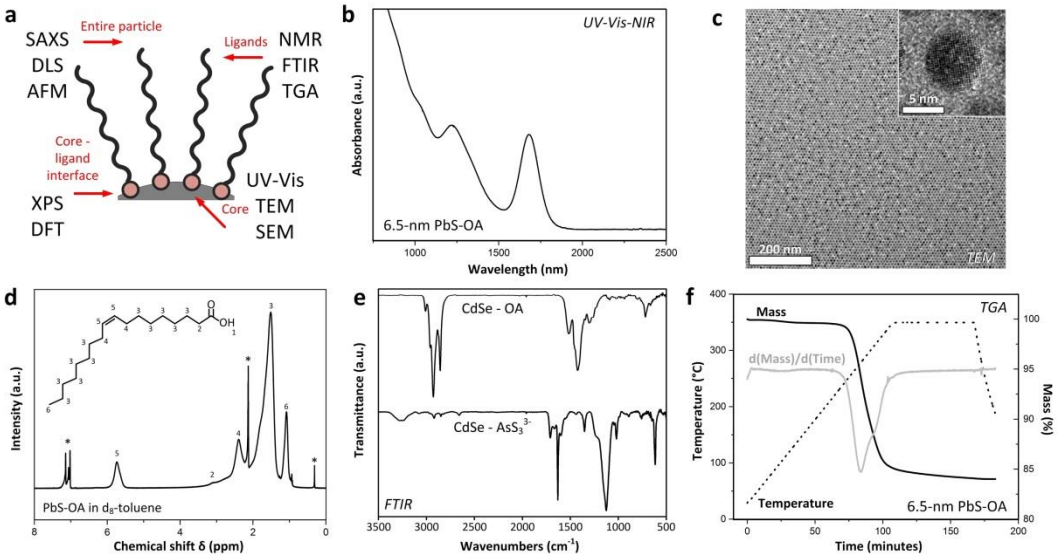

Figure 1.3. Characterization of NCs and NC surfaces. (a) Sketch summarizing useful techniques for analysis grouped by region probed. (b) UV-Vis-NIR Absorption spectrum of PbS NCs dispersed in tetrachloroethylene. This technique may be used for ensemble characterization of NC core size and size distribution. (c) TEM image of PbS NC array and inset, HRTEM revealing inorganic lattice fringes. (d) Proton NMR spectrum of PbS NCs capped with oleic acid surface ligands. Toluene solvent resonances are marked with asterisks. (e) FTIR spectrum of organic (top) and inorganic-capped (bottom) NCs deposited as film on KBr plate. (f) TGA plot of ligand loss upon heating NC solid film.

1.3.2. Techniques to probe nanocrystal surface ligands

Nuclear magnetic resonance (NMR) spectroscopy may be used to characterize surface ligands of NCs dispersed in solution (Figure 1.3d) following NMR fingerprints of spin-active nuclei (^{1}H, ^{13}C, ^{31}P and others).[18] The NMR peaks of surface-tethered ligands show significant broadening caused by dipolar coupling effects which cancel out for fast-tumbling free ligand molecules in solution. This broadening limits the utility of traditional one-dimensional NMR for NC surface analysis. Diffusion-ordered spectroscopy (DOSY), on the other hand, links a diffusion coefficient to each resonance, allowing the separation of signals from surface-bound and free ligand molecules. Heavy-nuclear NMR (for example ^{119}Sn) has proven useful in studies of NCs with inorganic ligands such as SnS_4^{4-}.[8]

Fourier transform infrared spectroscopy (FTIR) is a simple and reliable way to probe the NC surface, providing information on the structure of ligand molecules. NCs capped with organic ligands such as oleic acid (OAH, $CH_3(CH_2)_7CH=CH(CH_2)_7COOH$) show strong infrared absorption bands around 3,000 cm^{-1} and 1,500 cm^{-1}, corresponding to the C–H stretching and bending modes of surface-bound hydrocarbon molecules (Figure 1.3e, top). The width and position of infrared resonances can be used to investigate chain conformations and molecular order of the capping layer.[19] FTIR also allows for probing the displacement of hydrocarbon ligands (for example the exchange of organic for inorganic species; Figure 1.3e, bottom). Raman spectroscopy is particularly useful for characterizing inorganic ligands with heavy atoms vibrating at low frequencies.[20]

Thermal annealing of NC films can break down hydrocarbon ligands and expel decomposition products into the gas phase. The mass loss accompanying this process may be monitored using thermogravimetric analysis (TGA, Figure 1.3f) and used to obtain volatile mass fraction, from which ligand surface grafting density may be estimated (see also Chapter 6).

1.4. Preparation of nanocrystal superlattices

Nanocrystals may be coaxed into adopting ordered structures (superlattices) by a few techniques including evaporation of carrier solvent, destabilization of a colloidal solution, and sedimentation (Figure 1.4). Akin to the art of protein crystallization,[21] NC self-assembly is sensitive to several factors beyond quality of starting material. For instance, the choice of solvent, temperature, and substrate play a role in the ordering of NC superlattices. Undesired flocculation of particles in solution before triggering assembly by evaporation or destabilization can suppress ordering. As such, use of good solvent for aliphatic capping ligands (e.g. hydrocarbon liquids like hexane, octane, or toluene; chlorinated hydrocarbons like chloroform, tetrachloroethylene, chlorobenzene) promotes dispersal of the colloid and is a good starting point for assembly experiments. Gentle heating of the assembly solution facilitates ordering of NCs in superlattices. Because NCs experience thermodynamic drive to eliminate surface area if provided sufficient thermal energy to coalesce, thermal decomposition of the material presents a practical upper limit to assembly temperature.[22] In addition, the solvent vapor pressure is an important parameter for evaporative self-assembly experiments. Because the ordering process requires particles to diffuse through solution and sample various positions, use of volatile solvents may condense particles too rapidly to allow for self-assembly. Furthermore, the choice of support (i.e., solid or liquid subphase) influences the assembly outcome, setting dimensions and orientation of NC superlattices.

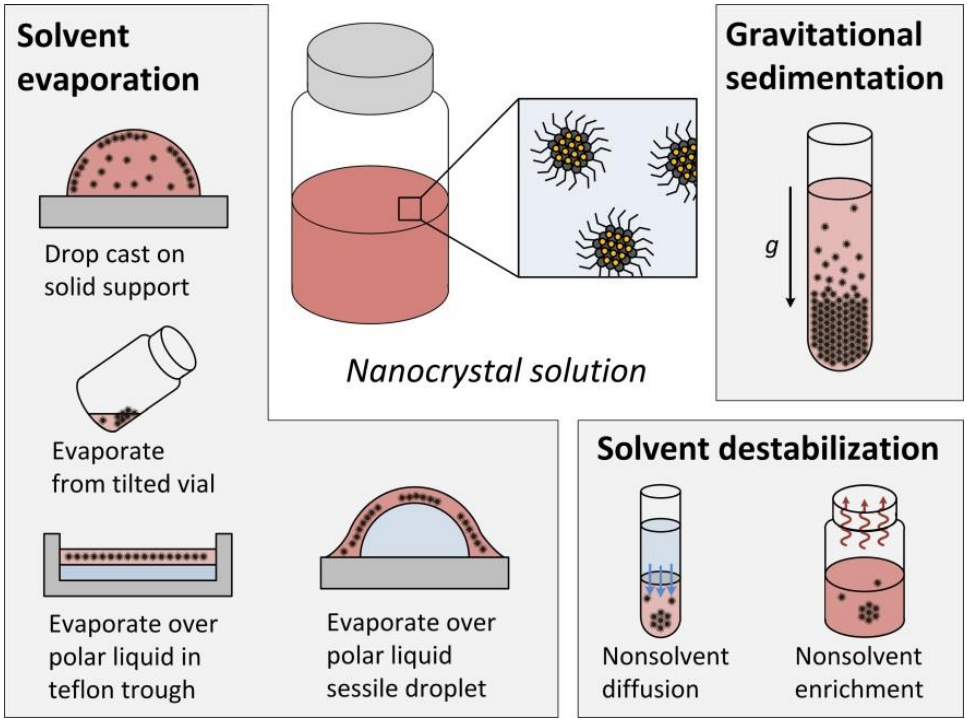

Figure 1.4. Experimental approaches to prepare NC superlattices include various evaporation techniques (left), which produce superlattice thin films, and destabilization or sedimentation techniques (right), which lead to three-dimensional superlattices.

1.4.1. Solvent evaporation

Evaporating a NC solution over a solid or liquid subphase typically produces two-dimensional superlattice thin films. Depending on the initial concentration of the NC solution and the area over which it is spread, such films may be deposited at sub-monolayer coverage and up to several unit cells thick. Evaporation-based assembly takes place at the late stages of evaporation when particles are crowded into a small volume of solvent, leading to superlattice thin films. Often, addition of excess surfactant can assist in the formation of long-range-ordered superlattices by re-passivating bare NC surfaces, preventing solvent dewetting of the subphase, and inducing depletion attraction.[23]

Practically speaking, there are a several methods to prepare NC superlattices via solvent evaporation (Figure 1.4, left). One approach is to simply place a drop (about 10 μL) of dilute NC solution onto solid support and allow it to dry over a couple of minutes. For hydrocarbon-capped NCs, a mixture of hexane and octane (9:1 by volume) has been effective in producing long-range ordered superlattices.[24] Similarly, gentle deposition of a droplet of NC solution upon a surface enables assembly via particle trapping at the air-liquid interface, forming extended two-dimensional superlattice membranes (Figure 1.5a,b).[25] In this approach, early-stage evaporation traps particles at the air-liquid interface, with subsequent nucleation and growth proceeding in two dimensions (Figure 1.5c-e). Evaporation-based assembly can also be carried out in a small vial, permitting tilting of the substrate contained within and resulting control over the direction of meniscus movement.[22] Spreading of NC solution over large substrate areas can be facilitated by doctor blade casting.[26] Polar liquids (e.g., diethylene glycol) immiscible with nonpolar NC solvents have been used as a platform for NC assembly, resulting in extended superlattice thin films (Figure 1.5f-h) which can be subsequently transferred to solid support for characterization.[27] Such an approach may be combined with Langmuir-Blodgett setup to impose lateral surface pressure and controllably condense NC monolayers ordered over wafer-scale areas.[28]

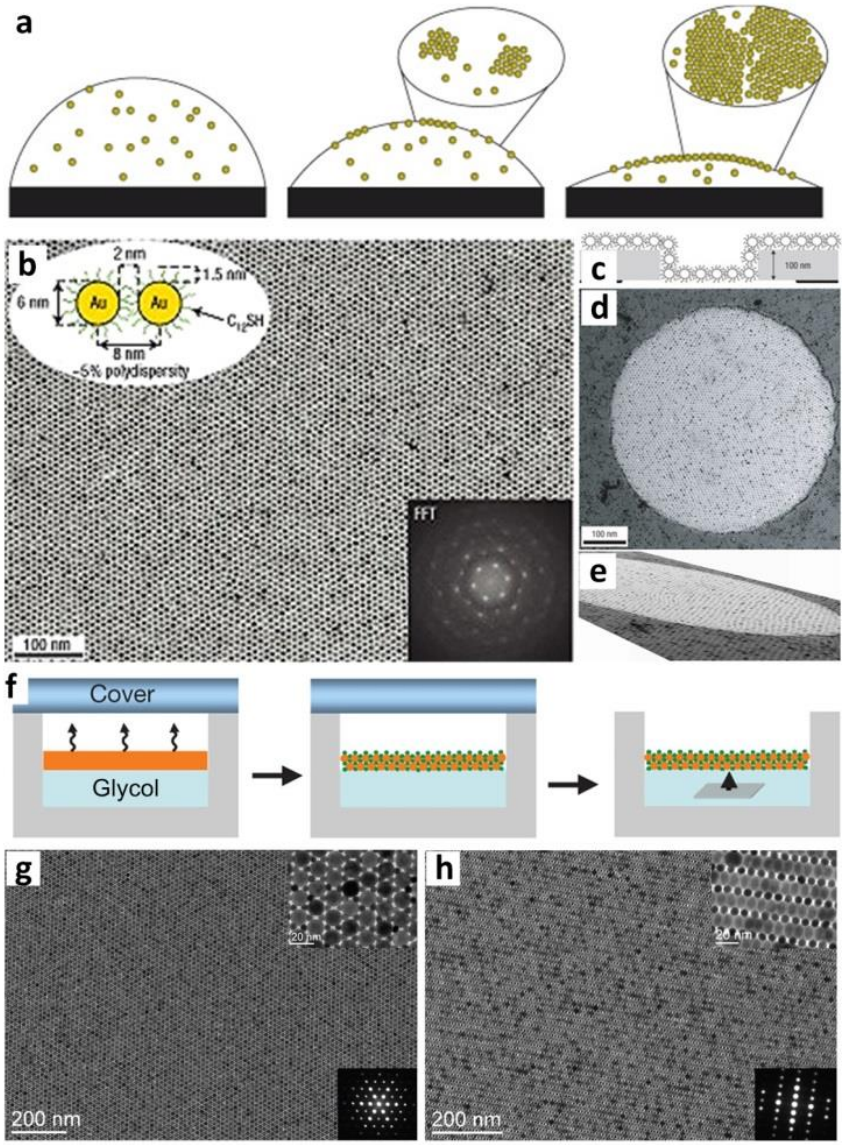

Figure 1.5. Self-assembly of colloidal nanocrystals at the air-liquid interface leads to superlattices with uniform thickness and large domain size. (a) Schematic illustration of Au nanocrystals captured by a quickly receding interface leading to monolayer island growth. (b) TEM overview of a long-range-ordered monolayer with hexagonal symmetry formed by rapid evaporation of a sessile toluene droplet containing 6-nm dodecanethiol-capped Au nanocrystals. Top inset: sketch of a pair of hydrocarbon-capped nanocrystals introducing nanocrystal diameter, ligand length, and interparticle separation; bottom inset: fast Fourier transform (FFT) of the superlattice. Adapted from ref.[23] (c) Sketch of the freestanding superlattice membrane formed by evaporation over a polar liquid subphase. (d) TEM image of a superlattice membrane draped over a 0.5μm-diameter hole, and (e) tilted projection of the same image. Adapted from ref.[29]. (f) Schematic illustration of BNSL interfacial assembly and the substrate transfer process. (g) TEM overview of (100) projection and (h) (110) projection of a AlB_2-type binary nanocrystal superlattice. Top insets: zoom of the structures; bottom insets: electron diffractograms. Adapted from ref.[27]

1.4.2. Solvent destabilization

Destabilization-based assembly (Figure 1.4, lower right) exploits attractive interactions between nanoparticles when solvent intermingling in NC capping layers becomes less favorable than overlap of ligands between neighboring NCs, promoting gradual clustering of NCs in solution. For hydrocarbon-capped NCs, slowly increasing polarity of the solution by controlled diffusion of nonsolvent is effective in inducing flocculation. In practice, this may be accomplished by placing a layer of nonsolvent above a NC solution contained in a test tube (e.g., ethanol above toluene Figure 1.6a), while avoiding significant intermixing of the two liquids during the transfer. Slow intermixing of the miscible liquids over several days induces controlled precipitation of faceted NC superlattices subsequently collected as sediment from the bottom of the tube. Alternatively, slow destabilization may be carried out by heating a premixed solvent/nonsolvent mixture to enrich the higher-boiling nonsolvent component (e.g., octane and 1-octanol).[30]

Such techniques can produce flat platelets (Figure 1.6b-d) or multiply-twinned polyhedra (Figure 1.6e-g) depending on particle size.[14] This general approach has also been used to assemble nanorod[31] and nanoplatelet[32] superlattices. Another destabilization-based technique for achieving three-dimensional superlattices involves inducing solvophobic interactions by disrupting a surfactant bilayer.[33] In this approach dodecyltrimethylammonium bromide (DTAB) surfactant is used to hydrophilize organic-capped NCs, forming a bilayer held together by van der Waals forces between aliphatic chains (Figure 1.6h). Subsequent exposure to polymer-containing ethylene glycol solution at 80°C decomposes the bilayer and leads to the formation of round superlattices with face-centered cubic (*fcc*) internal packing structure (Figure 1.6i-l). This approach has also been used to make spherical and needle-shaped superlattices of nanorods.[34]

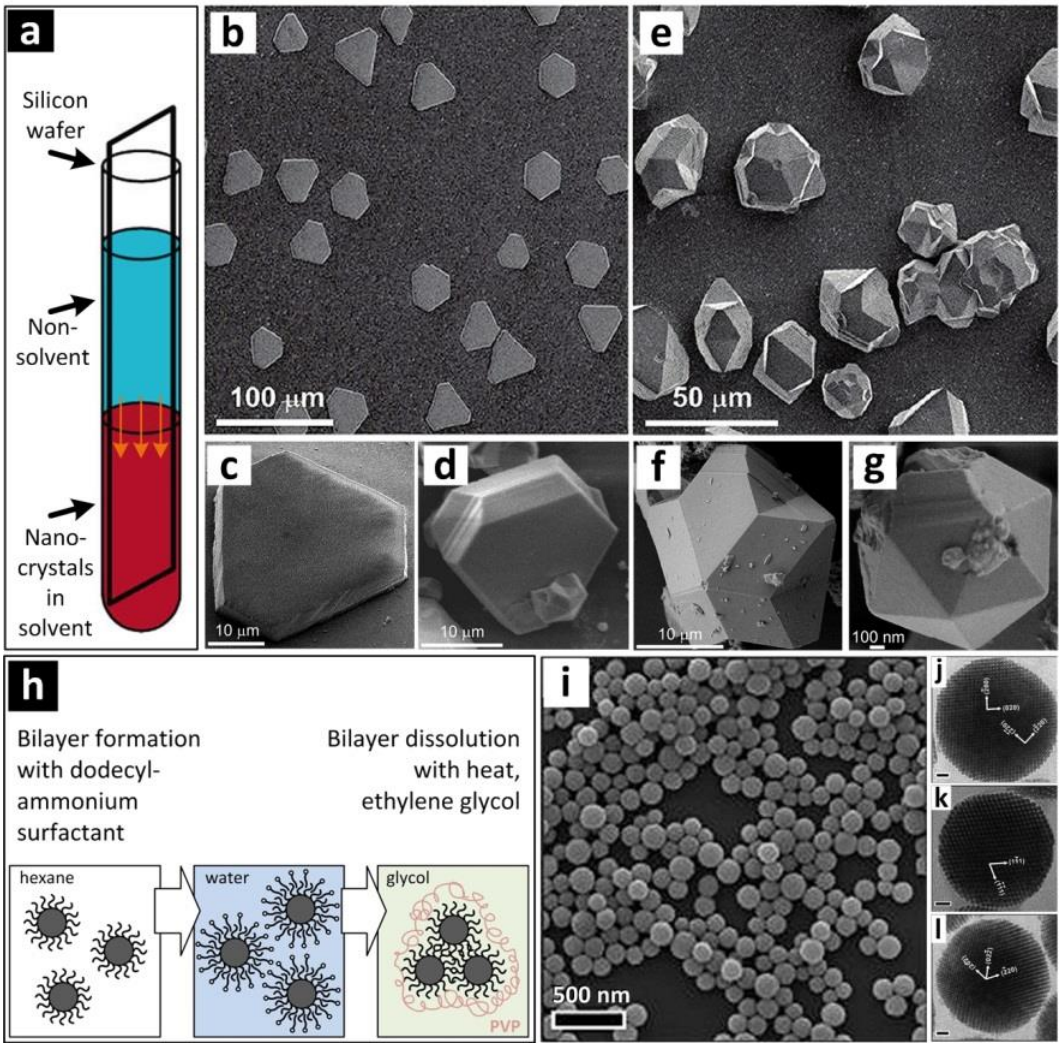

Figure 1.6. Destabilization-based assembly of spherical nanocrystals. (a) Schematic of self-assembly by slow diffusion of the nonsolvent into the dispersed nanocrystal colloid. (b) SEM overview of platelet-shaped superlattices formed from destabilization of a toluene solution of 3-nm PbS nanocrystals. (c,d) SEM zoom of individual platelet superlattices. (e) SEM overview of multiply-twinned superlattices with icosahedral or pentagonal (fivefold) symmetry formed from destabilization of toluene solution of 8-nm PbS nanocrystals. (f,g) SEM zoom of individual polyhedral superlattices. Adapted from ref.[14] (h) Schematic of self-assembly by decomposition of the surfactant bilayer. (i) SEM overview of spherical superparticles produced as shown in (h). (j-l) TEM zoom of individual superparticles with internal *fcc* crystallographic assignment. Scale bars, 20 nm. Adapted from ref.[33]

1.4.3. Nanocrystal sedimentation

A less common approach to assemble NC superlattices exploits gravitational sedimentation (Figure 1.4, upper right). Since gravity biases thermal motion of NCs with diameter approaching one micron, or NC core materials comprised of high-density metals, crowding-induced self-assembly can occur via sedimentation of NCs in the bottom of solvent. The propensity for particles to accumulate in the bottom of solution under the influence of gravity is considered by comparing the relative size of thermal energy k_BT and the gravitational potential energy mgd required to raise a particle of mass m by its own diameter d in Earth's gravity g.[36] The ratio of k_BT to *mgd* scales as d^{-4} and for 10-nm NCs, for example, is approximately 10^6, while for micron-sized particles it is below 1. Accordingly, even in the presence of repulsive interparticle interactions, the largest nano-objects (100 – 1000 nm) are expected to sediment under the force of gravity in all but the densest of liquids.[37]

1.5. Characterization of nanocrystal superlattices

Characterization techniques determine NC position and orientation within a superlattice, the size and orientation of superlattice domains, presence of crystal defects, and existence of secondary structures. Imaging (real-space) and scattering (reciprocal-space) techniques represent a complementary set of approaches for collecting local- and ensemble-structural information. While superlattice preparation requires only basic laboratory supplies typically including solvent, pipet, and a solid substrate (e.g., carbon or silicon), superlattice characterization is often carried out using sophisticated technology such as an electron microscope or a synchrotron facility.

1.5.1. Real-space superlattice characterization

Transmission electron microscopy (TEM) is a common method of probing superlattice structure. This technique sends an electron beam through a thin sample specimen, magnifying and focusing the transmitted electrons onto a detector screen, subsequently displayed on a computer as a digital image. TEM images represent a two-dimensional projection of a three-dimensional structure. Because electron scattering increases with atomic number, TEM image quality is best for high atomic number contrast between sample and support (e.g., PbS NCs on carbon, Figure 1.7a). For this reason, imaging the NC hydrocarbon capping layer can be challenging; however, the use of ultrathin or holey support (i.e., imaging arrays resting on graphene or suspended over a hole) enables partial visualization of the surface-bound molecules (Figure 1.7b).[38] A key strength of TEM for superlattice characterization is the ability to image a NC assembly along various crystallographic directions. In this approach, a series of images of a single domain is collected by tilting the sample holder with respect to the incident electron beam, enabling systematic characterization[39] of superlattices for which an analysis of the normal projection alone may fail to provide an unambiguous assignment (Figure 1.7c). Furthermore,

such a tilt series can be fed into iterative tomographic reconstruction software to obtain a three-dimensional rendering of the imaged superlattice (Figure 1.7d), including reconstruction of slices perpendicular to the plane of the support.[40] Alternatively, such slices may be directly imaged in TEM by physically cutting the superlattice with focused ion beam (Figure 1.7e).[26]

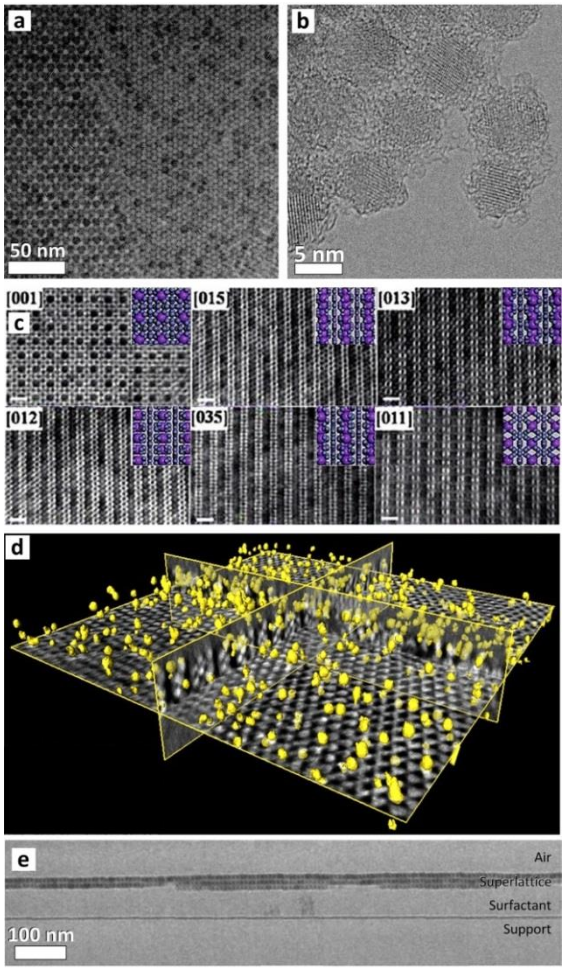

Figure 1.7. Transmission electron microscopy (TEM) characterization of nanocrystals, surface ligands, and self-assembled superlattices. (a) TEM image of *hcp* and *fcc* packing of 7-nm PbS nanocrystals capped with oleic acid surface ligands. (b) TEM image reveals dodecene ligands at the surface of Si NCs suspended over hole in support. Adapted from ref.[38] (c) TEM tilting experiments performed on $NaZn_{13}$-type binary superlattices of two sizes of Fe_3O_4 NCs (scale bars, 20 nm) reveal six different projections of the same structure. Adapted from ref.[39] (d) Tomographic reconstruction of a CdSe superlattice containing Au nanocrystals (highlighted in yellow) distributed randomly as substitutional dopants throughout the structure. Adapted from ref.[40] (e) Cross-sectional TEM image of superlattice of 11-nm $CoFe_2O_4$ nanocrystals obtained by focused ion beam slicing of silica-encapsulated nanocrystal thin film. Adapted from ref.[26]

A useful complement to TEM is scanning electron microscopy (SEM), which scans an electron beam in raster fashion across sample surface, detecting backscattered electrons. This technique probes the specimen surface, enabling imaging of NC superlattices that are too thick to permit electron transmission. SEM has been used to image, for example, three-dimensional polyhedral superlattices produced by solvent destabilization (Figure 1.8a). In addition, SEM is a convenient tool for probing the surface structure of superlattice thin films (Figure 1.8b). Similarly, atomic force microscopy (AFM) is a tool to characterize the surface of NC superlattices (Figure 1.8c). In this case, a probe tip is rastered across the sample surface, providing quantitative topographic information.

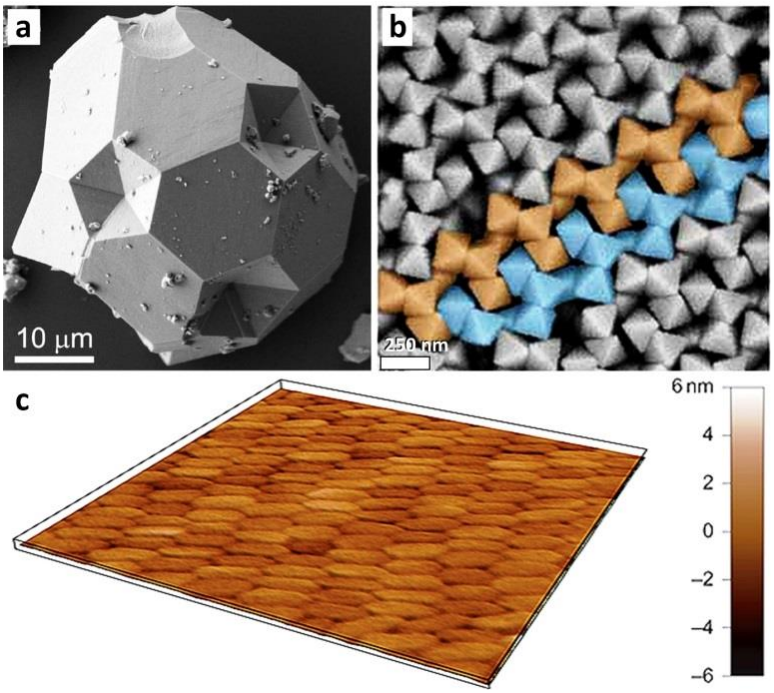

Figure 1.8. Characterization of the superlattice morphology and surface structure using scanning electron microscopy (SEM) and atomic force microscopy (AFM) techniques. (a) SEM image of a twinned three-dimensional superlattice of PbS nanocrystals formed by solvent destabilization. Adapted from ref.[14] (b) Silver octahedra assemble into a complex superstructure that consists of tetramer motifs (accented with false color) as elucidated by high-resolution SEM. Adapted from ref.[37] (c) Height profile of a liquid crystalline array of Au nanorods revealed by AFM. Adapted from ref.[41]

1.5.2. Reciprocal-space superlattice characterization

To obtain structural information averaged over large sample volume and to analyze complex NC superlattices, it is helpful to examine the structure in reciprocal space. One way to do this is to obtain the electron diffraction (ED) pattern of a NC superlattice by collecting transmitted electrons in the TEM diffraction plane. This allows one to distinguish between similar-looking arrangements in real space (Figure 1.9a,b). Analogously, one may perform a fast Fourier transform (FFT) on a real space image, an operation available in common image analysis software packages and numerical libraries. The Fourier transform is a plot of spatial frequencies in a periodic image, with each spot in reciprocal space corresponding to a lattice spacing in the real-space image (Figure 1.9c). In addition to characterizing the position of NCs within a superlattice at small scattering angles, FFT or ED data at high angle offers information concerning the orientation of atomic planes in inorganic cores. Such analysis helps identifying packings with orientational registry of inorganic cores (Figure 1.9c, upper inset).

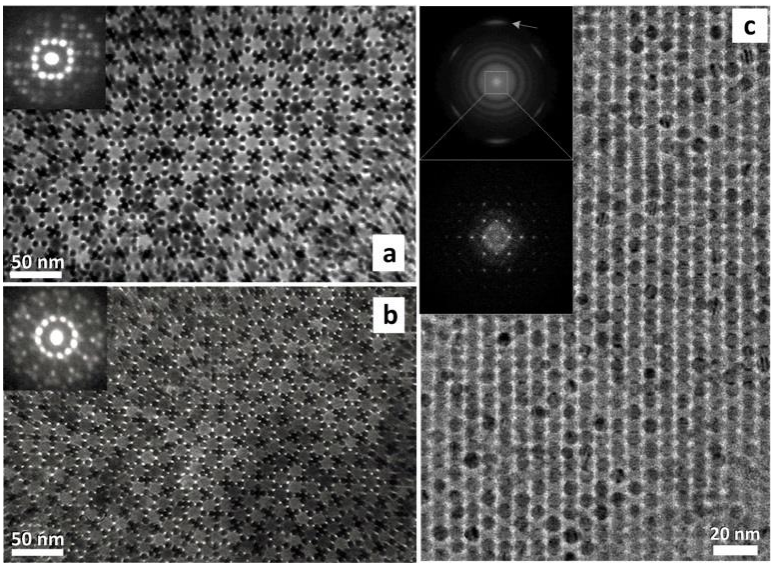

Figure 1.9. Reciprocal space analysis of superlattice thin films. (a) TEM overview of an Archimedean tiling binary superlattice comprised of Au and Fe_3O_4 nanocrystals. Inset: Electron diffractogram reveals fourfold rotational symmetry. (b) TEM overview of a dodecagonal quasicrystal binary superlattice assembled from the same nanocrystals. Inset: Electron diffractogram reveals twelvefold rotational symmetry. Note the clear difference in reciprocal space despite similar appearance of both structures in real space. Adapted from ref.[42] (c) *bcc* superlattice of PbS nanocrystals. Upper inset: FFT shows high-frequency arcs (indicated by arrow), which arise from atomic lattice fringes (wide angle). The presence of the arcs suggests orientational registry of the inorganic NC cores. Lower inset: zoom into the FFT center shows spots corresponding to superlattice periodicity (small angle).

Small-angle x-ray scattering (SAXS) is another powerful tool for characterizing NCs in solution and NC superlattices. SAXS measurement involves elastic scattering of x-radiation (photons of sub-nanometer wavelength) collected at a two-dimensional detector (Figure 1.10a). The intensity of x-rays scattered off a NC ensemble is determined by two parameters, the form factor, which takes into account particle shape and size, and the structure factor, which depends on the spatial arrangement of particles. The form factor dominates SAXS measurement for NCs dispersed in solution, enabling estimation of average particle size and shape as well as their distributions (Figure 1.10b).[43] When NCs are packed into an ordered arrangement, the SAXS pattern shows off-center spots corresponding to Bragg reflections from superlattice planes.

Structural data can be collected in transmission (TSAXS, Figure 1.10c) or reflection (grazing incidence, or GISAXS, Figure 1.10d) modes. Like FFT or ED, wide-angle reflections probe NC orientation within the superlattice. Furthermore, performing the measurement at ambient pressure enables monitoring the self-assembly process in situ as NCs move reversibly between dispersed, colloidal crystalline, and dry states upon solvent evaporation or condensation.[44]

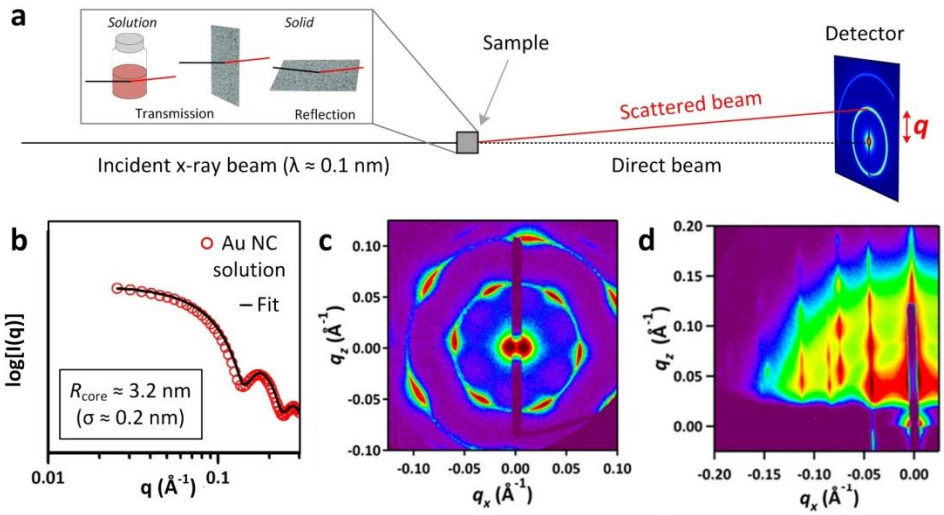

Figure 1.10. Small-angle x-ray scattering (SAXS) analysis of nanocrystal solutions and superlattice thin films. (**a**) Sketch of the SAXS experimental setup. (**b**) Radial profile of SAXS measurement of Au nanocrystals in solution (red circles) with fitted form factor for spheres (black trace). Such an analysis allows for estimation of average core size and standard deviation. Adapted from ref.[45] (**c**) Transmission SAXS measurement shows reflections off superlattice planes within a single domain of close-packed $CoFe_2O_4$ nanocrystals. Red pixels denote areas with highest detected counts. Adapted from ref.[46] (**d**) Grazing-incidence SAXS measurement of AlB_2-type binary superlattice comprised of Bi and Au nanocrystals. Adapted from ref.[46]

1.6. References

1 Murray, C. B., Norris, D. J. & Bawendi, M. G. Synthesis and characterization of nearly monodisperse CdE (E = sulfur, selenium, tellurium) semiconductor nanocrystallites. *Journal of the American Chemical Society* **115**, 8706-8715 (1993).

2 Yin, Y. & Alivisatos, A. P. Colloidal nanocrystal synthesis and the organic-inorganic interface. *Nature* **437**, 664-670 (2005).

3 Guzelian, A. A. *et al.* Synthesis of Size-Selected, Surface-Passivated InP Nanocrystals. *The Journal of Physical Chemistry* **100**, 7212-7219 (1996).

4 Prasad, B. L. V., Stoeva, S. I., Sorensen, C. M. & Klabunde, K. J. Digestive Ripening of Thiolated Gold Nanoparticles: The Effect of Alkyl Chain Length. *Langmuir* **18**, 7515-7520 (2002).

5 Wilcoxon, J. P., Martin, J. E. & Provencio, P. Size Distributions of Gold Nanoclusters Studied by Liquid Chromatography. *Langmuir* **16**, 9912-9920, (2000).

6 Love, J. C., Estroff, L. A., Kriebel, J. K., Nuzzo, R. G. & Whitesides, G. M. Self-Assembled Monolayers of Thiolates on Metals as a Form of Nanotechnology. *Chemical Reviews* **105**, 1103-1170, (2005).

7 Hakkinen, H. The gold-sulfur interface at the nanoscale. *Nat Chem* **4**, 443-455 (2012).

8 Kovalenko, M. V., Scheele, M. & Talapin, D. V. Colloidal Nanocrystals with Molecular Metal Chalcogenide Surface Ligands. *Science* **324**, 1417-1420, (2009).

9 Huang, J. *et al.* Surface Functionalization of Semiconductor and Oxide Nanocrystals with Small Inorganic Oxoanions (PO_4^{3-}, MoO_4^{2-}) and Polyoxometalate Ligands. *ACS Nano* **8**, 9388-9402 (2014).

10 Pellegrino, T. *et al.* Hydrophobic Nanocrystals Coated with an Amphiphilic Polymer Shell: A General Route to Water Soluble Nanocrystals. *Nano Letters* **4**, 703-707, (2004).

11 Silvera Batista, C. A., Larson, R. G. & Kotov, N. A. Nonadditivity of nanoparticle interactions. *Science* **350** (2015).

12 Piner, R. D., Zhu, J., Xu, F., Hong, S. & Mirkin, C. A. "Dip-Pen" Nanolithography. *Science* **283**, 661-663 (1999).

13 Zherebetskyy, D. *et al.* Hydroxylation of the surface of PbS nanocrystals passivated with oleic acid. *Science* **344**, 1380-1384, (2014).

14 Rupich, S. M., Shevchenko, E. V., Bodnarchuk, M. I., Lee, B. & Talapin, D. V. Size-Dependent Multiple Twinning in Nanocrystal Superlattices. *Journal of the American Chemical Society* **132**, 289-296, (2009).

15 Boles, M. A. & Talapin, D. V. Connecting the dots. *Science* **344**, 1340-1341 (2014).

16 Talapin, D. V., Rogach, A. L., Haase, M. & Weller, H. Evolution of an Ensemble of Nanoparticles in a Colloidal Solution: Theoretical Study. *The Journal of Physical Chemistry B* **105**, 12278-12285, (2001).

17 Boles, M. A., Ling, D., Hyeon, T. & Talapin, D. V. The surface science of nanocrystals. *Nat Mater* **15**, 141-153, (2016).

18 Hens, Z. & Martins, J. C. A Solution NMR Toolbox for Characterizing the Surface Chemistry of Colloidal Nanocrystals. *Chemistry of Materials* **25**, 1211-1221, (2013).

19 Badia, A., Cuccia, L., Demers, L., Morin, F. & Lennox, R. B. Structure and Dynamics in Alkanethiolate Monolayers Self-Assembled on Gold Nanoparticles: A DSC, FT-IR, and Deuterium NMR Study. *Journal of the American Chemical Society* **119**, 2682-2692, (1997).

20 Protesescu, L. *et al.* Atomistic Description of Thiostannate-Capped CdSe Nanocrystals: Retention of Four-Coordinate SnS4 Motif and Preservation of Cd-Rich Stoichiometry. *Journal of the American Chemical Society* **137**, 1862-1874, (2015).

21 Chayen, N. E. Turning protein crystallisation from an art into a science. *Current Opinion in Structural Biology* **14**, 577-583, (2004).

22 Bodnarchuk, M. I., Kovalenko, M. V., Heiss, W. & Talapin, D. V. Energetic and Entropic Contributions to Self-Assembly of Binary Nanocrystal Superlattices: Temperature as the Structure-Directing Factor. *Journal of the American Chemical Society* **132**, 11967-11977, (2010).

23 Bigioni, T. P. *et al.* Kinetically driven self assembly of highly ordered nanoparticle monolayers. *Nat Mater* **5**, 265-270, (2006).

24 Talapin, D. V. & Murray, C. B. PbSe Nanocrystal Solids for n- and p-Channel Thin Film Field-Effect Transistors. *Science* **310**, 86-89, (2005).

25 He, J. *et al.* Fabrication and Mechanical Properties of Large-Scale Freestanding Nanoparticle Membranes. *Small* **6**, 1449-1456, (2010).

26 Bodnarchuk, M. I. *et al.* Large-Area Ordered Superlattices from Magnetic Wüstite/Cobalt Ferrite Core/Shell Nanocrystals by Doctor Blade Casting. *ACS Nano* **4**, 423-431, (2009).

27 Dong, A., Chen, J., Vora, P. M., Kikkawa, J. M. & Murray, C. B. Binary nanocrystal superlattice membranes self-assembled at the liquid-air interface. *Nature* **466**, 474-477, (2010).

28 Aleksandrovic, V. *et al.* Preparation and Electrical Properties of Cobalt−Platinum Nanoparticle Monolayers Deposited by the Langmuir−Blodgett Technique. *ACS Nano* **2**, 1123-1130, (2008).

29 Mueggenburg, K. E., Lin, X.-M., Goldsmith, R. H. & Jaeger, H. M. Elastic membranes of close-packed nanoparticle arrays. *Nat Mater* **6**, 656-660, (2007).

30 Murray, C. B., Kagan, C. R. & Bawendi, M. G. Self-Organization of CdSe Nanocrystallites into Three-Dimensional Quantum Dot Superlattices. *Science* **270**, 1335-1338, (1995).

31 Talapin, D. V. *et al.* CdSe and CdSe/CdS Nanorod Solids. *Journal of the American Chemical Society* **126**, 12984-12988, (2004).

32 Abécassis, B., Tessier, M. D., Davidson, P. & Dubertret, B. Self-Assembly of CdSe Nanoplatelets into Giant Micrometer-Scale Needles Emitting Polarized Light. *Nano Letters* **14**, 710-715, (2014).

33 Zhuang, J., Wu, H., Yang, Y. & Cao, Y. C. Supercrystalline Colloidal Particles from Artificial Atoms. *Journal of the American Chemical Society* **129**, 14166-14167, (2007).

34 Wang, T. *et al.* Self-Assembled Colloidal Superparticles from Nanorods. *Science* **338**, 358-363 (2012).

35 P, A. & de Paula, J. *Physical Chemistry*. (Oxford University Press, 2006).

36 Jaeger, H. M., Nagel, S. R. & Behringer, R. P. Granular solids, liquids, and gases. *Reviews of Modern Physics* **68**, 1259-1273 (1996).

37 Henzie, J., Grünwald, M., Widmer-Cooper, A., Geissler, P. L. & Yang, P. Self-assembly of uniform polyhedral silver nanocrystals into densest packings and exotic superlattices. *Nat Mater* **11**, 131-137, (2012).

38 Panthani, M. G. *et al.* Graphene-Supported High-Resolution TEM and STEM Imaging of Silicon Nanocrystals and their Capping Ligands. *The Journal of Physical Chemistry C* **116**, 22463-22468, (2012).

39 Chen, J., Ye, X. & Murray, C. B. Systematic Electron Crystallographic Studies of Self-Assembled Binary Nanocrystal Superlattices. *ACS Nano* **4**, 2374-2381, (2010).

40 Cargnello, M. *et al.* Substitutional doping in nanocrystal superlattices. *Nature* **524**, 450-453, (2015).

41 Ye, X. *et al.* Competition of shape and interaction patchiness for self-assembling nanoplates. *Nat Chem* **5**, 466-473, (2013).

42 Talapin, D. V. *et al.* Quasicrystalline order in self-assembled binary nanoparticle superlattices. *Nature* **461**, 964-967, (2009).

43 Senesi, A. & Lee, B. Scattering functions of polyhedra. *Journal of Applied Crystallography* **48**, 565-577, (2015).

44 Weidman, M. C., Smilgies, D.-M. & Tisdale, W. A. Kinetics of the self-assembly of nanocrystal superlattices measured by real-time in situ X-ray scattering. *Nat Mater* advance online publication, (2016).

45 Diroll, B. T. *et al.* Quantifying “Softness” of Organic Coatings on Gold Nanoparticles Using Correlated Small-Angle X-ray and Neutron Scattering. *Nano Letters*, (2015).

46 Diroll, B. T. *et al.* X-ray Mapping of Nanoparticle Superlattice Thin Films. *ACS Nano* **8**, 12843-12850, (2014).

2. Nanocrystal surfaces: structure, reactivity, and influence over core properties

All nanomaterials share a common feature of large surface-to-volume ratio, making their surfaces the dominant player in many physical and chemical processes. Surface ligands — molecules that bind to the surface — are an essential component of nanomaterial synthesis, processing and application. Understanding the structure and properties of nanoscale interfaces requires an intricate mix of concepts and techniques borrowed from surface science and coordination chemistry. This chapter elaborates these connections and discusses the bonding, electronic structure and chemical transformations at nanomaterial surfaces, specifically focusing on the role of surface ligands in tuning and rationally designing properties of functional nanomaterials.

A bulk solid contains only a small concentration of surface atoms; as a result, broken chemical bonds on the exterior contribute minimally to material properties. For any substance, however, the surface-to-volume ratio scales inversely with linear dimensions. With shrinking size, the role of the surface increases, eventually becoming dominant. At the nanoscale, surfaces can significantly alter some properties (for example solubility or luminescence[1]) and generate completely new effects (such as surface plasmon resonance[2] or size-dependent catalytic activity[3]). This chapter shines a spotlight on the surface of nanomaterials and discusses various strategies to tame and make use of it. For the sake of consistency, we focus our discussion on nanocrystals (NCs), but most concepts can be applied to one-dimensional nanowires, two-dimensional nanoplatelets and other nanoscale objects.

Traditional surface science has established that the surfaces of large crystals can lower their energy by moving surface atoms away from lattice sites in the process of surface reconstruction,[4] dangling bonds can introduce new electronic states,[5] and foreign molecules (surfactants or adsorbates) can alter the energy and reactivity of a crystal surface.[6] All of these effects apply to NCs, although the small facet size and multiple edge- and corner sites complicate analysis and quantitative description. On the other hand, the chemical bond between a NC surface atom and surfactant molecule is similar to that between a metal ion and ligand in a coordination complex, offering a useful analogy between NCs and molecular compounds. We will use the term 'surface ligands' here to emphasize this surfactant–ligand duality. The set of ligands attached to a NC forms a 'capping' layer that saturates dangling bonds, screens the particle from its environment, and controls nucleation and growth kinetics during synthesis.[7] Ligands also influence the optical and electronic properties of NCs, and provide steric or electrostatic stabilization of the colloidal state required for NC synthesis, processing and some applications. Ligand exchange reactions extend the versatility of NC materials by allowing replacement of ligands optimized for synthesis with application-targeted species including organic or inorganic ions, clusters, and polymers.[8]

2.1. Structure and bonding at the nanocrystal-ligand interface

Nanocrystals consist of hundreds to thousands of atoms. Such particles are typically synthesized in a solution containing surface ligands with an anchoring headgroup tethered to the NC surface and a hydrocarbon tail directed away from it (Figure 2.1a). The equilibrium shape of the inorganic core minimizes the energy of exposed surface area and facet-specific energy of broken bonds. A polyhedral core, displaying only high-coordination surface atoms and slightly more exposed area than a sphere, is typical. For example, Au and PbS NCs often adopt a

cuboctahedral shape, terminated by (111) and (100) facets with the hexagonal and square arrangements of surface atoms shown in Figure 1.1b. If surface ligands selectively bind to certain facets of a growing NC, they reduce the surface energy of these facets relative to others. The ligand layer can also block delivery of new reagents to the NC surface. These thermodynamic and kinetic factors are widely used for synthesis of NCs with anisotropic shapes such as rods[9] and platelets.[10] The capping layer protecting each NC facet can be viewed as a miniature self-assembled monolayer (SAM). First prepared and characterized in the 1980s,[11] SAMs have served as the foundation for understanding organic/inorganic interfaces and provide a convenient starting point to describe NC surface ligands. For example, the binding pattern of *n*-alkanethiolate on extended Au (111) and (001) surfaces[12] can be used to create a first approximation of the capping layer protecting a cuboctahedral Au NC. The strong interaction between gold and sulfur atoms (~2 eV)[13] drives free surfactants to bind tightly to the metal surface. A weaker van der Waals interaction between hydrocarbon tails (~0.07 eV per CH_2 group[13]) encourages dense packing in the organic overlayer. On a flat surface, given time to adsorb and relax, a crystalline arrangement of surfactant molecules is formed in registry with the underlying substrate, with sulfurs typically occupying three-fold sites and alkyl tails tilted approximately 30° from the surface normal (Figure 1.1b). SAM grafting density is limited by the steric bulk of alkyl tails: the organic layer fills space completely, whereas the sulphur atoms remain separated by ~3 van der Waals diameters16 (Figure 1.1c). In addition to this 'standard model', alternative binding motifs including the RS–Au–SR 'staple' structure can be important at low surface coverage.[14]

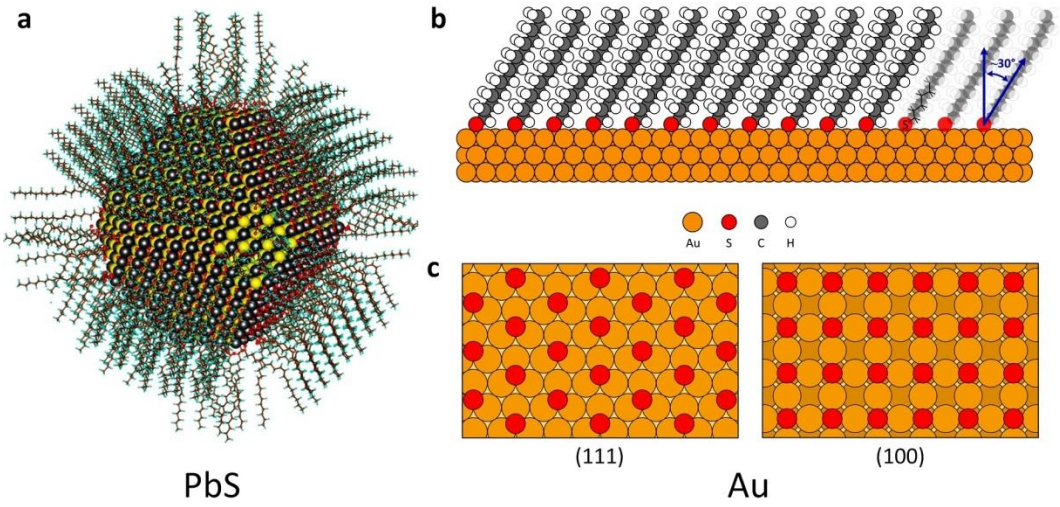

Figure 2.1. Capping-layer structure. (a) Calculated atomic structure of 5-nm diameter PbS NC capped with oleic acid. PbS(111) surfaces are terminated by oleate and hydroxide ions, PbS(100) by oleic acid. Adapted from ref.[15] (b) Binding pattern of sulfur headgroups (red spheres) on Au (111) and (100) facets. (c) Sketch of self-assembled monolayer (SAM) of hexadecanethiol molecules adsorbed to Au(111) surface as an idealized picture of a nanocrystal capping layer. Hydrocarbon chains are fully extended, tilted with respect to the surface normal, and in all-*trans* configuration. Adapted from ref.[13]

In contrast to extended flat surfaces, NC surfaces are encircled by vertex and edge sites, providing grafted chains with extra volume (Figure 2.1a). The relaxed competition for space between alkyl tails minimizes the role of hydrocarbon steric bulk in determining the grafting density of surfactants on NCs. As a result, higher capping-layer coverage is possible: 3-nm Au NCs can support n-decanethiolate surface densities of 6 nm^{-2}, as compared with 3 nm^{-2} on extended Au(111) (ref.[16]). Open space in the NC capping layer allows penetration of solvent molecules or ligand chains of neighboring NCs. This extra space also provides room for rotational conformations not available to molecules packed in a SAM, resulting in significant structural disorder: *gauche* defects are concentrated in the ends of alkyl chains and propagate towards the middle with increasing temperature.[17] Generally, capping-layer order is maximized for longer (C_{12}–C_{18}) chains tethered to the surface of larger-diameter (>5 nm) NCs.[18] Nanometer

dimensions and intrinsic heterogeneity (each NC typically exposes several facets with different patterns of surface atoms) make experimental study of NC surfaces challenging. Currently there is no technique that provides atomic-level reconstruction of the NC capping layer. Instead, a suite of methods should be applied to obtain complementary bits of information about the NC–ligand bonding, capping-layer structure, and interactions between surface ligands and the surrounding environment (see Chapter 1).[19]

Interaction between the NC core and ligand headgroup can be rationalized using the classification of covalent bonds,[20] originally proposed for metal coordination complexes and adapted to NCs by Owen and co-workers (Figure 2.2a).[21] Without going into full technical details, three classes of metal–ligand interaction may be distinguished based on the number of electrons involved, and the identity of the electron donor and acceptor groups. *L*-type ligands are neutral two-electron donors with a lone electron pair that datively coordinates surface metal atoms. Amines (RNH_2), phosphines (R_3P) and phosphine oxides (R_3PO) are examples of *L*-type ligands. *X*-type ligands are species that, in neutral form, have an odd number of valence-shell electrons, requiring one electron from the NC surface site to form a two-electron covalent bond. In practice, *M–X* bonds often cleave heterolytically, forming ionic, closed-shell fragments. As such, *X*-type ligands can be neutral radicals binding neutral surface sites (each with an unpaired electron) or, more commonly, monovalent ions binding oppositely charged sites at the NC surface. Examples of *X*-type ligands include carboxylates ($RCOO^-$), thiolates (RS^-) and phosphonates ($RPO(OH)O^-$), as well as inorganic ions (such as Cl^-, $InCl_4^-$, AsS_3^{3-}) or bound ion pairs (for example, $NEt_4^+I^-$) in nonpolar solvent. Nucleophilic (electron-rich) *L*- and *X*-type ligands bind to electron-deficient (electrophilic) surface sites with pronounced Lewis acidity, typically undercoordinated metal ions at the NC surface. The surface of metal chalcogenides,

oxides and other compound NCs also exposes electron-rich Lewis basic sites. These sites can interact with *Z*-type ligands, such as $Pb(OOCR)_2$ or $CdCl_2$, which bind through the metal atom as two-electron acceptors.[21] In addition, the surface of oxide NCs can bind protons (H^+), an example of positively charged, electrophilic *X*-type ligands.[22]

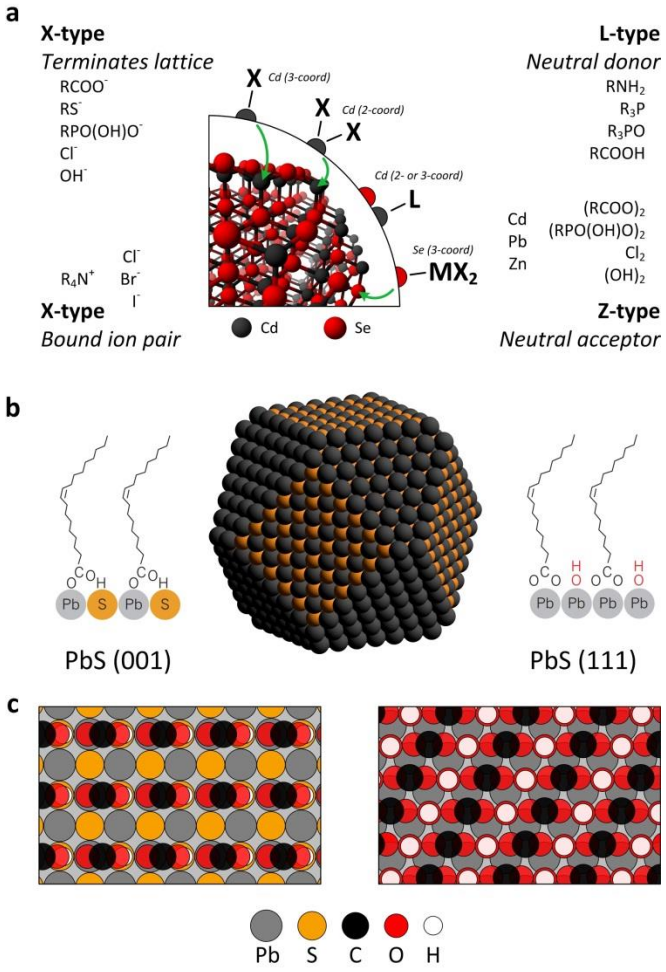

Figure 2.2. Chemistry of ligand binding. (a) Classification of ligand binding motifs at the surface of a CdSe nanocrystal. Adapted from ref.[21] Anionic *X*-type ligands bind to surface cations imparting electroneutrality to metal-rich NC facets. Neutral *L*-type electron donor ligands attach to electrophilic metal sites on stoichiometric NC facets. Neutral *Z*-type electron acceptor ligands bind to electron-rich undercoordinated Se atoms. Green arrows highlight examples of such atoms at the surface of a CdSe nanocrystal model. (b) Modeled 5-nm cuboctahedral PbS NC (center) with simplified illustrations of oleic acid binding as *L*-type ligand to (100) facets (left) and binding together with hydroxide as *X*-type oleate on Pb-terminated (111) facets (right). Adapted from ref.[23] (c,d) Sketches of calculated surface structure on PbS(100) and PbS(111). Adapted from ref.[15]

Following this classification, the composition and surface chemistry of NCs can be expressed in a convenient way. Cadmium selenide NCs, for example, capped by a combination of *L*- and *X*-type ligands, can be described as $(CdSe)_m(Cd_nX_pL_q)$, where *m* relates to the size of the NC core and *n*, *p* and *q* describe the ligand shell composition. Depending on the nature of exposed NC facets (polar or nonpolar), *L*- or *X*-type ligation can dominate. The measurement of metal-to-chalcogen ratio provides a simple way to access this information. CdSe and PbSe NCs synthesized in the presence of *X*-type ligands show metal-to-selenium ratios significantly exceeding unity.[24] In nonpolar solvents such as hexane or toluene, a large energetic penalty for charge separation requires the ratio between *L*- and *X*-type ligands to satisfy electrostatic neutrality and fit the formula $(CdSe)_m(CdX_2)_nL_q$. The last expression is particularly useful for describing neutral NCs capped with one kind of *X*-type and one kind of *L*-type ligand. On the other hand, in polar solvents such as water or dimethylformamide, NCs can carry charge: $[(CdSe)_m(Cd_nX_{2n+s}L_q)]^{s-}$ or $[(CdSe)_m(Cd_nX_{2n-s}L_q)]^{s+}$ compensated by counterions from the diffuse ion cloud around each NC in solution. The NC can support approximately one elemental charge per square nanometer of surface, or a few tens of charges per particle.[25] Such charging plays an important role in electrostatic stabilization of NC colloids (see Chapter 3).

Recent computational studies have revealed some counterintuitive aspects of NC surfaces subsequently verified by experiments. For example, density functional theory (DFT) calculations indicate that oleic acid (OAH), commonly used for NC synthesis, binds to the (100) facet of a PbS NC (the surface presenting a 'checkerboard' arrangement of lead and sulfur atoms; Figure 2.2b,c) as a bidentate *L*-type ligand with energy 0.16 eV per ligand. On the other hand, (111) facets of PbS NCs present a hexagonal layer of Pb atoms (Figure 2.2b,d) and develop a very different motif, with *X*-type oleate ions (OA^-) binding to surface Pb atoms more strongly at

0.52 eV per ligand.[15] The density of Pb atoms on PbS (111) surface (~8 Pb atoms nm^{-2}), however, prevents sterically demanding oleate ligands (the footprint of COO^- headgroup is ~0.3 nm^2) from saturating all dangling bonds. Both DFT calculations and experimental x-ray photoelectron spectroscopy (XPS) studies reported in ref.[15] suggest that compact *X*-type ligands (for example OH^-) bind to the PbS (111) facet together with bulky OA^- ligands (Figure 2.2d). Surface energy minimization suggests the following composition for 5-nm PbS NCs: $(PbS)_m[Pb_{(n+p)}(OH)_{2n}(OA)_{2p}(OAH)_q]$, with m = 1,385, n = 149, p = 120 and q = 48, where the ratio n:p may change depending on conditions (such as the water content in the synthesis solution). Existing experimental data support the computationally derived model of a cation-rich NC surface.[26] It is likely that the 'undercoat' of small *X*-type ligands (such as OH^- or Cl^-) is a common feature of most NC surfaces, incorporated (intentionally or not) through side reactions during NC synthesis.

2.2. Ligand exchange reactions

Surface ligands with *L*- or *X*-type headgroup and a hydrocarbon tail allow impressive control over the kinetics of NC nucleation and growth. In many cases, however, these ligands must be replaced by other surface-binding species better suited to the end application. The exchange of NC surface ligands is reminiscent of substitution reactions in coordination complexes. Solvent polarity and coordinating ability can affect the kinetics and mechanism of ligand exchange reactions at the NC surface. Typically, steric crowding of molecules in the capping layer favors a dissociative pathway that requires a bound ligand to desorb from the NC before a new one may enter from solution and attach to the surface. In nonpolar solvents, all species involved in the exchange reaction should be electrically neutral. For this reason, *L*-type

ligands (for example octylamine[27] on CdSe) rapidly adsorb and desorb from the NC surface at room temperature (exchanging species highlighted in bold):

$$(CdSe)_m(CdX_2)_n\mathbf{L}_q + \mathbf{L}' \rightarrow (CdSe)_m(CdX_2)_nL_{q-1}\mathbf{L}' + \mathbf{L} \quad (1)$$

L, L′ = RNH_2, R_3P, R_3PO, RCOOH or pyridine, for example. However, *X*-type ligands (for example oleate or phosphonate on CdSe) remain tightly bound because of the electrostatic penalty for charging induced by self-desorption of *X*-type ligands. Similarly, neutral *Z*-type ligands (for example cadmium oleate) can be displaced by other metal complexes[28]:

$$(CdSe)_m(\mathbf{CdX_2})_nL_q + \mathbf{Z}' \rightarrow (CdSe)_m(CdX_2)_{n-1}\mathbf{Z}'L_q + \mathbf{CdX_2} \quad (2)$$

Z′ = $Cd(RCOO)_2$, $Cd(RPO(OH)O)_2$, $CdCl_2$ or $AlCl_3$, for example.

On the other hand, exchange of tightly bound *X*-type ligands in nonpolar solution probably takes place by an associative pathway.[29] Replacement of these charged ligands can occur by cation transfer, whereby incoming and outgoing species exchange a proton[30] or other cation (for example trimethylsilyl[31] or alkylammonium):

$$(CdSe)_m(CdX_2)_{n-1}Cd\mathbf{X}_2L_q + \mathbf{EX}' \rightarrow (CdSe)_m(CdX_2)_{n-1}CdX\mathbf{X}'L_q + \mathbf{EX} \quad (3)$$

X, X′ = $RCOO^-$, $RPO(OH)O^-$, OH^- or Cl^-, for example; E = H^+, $(CH_3)_3Si^+$ or NR_4^+, for example.

Direct exchange of *X*-type for *L*-type ligands disturbs charge neutrality of the NC and is therefore highly unfavorable in nonpolar environments. Observation of such reactions (for example the exchange of *X*-type carboxylate or phosphonate ligands with *L*-type pyridine[32]) can be rationalized as a ligand-promoted *Z*-type displacement process,[21] where an incoming *L*-type

ligand aids the removal of an *X*-type ligand as a neutral metal–ligand complex, followed by coordination of the *L*-type ligand to the metal site on the (now charge-neutral) NC surface:

$$(CdSe)_m(\mathbf{CdX_2})_nL_q + \mathbf{2L'} \rightarrow (CdSe)_m(CdX_2)_{n-1}L_q\mathbf{L'} + \mathbf{L'\text{-}CdX_2} \quad (4)$$

X = $RCOO^-$ or $RPO(OH)O^-$, for example; L = pyridine or RNH_2, for example.

Oxide NCs can bind neutral carboxylic acid ligands as pairs of negatively and positively charged *X*-type ligands ($RCOO^-$ and H^+, respectively), thus offering a pathway for exchange between *L*- and *X*-type ligands.[22] Along these lines, since the *L*-, *X*-, *Z*-type classification of NC ligands was developed primarily from experiments with CdSe, future work beyond the model systems will be important to assess the generality of such a framework for rationalizing inorganic core composition, feasible ligand exchange reactions and other aspects of NC surface chemistry.

The use of polar solvents lifts the requirement for an electrically neutral NC surface, permitting additional ligand exchange pathways. As a result, in polar solvents, charged *X*-type ligands can desorb and exchange via dissociative pathways[33]:

$$[(CdSe)_m(Cd_n\mathbf{X_{2n+s}}L_q)]^{s-} + \mathbf{X'^-} \rightarrow [(CdSe)_m(Cd_nX_{2n+s-1}\mathbf{X'}L_q)]^{s-} + \mathbf{X^-} \quad (5)$$

X, X′ = $RCOO^-$, $(NH_4)S^-$, SCN^-, $In_2Se_4^{2-}$ or $PbCl_3^-$, for example.

Moreover, special reagents (HBF_4 or Et_3OBF_4) can be used to selectively attack and cleave the NC–ligand bond by protonation or alkylation of surface ligands.[25] Cleavage of *X*-type ligands in the presence of weakly nucleophilic anions (for example BF_4^- or PF_6^-) leaves behind uncompensated positive surface charge that allows electrostatic stabilization and further functionalization of the NC surface by weakly coordinating labile solvent molecules:

$$(CdSe)_m(CdX_2)_nL_q + 2n\mathbf{EBF_4} + p\mathbf{L'} \rightarrow$$

$$[(CdSe)_m(Cd_nL_q\mathbf{L'_p})]_{2n}^{+} + 2n\mathbf{BF_4}^{-} + [2n\mathbf{EX}] \quad (6)$$

E = H^+, Et_3O^+ or NO^+, for example; L′ = DMF.

Completion of ligand exchange is influenced by the difference in ligand affinities to the NC surface and the relative abundance of incoming and outgoing ligands. Although mass action favours binding of the ligand present in excess, headgroup-specific surface affinity can prevent displacement of strongly binding species (for example phosphonate-capped CdSe in the presence of oleic acid[34]). The ligand affinity can be rationalized in terms of electronic, entropic and steric effects. The first case can be illustrated by application of the hard–soft acid–base (HSAB) principle[35] for predicting the strength of NC–ligand binding. Classifying Lewis acids and bases into 'hard' and 'soft' categories, HSAB anticipates that strong bonds are formed by electrostatic interaction between hard Lewis acid–base pairs and by covalent interaction between soft pairs, whereas weak association is observed between members of opposite groups. The gold–sulfur bond, a classic example of robust association between soft species, is widely used to anchor ligands to the surface of Au NCs.[14] In contrast, hard bases (for example ligands with oxygen-containing headgroups such as carboxylates) show poor affinity to Au NCs with soft surface sites but bind strongly to NCs with more ionic lattices and harder surface sites, such as ZnSe and CdSe (ref.[25]). For compound NCs, the hardness of metal surface sites depends on the hardness of the anion sublattice. For example, although the free In^{3+} ion is itself a hard Lewis acid, indium sites on the InAs NC surface are bound to several soft arsenic atoms, and thus rendered rather soft Lewis acids.[25] In molecular chemistry this is known as the 'symbiotic effect', where soft (hard) ligands soften (harden) the atom to which they are bound.[35] The effective strength of capping-layer adhesion can be significantly increased through the chelate effect, accounting for

enhanced affinity of ligands containing two or more binding groups as compared with monodentate ligands. Examples of chelating ligands include molecules containing carboxylate, dopamine[36] and dithiol (for example dihydrolipoic acid[37]) anchoring groups. Steric effects also play a role in capping-layer attachment: bulky tert-butylthiolate ligands pack on CdSe NC surface at ~2 nm^{-2} at full coverage[38] as compared with ~4 nm^{-2} packing of *n*-alkylthiolate ligands.[39]

Although metal coordination complexes serve as a convenient foundation for understanding NC–ligand binding, the transfer of concepts explaining binding strength (such as HSAB, chelation or steric profile) from molecular to NC systems is not entirely straightforward. For example, interaction of a ligand with various crystallographic facet surface patterns and edge/vertex sites opens up a manifold of potential binding modes and corresponding NC– ligand affinities. Future computational efforts must confront the intrinsic heterogeneity of such systems by considering binding of a given ligand across categories of surface atoms, taking into account potential differences in hard/soft character and steric accessibility of each unique surface site. Such work may allow identification of the factors or qualitative chemical concepts, if any, that govern the strength of NC–ligand binding.

2.3. Surface ligands and nanocrystal electronic structure

Surface ligands can directly influence the optical, electrical, magnetic and catalytic properties of NCs. Here we use semiconductor quantum dots (QDs) to demonstrate examples of such effects. In a QD, the valence and conduction bands are split into discrete, quantum-confined states[40] that give rise to size-tunable luminescence colors. However, undercoordinated surface atoms with dangling bonds often contribute a set of electronic states with energies lying between the highest occupied and lowest unoccupied quantum-confined orbitals of the QD (Figure 2.3a,

red lines). These localized states behave as traps for electrons or holes, quenching luminescence and hampering the performance of NC-based devices.

Bonding between the NC surface atom and ligand frontier orbital generates a new set of molecular orbitals with bonding (σ) and antibonding (σ*) character, with bonding orbitals stabilized and antibonding orbitals destabilized with respect to the energies of non-interacting surface atom and ligand (Figure 2.3a). The formation of a strong covalent bond between the surface atom and ligand shifts the energies of σ- and σ*-orbitals outside the bandgap and cleans the bandgap of trap states responsible for fast nonradiative recombination. This molecular orbital picture agrees with DFT calculations showing the disappearance of mid-gap states in ligand-passivated NCs.[41]

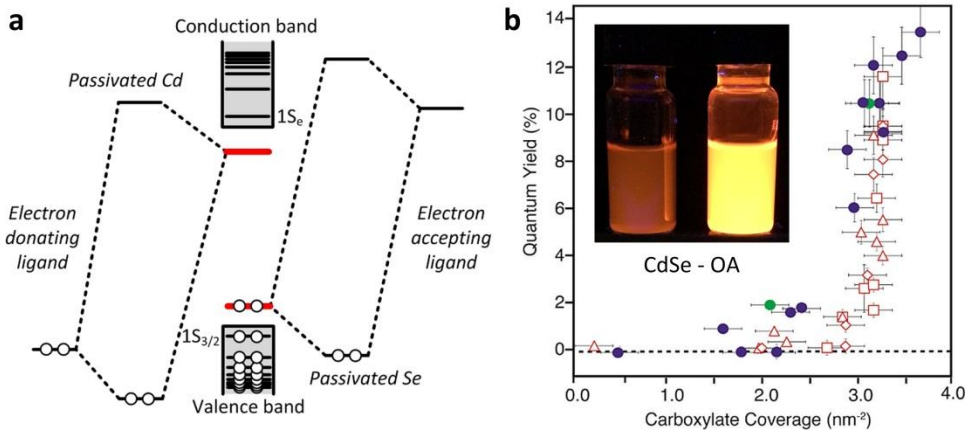

Figure 2.3. Effect of ligands on nanocrystal surface states. (a) Simplified molecular orbital diagram of a CdSe quantum dot showing that the energies of Cd and Se surface electronic states (red levels) are pushed outside the bandgap upon ligand binding. HOMO, highest occupied molecular orbital; LUMO, lowest unoccupied molecular orbital. (b) Experimental photoluminescence quantum yield of CdSe quantum dot samples with different cadmium oleate (OA) surface coverage. Different symbols correspond to various conditions of the nanocrystal surface treatment with the Lewis base *L'* = $(CH_3)_2NCH_2CH_2N(CH_3)_2$ as described in equation 4. Error bars represent uncertainty of ligand surface density and nanocrystal solution concentration estimates. Inset: photograph of colloidal CdSe quantum dots with high coverage (right) and low coverage (left) of oleate ligands.

Preserving QD luminescence requires elimination of mid-gap trap states. However, the relationship between saturation of surface sites and NC electronic structure is not yet clear. For example, despite a CdSe surface atom density of ~6 nm^{-2}, a tremendous drop in CdSe luminescence occurs at modest oleate coverage of ~3 nm^{-2} (ref.[21], Figure 2.3b). As such, establishing the link between NC surface structure and optical properties remains a crucial open question in the field. Surface passivation upon ligand binding is common but not universal: some ligands introduce new mid-gap electronic states and increase the rate of non-radiative relaxation: alkanethiol ligands, for example, quench luminescence of CdSe QDs by fast hole trapping.[42]

Ligands can also influence the absolute energy of QD electronic states. Figure 2.4a shows the energies of 1S(h) and 1S(e) states of PbS QDs (~3.5 nm diameter), measured by ultraviolet photoelectron spectroscopy (UPS), when capped with different surface ligands. The observed variation of band energies (~0.9 eV) across several ligand choices is large enough to be comparable to the bandgap (~1.2 eV) of these QDs. This effect has electrostatic origin: a surface-bound ligand molecule generates an electric dipole. If dipoles point toward the NC center, the electric field potential shifts all energy levels down, and for the opposite case, vice-versa (Figure 2.4b).[43] The orientation and magnitude of the surface dipole is determined by two competing contributions: the interfacial dipole formed between the surface atom and ligand headgroup, and any intrinsic dipole associated with ligand molecular structure. For Lewis-basic ligands, the interfacial dipole points from the ligand towards the metal ($L^{\delta-} \rightarrow M^{\delta+}$), while the intrinsic ligand dipole depends on its chemical structure and binding mode, approaching zero for atomic ligands (halides, for example). The largest ligand-induced downward shift of electronic energy levels is observed for halide ion ligands (Figure 2.4a). Because all energy levels are shifted by the same energy, this effect is not observable in absorption or luminescence spectra. However, because the

energy of highest occupied and lowest unoccupied states dictates ionization potential and electron affinity, the absolute energies of electronic states are central to operation of solar cells, light-emitting diodes and other NC-based devices.[44,45]

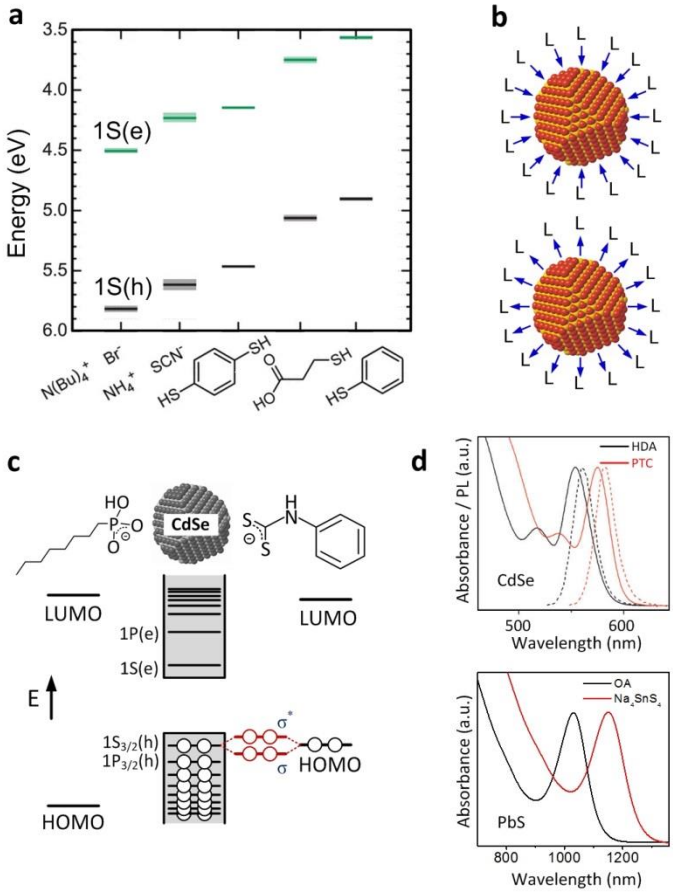

Figure 2.4. Effect of surface ligands on electronic states within the nanocrystal inorganic core. (a) Surface ligands influence the energy of highest occupied, 1S(h), and lowest unoccupied, 1S(e), states of PbS quantum dots, measured by ultraviolet photoelectron spectroscopy for representative organic and inorganic ligands: bromide, thiocyanate, benzenedithiol, 3-mercaptopropionic acid and benzenethiol. Adapted from ref.[43] (b) The shift of 1S(h) and 1S(e) states is caused by surface dipoles, shown as blue arrows, between surface atoms and ligand molecules. (c) Qualitative illustration of 'non-innocent' ligand phenyldithiocarbamate (PTC) mixing with CdSe $1S_{3/2}$ hole state (right), giving rise to states with mixed core–ligand character (shown in red). HOMO and LUMO energies of typical hydrocarbon ligands preclude strong mixing with nanocrystal quantum-confined states (left). (d) Development of electronic states with mixed nanocrystal–ligand character relaxes quantum confinement and redshifts the absorption features of CdSe quantum dots capped with PTC ligands and of PbS quantum dots capped with SnS_4^{4-} ligands. PL, photoluminescence; a.u., arbitrary units; HDA, hexadecylamine. Adapted from ref.[46]

In the above examples, the QD absorption spectrum was set by electronic transitions within the inorganic core, and the effect of surface ligands on energy and oscillator strength of these transitions was assumed to be negligible. For typical aliphatic ligands (for example alkyl carboxylates, phosphonates, amines) this is indeed the case, as ligand frontier orbital energies are far from QD core states, maintaining strong ligand character even when bound to the QD surface. On the other hand, ligands with redox potentials comparable to the QD electron affinity and ionization potential promote state mixing between ligands and the inorganic core. In coordination chemistry, ligands that create a set of electronic states with strong metal–ligand character are referred to as 'non-innocent' ligands.[47] Analogously, when the symmetry and energy of ligand and crystallite frontier orbitals align (Figure 2.4c), interfacial states with mixed QD–ligand character arise, allowing core wavefunctions to extend across the inorganic/organic interface into the ligand shell. Phenyldithiocarbamate (PTC) ligands, for example, reduce the optical bandgap of CdSe NCs by up to ~0.2 eV by delocalizing the exciton hole via mixing with QD states near the valence band edge[46] (Figure 2.4c; Figure 2.4d, top). Similarly, exchange of oleate ligands for SnS_4^{4-} or AsS_3^{3-} results in redshifted excitonic absorption peaks of PbS QDs (Figure 2.4d, bottom). These examples show that practically every physical property of semiconductor QDs (bandgap, ionization potential, electron affinity, luminescence efficiency and others) can be tailored by surface ligands. The same holds true for other classes of NC materials, with ligands influencing the surface plasmon resonance of Au NCs,[48] catalytic properties of $CoPt_3$ NCs,[49] magnetic properties of Fe_3O_4 NCs,[50] and so on. These are active areas of ongoing research.

2.4. Acknowledgements

I am grateful to my advisor, Prof. Dmitri Talapin, for pointing me to ref.[15] in this section and highlighting the opportunity it presented us to add atomic-level rigor to descriptions of the ligand exchange reactions routinely used by our group and others. Furthermore, I would like to thank Prof. Taeghwan Hyeon of the Institute for Basic Science in Seoul, Korea and Prof. Daishun Ling of Zhejiang University in Zhejiang, China for their contributions to the bioapplications section of ref.[51]. For the sake of brevity, the discussion of surface ligand design for biological and electronic applications of colloidal nanocrystals has been omitted from this chapter. The interested reader is referred to ref.[51] for this information.

2.5. References

1 Murray, C. B., Kagan, C. R. & Bawendi, M. G. SYNTHESIS AND CHARACTERIZATION OF MONODISPERSE NANOCRYSTALS AND CLOSE-PACKED NANOCRYSTAL ASSEMBLIES. *Annual Review of Materials Science* **30**, 545-610, (2000).

2 Ozbay, E. Plasmonics: Merging Photonics and Electronics at Nanoscale Dimensions. *Science* **311**, 189-193, (2006).

3 Bell, A. T. The Impact of Nanoscience on Heterogeneous Catalysis. *Science* **299**, 1688-1691 (2003).

4 Giessibl, F. J. Atomic Resolution of the Silicon (111)-(7x7) Surface by Atomic Force Microscopy. *Science* **267**, 68-71 (1995).

5 Chadi, D. J. Atomic and Electronic Structures of Reconstructed Si(100) Surfaces. *Physical Review Letters* **43**, 43-47 (1979).

6 Laibinis, P. E. *et al.* Comparison of the structures and wetting properties of self-assembled monolayers of n-alkanethiols on the coinage metal surfaces, copper, silver, and gold. *J. Am. Chem. Soc.* **113**, 7152-7167 (1991).

7 Yin, Y. & Alivisatos, A. P. Colloidal nanocrystal synthesis and the organic-inorganic interface. *Nature* **437**, 664-670 (2005).

8 Kovalenko, M. V. *et al.* Prospects of Nanoscience with Nanocrystals. *ACS Nano* **9**, 1012-1057, (2015).

9 Peng, X. *et al.* Shape control of CdSe nanocrystals. *Nature* **404**, 59-61 (2000).

10 Ithurria, S. *et al.* Colloidal nanoplatelets with two-dimensional electronic structure. *Nat Mater* **10**, 936-941 (2011).

11 Nuzzo, R. G., Zegarski, B. R. & Dubois, L. H. Fundamental studies of the chemisorption of organosulfur compounds on gold(111). Implications for molecular self-assembly on gold surfaces. *J. Am. Chem. Soc.* **109**, 733-740 (1987).

12 Dubois, L. H., Zegarski, B. R. & Nuzzo, R. G. Molecular ordering of organosulfur compounds on Au(111) and Au(100): Adsorption from solution and in ultrahigh vacuum. *J. Chem. Phys.* **98**, 678-688 (1993).

13 Dubois, L. H. & Nuzzo, R. G. Synthesis, Structure, and Properties of Model Organic Surfaces. *Annual Review of Physical Chemistry* **43**, 437-463 (1992).

14 Hakkinen, H. The gold-sulfur interface at the nanoscale. *Nat Chem* **4**, 443-455 (2012).

15 Zherebetskyy, D. *et al.* Hydroxylation of the surface of PbS nanocrystals passivated with oleic acid. *Science* **344**, 1380-1384, (2014).

16 Hostetler, M. J., Stokes, J. J. & Murray, R. W. Infrared Spectroscopy of Three-Dimensional Self-Assembled Monolayers: N-Alkanethiolate Monolayers on Gold Cluster Compounds. *Langmuir* **12**, 3604-3612, (1996).

17 Badia, A., Cuccia, L., Demers, L., Morin, F. & Lennox, R. B. Structure and Dynamics in Alkanethiolate Monolayers Self-Assembled on Gold Nanoparticles: A DSC, FT-IR, and Deuterium NMR Study. *Journal of the American Chemical Society* **119**, 2682-2692, (1997).

18 Frederick, M. T., Achtyl, J. L., Knowles, K. E., Weiss, E. A. & Geiger, F. M. Surface-Amplified Ligand Disorder in CdSe Quantum Dots Determined by Electron and Coherent Vibrational Spectroscopies. *Journal of the American Chemical Society* **133**, 7476-7481, (2011).

19 Protesescu, L. *et al.* Atomistic Description of Thiostannate-Capped CdSe Nanocrystals: Retention of Four-Coordinate SnS4 Motif and Preservation of Cd-Rich Stoichiometry. *Journal of the American Chemical Society* **137**, 1862-1874, (2015).

20 Green, M. L. H. A new approach to the formal classification of covalent compounds of the elements. *Journal of Organometallic Chemistry* **500**, 127-148, (1995).

21 Anderson, N. C., Hendricks, M. P., Choi, J. J. & Owen, J. S. Ligand Exchange and the Stoichiometry of Metal Chalcogenide Nanocrystals: Spectroscopic Observation of Facile Metal-Carboxylate Displacement and Binding. *Journal of the American Chemical Society* **135**, 18536-18548, (2013).

22 De Roo, J. *et al.* Carboxylic-Acid-Passivated Metal Oxide Nanocrystals: Ligand Exchange Characteristics of a New Binding Motif. *Angewandte Chemie International Edition* **54**, 6488-6491, (2015).

23 Boles, M. A. & Talapin, D. V. Connecting the dots. *Science* **344**, 1340-1341 (2014).

24 Moreels, I. *et al.* Composition and Size-Dependent Extinction Coefficient of Colloidal PbSe Quantum Dots. *Chemistry of Materials* **19**, 6101-6106, (2007).

25 Nag, A. *et al.* Metal-free Inorganic Ligands for Colloidal Nanocrystals: S^{2-}, HS^{-}, Se^{2-}, HSe^{-}, Te^{2-}, HTe^{-}, TeS_3^{2-}, OH^{-}, and NH_2^{-} as Surface Ligands. *J. Am. Chem. Soc.* **133**, 10612-10620 (2011).

26 Luther, J. M. & Pietryga, J. M. Stoichiometry Control in Quantum Dots: A Viable Analog to Impurity Doping of Bulk Materials. *ACS Nano* **7**, 1845-1849, (2013).

27 Fritzinger, B. *et al.* In Situ Observation of Rapid Ligand Exchange in Colloidal Nanocrystal Suspensions Using Transfer NOE Nuclear Magnetic Resonance Spectroscopy. *Journal of the American Chemical Society* **131**, 3024-3032, (2009).

28 Lingley, Z., Lu, S. & Madhukar, A. A High Quantum Efficiency Preserving Approach to Ligand Exchange on Lead Sulfide Quantum Dots and Interdot Resonant Energy Transfer. *Nano Letters* **11**, 2887-2891, (2011).

29 Hostetler, M. J., Templeton, A. C. & Murray, R. W. Dynamics of Place-Exchange Reactions on Monolayer-Protected Gold Cluster Molecules. *Langmuir* **15**, 3782-3789, (1999).

30 Fritzinger, B., Capek, R. K., Lambert, K., Martins, J. C. & Hens, Z. Utilizing Self-Exchange To Address the Binding of Carboxylic Acid Ligands to CdSe Quantum Dots. *Journal of the American Chemical Society* **132**, 10195-10201, (2010).

31 Owen, J. S., Park, J., Trudeau, P.-E. & Alivisatos, A. P. Reaction Chemistry and Ligand Exchange at Cadmium−Selenide Nanocrystal Surfaces. *Journal of the American Chemical Society* **130**, 12279-12281, (2008).

32 Gur, I., Fromer, N. A., Geier, M. L. & Alivisatos, A. P. Air-Stable All-Inorganic Nanocrystal Solar Cells Processed from Solution. *Science* **310**, 462-465 (2005).

33 Fedin, I. & Talapin, D. V. Probing the Surface of Colloidal Nanomaterials with Potentiometry in Situ. *Journal of the American Chemical Society* **136**, 11228-11231, (2014).

34 Gomes, R. *et al.* Binding of Phosphonic Acids to CdSe Quantum Dots: A Solution NMR Study. *The Journal of Physical Chemistry Letters* **2**, 145-152, (2011).

35 Pearson, R. G. Absolute electronegativity and hardness: application to inorganic chemistry. *Inorganic Chemistry* **27**, 734-740, (1988).

36 Xu, C. *et al.* Dopamine as A Robust Anchor to Immobilize Functional Molecules on the Iron Oxide Shell of Magnetic Nanoparticles. *Journal of the American Chemical Society* **126**, 9938-9939, (2004).

37 Medintz, I. L., Uyeda, H. T., Goldman, E. R. & Mattoussi, H. Quantum dot bioconjugates for imaging, labelling and sensing. *Nat Mater* **4**, 435-446 (2005).

38 Webber, D. H. & Brutchey, R. L. Ligand Exchange on Colloidal CdSe Nanocrystals Using Thermally Labile tert-Butylthiol for Improved Photocurrent in Nanocrystal Films. *Journal of the American Chemical Society* **134**, 1085-1092, (2011).

39 Munro, A. M., Jen-La Plante, I., Ng, M. S. & Ginger, D. S. Quantitative Study of the Effects of Surface Ligand Concentration on CdSe Nanocrystal Photoluminescence. *The Journal of Physical Chemistry C* **111**, 6220-6227, (2007).

40 Brus, L. Electronic wave functions in semiconductor clusters: experiment and theory. *The Journal of Physical Chemistry* **90**, 2555-2560, (1986).

41 Ip, A. H. *et al.* Hybrid passivated colloidal quantum dot solids. *Nat Nano* **7**, 577-582, (2012).

42 Aldana, J., Wang, Y. A. & Peng, X. Photochemical Instability of CdSe Nanocrystals Coated by Hydrophilic Thiols. *Journal of the American Chemical Society* **123**, 8844-8850, (2001).

43 Brown, P. R. *et al.* Energy Level Modification in Lead Sulfide Quantum Dot Thin Films through Ligand Exchange. *ACS Nano* **8**, 5863-5872, doi:10.1021/nn500897c (2014).

44 Chuang, C.-H. M., Brown, P. R., Bulović, V. & Bawendi, M. G. Improved performance and stability in quantum dot solar cells through band alignment engineering. *Nat Mater* **13**, 796-801, (2014).

45 Ning, Z. *et al.* Air-stable n-type colloidal quantum dot solids. *Nat Mater* **advance online publication**, (2014).

46 Frederick, M. T. & Weiss, E. A. Relaxation of Exciton Confinement in CdSe Quantum Dots by Modification with a Conjugated Dithiocarbamate Ligand. *ACS Nano* **4**, 3195-3200, (2010).

47 Boyer, J. L., Rochford, J., Tsai, M.-K., Muckerman, J. T. & Fujita, E. Ruthenium complexes with non-innocent ligands: Electron distribution and implications for catalysis. *Coordination Chemistry Reviews* **254**, 309-330, (2010).

48 Malinsky, M. D., Kelly, K. L., Schatz, G. C. & Van Duyne, R. P. Chain Length Dependence and Sensing Capabilities of the Localized Surface Plasmon Resonance of Silver Nanoparticles Chemically Modified with Alkanethiol Self-Assembled Monolayers. *Journal of the American Chemical Society* **123**, 1471-1482, (2001).

49 Kwon, S. G. *et al.* Capping Ligands as Selectivity Switchers in Hydrogenation Reactions. *Nano Letters* **12**, 5382-5388, (2012).

50 Duan, H. *et al.* Reexamining the Effects of Particle Size and Surface Chemistry on the Magnetic Properties of Iron Oxide Nanocrystals: New Insights into Spin Disorder and Proton Relaxivity. *The Journal of Physical Chemistry C* **112**, 8127-8131, (2008).

51 Boles, M. A., Ling, D., Hyeon, T. & Talapin, D. V. The surface science of nanocrystals. *Nat Mater* **15**, 141-153, (2016).

3. Fundamental aspects of nanocrystal self-assembly

This section summarizes the theory of nanocrystal interactions and examines basic principles governing nanocrystal self-assembly from perspectives borrowed from the comparatively established fields of micrometer colloid and block copolymer ordering.

3.1. Qualitative treatment of nanocrystal interactions

Self-assembly brings a set of particles from a dilute state to one in which particles are contacting their nearest neighbors. As such, it is important to consider the various contributions to the NC-NC interaction throughout the self-assembly process. These interactions include van der Waals forces between inorganic cores and between surface ligands as well as osmotic, electrostatic, and elastic contributions.[1] The combination of the interactions is commonly described by an effective interparticle pair interaction.[2]

3.1.1. Interparticle potentials at the ordering transition

Colloidal NC solutions remain in the dispersed state as long as the pair potential is dominantly repulsive (Figure 3.1a, darkest trace). Tethering molecular chains (e.g., hydrocarbon surfactants or neutral polymers) to the NC surface enables steric stabilization of NCs, while adsorption of charged species leads to electrostatically stabilized colloids (Figure 3.1b,c). These cases form two fundamentally different mechanisms to colloidal stabilization and provide complementary approaches to disperse NCs in nonpolar and polar solvents, respectively. Such mechanisms need not be mutually exclusive: chains with ionizable groups allow for both to be combined together in the special case of electrosteric stabilization using polyelectrolyte ligands.[3]

Aggregation of NCs can be induced by, for example, removal of solvent, reduction of solvent quality via nonsolvent addition or cooling the solution, and desorption of or cross-linking

of capping ligands. During this process, the effective interparticle interaction changes from repulsive to attractive. In the dried state, NCs are linked firmly together by the interparticle matrix comprised of surface ligands. Complete removal of solvent freezes a collection of NCs into a superlattice with interparticle separation set by the balance between ligand elastic repulsion and van der Waals attraction forces. Associated NCs then sit in a deep potential well that far exceeds the characteristic thermal energy (k_BT) of the system (Figure 3.1a, lightest trace).

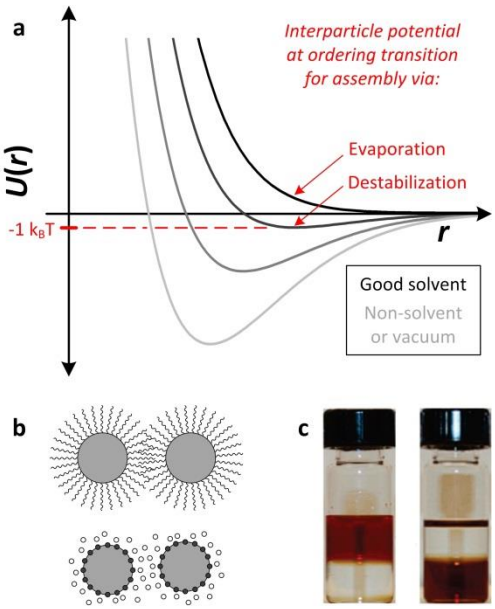

Figure 3.1. Pair interactions of nanocrystals in the dispersed state and the assembled state. (a) Evolution of the effective pair interaction potential U at interparticle separation distance r for nanocrystals from the beginning (darkest trace, dispersed state) to the end point (lightest trace, close-packed state) during the self-assembly experiment. This plot was constructed using 6-12 powerlaw potentials and serves only as a qualitative representation of nanocrystal pair interactions. (b) Sketch of a pair of interacting nanocrystals with hydrocarbon (top) and ionic (bottom) surface ligands. (c) Sterically stabilized solution of oleate-capped CdSe in nonpolar toluene phase (left photo, upper layer). Exchange of oleate ligands to potassium sulfide results in a phase transfer of the nanocrystals to the polar formamide phase (right photo, bottom layer). Adapted from ref.[4]

Rapid destabilization results in uncontrolled, out-of-equilibrium growth of disordered NC aggregates producing dendrites or gel networks.[5] On the other hand, faceted, polyhedral

superlattices can be obtained by assembly near equilibrium conditions,[6] where interparticle attractions remain comparable to k_BT for a sufficiently long time to allow NCs to sample multiple sites on the superlattice surface before irreversible attachment.

3.1.2. Equilibrium shape of nanocrystal superlattices

The shape (morphology) of the superlattice polyhedron that results from destabilization-based self-assembly can be rationalized using thermodynamic principles. Like any finite-size solid, including the NC itself, a NC superlattice has facet-specific surface energies arising from the reduced coordination of the particles at the surface as compared with those in the superlattice bulk. While NCs have twelve nearest neighbors in the interior of a close-packed superlattice, NCs at the surface have eight nearest neighbors on (100), seven on (110), and nine on (111) facets (Figure 3.2a-c). By simply counting the number of broken bonds, it is possible to predict that the surface energy of these facets increases as $E_{111} < E_{100} < E_{110}$. A surface energy minimizing polyhedron (known as Wulff polyhedron) then has facet surface areas increasing as $A_{111} > A_{100} > A_{110}$ (Figure 3.2d). Furthermore, by incorporating low-energy twin plane defects within the interior, polyhedral superlattices may present exclusively (111) facets with icosahedral shape (Figure 1.6g).[6]

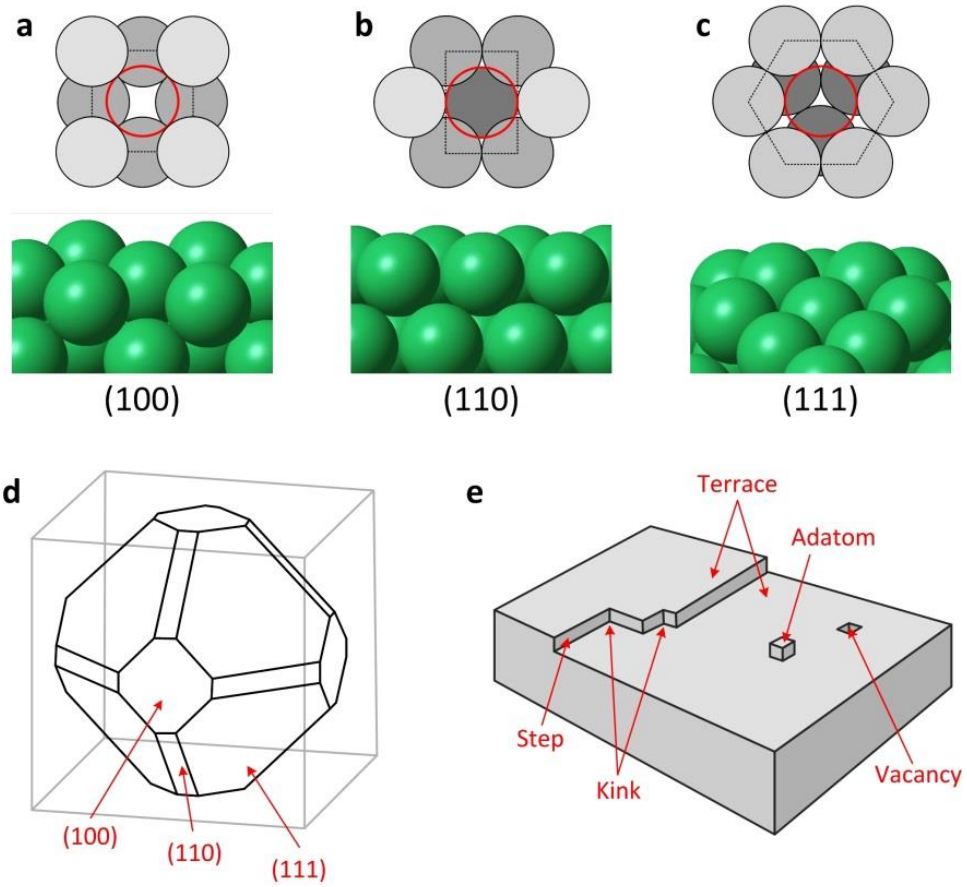

Figure 3.2. Surface area and broken contacts at the superlattice surface determine facet surface energy and the morphology of superlattices formed with destabilization-based assembly. Here we show the *fcc* lattice as an example. (a) A (100) surface nanocrystal (red circle) has eight nearest neighbors, four in-plane (light grey) and four below (dark grey). Modeled three-dimensional structure shown underneath. (b) A (110) surface nanocrystal has seven neighbors, two in-plane and five below. (c) A (111) surface nanocrystal has nine neighbors, six in-plane and three below. (d) A superlattice seeks to minimize the total surface energy by adopting a shape that preferentially expresses low-energy facets. Shown here: polyhedron with relative facet areas $A_{111} > A_{100} > A_{110}$. (e) Illustration of the step-terrace-kink model for monomer addition to a growing crystal. Adapted from ref.[7]

3.1.3. Superlattice nucleation, growth, and coalescence

The equilibrium (or near-equilibrium) aggregation of NCs into a superlattice is a phase transition that proceeds via nucleation and growth. Because nucleation is sensitive to impurities in the system, it is important to distinguish between homogeneous nucleation and heterogeneous nucleation. Homogeneous nucleation occurs in solution and requires overcoming a nucleation barrier. Reducing solvent quality or increasing particle volume fraction by evaporation increases the nucleation rate by lowering the nucleation barrier. On the other hand, rapid evaporation or destabilization can lead to barrierless aggregation via spinodal decomposition[8] into NC-rich and NC-poor areas similar to demixing observed upon cooling a two fluids below critical temperature of miscibility. However, such far-from-equilibrium processes typically produce disordered NC solids.

Heterogeneous (templated) nucleation near an interface (wall) can be significantly faster than homogeneous nucleation because the presence of a surface naturally preorders the colloid. After nucleation, growth proceeds via addition of individual NCs or groups of NCs to the growing seed. Growth speed is limited by the availability of NCs from solution and the energetics of surface defect formation. A simple model for surface defect formation is the terrace-ledge-kink model (Figure 3.2e), which predicts that NC integration into a growing superlattice is influenced by the number of bonds formed upon attachment. Under attractive interparticle interactions, growth proceeds quickly at vacancies, kinks and steps, which enable formation of many NC-NC contacts. On the other hand, steps and terraces are comparatively stable due to fewer contacts established upon NC adsorption.

To minimize total surface energy, a collection of NCs that finds itself in the absence of good solvent prefers the aggregation into a single Wulff polyhedron. In practice, however,

solvent destabilization allows multiple nucleation sites and produces many superlattice domains from a collection of particles. This leaves more surface area (broken bonds) than if all particles incorporated themselves in a single superlattice. Larger aggregates move slower in solution than individual NCs or small aggregates, inhibiting coalescence of superlattice domains. However, their mass promotes large superlattices to sediment in the bottom of the container , assisting densification. The barrier to nucleation by solvent destabilization is thus sufficiently low, and the barrier to merging of domains sufficiently high, such that many nuclei form but cannot completely coalesce (Figure 3.3, left pathway). In contrast, evaporation-based self-assembly often nucleates superlattices under thin-film confinement, for example at the air-liquid interface,[9] and in the absence of significant attractive interparticle interactions, producing two-dimensional films (Figure 3.3, right pathway). These films will typically start out polycrystalline but can improve by defect repair and healing of internal interfaces given sufficiently slow solvent evaporation.

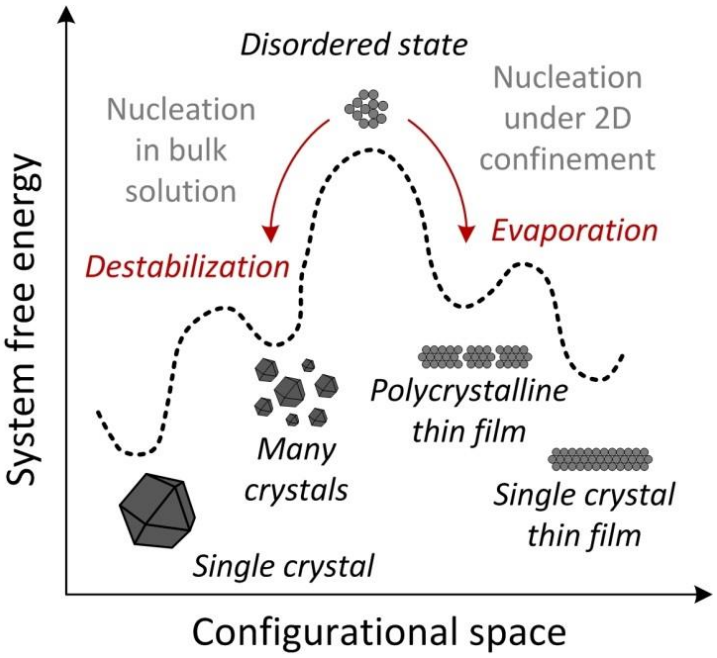

Figure 3.3. Superlattice morphology and free energy landscape of nanocrystal self-assembly at the disorder-order transition. A collection of nanocrystals transitions from the disordered state with high free energy (top) to an ordered state with lower free energy. Polyhedral superlattices form if nucleation occurs in the absence of boundary conditions (left pathway), while thin film superlattices result under geometric confinement (right pathway).

3.2. Fundamental contributions to interparticle forces

NC self-assembly is affected by the interplay of many chemical and physical forces. The equilibrium superlattice structure is the one that minimizes the system free energy (F), expressed in terms of energetic (U) and entropic (S) components as $F = U - TS$.[1] Similarly, the free energy change ΔF upon self-assembly provides the driving force for ordering and results from corresponding changes in system internal energy and entropy, $\Delta F = \Delta U - T\Delta S$.

3.2.1. Core contributions to free energy

Internal energy change of the assembling system can be broken approximately into core and ligand contributions, $\Delta U \approx \delta U_{\text{cores}} + \delta U_{\text{ligands}}$, as can be entropy, $\Delta S \approx \delta S_{\text{cores}} + \delta S_{\text{ligands}}$. Energetic interactions between NC cores are described by the set of van der Waals interactions, $\delta U_{\text{cores}} \approx \delta U_{\text{vdW}} \approx \delta U_{\text{London}} + \delta U_{\text{Keesom}} + \delta U_{\text{Debye}}$. The first term, the London dispersion attraction[10] between instantaneously induced dipoles, is present for all NC core materials. The second and third terms are dipole – induced dipole and dipole-dipole interactions, respectively, which relate to materials with permanent electric dipole moments (e.g., CdSe). The combined strength of all three is described by the Hamaker constant A. In the general case, magnetic dipole moments (e.g., Fe_3O_4) and Coulombic interactions between charged particles may also be present. For charged NCs there exist additional contributions from charge-charge, charge-dipole, and charge – induced dipole to the system internal energy.[11] Particle core entropy has configurational, translational, and rotational terms, $\delta S_{\text{cores}} \approx \delta S_{\text{conf}} + \delta S_{\text{trans}} + \delta S_{\text{rot}}$. The first term is related to rearrangements of the particles in the system ignoring local effects. In the superlattice it counts the number of ways to exchange particles. The other two terms handle local motions only, such as individual or collective vibrations about equilibrium positions and orientations.

3.2.2. Ligand contributions to free energy

When sterically stabilized particles contact in good solvent, densification of ligand segments results in an osmotic penalty, $\delta S_{\text{ligands}} \approx \delta S_{\text{osmotic}}$.[12] Similarly, for charge-stabilized NCs dispersed in polar solvent, condensation of counterion clouds gives rise to osmotic pressure between surfaces. In addition, upon interpenetration of hydrocarbon coronas, compression or extension of backbone can distort torsion angles along the chain and introduce *gauche* defects, giving rise to elastic energetic penalty upon contact.[13] In the absence of good solvent, this elastic resistance to chain deformation balances the attractive London dispersion interaction between aliphatic chains: $\delta U_{\text{ligands}} \approx \delta U_{\text{elastic}} + \delta U_{\text{London}}$.

3.2.3. Van der Waals forces between nanocrystal cores

The van der Waals interaction between inorganic cores stems from transient fluctuations in the distribution of electrons. It is typically attractive and favors flocculation of the colloid. Interatomic van der Waals attraction may be expressed as

$$U_{\text{vdW}}(r) = -\frac{C\rho_1\rho_2}{r^6} \tag{1}$$

where ρ_1 and ρ_2 are the number of atoms per unit volume in two interacting bodies and the constant C is the coefficient in the interparticle interaction. This constant is large for materials with free electrons (e.g., metals). The total van der Waals energy of attraction between two particles with volumes V_1 and V_2 can be obtained by pairwise summation of van der Waals interaction between all atoms in the constituent particles,

$$U_{\text{vdW}} = -\int_{V_1} dV_1 \int_{V_2} dV_2 \frac{C\rho_1\rho_2}{r^6} \tag{2}$$

This integral can be solved analytically[10] for two spherical NC cores with radii R_1 and R_2,

$$U_{\mathrm{vdW}}(r) = -\frac{A}{3}\left[\frac{R_1R_2}{r^2-(R_1+R_2)^2}+\frac{R_1R_2}{r^2-(R_1-R_2)^2}+\frac{1}{2}\ln\left(\frac{r^2-(R_1+R_2)^2}{r^2-(R_1-R_2)^2}\right)\right] \qquad (3)$$

with Hamaker constant $A = \pi^2 C\rho_1\rho_2$. A good approximation at close contact, $d = r - R_1 - R_2 \ll \min(R_1,R_1)$, is

$$U_{\mathrm{vdW}}(d) = -\frac{A}{6d}\frac{R_1R_2}{R_1+R_2} \qquad (4)$$

This equation forms the basis of the Derjaguin approximation,[14] which estimates the van der Waals energy between two particles of arbitrary shape from the curvature of their surfaces and integration of the interaction energy of infinite parallel plates.

3.2.4. Steric stabilization of nanocrystals

The van der Waals interactions between NC cores can be sufficiently screened by the ligand shell to impart predominantly repulsive interactions and maintain stable colloidal solutions of even strongly interacting materials (e.g., metals with large Hamaker constant A). Osmotic and elastic repulsion between chains in good solvent form the basis of steric stabilization of hydrocarbon- and polymer-capped NCs and beads, as well as solutions of surfactant, dendron, and polymer micelles. In this case, good solvent implies negative free energy of chain-solvent mixing.[15] An osmotic term resulting from unfavorable exclusion of solvent molecules from the ligand interaction region acts upon a pair of particles as soon as their ligand coronas begin to overlap. This effect occurs over the whole range of steric interaction, beginning at interparticle distances d lower than twice the width L of the capping layer ($d < 2L$). Compression of the ligand chains results in an elastic contribution to the potential at smaller

surface separations. Because this elastic component quickly exceeds thermal energy, the predominant region sampled during a Brownian collision is the moderate interpenetration ($L < d < 2L$) domain.[13]

In the interpenetration domain, the free energy of interpenetration of two chains tethered to the NC surfaces brought from infinite separation together in volume dV may be expressed with Flory-Krigbaum theory[16] as

$$\Delta G = 2k_B T \frac{{v_s}^2}{v_i}\left(\frac{1}{2} - \chi\right)\int_V \varphi_1 \varphi_2 \, dV \tag{5}$$

where v_s, v_i, and χ are the Kuhn segment volume, solvent molecular volume, and Flory-Huggins chain-solvent interaction parameter, respectively. The segment density distribution functions φ_1 and φ_2 are derived from the geometry of a cone-shaped available ligands volume and can be evaluated numerically. Accordingly, in good solvent ($\chi < 1/2$), intermingling of hydrocarbon segments from neighboring NCs is penalized ($\Delta G > 0$), and particles experience repulsion upon contact. On the other hand, clustering of NCs is favorable in poor solvent (for $\chi > 1/2$, $\Delta G < 0$).

From this analysis it can also be seen that the steric repulsion strength depends on grafting surface curvature.[17] On highly curved surfaces, found for example on small NCs or the tips of pointy NCs, each ligand enjoys access to a large cone-shaped volume. In this case, segment density φ rapidly decays away from the grafting surface. The spatial concentration of ligand segments given by the overlap integral $\int_V \varphi_1 \varphi_2 \, dV$, and thus the free energy change upon corona interpenetration, is small. In contrast, for nearly flat surfaces, the overlap integral, and thus $|\Delta G|$, is large. Such logic predicts increasing per-ligand repulsion energy with decreasing

surface curvature (see also Chapter 4) and might account for the counterintuitive propensity of smaller NCs to form clusters in solution.[18]

Importantly, the total steric interaction energy between two particles is the sum of individual ligand-ligand potentials given in Eq. (5). For the case of NC diameter greatly exceeding the thickness of ligand capping layer, accurate estimation of interparticle interaction can make use of the Derjaguin approximation. However, this approach greatly overestimates the steric repulsion between particles with stabilizing shell thickness on the order of particle diameter (e.g., sub-10nm NCs capped with C_{18}-length hydrocarbons), where tilting of chains away from the contact axis can be significant.[19] Modeling steric interaction between particles with comparable diameter and corona thickness remains an area of active research.[20]

Enhancing steric stabilization is a strategy to improve self-assembly success. One possibility is introducing unsaturation along the hydrocarbon backbone (e.g., *cis*-9-octadecyl chains of oleic acid or oleylamine) to suppress the tendency of long-chain saturated (e.g., stearic acid or octadecylamine) ligands to crystallize on the NC surface, promoting chain-solvent mixing and NC solubility. Tethering end-functionalized polymers[21] to the NC surface is another possibility. Such chains can be considered entropic springs with elastic response from both stretching and compressive deviations from random-walk dimensions.[15]

3.2.5. Hydrocarbon ligand packing in nanocrystal solids

At the late stage of drying a NC solution, or upon nonsolvent addition, interpenetrating coronas are no longer swollen with solvent molecules and begin to freeze together under the influence of attractive van der Waals interactions between hydrocarbon chains. The attraction experienced by two parallel chains[22] scales with the length L of overlap and decays quickly with backbone separation x as

$$U_{\mathrm{vdW}}(x) = -A\frac{3\pi}{8\lambda^2}\frac{L}{x^5} \tag{6}$$

where λ is the sp^3 carbon-carbon bond length ($\lambda \approx 0.15$ nm) and A is the Hamaker constant ($A \approx$ 0.1 kcal/mol) for attraction between methylene units whose centers are separated by roughly 0.5 nm in the close-packed ligand bundle.

Hydrocarbon chains tethered to a flat surface readily crystallize into an all-parallel backbone arrangement.[23] Predictions from molecular dynamics simulations and experimental analysis using vibrational spectroscopy indicate that bundles of parallel ligand chains can form on the surface of NCs in the absence of good solvent.[24,25] Such bundling is most common for longer ($C_{12} - C_{18}$) chains tethered to the surface of larger-diameter particles. On the other hand, vibrational spectroscopy has revealed that ligands in NC solids have a significant concentration of gauche defects in the chain ends, which propagate towards the interior with increasing temperature.[26] Upon addition of nonsolvent to the NC solution, coronas contract to reduce contact with poor solvent and NCs cluster for the same reason. Upon evaporation of a NC solution, however, hydrocarbon coronas are swollen with solvent when NCs are initially crowded together. As a result, interparticle separations are typically 33% larger for evaporation-based assembly than for destabilization-based assembly.[27]

The packing of hydrocarbon chains between NC cores and the resulting interparticle separations (Figure 3.4a) has not only been treated with molecular dynamics simulations but also using simple geometric models. These models postulate space-filling of ligands along the bond axis (optimal packing model,[28]; Figure 3.4b) or space-filling of ligands within the entire volume of the corona overlap (overlap cone model,[20]; Figure 3.4c). Experimental separations (see also Chapter 5) measured from TEM images of hexagonally ordered monolayers of alkanethiol-capped Au NCs are consistent with the first model (Figure 3.4d,e).[29] However, they also confirm the existence of many-body interactions between NC capping layers predicted by the second model, which cause the effective corona thickness to vary with NC coordination number (Figure 3.4f,g). Together, molecular dynamics simulations and experimental data suggest that the NC ligand corona is a deformable surface coating that can support a variety of chain packing structures in the NC superlattice depending on chain length, surface curvature, and coordination state.

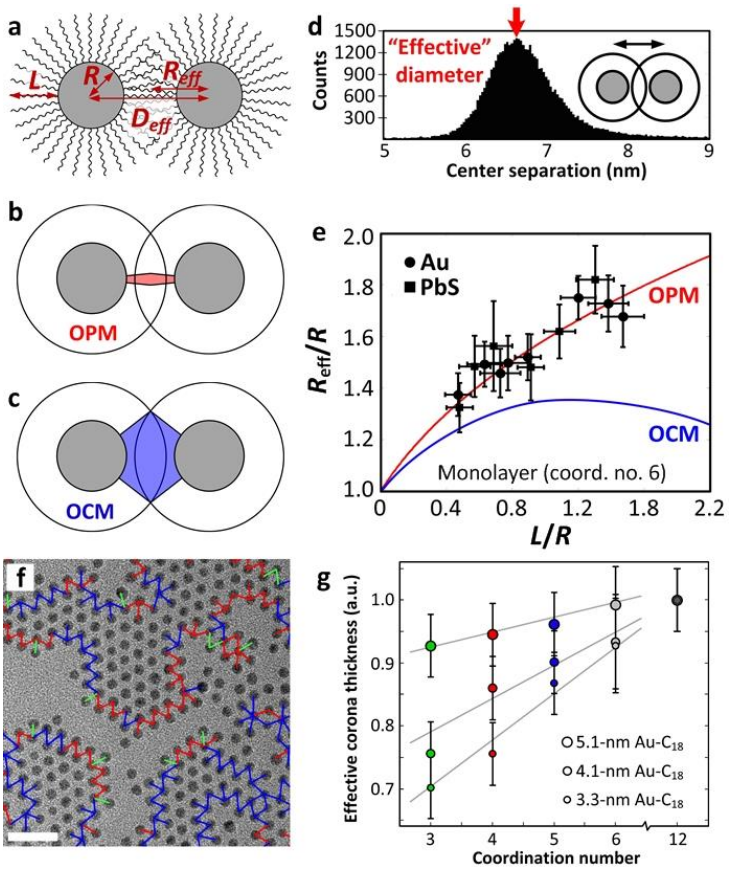

Figure 3.4. Packing of hydrocarbon ligands in nanocrystal superlattices. (a) Sketch of interdigitating hydrocarbon coronas between a nanocrystal pair showing core radius *R*, ligand length *L*, and effective radius R_{eff}. (b) Illustration of the optimal packing model prediction of a small axial volume of space-filling hydrocarbons between nanocrystal cores. (c) Sketch of the overlap cone model prediction of a larger overlap volume with space-filling hydrocarbons. (d) Histogram plot of the reduced separations measured from TEM images of hexagonally ordered monolayer of alkanethiol-capped Au nanocrystals. (e) Summary of the TEM measurements collected from several ligand length - core radius combinations using Au and PbS nanocrystals. (f) TEM image showing various coordination states of nanocrystals deposited at sub-monolayer surface coverage. (g) Deformability of the hydrocarbon corona revealed by the measured reduction in effective nanocrystal size in low-coordination position. Adapted from ref.[29] For full details, see Chapter 5.

3.2.6. Electrostatic stabilization

Adsorption of charged ions enables dispersion of NCs in polar solvent (Figure 3.1b, bottom and Figure 3.1c, right). Such surfaces may be obtained by ligand exchange of hydrocarbon-capped NCs[30] or by synthesizing NCs directly in polar medium (e.g., citrate-capped Au NCs,[31] thioglycolic acid capped CdTe, ref.[32]). The NC surface charge is then balanced by oppositely charged counterions surrounding the particle. Solvents with high dielectric constant (e.g., water, formamide) efficiently screen the electrostatic attraction between surface-bound ions and charge-neutralizing counterions, promoting the formation of an electrical double layer. Close approach of charge-stabilized NCs in polar solution results in the overlap of counter-ion clouds, inducing a local osmotic pressure between surfaces, which results in an effective repulsion. Reducing the dielectric screening of the solvent by addition of less polar liquids (e.g., toluene, acetonitrile) induces collapse of the counterion cloud, enabling close approach of NC surfaces and promoting flocculation.

The interaction potential between a pair of charge-stabilized NCs, including both electrostatic repulsion and van der Waals core-core attraction, is often treated in a first approximation using Derjaguin, Landau, Verwey and Overbeek (DLVO) theory.[12] The repulsive term decreases approximately exponentially with particle separation and can be estimated using the Derjaguin approximation at small separations and linear superposition at larger distances.[33] Analytical approximations provide an alternative to numerical integration. For example, the screened Coulomb (Yukawa) repulsive potential for two spheres of charge Z_1 and Z_2 in solution, separated by distance $r > \kappa^{-1}$ is given by

$$U_{\mathrm{sC}}(r) = \frac{Z_1 Z_2 \lambda_B}{(1+\kappa R_1)(1+\kappa R_1)} \frac{\exp(-\kappa(r - R_1 - R_2)}{r} \qquad (7)$$

Here κ^{-1} is the Debye screening length, $\lambda_B = e^2/(4\pi\varepsilon_0\varepsilon_r k_B T)$ the Bjerrum length, and charge is expressed in units of the elementary charge e. The total DLVO interaction energy is then the sum of the repulsive electrostatic (Coulombic) and attractive van der Waals terms.

3.2.7. Abundance of interparticle forces and simplifying assumptions for self-assembly

While the above considerations give a rough idea of various factors governing NC self-assembly, other terms might be present depending on the chemistry of the system and the experimental setup.[34-36] The abundance of contributing elements to the interparticle potential, unknown relative weights of each term, non-linear and non-additive coupling and evolution during self-assembly, the finite size of solvent molecules and solvated ions, inhomogeneity of the NC and its surroundings, and other effects make devising an accurate expression for the total free energy of the system extraordinarily complicated.[37] At present, the treatment of NC self-assembly in theory and simulation requires simplifying assumptions concerning particle shape (i.e., perfect spheres, cubes, etc.) and interactions at the disorder-order transition (purely repulsive, attractive, or absent). Fortunately, fundamental factors (like NC core geometry) often dominate the formation of superlattices, allowing coarse-grained models to explain many of the outcomes of self-assembly experiments.

3.3. Self-assembly of hard particles: entropy maximization and dense packings

Predicting the self-assembly of NCs into ordered superlattices requires comparing the relative stability of candidate structures. In general, taking into account all energetic or entropic contributions present in the system is not possible. Approximations are necessary to estimate free energies numerically. Yet, just like Pauling's rules proved useful in understanding the structure of ionic compounds in the early days of crystallography,[38] rather general considerations help to clarify the role of particle shape[39] and elucidate the relationship between geometry of building blocks and the superlattice into which they assemble.[40] The hard particle model is a good approximation for NCs with predominantly repulsive interactions or with only weak attraction over short distances.

3.3.1. Entropy maximization principle for hard particles

It was established in the 1950s that crystallization of particles can occur even when energetic interactions are entirely absent. Entropy-driven crystallization of hard spheres, the so-called Kirkwood-Alder transition, was predicted theoretically[41,42] and subsequently observed in concentrated solutions of micron-sized colloidal beads with steep repulsive (i.e., nearly-hard) interactions (Figure 3.5a).[43,44] Such particles experience strong repulsion upon contact and are well described by the hard sphere model (Figure 3.5b). Hard particles interact solely through excluded volumes. They strive to minimize Helmholtz free energy $F = -TS$ under the condition of constant volume V, and minimize Gibbs free energy $G = PV - TS$ under the condition of constant pressure P. Importantly, the most stable phase of a hard particle system at a given volume corresponds to the phase maximizing the total entropy of the system.

By measuring all energies and pressure in units of $k_B T$ the phase behavior of a hard particle system becomes independent of temperature and only dependent on particle volume

fraction (Figure 3.5c). The volume fraction (also called packing density or packing fraction) $\phi = NV_0/V$ is the ratio of the average particle volume $V_0 = \sum_i V_i /N$ to the volume V/N available to each particle in the system. Dimensionless free energy and pressure are then defined as $F^* = F/k_BT$ and $P^* = PV_0/k_BT$, respectively.

When suspended in fluid at high volume fraction, a collection of hard particles has greater total entropy in an ordered crystal than as a disordered fluid (Figure 3.5d,e). Specifically, the configurational entropy loss incurred by collective ordering of mean particle positions (loss of configurational entropy) is more than offset by extra free volume ("wiggle room") afforded to particles for local vibrations around their equilibrium lattice positions and rotations about their average orientations in the colloidal crystal (gain of translational and rotational entropy). In other words, the increase in visible order is associated with an increase in microscopic disorder.[45]

The entropy of *N* particles may be expressed using free volume theory[46] in terms of the volume faction ϕ and the structure-dependent jamming limit ϕ_c as

$$S \approx k_B f N \ln\left[\frac{\phi_c}{\phi} - 1\right] + S_c \qquad (8)$$

where f is the effective number of degrees of freedom per particle and S_c is an additive constant due to collective exclusion-volume effects. The jamming limit is defined as the density that can be reached with rapid compression. While free volume theory is only an approximation, it becomes exact at high density, i.e., close to ϕ_c. This means the densest phase is then thermodynamically favored. Only if several configurations have the same density does the additive factor S_c matter. Because spheres can be packed in *fcc* up to $\phi_c \approx 0.74$ before jamming, *fcc* must be more stable than a disordered collection of spheres that only accommodates spheres up to a limit of $\phi_c \approx 0.64$ before becoming jammed.

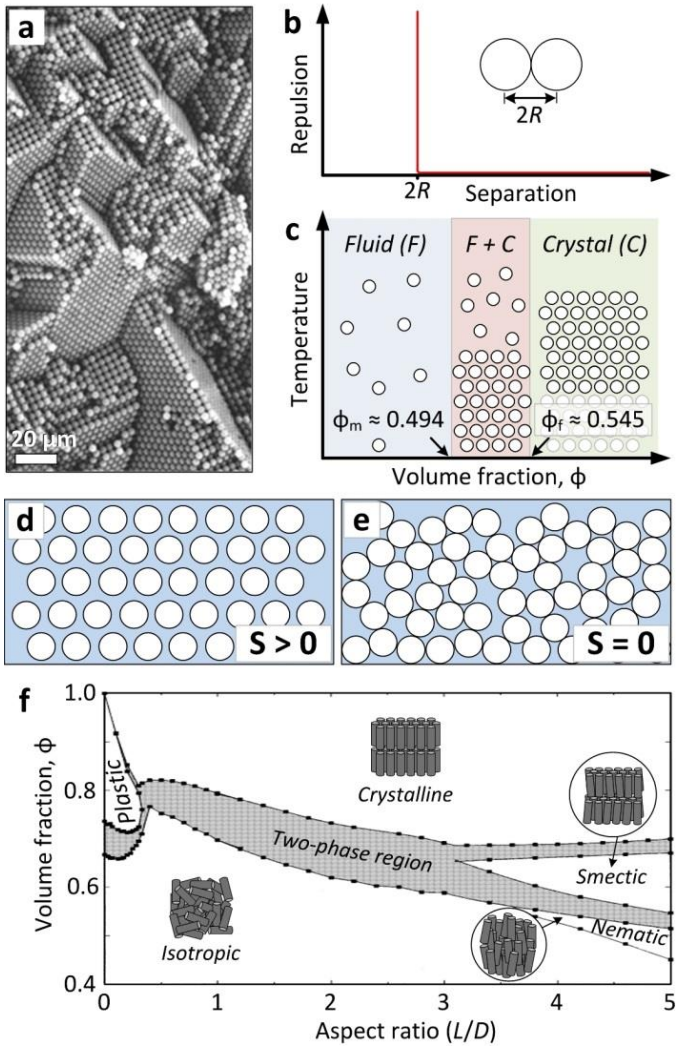

Figure 3.5. Entropy-driven crystallization of hard spheres. (**a**) SEM image of close-packed spherical colloidal beads. Adapted from ref.[52] (**b**) Hard sphere interaction potential. (**c**) Phase diagram of non-interacting spheres showing fluid phase at low density, crystal at high density, and coexistence of the two phases over an intermediate density range. Adapted from ref.[53] (**d,e**) The accessible free volume available to each particle increases upon adoption of an ordered colloidal crystal state (d) instead of a jammed state (e). In this schematic we ignore rattlers, which sets $S_c = 0$. (**f**) Phase diagram of non-interacting spherocylinder rods as a function of shape anisotropy and density. Adapted from ref.[54]

Entropy-driven ordering is predicted for mixtures of two sizes of hard spheres.[47] Similarly, non-interacting anisotropic particles (e.g., rods or plates) at sufficiently high volume fraction may align, moving from isotropic solution to liquid crystalline state (Figure 3.5f).[48] This

process, known as the Onsager transition,[49] increases entropy at the expense of rotational entropy, and is predicted for ellipsoids of length-to-breadth ratio of more than 2 or less than 0.5.[50] For anisotropic particles, entropy maximization leads to complex phases including entropically-driven solid-solid phase transitions.[51]

3.3.2. Dense packings as candidate structures for nanocrystal superlattices

One assumption has routinely been invoked for predicting the outcome of NC self-assembly: dense packings are favored. Dense packings appear for hard particles in the high-pressure/high-density limit. In this limit, the PV term in the Gibbs free energy dominates the entropy term TS. A densest packing (minimal V) will eventually be the maximum entropy state and therefore be most stable. This can be seen directly from free volume theory, Eq. (8). Densest packings have the same meaning for hard particle systems as thermodynamic ground states for systems of interacting particles. They are states reached when all dynamics of the system has ceased and entropy can be ignored. Finding the densest packing for a given shape is thus a natural starting point for predicting the structure of self-assembled NC superlattices.

Searching for the densest packing is a special case of a mathematical optimization problem and has a long history that goes back to ancient Greece. Framed as part of the 18th of 21 problems[55] proposed by David Hilbert in 1900, mathematicians were challenged to find the optimal way to "build up space from congruent polyhedra". The plain wording, however, belies its complexity. More than a century after Hilbert's list, it has been proven for only one shape, the sphere. The Kepler-Hales theorem states that face-centered cubic (*fcc*), hexagonal close-packed (*hcp*), and other stacking variants of hexagonal layers are the densest arrangements for spheres (Figure 3.6a,b), filling $\phi_{\mathrm{fcc}} = \pi/\sqrt{18} = 74.04\ldots\%$ of space.[56] Resolving the entropy difference between these two phases requires high-precision free energy calculations. The outcome of the

calculation is a small entropic preference of $\Delta s = 0.001164(8)k_B$ per sphere for *fcc*[57] over *hcp* due to phonon contributions.[58] Optimal packings for space-filling solids (the cube, for example, and several other polyhedra[59,60]) are also known and represent trivial Hilbert solutions. Only with the advent of modern computers it became possible to study the packing of a wide range of shapes numerically. Many solutions have been found that are believed to be optimal or at least near optimal. Yet, due to the complexity of the packing problem, searching for new rigorous mathematical results has turned out to be extremely difficult even in simple situations. Small steps forward thus represent significant mathematical advancements.[61]

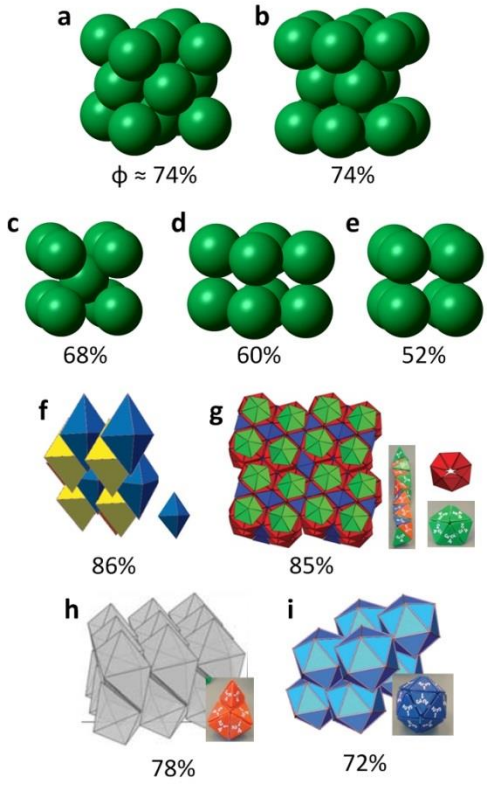

Figure 3.6. Dense and less dense crystalline arrangements of spheres and tetrahedra. (**a**) Unit cell of spheres packed in *fcc* arrangement. (**b**) Structural motif of spheres in *hcp*. (**c**) Unit cell of spheres in *bcc* packing. (**d**) Unit cell of spheres in simple hexagonal packing. (**e**) Unit cell of spheres in simple cubic packing. (**f**) Double dimer (densest known) tetrahedron packing. Adapted from refs.[62,63] (**g**) Quasicrystalline tetrahedron packing. Adapted from ref.[64] (**h**) Wagon wheel (nonamer) tetrahedron packing. Adapted from ref.[65] (**i**) Icosahedron (20-mer) tetrahedron packing. Adapted from ref.[66].

For hard spheres, the ordered phases observed in the Kirkwood-Alder transition coincide with the densest packing of spheres, yielding primarily *fcc* or *hcp* arrangements. Alternative candidate structures such as *bcc*, simple hexagonal (*sh*), and simple cubic (*sc*) (Figure 3.6c-e) have packing densities of 68%, 60%, and 52%, respectively, leaving more void space in the lattice than *fcc* and *hcp* (Figure 3.6f). Such arrangements of hard spheres are not stable, because they provide less free volume for translations in the colloidal crystal than *fcc* and *hcp* packing.

The packing of polyhedra is particularly relevant in the context of NC self-assembly because polyhedral NCs are frequently encountered as energy-minimizing Wulff shapes of NCs comprised of an atomic single crystal or twinned polycrystal.[67-70] Densest packings of most regular convex[51] and concave[71,72] polyhedra, as well as families of polyhedra,[73-75] have been reported using numerical techniques. The regular tetrahedron, for example, is the simplest Platonic solid. It has pyramid shape with four equilateral triangle sides. In one of the earliest recorded mistakes in the history of mathematics, Aristotle suggested that the regular tetrahedron tile space completely.[76] In fact, no such arrangement is possible, although a series of recent works[62-65,77] demonstrated that there exist several ways to pack tetrahedra more densely than spheres (Figure 3.6f-i). Self-assembly of tetrahedrally-shaped colloids mediated by excluded volume interactions can be expected to produce such arrangements. In the case of oleic acid capped 10-nm CdSe nanotetrahedra, however, self-assembly produces an unexpectedly open superlattice arrangement with tip-to-tip contacts between particles (see Chapter 4).

3.3.3. Dense packings of binary hard particle mixtures

The search for dense packings of two sizes of spheres was encouraged by the discovery of gem opals comprised of bidisperse silica beads.[78] Binary sphere mixtures often pack more densely than a single component alone, for example, by filling the voids in a close-packed sphere lattice with smaller spheres. When evaluating ways to densely pack sphere mixtures, there are two degrees of freedom that influence the maximally achievable packing density: the radius ratio (or size ratio), $\gamma = R_{\mathrm{B}}/R_{\mathrm{A}}$, and the stoichiometry, $x = n_{\mathrm{B}}/(n_{\mathrm{A}} + n_{\mathrm{B}})$, of the large (A) and small (B) spheres. Recent studies[79-82] uncovered more than fifteen unique binary sphere packings that exceed the densest single-component (*fcc*) arrangement (Figure 3.7). Such analyses provide a natural starting point for anticipating the structures formed by spherical NCs that seek to maximize packing density at high particle volume fraction. However, in the limit of similar sphere radii ($\gamma > 0.66$), phase separation into separate *fcc* (or *hcp*) lattices of large and small spheres provides the densest packing, while in the limit of very disparate sizes ($\gamma < 0.2$) depletion effects strongly disfavor the achievement of dense packings in experiment.

Beyond these space-filling considerations, configurational entropy and entropy of mixing provide an additional driving force for cocrystallization of two sizes of hard spheres at intermediate density. Such second-order effects can stabilize binary structures that compete with, but do not exceed, the density of phase-separated packings. Examples are the $NaZn_{13}$ arrangement within size ratio range $0.54 < \gamma < 0.61$, ref.[47] and Laves phases within $0.76 < \gamma < 0.84$, refs.[83,84] In this way, translational and configurational contributions to system entropy can stabilize a hard sphere binary crystal in some instances if its density is above about 65%. So far the complete phase behavior of binary sphere mixtures, and thus the role of entropy for the

formation of binary sphere crystals, has not been investigated for all values of the radius ratio, stoichiometry, and packing density.

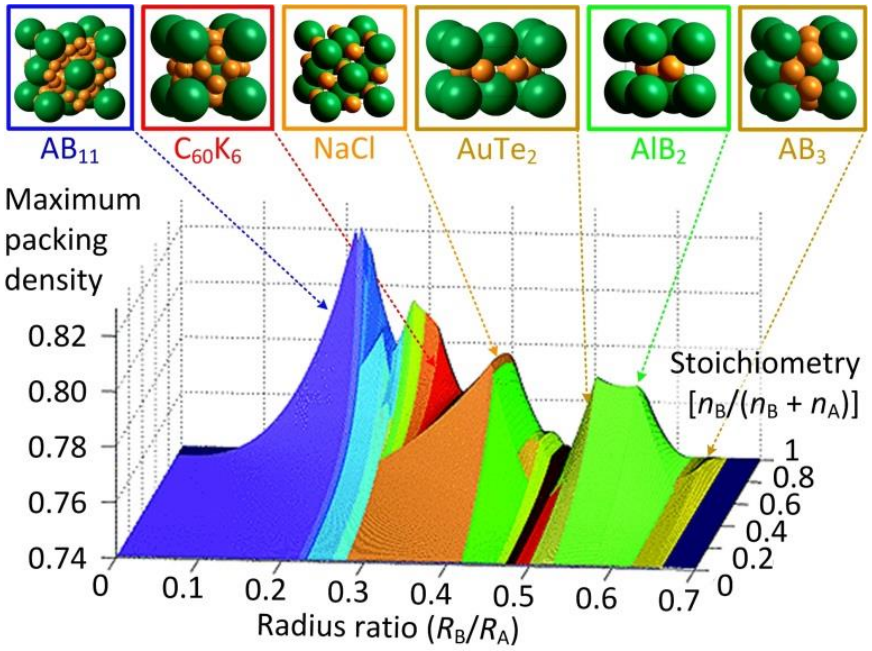

Figure 3.7. Summary of densest known binary sphere packings. Maximum packing density (z-axis) surface plot shown as a function of radius ratio (x-axis) and stoichiometry (y-axis). Unit cells or characteristic structural motifs for selected structures are shown above. The proposed maximum density is claimed by the AB_{11} structure, which fills space with about 82% efficiency at radius ratio close to 0.22. The radius ratio for which binary packings exceed single-component close packing is $\gamma < 0.66$. Adapted from ref.[79]

The phase diagram of mixtures of spheres and rods is even more complex because it contains the rod aspect ratio as a third parameter. Although the packing of rods and spheres has not been investigated in full generality, at least one binary structure of spheres and rods with aspect ratio 2 exceeds the density of demixed phases (Figure 3.8a). Closely related to the AlB_2 arrangement of spheres, this AB_2-type binary phase has a stability range of $0.5 < \gamma = R_{\text{sphere}}/R_{\text{rod}} < 0.58$, similar to where an equivalent phase is found in a binary sphere mixture (Figure 3.8b). The rod-sphere system is an example where the densest packing is not the only

ordered maximum entropy solution. At intermediate density, bulk demixing into rod-rich and rod-poor phases and microphase separation into a variety of morphologies have been predicted and observed in experiment (Figure 3.8c).[85,86] Cocrystallization is expected if these competitor phases are avoided, as recently confirmed in an investigation of experimental phase behavior of rod- and sphere-shaped NCs.[87]

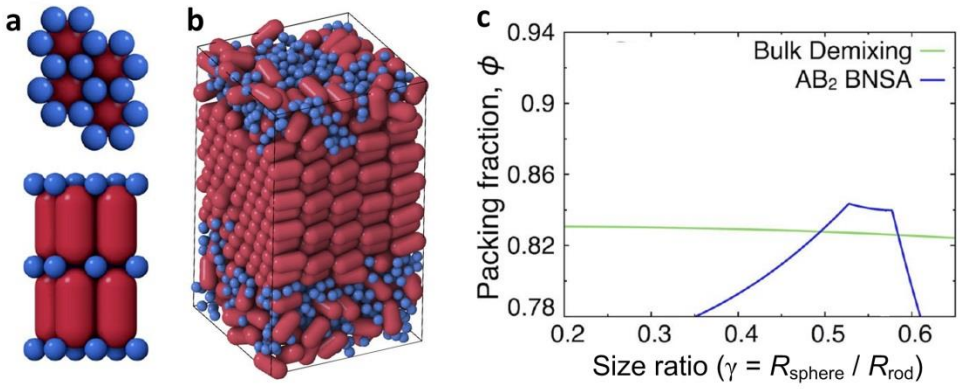

Figure 3.8. Packing rods and spheres. (**a**) Modeled AB_2 packing of rods and spheres at size ratio 0.56. (**b**) At intermediate volume fraction, simulations predict phase separation into rod crystal and mixed fluid. (**c**) Plot of packing efficiency of phase-separated (green trace) and AB_2-type binary nanocrystal shape alloy (BNSA, blue trace) for simple hard rod (spherocylinder) and sphere shapes. Excluded volume (hard particle) interactions between rods and spheres stabilize dense binary structures at size ratios $0.50 < \gamma < 0.58$. Adapted from ref.[87]

3.3.4. Cataloging stable phases of hard polyhedra

Packing arguments[88] and self-assembly studies may be extended to all manner of hard shapes to predict their phase behavior and contribute to an understanding of the relationship between particle shape and the preferred thermodynamic phase. To this end, Monte Carlo simulations revealed a large diversity of ordered maximum entropy phases in systems of hard polyhedra belonging to Platonic, Archimedean, Catalan, and Johnson solid groups,[51] many of which are experimentally accessible for NCs prepared by colloidal synthetic techniques. At

intermediate density in the $0.5 < \phi < 0.6$ range, spontaneous ordering occurs for a majority of high-symmetry polyhedra. Nucleation and growth leads to well-ordered superlattices and is generally fast. The exceptions are lower-symmetry polyhedra, which remained disordered even after prolonged simulation. On the other hand, particularly densely packing polyhedra (e.g., cubes and rhombic dodecahedra) order faster than spheres.

The assembly behavior of polyhedra can be predicted from particle sphericity and local order in the fluid. Sphericity is measured by the isoperimetric quotient $36\pi V^2/A^3$ for a particle with volume V and surface area A, normalized such that the isoperimetric quotient for a sphere is 1.[51] Three structural categories including mesophases[89] (Figure 3.9a) were observed: those with translational and orientational order (crystals), solely orientational order, and solely translational order. The roundest shapes prefer to arrange on a lattice without preference for particle orientation (plastic crystals or rotator crystals), while a large flat surface directs particles onto a lattice with orientational registry (nematic, smectic, and columnar/discotic liquid crystals), as shown in Figure 3.9b. Ordered phases can be surprisingly complex, and include the close-packed sphere lattices *fcc* and *hcp*, the soft particle lattice *bcc*, the topologically close-packed (Frank-Kasper and pseudo Frank-Kasper[90,91]) phases γ-brass, β-Mn, β-W (isostructural to the A15 phase) for weakly faceted spheres, a few Bravais lattices, and a few others including diamond (Figure 3.9a). In addition to these single-polyhedron assemblies, the phase behavior of binary mixtures of polyhedra has recently been investigated.[92]

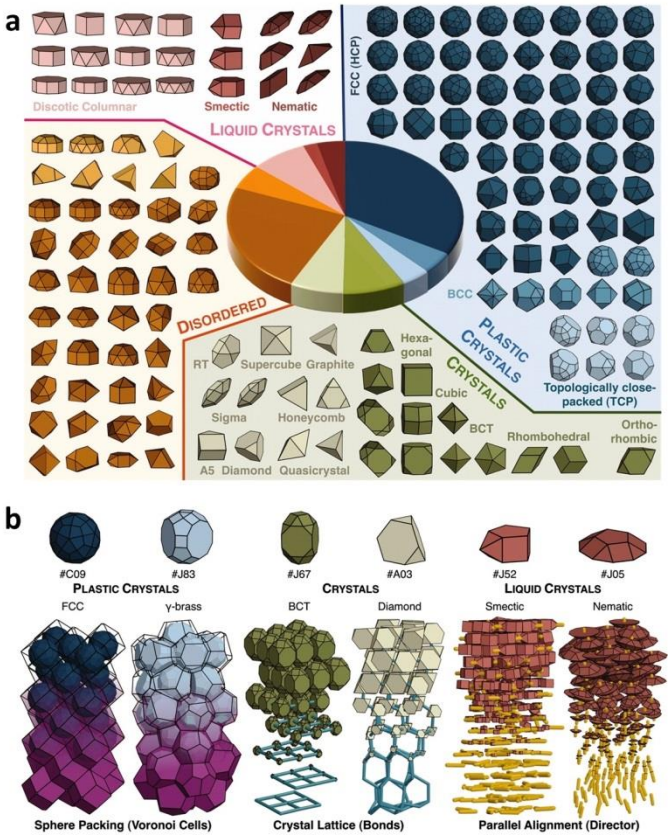

Figure 3.9. Cataloging the phases formed by Monte Carlo computer simulations of 145 convex polyhedra. (**a**) Illustrations of the polyhedra forming crystals, plastic (rotator) crystals, liquid crystals, and glasses. (**b**) Representative particle shapes that select one of the three phase families. Nearly spherical polyhedra rotate in the ordered phase (plastic crystal), facetted polyhedra resemble covalent (directionally-bonded) crystals, and asymmetric polyhedra only partially order their position (liquid crystal). Adapted from refs.[51,59]

3.4. Self-assembly of soft particles: internal surface area minimization

So far, we rationalized the phase behavior of NCs by considering only the shape of the particle core in the hard particle model. However, after synthesis, colloidal NCs are typically covered by a layer of hydrocarbon surface ligands. he presence of this corona of semi-flexible "hairs" has two effects. It softens the interaction of the inorganic cores and results in an effective NC shape that is always more spherical than the underlying core. These effects limit the applicability of the hard particle model to surfactant-stabilized NCs. The soft particle model replaces the hard particle assumption of perfect particle rigidity by the assumption of perfect particle elasticity coupled with incompressibility. In other words, soft particles can deform as long as their volume does not change.

3.4.1. Hard and soft particles are two extremes to model nanocrystals

The prime example of soft particles are block copolymer micelles. Block copolymers are a class of macromolecules with two or more chemically-distinct polymer segments (blocks), which may be, for example, hydrophobic and hydrophilic (poly(styrene)-block-poly(ethylene oxide), PS-PE). They adopt a number of ordered nanostructured phases including the spherical phase, where the minority block segregates into spheres surrounded by a corona of chains of the major component.[93] The polymer melts are easily deformable, but necessarily completely fill space because liquids do not support local density variations. Using this logic, block copolymer micelles may be considered, in good approximation, as incompressible, deformable particles.

While the self-assembly of hard particles is driven by maximization of packing density in the limit of high pressure, soft particles strive to minimize contact area between particles in the limit of low temperature.[94] For block copolymer micelles, this minimization is caused by the conformational entropy penalty associated with elastic chain deformation. Density-maximization

and area-minimization lead to different solutions. For example, while hard spheres frequently assemble into *fcc* and *hcp* arrangements, block copolymer micelles do not. Instead, these soft particles typically prefer to adopt *bcc* ordering.[95]

The combination of rigid inorganic core and soft organic corona naturally places colloidal NCs in-between the hard particle model and the soft particle model (Figure 3.10). Perhaps unsurprisingly, therefore, colloidal NCs, often with 2 – 10 nm core diameter and C_8 – C_{18} (about 1 – 2 nm length) hydrocarbon surfactant shells, self-assemble into phases characteristic of both dense packings and contact area-minimizing configurations.[96] Interestingly, the search for minimal-area soft particle phases, like the search for dense-packing hard particle phases and Hilbert's 18th problem, appears to conveniently intersect with another famous problem of mathematics.

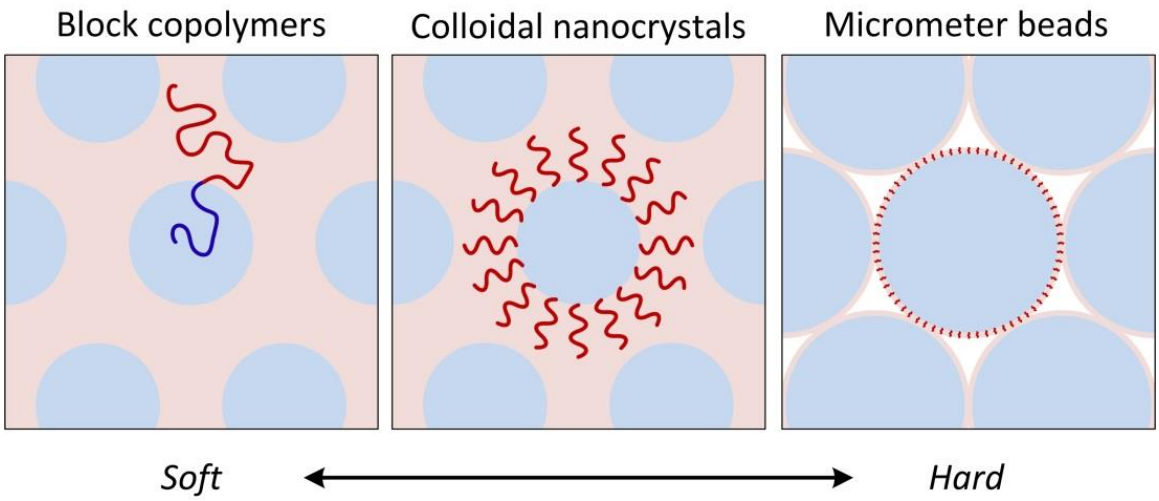

Figure 3.10. Schematic illustration of colloidal nanocrystals bearing similarity to both block copolymer systems (left: soft particles) and micron-sized colloidal beads (right: hard particles).

3.4.2. Area-minimizing principle and tetrahedral close-packing

In 1887, Lord Kelvin asked the question: what regular partition of space into cells of equal volume has the smallest surface area of cells? This concept is also known as the internal surface area-minimization principle (or in short, area-minimization principle). Kelvin proposed the *bcc* lattice to be the most area-minimizing structure. *Bcc* was considered optimal for more than one hundred years until Weaire and Phelan uncovered a more efficient partitioning of space, the A15 phase.[97] Isostructural with Cr_3Si and β-tungsten, the A15 structure features mutually orthogonal dimers centered on the faces of a *bcc* lattice (Figure 3.11a). It is a poor choice for efficient sphere packing, having a similar density as the simple cubic lattice (52%). However, A15 represents a partitioning of space with even less internal surface area than Kelvin's choice of *bcc* arrangement.

The property of efficiently partitioning space is captured by examining the shape of the Voronoi cell (also known as Wigner-Seitz polyhedron). The Voronoi cell is the space available to each particle on the lattice, or mathematically speaking, the volume that comprises all points in space that are closer to a given particle than to any other. An equivalent formulation of Kelvin's question is: Which structure maximizes the average isoperimetric quotient for its Voronoi cells? A15 (isoperimetric quotient 0.764) narrowly beats *bcc* (0.757), which in turn beats *fcc* (0.741). Since the pentagonal dodecahedral and tetrakaidecahedral Voronoi cells of A15 (Figure 3.11b) are more spherical than the truncated octahedral Voronoi cell of the *bcc* lattice, they require less deformation of a spherical soft hydrocarbon shell.

The Frank-Kasper phase family is defined to comprise all phases that feature exclusively tetrahedral voids (i.e., they are tetrahedrally-close-packed, *tcp*).[90,91] Notably, the A15 arrangement is an example of a Frank-Kasper phase. Only tetrahedral voids are present in A15 as

evidenced by its fully triangulated coordination polyhedra (Figure 3.11c). One third of the voids in the *fcc* lattice, by contrast, are octahedral. Frank-Kasper phases generally have Voronoi cells with high values of the isoperimetric quotient.

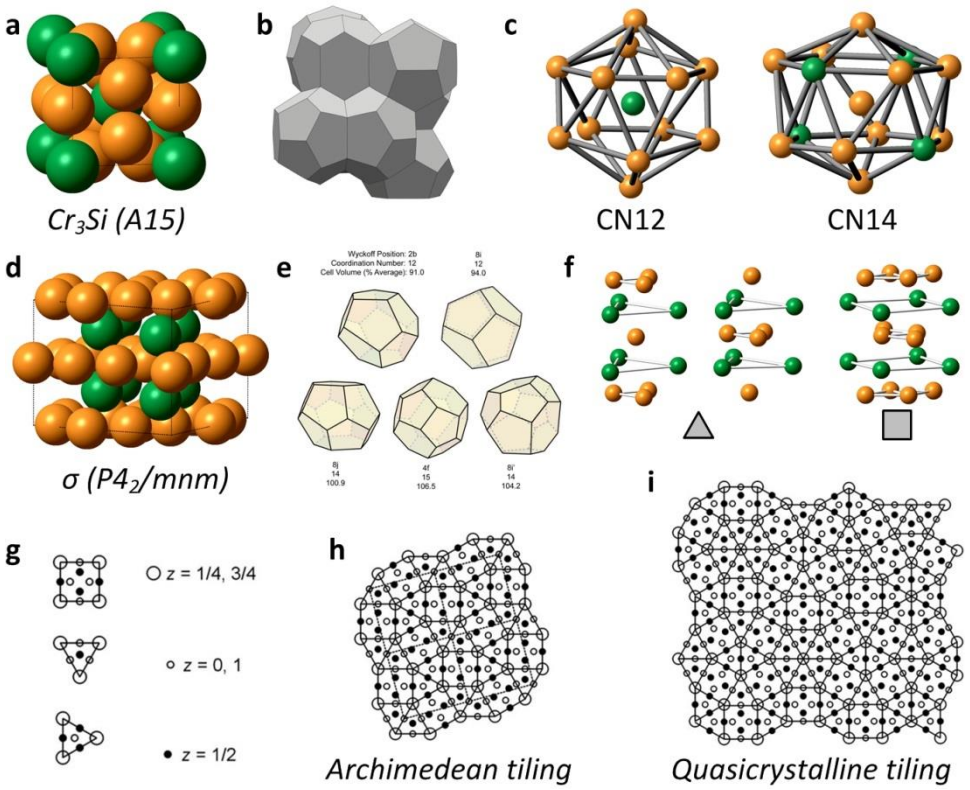

Figure 3.11. Frank-Kasper phases are tetrahedrally close-packed structures. (**a**) The A15 phase divides space into equal-volume partitions with minimal internal surface area. The unit cell is comprised of a *bcc* sublattice (green spheres) with face-centered sites (orange spheres) positioned along three mutually perpendicular, interlocking columns. (**b**) Dodecahedra and tetrakaidecahedra are the Voronoi cells of the A15 phase. Adapted from ref.[98] (**c**) Coordination polyhedra for sites in the A15 phase. Note that the polyhedra have exclusively triangular faces, which means A15 has only tetrahedral voids. (**d,e**) Relaxing the requirement for equal-volume partitions, the Frank-Kasper σ phase has even less internal surface area than the A15 phase. The σ-phase unit cell is comprised of 30 spheres, with 8j particles forming tiling vertices highlighted in green. (**f**) Decomposition into triangle (left) and square (right) tiling units. (**g**) Space-filling polyhedra with volumes shown underneath. Adapted from ref.[99] (**h,i**) Tiling from triangle and square units with only $3.4.3^2.4$ vertices in the σ phase and by including other vertices in a dodecagonal quasicrystal. Adapted from ref.[100]

An arrangement with even less internal surface area emerges if Kelvin's requirement for equal-volume partitions is removed. The new optimal phase, the Frank-Kasper σ phase, isostructural with intermetallic $Fe_{46}Cr_{54}$, has an unusually large (30 particles) unit cell (Figure 3.11d). The σ phase divides space into five distinct Voronoi polyhedra with about 15% spread in volumes (Figure 3.11e) and is comprised of triangle (Zr_4Al_3) and square (Cr_3Si) tiling units (Figure 3.11f,g).

These two polygonal units can be used to construct tilings of the plane. They can be arranged periodically in the $3.4.3^2.4$ Archimedean tiling (Figure 3.11h) with three triangles and two squares meeting at each vertex and no sharing of edges between squares. A quasicrystalline (QC) arrangement results by incorporating 3^6 vertices (six triangles meeting at a point, Figure 3.11i). The appearance of such complex phases is no surprise because tetrahedral local order is incompatible with long-range order and thus difficult to extend linearly.

Intriguingly, A15, σ, and QC are readily observed in soft matter systems such as micelle-forming block copolymers,[99,101] dendrons,[100,102] and surfactant solutions[103] (Figure 3.12) and can even be targeted via precisely controlled positional interactions between micelles of giant macromolecular tetrahedra.[104] There is significant overlap between the phases observed for soft micelles and colloidal NCs: for example, Frank-Kasper $MgZn_2$ (C14 Laves phase), σ, and QC phases result from assembly of binary NC mixtures. The area-minimizing, tetrahedrally close-packed, and often complex arrangements like Frank-Kasper A15, σ, and QC phases would not be uncovered by searching for efficient sphere packings but naturally arise when interactions between soft ligand shells are taken into account.

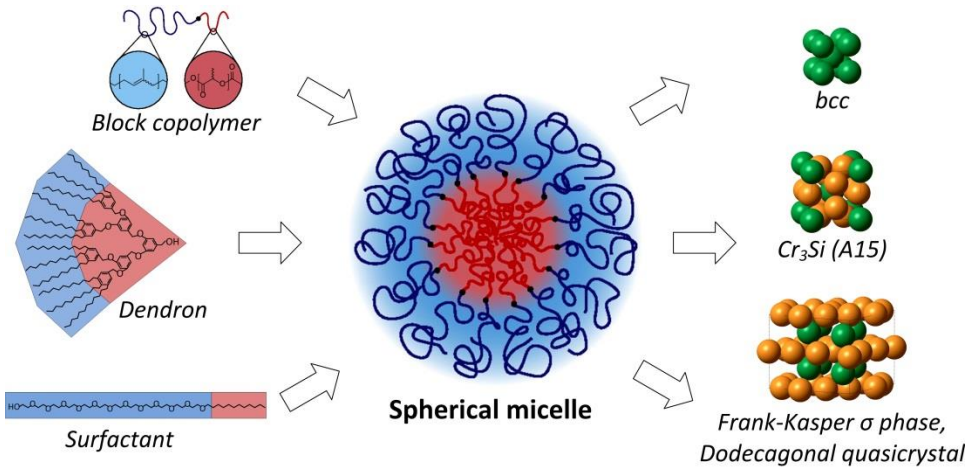

Figure 3.12. Experimental soft matter systems ordering onto area-minimizing lattices. Organic molecules such as block copolymers, dendrons, and surfactants (e.g., from top left to bottom left, polyisoprene-*b*-lactide, 3,4,5-tris-(*n*-dodecyl)benzyloxy, and dodecyl-polyethylene glycol) assemble into hairy spherical micelles (center) with phase behavior reminiscent of nanocrystal superlattices, including tetrahedrally close packed Frank-Kasper sigma phase, quasicrystal, and A15 (Weaire-Phelan) structure, as well as *bcc* phase. Center panel adapted from ref.[101]

3.4.3. Area-minimizing principle for hydrocarbon-capped nanocrystal superlattices

Only some of the phases experimentally observed for nearly spherical NCs are explained by hard-sphere packing arguments. For example, the *bcc* phase is a sub-optimal sphere packing arrangement (Figure 3.6) but is frequently observed upon evaporating solutions of quasi-spherical NCs. NC "softness", expressed as L/R, where L is the molecular length of the capping ligand and R is the radius of the inorganic core, plays a crucial role in selecting between close-packed and non-close-packed sphere arrangements: alkanethiol-capped metal NCs experience an *fcc*-to-*bcc* transition for $L/R > 0.7$.[96,105] Similar arguments also hold for DNA-mediated nanoparticle assembly into the *bcc* phase, where long linkers were identified as the cause for the deviation from close-packing.[106]

Along these lines, recent attempts to rationalize NC superlattice phase behavior have evaluated superlattice packings on the basis of an area-minimization principle. Assuming

hydrocarbon chains must fill the interparticle matrix after solvent evaporation, the shape of the space afforded to each particle (Voronoi cell or Wigner-Seitz polyhedron) packed in *fcc* or *bcc* arrangements (Figure 3.13a,b) determines the extent to which ligands are forced to compress or expand to fill space (Figure 3.13c). Plotting the distance separating the polyhedron center and all points on its surface reveals a wider spread for the rhombic decahedron (*fcc* cell) than the cuboctahedron (*bcc* cell), implying a larger elastic penalty for hydrocarbon capping ligands packed in the *fcc* arrangement (Figure 3.13d). Accordingly, for NCs with significant soft character contributed by surface-tethered hydrocarbon ligands, phase behavior reflects a contribution from both sphere packing and area-minimizing components. Such arguments have been extended to rationalize the recent experimental observation of the C14 Laves (Frank-Kasper) phase assembled from monodisperse 2-nm Au NCs capped with hexanethiol ligands and with $L/R \approx 0.84$.[107] Furthermore, evidence of an area-minimizing contribution to NC assembly has been observed for the case of binary superlattices of spherical NCs. In one notable example, solid-state binary assembly via Ostwald ripening monodisperse NC superlattices heated above 120°C yielded only Frank-Kasper or pseudo Frank-Kasper binary structures.[108] In these cases, the absence of large octahedral voids in the tetrahedrally close-packed phases, and resulting minimal distortion of surface-bound hydrocarbon chains required to fill the interparticle matrix, may be the driving force to form such unusual sphere packing arrangements.

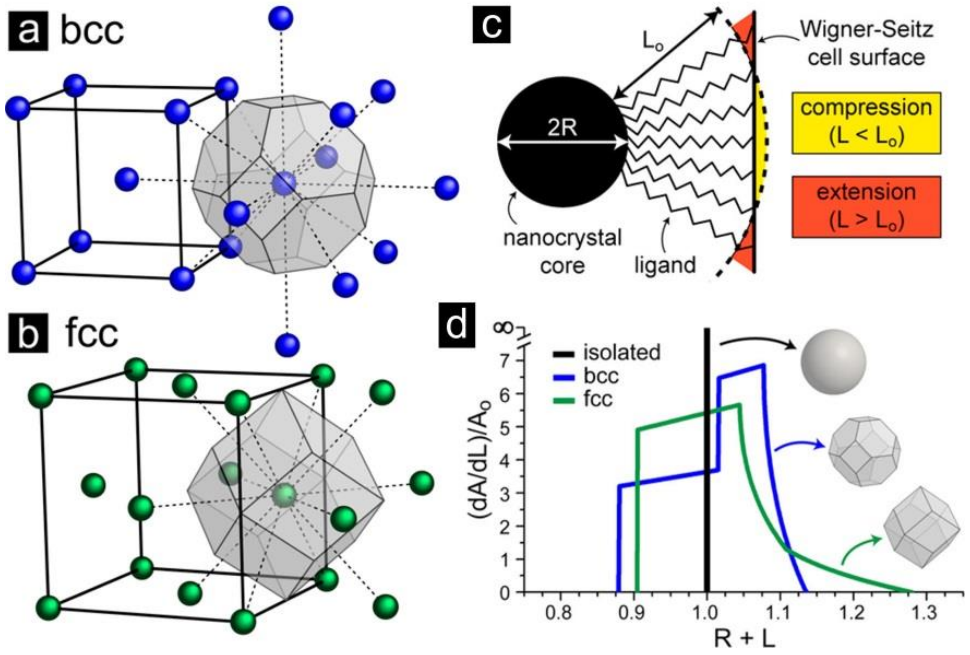

Figure 3.13. Wigner-Seitz (WS) evaluation of sphere packings. The *bcc* structure requires less distortion of the ligand corona than *fcc* arrangement. (**a**) *bcc* unit cell and the corresponding WS polyhedron. (**b**) *bcc* unit cell and the corresponding WS polyhedron. (**c**) Illustration of the compression and extension of hydrocarbon chains required to occupy the entire WS cell. (**d**) Asphericity of both WS cells. The spread in center-to-surface distances of the *bcc* WS polyhedron (blue trace) is narrower than that of the *fcc* WS polyhedron (green trace), and thus requires less distortion of capping ligands. Adapted from ref.[221]

3.5. Acknowledgements

I would like to thank Prof. Michael Engel of the Friedrich Alexander University in Nuremberg, Germany for his tremendous help in articulating the ideas contained within this chapter. We share first authorship of the forthcoming article (*Chem. Rev.* 2016) on which this chapter is based. For the sake of brevity, the discussion found in our review cataloging superlattices assembled from various-shaped hydrocarbon-capped NCs, as well as superlattices assembled from NCs with structure-directing surface ligands, has been omitted from this chapter. The interested reader is referred to this article for the extended discussion.

3.6. References

1 Shevchenko, E. & Talapin, D. in *Semiconductor Nanocrystal Quantum Dots* (ed AndreyL Rogach) Ch. 5, 119-169 (Springer Vienna, 2008).

2 Schapotschnikow, P., Pool, R. & Vlugt, T. J. H. Molecular Simulations of Interacting Nanocrystals. *Nano Letters* **8**, 2930-2934, (2008).

3 Fritz, G., Schädler, V., Willenbacher, N. & Wagner, N. J. Electrosteric Stabilization of Colloidal Dispersions. *Langmuir* **18**, 6381-6390, (2002).

4 Nag, A. *et al.* Metal-free Inorganic Ligands for Colloidal Nanocrystals: S^{2-}, HS^{-}, Se^{2-}, HSe^{-}, Te^{2-}, HTe^{-}, TeS_3^{2-}, OH^{-}, and NH_2^{-} as Surface Ligands. *J. Am. Chem. Soc.* **133**, 10612-10620 (2011).

5 Witten, T. A. & Sander, L. M. Diffusion-Limited Aggregation, a Kinetic Critical Phenomenon. *Physical Review Letters* **47**, 1400-1403 (1981).

6 Rupich, S. M., Shevchenko, E. V., Bodnarchuk, M. I., Lee, B. & Talapin, D. V. Size-Dependent Multiple Twinning in Nanocrystal Superlattices. *Journal of the American Chemical Society* **132**, 289-296, (2009).

7 P, A. & de Paula, J. *Physical Chemistry*. (Oxford University Press, 2006).

8 Ge, G. & Brus, L. Evidence for Spinodal Phase Separation in Two-Dimensional Nanocrystal Self-Assembly. *The Journal of Physical Chemistry B* **104**, 9573-9575, (2000).

9 Bigioni, T. P. *et al.* Kinetically driven self assembly of highly ordered nanoparticle monolayers. *Nat Mater* **5**, 265-270, (2006).

10 Hamaker, H. C. The London—van der Waals attraction between spherical particles. *Physica* **4**, 1058-1072, (1937).

11 Shevchenko, E. V., Talapin, D. V., Kotov, N. A., O'Brien, S. & Murray, C. B. Structural diversity in binary nanoparticle superlattices. *Nature* **439**, 55-59, (2006).

12 Israelachvili, J. N. *Intermolecular and Surface Forces*. (Elsevier, 2011).

13 Saunders, A. E. & Korgel, B. A. Second Virial Coefficient Measurements of Dilute Gold Nanocrystal Dispersions Using Small-Angle X-ray Scattering. *The Journal of Physical Chemistry B* **108**, 16732-16738, (2004).

14 Derjaguin, B. Untersuchungen über die Reibung und Adhäsion, IV. *Kolloid-Zeitschrift* **69**, 155-164, (1934).

15 Rubinstein, M. & Colby, R. *Polymer Physics*. (Oxford University Press, 2003).

16 Napper, D. H. Steric stabilization. *Journal of Colloid and Interface Science* **58**, 390-407, (1977).

17 Boles, M. A. & Talapin, D. V. Self-Assembly of Tetrahedral CdSe Nanocrystals: Effective "Patchiness" via Anisotropic Steric Interaction. *Journal of the American Chemical Society* **136**, 5868-5871, (2014).

18 Mattoussi, H., Cumming, A. W., Murray, C. B., Bawendi, M. G. & Ober, R. Properties of CdSe nanocrystal dispersions in the dilute regime: Structure and interparticle interactions. *Physical Review B* **58**, 7850-7863 (1998).

19 Matsen, M. W. Effect of Chain Tilt on the Interaction between Brush-Coated Colloids. *Macromolecules* **38**, 4525-4530, (2005).

20 Schapotschnikow, P. & Vlugt, T. J. H. Understanding interactions between capped nanocrystals: Three-body and chain packing effects. *The Journal of Chemical Physics* **131**, 124705-124713 (2009).

21 Fischer, S., Salcher, A., Kornowski, A., Weller, H. & Förster, S. Completely Miscible Nanocomposites. *Angewandte Chemie International Edition* **50**, 7811-7814, (2011).

22 Salem, L. Attractive Forces between Long Saturated Chains at Short Distances. *J. Chem. Phys.* **37**, 2100, (1962).

23 Dubois, L. H. & Nuzzo, R. G. Synthesis, Structure, and Properties of Model Organic Surfaces. *Annual Review of Physical Chemistry* **43**, 437-463 (1992).

24 Luedtke, W. D. & Landman, U. Structure, Dynamics, and Thermodynamics of Passivated Gold Nanocrystallites and Their Assemblies. *The Journal of Physical Chemistry* **100**, 13323-13329, (1996).

25 Morris-Cohen, A. J., Malicki, M., Peterson, M. D., Slavin, J. W. J. & Weiss, E. A. Chemical, Structural, and Quantitative Analysis of the Ligand Shells of Colloidal Quantum Dots. *Chemistry of Materials* **25**, 1155-1165, (2013).

26 Badia, A., Cuccia, L., Demers, L., Morin, F. & Lennox, R. B. Structure and Dynamics in Alkanethiolate Monolayers Self-Assembled on Gold Nanoparticles: A DSC, FT-IR, and Deuterium NMR Study. *Journal of the American Chemical Society* **119**, 2682-2692,

(1997).

27 Lee, B. *et al.* Comparison of Structural Behavior of Nanocrystals in Randomly Packed Films and Long-Range Ordered Superlattices by Time-Resolved Small Angle X-ray Scattering. *Journal of the American Chemical Society* **131**, 16386-16388, (2009).

28 Landman, U. & Luedtke, W. D. Small is different: energetic, structural, thermal, and mechanical properties of passivated nanocluster assemblies. *Faraday Discussions* **125**, 1-22, (2004).

29 Boles, M. A. & Talapin, D. V. Many-Body Effects in Nanocrystal Superlattices: Departure from Sphere Packing Explains Stability of Binary Phases. *Journal of the American Chemical Society* **137**, 4494-4502, (2015).

30 Boles, M. A., Ling, D., Hyeon, T. & Talapin, D. V. The surface science of nanocrystals. *Nat Mater* **15**, 141-153, (2016).

31 Schmid, G. Large clusters and colloids. Metals in the embryonic state. *Chemical Reviews* **92**, 1709-1727, (1992).

32 Gaponik, N. *et al.* Thiol-Capping of CdTe Nanocrystals: An Alternative to Organometallic Synthetic Routes. *The Journal of Physical Chemistry B* **106**, 7177-7185, (2002).

33 Walker, D. A., Kowalczyk, B., de la Cruz, M. O. & Grzybowski, B. A. Electrostatics at the nanoscale. *Nanoscale* **3**, 1316-1344, (2011).

34 Bishop, K. J. M., Wilmer, C. E., Soh, S. & Grzybowski, B. A. Nanoscale Forces and Their Uses in Self-Assembly. *Small* **5**, 1600-1630, (2009).

35 Luo, D., Yan, C. & Wang, T. Interparticle Forces Underlying Nanoparticle Self-Assemblies. *Small* **11**, 5984-6008, (2015).

36 Min, Y., Akbulut, M., Kristiansen, K., Golan, Y. & Israelachvili, J. The role of interparticle and external forces in nanoparticle assembly. *Nat Mater* **7**, 527-538 (2008).

37 Silvera Batista, C. A., Larson, R. G. & Kotov, N. A. Nonadditivity of nanoparticle interactions. *Science* **350** (2015).

38 Pauling, L. THE PRINCIPLES DETERMINING THE STRUCTURE OF COMPLEX IONIC CRYSTALS. *Journal of the American Chemical Society* **51**, 1010-1026, (1929).

39 Glotzer, S. C. & Solomon, M. J. Anisotropy of building blocks and their assembly into complex structures. *Nat Mater* **6**, 557-562 (2007).

40 Cademartiri, L., Bishop, K. J. M., Snyder, P. W. & Ozin, G. A. Using shape for self-assembly. *Philosophical Transactions of the Royal Society of London A: Mathematical, Physical and Engineering Sciences* **370**, 2824-2847 (2012).

41 Kirkwood, J. G. Molecular Distribution in Liquids. *J. Chem. Phys.* **7**, 919, (1939).

42 Alder, B. J. & Wainwright, T. E. Phase Transition for a Hard Sphere System. *J. Chem. Phys.* **27**, 1208, (1957).

43 Pusey, P. N. & Megen, W. v. Phase behaviour of concentrated suspensions of nearly hard colloidal spheres. *Nature* **320**, 340-342, (1986).

44 Zhu, J. *et al.* Crystallization of hard-sphere colloids in microgravity. *Nature* **387**, 883-885 (1997).

45 Frenkel, D. Entropy-driven phase transitions. *Physica A: Statistical Mechanics and its Applications* **263**, 26-38, (1999).

46 Barrat, J. L. & Hansen, J. P. *Basic Concepts for Simple and Complex Liquids*. (Cambridge University Press, 2003).

47 Eldredge, M. D. Entropy-driven formation of a superlattice in a hard-sphere binary mixture. **365**, 35-37 (1993).

48 Lekkerkerker, H. N. W. & Vroege, G. J. Liquid crystal phase transitions in suspensions of mineral colloids: new life from old roots. *Philosophical Transactions of the Royal Society of London A: Mathematical, Physical and Engineering Sciences* **371** (2013).

49 Onsager, L. THE EFFECTS OF SHAPE ON THE INTERACTION OF COLLOIDAL PARTICLES. *Annals of the New York Academy of Sciences* **51**, 627-659, (1949).

50 Frenkel, D., Mulder, B. M. & McTague, J. P. Phase Diagram of a System of Hard Ellipsoids. *Physical Review Letters* **52**, 287-290 (1984).

51 Damasceno, P. F., Engel, M. & Glotzer, S. C. Predictive Self-Assembly of Polyhedra into Complex Structures. *Science* **337**, 453-457, (2012).

52 Jiang, P., Bertone, J. F., Hwang, K. S. & Colvin, V. L. Single-Crystal Colloidal Multilayers of Controlled Thickness. *Chemistry of Materials* **11**, 2132-2140, (1999).

53 Anderson, V. J. & Lekkerkerker, H. N. W. Insights into phase transition kinetics from colloid science. *Nature* **416**, 811-815 (2002).

54 Bolhuis, P. & Frenkel, D. Tracing the phase boundaries of hard spherocylinders. *J. Chem. Phys.* **106**, 666 (1997).

55 Hilbert, D. Mathematical Problems. *Bull. Amer. Math. Soc.* **8**, 437-479, (1902).

56 Hales, T. C. Historical Overview of the Kepler Conjecture. *Discrete & Computational Geometry* **36**, 5-20, (2006).

57 Bolhuis, P. G., Frenkel, D., Mau, S.-C. & Huse, D. A. Entropy difference between crystal phases. *Nature* **388**, 235-236 (1997).

58 Elser, V. Phonon contribution to the entropy of hard-sphere crystals. *Physical Review E* **89**, 052404 (2014).

59 Schultz, B. A., Damasceno, P. F., Engel, M. & Glotzer, S. C. Symmetry Considerations for the Targeted Assembly of Entropically Stabilized Colloidal Crystals via Voronoi Particles. *ACS Nano* **9**, 2336-2344, (2015).

60 Grunbaum, B. & Shephard, G. C. *Tilings and Patterns*. (1990).

61 Kallus, Y. The 3-ball is a local pessimum for packing. *Advances in Mathematics* **264**, 355-370, (2014).

62 Chen, E. R., Engel, M. & Glotzer, S. C. Dense Crystalline Dimer Packings of Regular Tetrahedra. *Discrete & Computational Geometry* **44**, 253-280, (2010).

63 Kallus, Y., Elser, V. & Gravel, S. Dense Periodic Packings of Tetrahedra with Small Repeating Units. *Discrete & Computational Geometry* **44**, 245-252, (2010).

64 Haji-Akbari, A. *et al.* Disordered, quasicrystalline and crystalline phases of densely packed tetrahedra. *Nature* **462**, 773-777, (2009).

65 Chen, E. A Dense Packing of Regular Tetrahedra. *Discrete & Computational Geometry* **40**, 214-240, (2008).

66 Torquato, S. & Jiao, Y. Dense packings of the Platonic and Archimedean solids. *Nature* **460**, 876-879, (2009).

67 Huang, M. H. & Lin, P.-H. Shape-Controlled Synthesis of Polyhedral Nanocrystals and Their Facet-Dependent Properties. *Advanced Functional Materials* **22**, 14-24, (2012).

68 Quan, Z. & Fang, J. Superlattices with non-spherical building blocks. *Nano Today* **5**, 390-411, (2010).

69 Sau, T. K. & Rogach, A. L. Nonspherical Noble Metal Nanoparticles: Colloid-Chemical Synthesis and Morphology Control. *Advanced Materials* **22**, 1781-1804, (2010).

70 Niu, W. & Xu, G. Crystallographic control of noble metal nanocrystals. *Nano Today* **6**, 265-285, (2011).

71 de Graaf, J., van Roij, R. & Dijkstra, M. Dense Regular Packings of Irregular Nonconvex Particles. *Physical Review Letters* **107**, 155501 (2011).

72 de Graaf, J., Filion, L., Marechal, M., van Roij, R. & Dijkstra, M. Crystal-structure prediction via the Floppy-Box Monte Carlo algorithm: Method and application to hard (non)convex particles. *J. Chem. Phys.* **137**, 214101 (2012).

73 Damasceno, P. F., Engel, M. & Glotzer, S. C. Crystalline Assemblies and Densest Packings of a Family of Truncated Tetrahedra and the Role of Directional Entropic Forces. *ACS Nano* **6**, 609-614, (2011).

74 Gantapara, A. P., de Graaf, J., van Roij, R. & Dijkstra, M. Phase Diagram and Structural Diversity of a Family of Truncated Cubes: Degenerate Close-Packed Structures and Vacancy-Rich States. *Physical Review Letters* **111**, 015501 (2013).

75 Chen, E. R., Klotsa, D., Engel, M., Damasceno, P. F. & Glotzer, S. C. Complexity in Surfaces of Densest Packings for Families of Polyhedra. *Physical Review X* **4**, 011024 (2014).

76 Lagarias, J. C. & Zong, C. Mysteries in Packing Regular Tetrahedra. *Notices of the American Mathematical Society* **59**, 1540-1549, (2012).

77 Conway, J. H. & Torquato, S. Packing, Tiling, and Covering with Tetrahedra. *Proceedings of the National Academy of Sciences of the United States of America* **103**, 10612-10617, (2006).

78 Murray, M. J. & Sanders, J. V. Close-packed structures of spheres of two different sizes II. The packing densities of likely arrangements. *Philosophical Magazine A* **42**, 721-740, (1980).

79 Hopkins, A. B., Stillinger, F. H. & Torquato, S. Densest binary sphere packings. *Physical Review E* **85**, 021130 (2012).

80 O'Toole, P. I. & Hudson, T. S. New High-Density Packings of Similarly Sized Binary Spheres. *The Journal of Physical Chemistry C* **115**, 19037-19040, (2011).

81 Filion, L. & Dijkstra, M. Prediction of binary hard-sphere crystal structures. *Physical Review E* **79**, 046714 (2009).

82 Kummerfeld, J. K., Hudson, T. S. & Harrowell, P. The Densest Packing of AB Binary Hard-Sphere Homogeneous Compounds across all Size Ratios. *The Journal of Physical Chemistry B* **112**, 10773-10776, (2008).

83 Hynninen, A.-P., Thijssen, J. H. J., Vermolen, E. C. M., Dijkstra, M. & van Blaaderen, A. Self-assembly route for photonic crystals with a bandgap in the visible region. *Nat Mater* **6**, 202-205 (2007).

84 Hynninen, A. P., Filion, L. & Dijkstra, M. Stability of LS and LS_2 crystal structures in binary mixtures of hard and charged spheres. *J. Chem. Phys.* **131**, 064902 (2009).

85 Adams, M., Dogic, Z., Keller, S. L. & Fraden, S. Entropically driven microphase transitions in mixtures of colloidal rods and spheres. *Nature* **393**, 349-352 (1998).

86 Dogic, Z., Frenkel, D. & Fraden, S. Enhanced stability of layered phases in parallel hard spherocylinders due to addition of hard spheres. *Physical Review E* **62**, 3925-3933 (2000).

87 Ye, X. *et al.* Shape Alloys of Nanorods and Nanospheres from Self-Assembly. *Nano Letters* **13**, 4980-4988, u (2013).

88 Torquato, S. & Stillinger, F. H. Jammed hard-particle packings: From Kepler to Bernal and beyond. *Reviews of Modern Physics* **82**, 2633-2672 (2010).

89 Agarwal, U. & Escobedo, F. A. Mesophase behaviour of polyhedral particles. *Nat Mater* **10**, 230-235, (2011).

90 Frank, F. C. & Kasper, J. S. Complex alloy structures regarded as sphere packings. II. Analysis and classification of representative structures. *Acta Crystallographica* **12**, 483-499, (1959).

91 Shoemaker, D. P. & Shoemaker, C. B. Concerning the relative numbers of atomic coordination types in tetrahedrally close packed metal structures. *Acta Crystallographica Section B* **42**, 3-11, (1986).

92 Khadilkar, M. R., Agarwal, U. & Escobedo, F. A. Phase behavior of binary mixtures of hard convex polyhedra. *Soft Matter* **9**, 11557-11567, (2013).

93 Bates, F. S. & Fredrickson, G. H. Block Copolymers: Designer Soft Materials. *Physics Today* **52**, 32-38, (1999).

94 Ziherl, P. & Kamien, R. D. Maximizing Entropy by Minimizing Area: Towards a New Principle of Self-Organization. *The Journal of Physical Chemistry B* **105**, 10147-10158, (2001).

95 Leibler, L. Theory of Microphase Separation in Block Copolymers. *Macromolecules* **13**, 1602-1617, (1980).

96 Whetten, R. L. *et al.* Crystal Structures of Molecular Gold Nanocrystal Arrays. *Accounts of Chemical Research* **32**, 397-406, (1999).

97 Weaire, D. & Phelan, R. A counter-example to Kelvin's conjecture on minimal surfaces. *Philosophical Magazine Letters* **69**, 107-110, (1994).

98 Ball, P. Scientists make the 'perfect' foam. (Nature, 2011).

99 Lee, S., Bluemle, M. J. & Bates, F. S. Discovery of a Frank-Kasper σ Phase in Sphere-Forming Block Copolymer Melts. *Science* **330**, 349-353 (2010).

100 Zeng, X. *et al.* Supramolecular dendritic liquid quasicrystals. *Nature* **428**, 157-160, (2004).

101 Lee, S., Leighton, C. & Bates, F. S. Sphericity and symmetry breaking in the formation of Frank–Kasper phases from one component materials. *Proceedings of the National Academy of Sciences* **111**, 17723-17731 (2014).

102 Ungar, G., Liu, Y., Zeng, X., Percec, V. & Cho, W.-D. Giant Supramolecular Liquid Crystal Lattice. *Science* **299**, 1208-1211, (2003).

103 Sakya, P., Seddon, J. M., Templer, R. H., Mirkin, R. J. & Tiddy, G. J. T. Micellar Cubic Phases and Their Structural Relationships: The Nonionic Surfactant System C12EO12/Water. *Langmuir* **13**, 3706-3714, (1997).

104 Huang, M. *et al.* Selective assemblies of giant tetrahedra via precisely controlled positional interactions. *Science* **348**, 424-428 (2015).

105 Goodfellow, B. W. & Korgel, B. A. Reversible Solvent Vapor-Mediated Phase Changes in Nanocrystal Superlattices. *ACS Nano* **5**, 2419-2424, (2011).

106 Thaner, R. V. *et al.* Entropy-Driven Crystallization Behavior in DNA-Mediated Nanoparticle Assembly. *Nano Letters* **15**, 5545-5551, (2015).

107 Hajiw, S., Pansu, B. & Sadoc, J.-F. Evidence for a C14 Frank–Kasper Phase in One-Size Gold Nanoparticle Superlattices. *ACS Nano* **9**, 8116-8121, (2015).

108 Goodfellow, B. W. *et al.* Ordered Structure Rearrangements in Heated Gold Nanocrystal Superlattices. *Nano Letters* **13**, 5710-5714, (2013).

4. Self-assembly of tetrahedral CdSe nanocrystals: effective patchiness via anisotropic steric interaction

Controlling the spontaneous organization of nanoscale objects remains a fundamental challenge of materials design. Here we present the first characterization of self-assembled superlattices comprised of tetrahedral nanocrystals. We observe self-assembly of CdSe nanotetrahedra into an open structure (estimated space-filling fraction $\varphi \approx 0.59$) which has not been anticipated by many recent theoretical studies and simulations of tetrahedron packings. This finding highlights a gap in the understanding of the hierarchy of energy scales acting on colloidal NCs during the self-assembly process. We propose strong dependence of ligand interaction potential on NC surface curvature. This effect favors spatial proximity of vertices in the dense colloidal crystal and may be considered an emergent "patchiness" acting through chemically identical ligand molecules.

4.1. Dense tetrahedron packings

4.1.1. Mathematical constructions

Tetrahedron packing has been studied theoretically and computationally for many years. Spurring a recent revival in interest, Conway and Torquato showed that twenty tetrahedra may be packed into an icosahedron and subsequent lattice packing of icosahedra produces an arrangement of tetrahedra with density $\varphi \approx 0.72$.[1] In 2008, by constructing an eighteen-tetrahedron cluster and finding a suitable lattice packing of clusters, Chen reported a packing with $\varphi \approx 0.78$,[2] providing the first example of an arrangement of tetrahedra which fills space more densely than the *fcc* arrangement of spheres ($\varphi \approx 0.74$). The following year, Haji-Akbari et al. used Monte Carlo simulations to compress a fluid of hard tetrahedra to a quasicrystalline

phase with packing density $\varphi \approx 0.82$ and made a new periodic structure with 82 particles per unit cell and density $\varphi \approx 0.85$.[3] The current record is claimed by a double-dimer packing with four tetrahedra per unit cell and $\varphi \approx 0.86$.[4]

In parallel, much effort has been devoted to understanding packing behavior of various "imperfect" tetrahedra. Phase diagrams have been calculated for tetrahedral particles with various degrees of truncation,[5] for tetrahedrally-truncated spheres,[6] and for tetrahedral "puffs".[7] Simulations of hard faceted particles inspired conceptual development of "directional entropic forces" (DEFs) guiding assembly of anisotropic particles toward structures with parallel facet alignment.[8] In contrast to enthalpic patchiness (arising from, for example, molecular patterning[9] or DNA functionalization[10]) DEFs promote local dense packing.

4.1.2. Physical tetrahedra

Despite progress in mathematical constructions of tetrahedron (and pseudo-tetrahedron) packings, there exist only a few experimental investigations of such packings. In one example, Jaoshvili et al. poured tetrahedral dice into containers and used volumetric measurement to determine random close packings of tetrahedra have density 0.76 ± 0.02.[11] On the other hand, a similar set of experiments performed using polyhedral plastic dice spanning the entire family of Platonic solids revealed lower observed tetrahedron packing fractions ($0.51 < \phi < 0.64$) when allowed to sediment inside a container by mechanical vibration.[12]

4.1.3. Packing problem treatment of nanocrystal assembly

Several recent studies suggest that self-assembly of semiconductor (CdSe, PbSe, etc.) NCs into SLs is an entropy-driven process.[13] This approach treats NC assembly as a packing problem (see Chapter 3) with entropic stabilization of dense ordered phases. Indeed, spherical NCs typically arrange themselves in *fcc* or *hcp* packings, the most dense arrangements (both $\varphi \approx$

0.74) possible for spheres.[14] The role of translational entropy in driving NC assemblies to most-dense configurations suggests that colloidal NCs might offer insight into the mathematical problem of finding dense arrangements of non-spherical objects. On the other hand, tailoring soft interactions between NCs may enable formation of structures not anticipated for hard objects.

4.2. Synthesis and characterization of CdSe nanotetrahedra

In this work we study the self-assembly of tetrahedral CdSe nanocrystals. Following a recipe outlined by Liu et al.,[15] zinc blende phase CdSe tetrahedra were synthesized by reacting cadmium oleate with elemental selenium in ODE at 250°C. Tetrahedral NC shape results from NC growth occurring preferentially along (100) crystallographic directions due to weaker binding of oleic acid ligands to the CdSe (100) surface than CdSe (111).

4.2.1. Colloidal synthesis of tetrahedrally-shaped CdSe

This reaction proceeds in two steps. First, stirring cadmium acetate precursor in the presence of excess oleic acid (OA) at 120°C forms a cadmium oleate complex:

$$\mathrm{Cd(CH_3CO_2)_2 + OA \quad \rightarrow \quad Cd(OA)_2 + CH_3CO_2H} \qquad (1)$$

Then, this cadmium oleate complex is injected into a solution of selenium dissolved in 1-octadecene (ODE) at 250°C:

$$\mathrm{Cd(OA)_2 + CH_3CO_2H + Se \xrightarrow{ODE,250°C} CdSe\ tetrahedra} \qquad (2)$$

The presence of acetic acid (CH_3CO_2H) is crucial to the growth of anisotropic nanostructures.[16] Degassing the reaction mixture in step (1) will result in growth of spherical NCs. On the other hand, branched, tetrahedral, or cubic NC shapes are accessible if the presence

of acetic acid in the cadmium precursor solution is preserved by avoiding evacuation of the flask during formation of the cadmium oleate complex.

Temperature is another crucial parameter in this procedure: while 8-nm edge length tetrahedra (measured from microscopy images) were obtained by injecting at 270°C (Figure 4.1a,b), 10-nm tetrahedra were obtained by injecting at 250°C (Figure 4.1c,d). In both cases, growth was allowed to proceed for 20 minutes at 250°C. Higher injection temperature creates more nuclei to compete for the same monomer supply, producing smaller NCs after completion of the reaction. On the other hand, injecting at 270°C and holding the reaction at 270°C produces cubic CdSe NCs (Figure 4.1e,f).

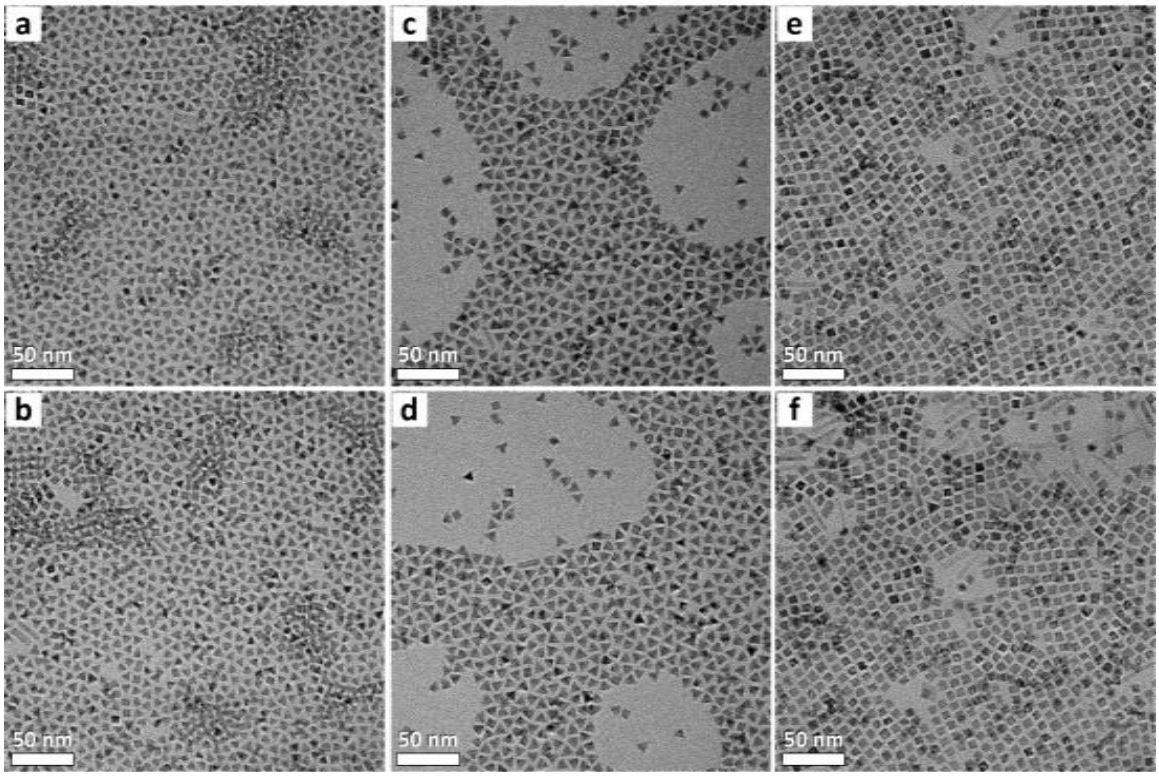

Figure 4.1. Shape-controlled synthesis of zinc blende CdSe NCs. (a,b) Injecting cadmium oleate into selenium-octadecene at 270°C and holding reaction at 250°C produces CdSe tetrahedra with edge length of 8 nm. (c,d) Injecting at 250°C and holding at this temperature during the entire reaction produces 10-nm CdSe tetrahedra. (e,f) Injecting at 270°C and holding at this temperature during the entire reaction produces 10-nm CdSe cubes.

4.2.2. Characterization of tetrahedrally-shaped CdSe

Zinc blende phase CdSe tetrahedra and cubes were characterized by transmission electron microscopy (TEM) and absorption (UV-Vis-NIR) spectroscopy. These are core-sensitive techniques (Chapter 1) enabling estimation of NC size and shape. In addition, oleate ligands installed from synthesis on the surface of CdSe NCs were characterized by Fourier Transform infrared (FT-IR) spectroscopy, enabling identification of surface-bound chemical species, and thermogravimetric analysis (TGA), which allows for estimation of relative abundance (mass fraction or volume fraction) of organic and inorganic components in NC solid films.

In the first case, TEM confirmed size- and shape-uniform tetrahedra or cubes (Figure 1.1). Absorption spectroscopy probes electronic transitions within the inorganic core. This analysis revealed several pronounced absorption peaks for tetrahedrally-shaped NCs (Figure 4.2a,b) close to the CdSe bulk band gap (eV, or nm) Similar, but comparatively washed out, features were found for cubic NCs (Figure 4.2c).

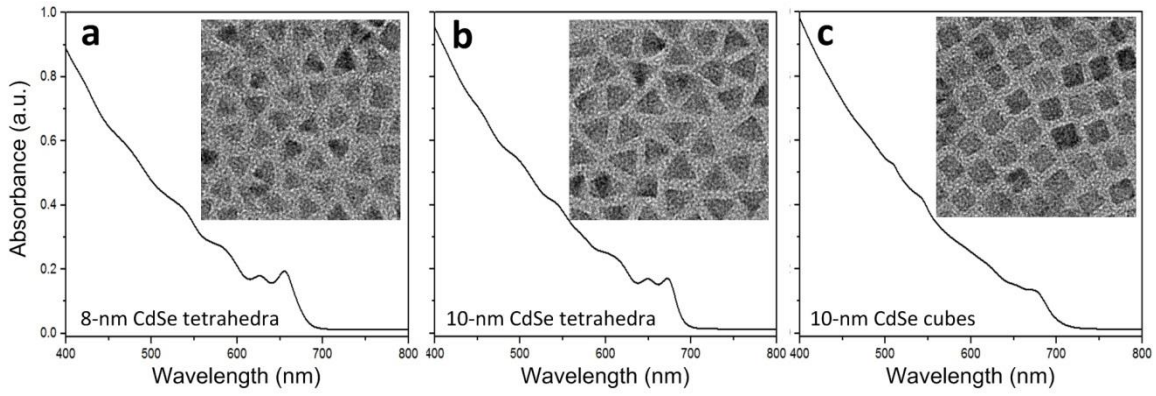

Figure 4.2. Characterization of anisotropic CdSe NCs using UV-Vis-NIR absorption spectroscopy. Visible – near infrared absorption spectra of (a) 8-nm edge length tetrahedra, (b) 10-nm edge length tetrahedra, and (c) 10-nm edge length cubes. Inset: TEM of corresponding NCs.

The oleate ligands capping the surface of CdSe tetrahedra were probed FT-IR, revealing absorption in the mid-infrared corresponding to excitation of hydrocarbon ligand vibrational modes (Figure 4.3a). Absorbance bands at 2800 – 3000 cm^{-1} correspond to hydrocarbon C-H stretching modes, those at 500 – 1500 cm^{-1} correspond to C-H bending modes, and the band at 1540 cm^{-1} was assigned to cadmium carboxylate C=O stretch. Assignment of vibrational modes was made using ref.[17]

In addition, TGA was used to estimate the organic mass fraction of 10-nm CdSe tetrahedra (Figure 4.3b). A 10mg sample of the dried NC solid was to a temperature exceeding thermal decomposition of surface ligands leaving behind a bulk CdSe powder free of hydrocarbons. The mass loss accompanying such a process was used to estimate the volume of organic ligands per particle, and the effective packing fraction of the NC superlattice including ligand contribution to particle volume (Section 4.4.4).

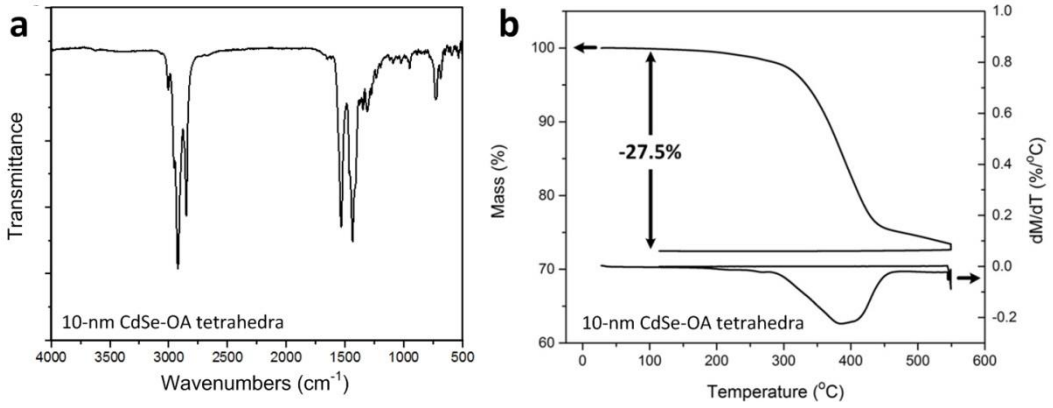

Figure 4.3. Characterization of oleic acid surface ligands on 10-nm edge length tetrahedral CdSe NCs using FT-IR spectroscopy and thermogravimetric analysis.

4.3. Self-assembly of CdSe nanotetrahedra

Self-assembly was carried out by evaporation of carrier solvent and destabilization of the colloidal solution via slow addition of nonsolvent (see also Chapter 1, Figure 1.4).

4.3.1. Evaporation-based self-assembly

CdSe nanotetrahedra capped with oleate surface ligands were self-assembled by evaporation (Section 1.4.1) from dilute octane solution over a tilted vial containing a TEM grid. Initial inspection of the grid showed three different arrangements (Figure 4.4), which could either be three distinct structures or various crystallographic projections of the same superlattice.

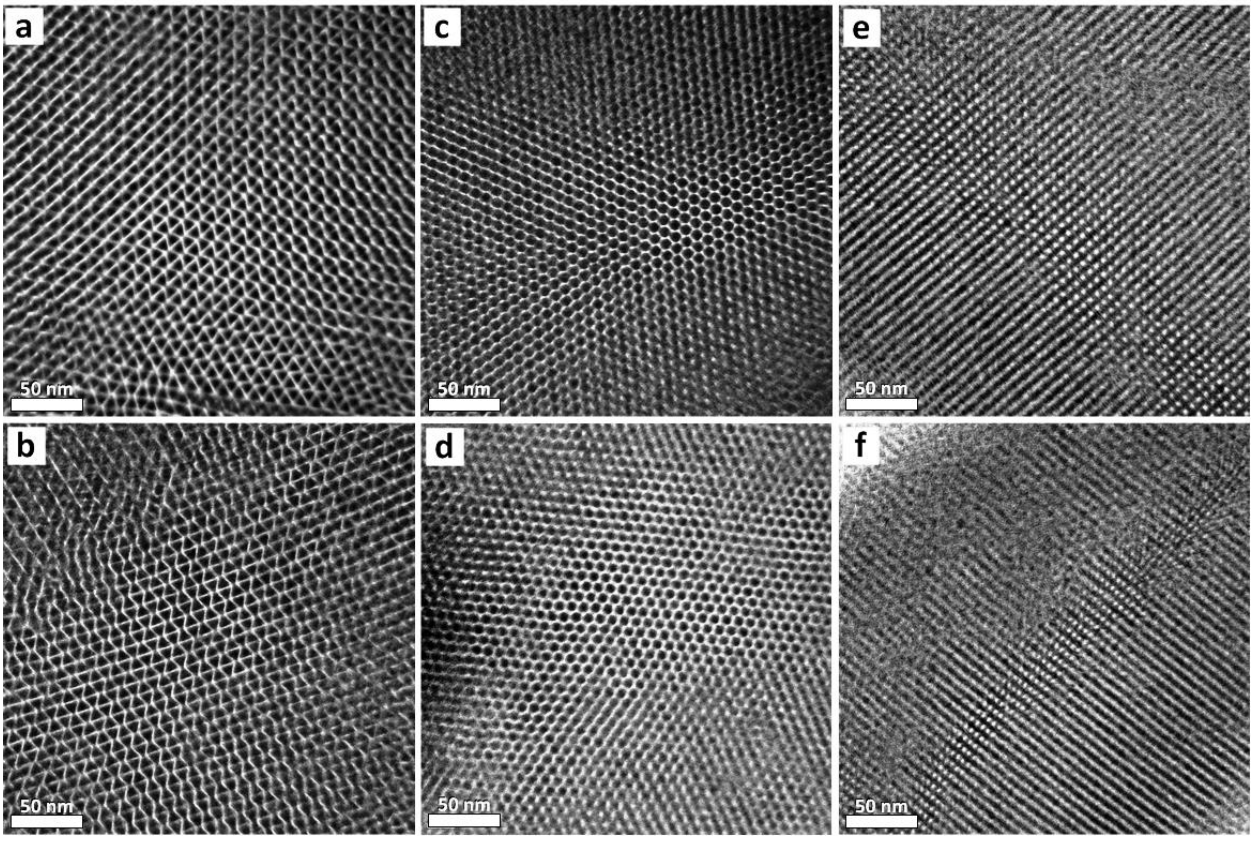

Figure 4.4. Three projections of thin film superlattices produced by evaporation of oleate-capped 10-nm CdSe tetrahedra from octane solvent.

4.3.2. Destabilization-based self-assembly

Slow destabilization of colloidal solutions of anisotropic CdSe NCs was used to obtain three-dimensional NC solids (Section 1.4.2). This procedure was applied to oleate-capped 10-nm CdSe tetrahedra (Figure 4.5, first three columns) and oleate-capped 10-nm CdSe cubes (Figure 4.5, fourth column). Disordered platelet-shaped aggregates were observed when the same procedure was applied to hexanoate-capped 10-nm CdSe tetrahedra.

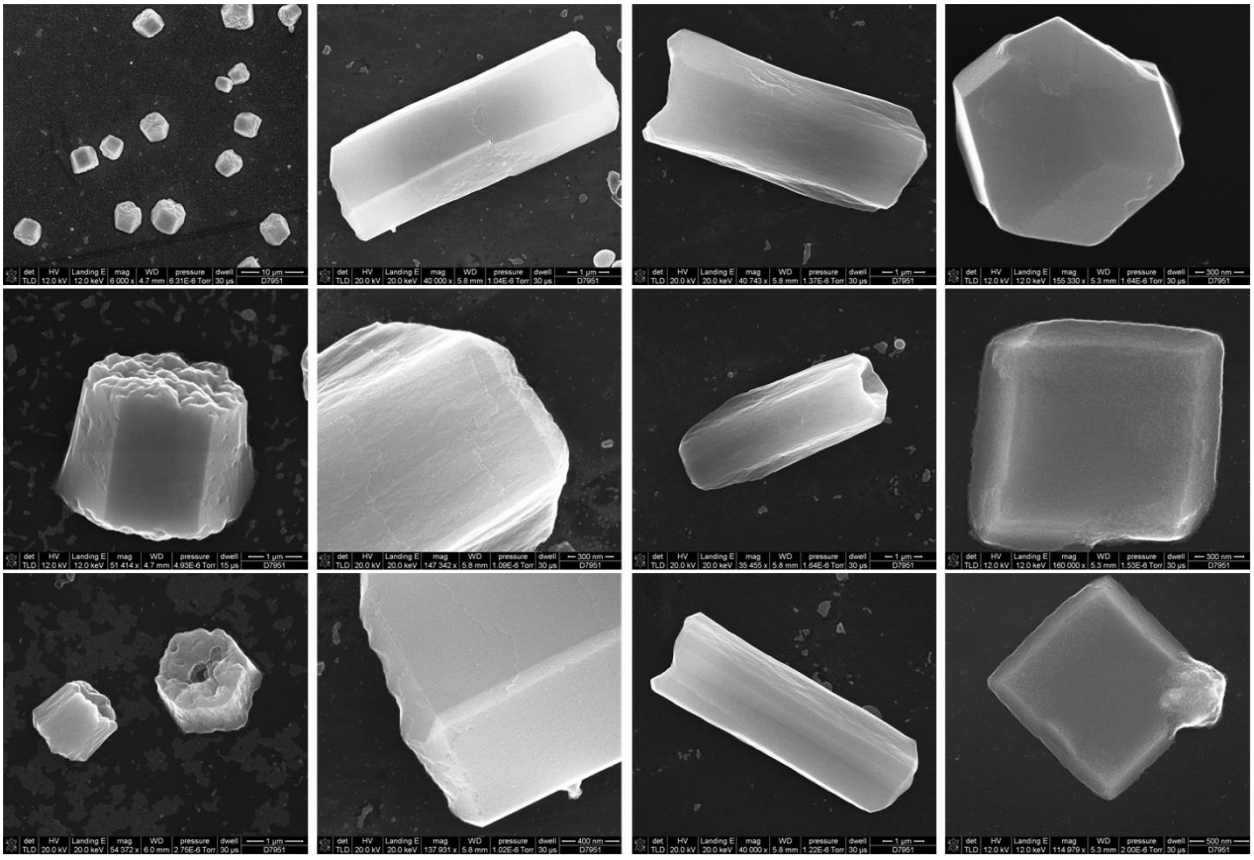

Figure 4.5. Three-dimensional superlattices and aggregates of anisotropic CdSe NCs obtained by slow destabilization with ethanol non-solvent. (First column) Destabilization of toluene solution of 10-nm CdSe tetrahedra produced short (1:1 aspect ratio), hexagonal prismatic crystals that may occasionally grow by screw dislocations, as evidence by hole in the center of some (bottom). (Second and third columns) Destabilization of tetrachloroethylene solution of the same NCs produced longer (4:1 aspect ratio) hexagonal prismatic crystals. (Fourth column) Destabilization of tetrachloroethylene solutions of cubic 10-nm CdSe NCs produced rhombic dodecahedral and plate-shaped crystals.

4.4. Structural assignment and superlattice modeling

4.4.1. Microscopy tilting experiments

The structure of self-assembled superlattices of these CdSe tetrahedra was elucidated using TEM tilting experiments. Three characteristic projections of the tetrahedron superlattice were observed: one revealing tetrahedra as equilateral triangles of alternating orientation, another presenting a rectangular lattice, and a third showing hexagonal arrangement of NCs. Tilting experiments revealed these three arrangements are indeed different projections of the same crystal (Figure 4.6, top). A structural model consistent with the TEM observations was constructed in MATLAB and is shown next to the corresponding superlattice projections (Figure 4.6, bottom).

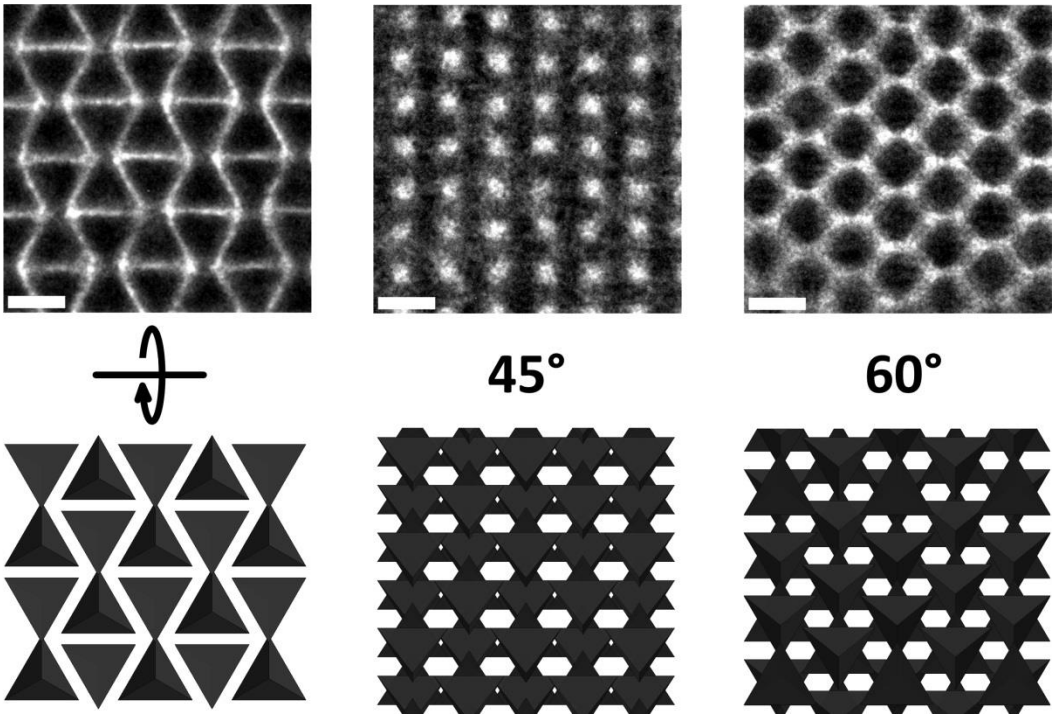

Figure 4.6. TEM tilt series elucidates structure of superlattice comprised of 10-nm oleate-capped CdSe tetrahedra. The projection presenting alternating triangles (left) may be tilted to reveal crystallographic projections showing rectangular (center) and hexagonal (right) arrangement of NCs. Top: TEM images. Scale bars, 10 nm. Bottom: modeled structure.

4.4.2. Crystal modeling with MATLAB

To make this crystallographic assignment, three candidate structures were generated by permutation of tetrahedron orientation. These three all show the observed "alternating triangles" projection, but only one matches all three projections (Figure 4.7).

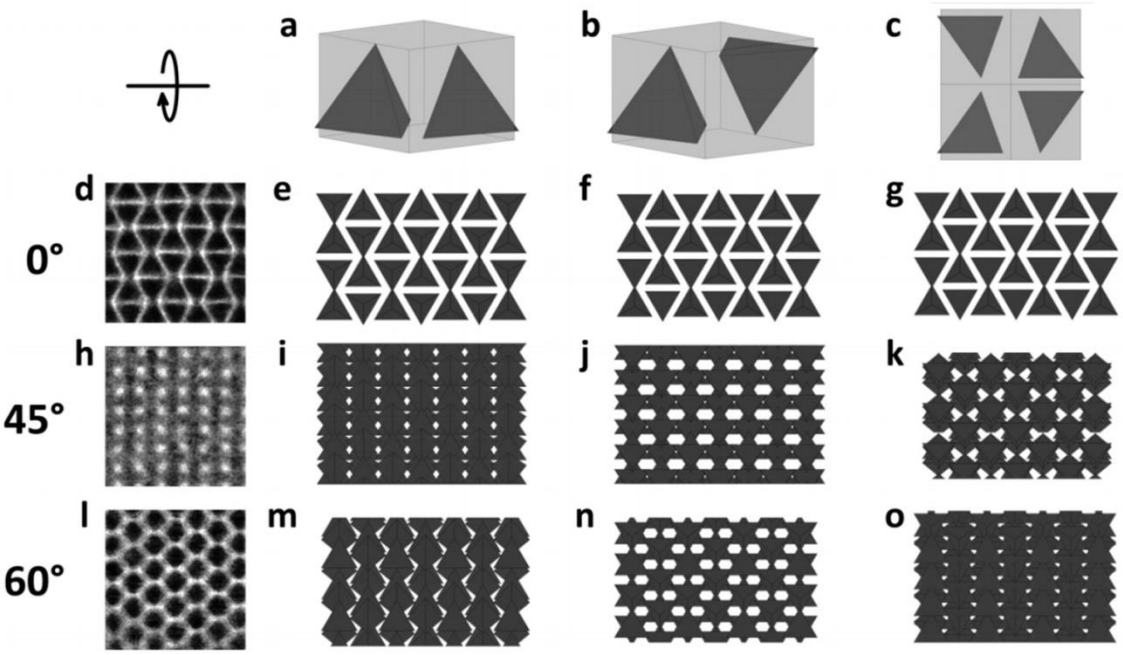

Figure 4.7. Elimination of alternative candidate superlattice structures. (a-c) Candidate unit cells able to produce the experimental alternating triangles arrangement (d-g). (h-k) CdSe superlattice and three modeled structures viewed 45° from "triangles" projection. (l-o) CdSe superlattice and three modeled structures viewed from 60° from "triangles" projection.

The superlattice of CdSe tetrahedra has a two-particle fundamental cell with tetrahedra in opposite orientations (Figure 4.8a). It has C_{2h} (2/m) symmetry with a center of inversion, and can be reconstructed by placement of the inversion center of the dimer unit on the lattice points of a base-centered orthorhombic Bravais lattice (Figure 4.8b). Ignoring the contribution of ligands, the structure may be isotropically compressed to establish contacts between neighboring particles (Figure 4.8c). In this case, three of the four tetrahedron vertices are in contact with the vertices of neighbors, while the fourth vertex makes contact with the face of a neighbor within the same column.

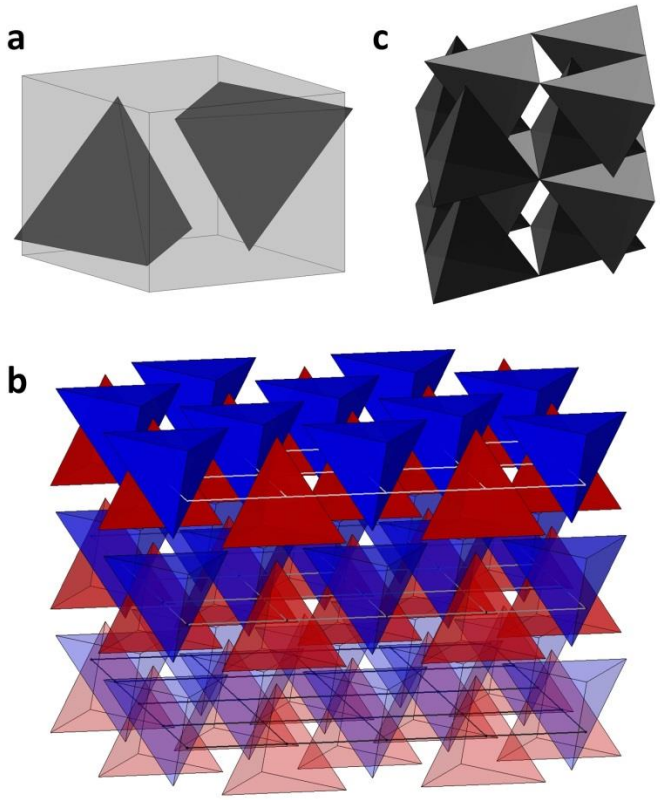

Figure 4.8. Modeling the CdSe tetrahedron superlattice structure. (a) Two-particle unit cell featuring tetrahedra in opposite orientations. (b) Side-view of the structure using lattice parameters measured from experiment. Upward- (downward-) pointing tetrahedra are colored in red (blue). (c) Ignoring the contribution of surface ligands, the structure can be condensed into a packing with alternating columns of tetrahedra in face-vertex contact and the remaining three vertices making contact with vertices of neighboring tetrahedra.

4.4.3. Twinning defects in tetrahedron superlattices

A twin plane involves the oriented association of two domains of the same crystalline phase which are related to each other by some symmetry operation that does not belong to the symmetry of the crystal.[18,19] These low-energy defects are by far the most common structural defect observed in superlattices of CdSe tetrahedra (Figure 4.9).

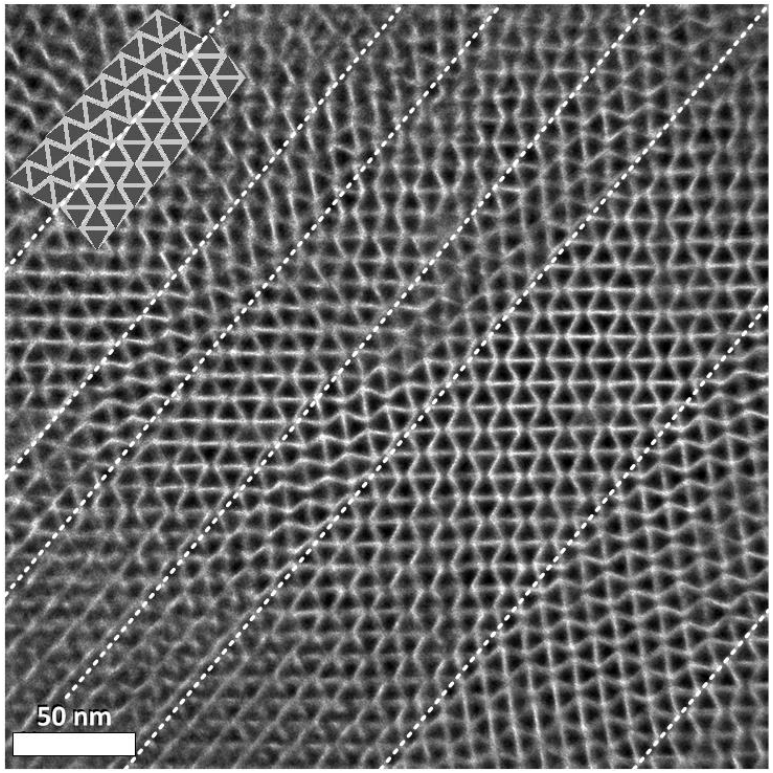

Figure 4.9. Twin plane defects (marked with dotted lines) in superlattices of tetrahedral CdSe NCs. Upper left inset: model of mirror reflection of the lattice across the twin boundary.

4.4.4. Experimental superlattice dimensions and packing fraction

The density of this superlattice might be estimated in one of two ways. If ligand shells are ignored, the tetrahedron crystal structure can be approximated by columns of tetrahedra in face-vertex contact (Figure 4.8c). The volume fraction a tetrahedron occupies within its circumscribed triangular prism is approximately $\varphi \approx 0.33$. On the other hand, inclusion of ligands produces a space-filling estimate of $\varphi \approx 0.59$ (Section 4.6.3). By this measure, our superlattice of tetrahedra is ~22% less dense than Chaikin's randomly-packed tetrahedral dice ($\varphi \approx 0.76$) and ~31% less dense than the current record (double dimer) packing ($\varphi \approx 0.86$) for perfect tetrahedra.

The experimental lattice dimensions were used to construct a model of the oleate-capped 10-nm CdSe tetrahedral NC superlattice (Figure 4.10a). The surface-to-surface distances are also illustrated for tetrahedral cores (dark grey) surrounded by oleate ligand shell (light grey) created by translating tetrahedron faces outwards (cantellation) by 2 nm (Figure 4.10b-e).

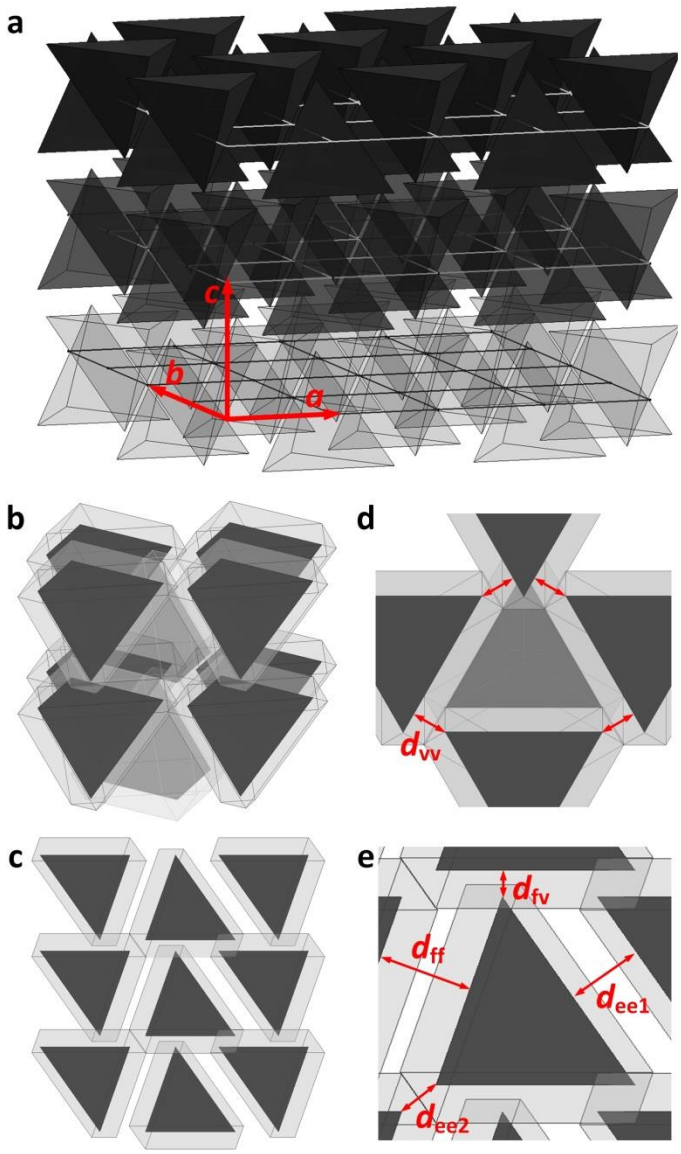

Figure 4.10. Modeled oleate-capped 10-nm CdSe tetrahedral NC superlattice with interparticle separations fitted to experimental measurements. (a) Modeled structure showing extracted lattice parameters *a*, *b*, and *c*. (b,c) Views of modeled tetrahedral NC superlattice with oleate ligand shell modeled by cantellation of tetrahedron faces. (d,e) Illustrated separations extracted using geometrical arguments presented in this section.

4.5. Stability of open superlattice of CdSe tetrahedra

This observation of an open superlattice appears to contradict the widely-accepted notion that semiconductor NCs should self-assemble into the (entropically-favored) densest structure. It also suggests that recent simulations of entropy-driven tetrahedron packing[3,5-7] may be lacking some input parameters which play an important role during the self-assembly of real NCs. In fact, this observation of low-density NC SLs supported by vertex-to-vertex contacts is not the first of its kind: ~10-nm colloidal Pt_3Ni octahedra self-assemble into low-density *bcc* structure (estimated space-filling factor of $\varphi \approx 0.48$ including oleylamine ligands) with exclusively vertex-to-vertex contacts[20] instead of, for example, the dense Minkowski packing of octahedra with $\varphi \approx 0.95$. In the remaining text we discuss effects which could lead to structures supported by vertex-to-vertex contacts instead of face-to-face contacts.

The soft potentials acting between NCs can either give rise to a new, low-density ground state of the system or lead to a specific assembly pathway followed by jamming of superlattice structure at low density. Recent simulations by Geissler[21] and Glotzer[22] groups predict impressively complex ground states for soft spheres. Here we show that non-spherical soft NCs bring new complexity and new opportunities compared to their spherical counterparts.

4.5.1. Evolution of particle shape during the assembly process

Tetrahedral CdSe NCs used in this work are comprised of a core of CdSe, faces formed from Cd-terminated (111) facets, and a corona of oleic acid (OA) or stearic acid (SA) molecules covalently bound to surface Cd atoms. The inorganic core vertex radius of curvature is estimated to be on the order of ~0.5 nm from TEM images (Figure 4.16). The soft organic coating imparts a more significant perturbation to the tetrahedral NC shape. Since interaction between surface ligands is purely repulsive in the presence of good solvent used in our assembly experiments,[23]

ligand molecules can be expected to radiate isotropically from the tetrahedron surface when the NC is immersed in solution. The shape which best captures this effect is the tetrahedron "puff" (Figure 4.11a). The perfect tetrahedron has asphericity ratio (the quotient of circumscribed and inscribed spheres, $\gamma = R_{out}/R_{in}$) of 3. Ligand molecules radiating from the tetrahedron surface will decrease the asphericity ratio, effectively rounding the shape of the NC. For a 2-nm fully-extended ligand molecule[24] and 10-nm CdSe tetrahedron edge length, asphericity can be calculated as $\gamma = (R_{out} + L_{OA})/(R_{in} + L_{OA}) \approx 2$, where L_{OA} is extended OA ligand length. Such puffs may approximate the physical shape of our CdSe NCs in good solvent. On the other hand, interaction between ligands is strongly attractive in the absence of good solvent.[23] In later stages of the assembly process, when carrier solvent is evaporated, the hydrocarbon tails of ligand molecules bundle together[25,26] to maximize van der Waals attraction. During solvent evaporation, the physical shape of tetrahedral CdSe-OA NCs evolves from a "puff" to a cantellated tetrahedron, with tetrahedron faces translated outwards by an "effective" ligand length (Figure 4.11b). This type of shape evolution should be typical for all non-spherical particles.

Shape evolution may have important implications on the self-assembly pathway of tetrahedral CdSe NCs. For puffs with asphericity $\gamma = 2$, densest packing was observed for an arrangement strikingly similar to our observed tetrahedral CdSe NC superlattice.[7] In addition, for $\gamma \approx 2$, packing of puffs reaches a local maximum, $\varphi \approx 0.83$, which may point to translational entropy as a significant factor pre-arranging puff-shaped CdSe NCs toward a colloidal crystal state that further evolves toward the superlattice structure shown in Figure 4.8.

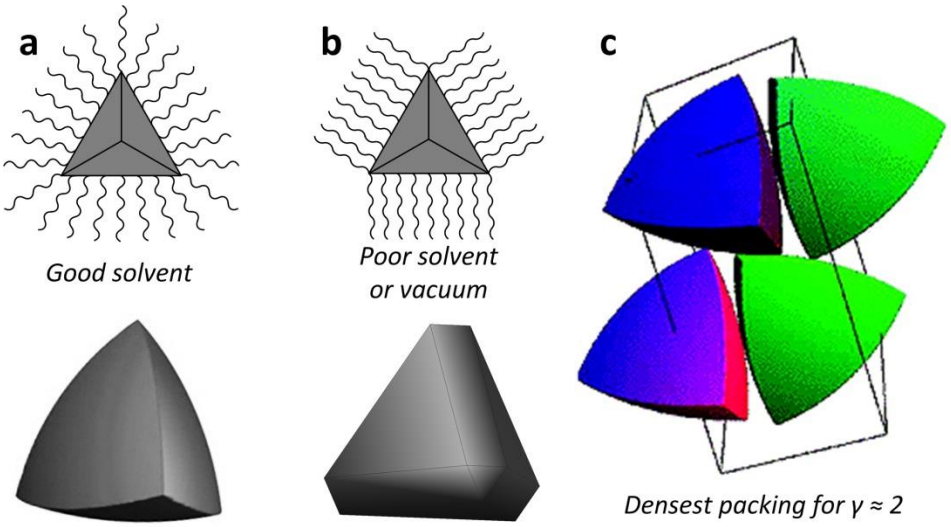

Figure 4.11. Proposed shape evolution of tetrahedral NCs during solvent evaporation and dense packing of tetrahedron "puffs" with swollen ligand corona. (a) Isotropic swelling of surface ligands in good solvent (top) leads to puffed tetrahedron shape (bottom). (b) Bundling of ligands in the absence of solvent (top) produces cantellated tetrahedron shape (bottom). (c) Calculated densest packing of puffed tetrahedra with asphericity ratio γ ≈ 2. Adapted from ref.[7]

4.5.2. Rotational entropy penalizes face-to-face contacts

In addition to translational entropy, rotational entropy may play an important role in ensembles of non-spherical particles, generally favoring open lattice structures[27] which leave room for partial rotation of individual particles. For non-spherical objects, rotational entropy can also play a role in determining the pathway from dilute particle assembly to the final state of the superlattice. For example, a recent study[28] demonstrated the interplay between translational and rotational entropy for two-dimensional Brownian hard-square colloids, whereby compression causes the ensemble of squares to experience an order-order transition from hexagonal rotator crystal to a rhombic phase which maximizes the sum of translational and rotational entropies of individual squares. In the case of faceted NCs, parallel facet alignment of face-to-face contacts

will strongly suppress independent NC rotations, whereas vertex-to-vertex contacts do not restrict rotational degrees of freedom. At intermediate densities, where rotational entropy can make a significant contribution to total system free energy, a rotator crystal of tetrahedra (Figure 4.12) might be expected.

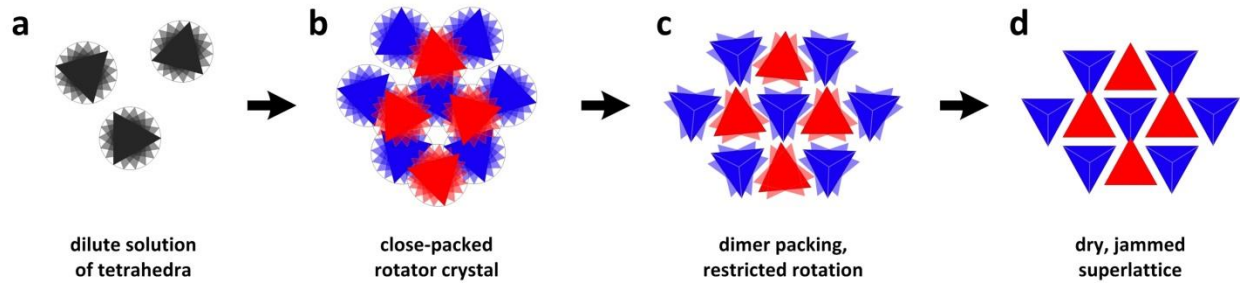

Figure 4.12. Possible pathway for evaporation-based assembly of tetrahedral NCs. (a) In dilute solution, NCs are far from one another and have random positions and orientations. (b) At intermediate density, a plastic/rotator crystal of tetrahedra packing as effectively spherical particles adopts close-packed (e.g., *fcc* or *hcp*) structure. (c) Upon further removal of solvent, NCs establish permanent contact with neighbors, favoring tip-to-tip packing with low steric repulsion (see next section). (d) Complete removal of solvent firmly links NCs into place.

4.5.3. Surface curvature gives rise to anisotropic steric interactions

Anisotropic pair potentials imparted by "sticky patches" can control the ground state of particle assemblies.[29] The implied placement of ligand molecules with different chemical functionalities to form attractive interaction sites (patches), however, appears to be a challenging synthetic problem.[8] Indeed, patchiness can be obtained by placement of the same ligand molecule at different locations on the NC surface: electrostatic patchiness has been demonstrated with non-spherical metal NCs, whereby local particle curvature influences the pH at which mercaptoundecanoic acid ligands are protonated.[30] Here we show that local surface curvature can significantly affect the pair potentials for even chemically identical ligand molecules.

In good solvent, hydrocarbon chains of ligands bound to the CdSe NC surface behave as a stretched polymer brush, imparting repulsive pair potentials to NCs and colloidal stability in nonpolar solvents. An osmotic term resulting from unfavorable exclusion of solvent molecules from the ligand interaction region acts upon the pair of particles as soon as their ligand coronas begin to overlap. This effect occurs during the whole range of steric interaction, beginning at interparticle distances lower than twice the capping layer width ($D < 2L$). Compression of ligand chains results in an elastic contribution to the potential at smaller surface separations. Because this elastic component quickly exceeds thermal energy, the predominant region sampled during a Brownian collision is the moderate interpenetration ($L \leq D < 2L$) domain.[31] The steric potential onset may therefore be approximated by only the osmotic term: $V_{\text{steric}} \approx V_{\text{osmotic}}$.

Discussions[32] of steric stabilization of NCs have relied on theory developed for spherical polymer brushes[31] using the Derjaguin approximation. While this approach provides a good estimate for large particles ($R \gg L$), it significantly overestimates the strength of repulsion between particles whose radii and ligand length are similar ($R \sim L$).[33] To circumvent the shortcomings of traditional repulsion energy estimates for high-curvature geometries we employ the Flory-Krigbaum expression[34] for free energy of mixing of two chains tethered to surfaces 1 and 2 and brought together in volume dV starting from infinite separation:

$$V_{steric} = 2k_B T \cdot \frac{v_s^2}{v_i} \cdot \left(\frac{1}{2} - \chi\right) \cdot \int_V \varphi_1 \varphi_2 \, dV$$

where v_s, v_i, and χ are Kuhn segment volume, solvent molecular volume, and Flory-Huggins chain-solvent interaction parameter, respectively. The segment density distribution functions φ_1, φ_2 are derived from the geometry of a cone-shaped available volume for ligands tethered to

spheres.[35] For a ligand tethered to high-curvature surface, the rapid decay of φ with increasing distance h from the surface leads to small overlap integral $S_{12} = \int_{d-L}^{L} \hat{\varphi}_1 \hat{\varphi}_2 \, dh$ and small repulsive mixing energies. In the limit of $R \rightarrow \infty$, $\varphi(h)$ = const. for $0 < h \leq L$ and overlap integral S_{12} increases linearly with decreasing h.

For interaction between vertex ligands we calculated the mixing energy of two chains with rapidly decaying segment density distribution functions characteristic of the large conical volume available to a ligand bound to a surface of high curvature (Figure 4.13a,b). Here we used the estimated radius of curvature of the tetrahedron vertex, $R_{\text{vertex}} \sim 0.5$ nm. Interaction between tetrahedron faces was approximated with the estimated equivalent radius of curvature of the tetrahedron face $R_{\text{face}} \sim 15$ nm (Figure 4.16). Mixing energies per ligand for vertex-vertex and face-face interactions in good solvent in the moderate interpenetration domain ($L \leq D < 2L$) predict a much stronger repulsion between tetrahedron faces compared with tetrahedron vertices (Figure 4.13c). In the center of this region ($D/L = 1.5$ on the normalized abscissa), osmotic repulsion between face-bound ligands is predicted to be approximately an order of magnitude larger than between vertex-bound ligands. Not considered in this analysis is the bending of ligands away from the contact axis, or "chain tilt", likely to occur in contacts between ligands tethered to highly curved surfaces and further reduce osmotic repulsion.[36]

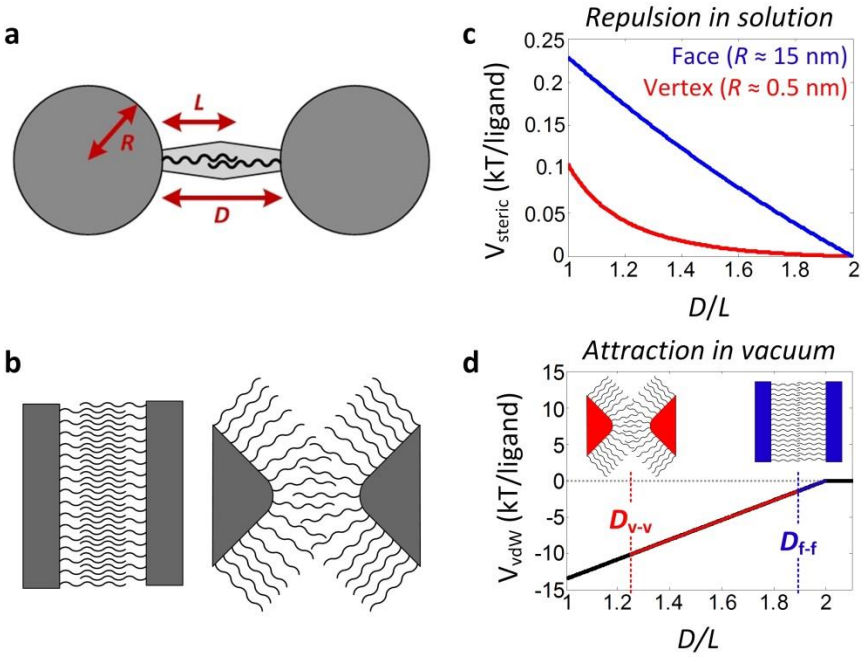

Figure 4.13. Grafting surface curvature and resulting anisotropic steric interaction. (a) Sketch of interacting pair of ligands tethered to surfaces of curvature *R* with reduced separation *D*/*L*. (b) Sketch of ligand interaction between planar (left) and curved (right) surfaces. (c) Calculated repulsive osmotic energy for a face-bound (blue) and vertex-bound (red) ligand at intermediate separation ($L < D < 2L$) in good solvent. (d) Calculated attractive van der Waals energy for two ligands in vacuum with interaction length determined by separation of grafting surfaces. The vertex-vertex separation distance measured in the superlattice is marked with red trace; the blue trace position corresponds to a calculated equilibrium face-face distance based on the balance of vdW and elastic energies.

The observed ~μm^2-size domains for tetrahedron SLs suggests vertex-to-vertex contacts are sufficiently robust to prevent collapse of the low-density structure after solvent evaporation. The deep interpenetration of hydrocarbon chains bound to surfaces of high curvature may be responsible for this preservation of structural integrity. We estimated the vdW potential between two ligands in vacuum as a function of surface curvature and grafting surface separation using the expression given by Salem for interaction between long saturated hydrocarbon chains.[37] At a surface separation equal to the measured distance between tetrahedron vertices in the superlattice

($D_{v\text{-}v} \sim 2.5$ nm), we estimate ligand vdW interaction strength of ~10 k_BT (Figure 4.13, red trace). The ~5.1-nm separation measured between tetrahedron faces in the CdSe superlattice precludes contact between ligands. To estimate interaction strength between face-bound ligands we used experimentally-determined Young's modulus ($E \sim 1$ GPa) for C_{18}-length self-assembled monolayers[38] to construct a vacuum potential for face-bound ligands, incorporating attractive vdW and repulsive elastic components.[35] With a shallow minimum at $D_{f\text{-}f} \sim 3.75$ nm, the per-ligand vdW energy is predicted to be ~1.5 k_BT (Figure 4.13, blue trace).

Both effects of strong repulsion per ligand between flat facets of tetrahedral NCs in good solvent and strong attraction per ligand between vertices of tetrahedral NCs in poor solvent or vacuum act to stabilize vertex-to-vertex contacts and penalize face-to-face contacts in the superlattice of CdSe tetrahedra. This observation may help to explain the prevalence of contacts between vertices of organic-capped nanotetrahedra investigated in this work and nanoctahedra explored by Smilgies and coworkers.[20] Incorporation of such an effect into thermodynamic simulations might represent a step towards the merging of theoretically-predicted and experimentally-observed packings of anisotropic nanoparticles which is needed to transform NC self-assembly into a powerful and predictable method for materials design.

4.6. Appendix: measurements and calculations

4.6.1. Measurement of tetrahedron edge length and rounding of tips

The first step to estimate experimental packing density of the superlattice is to obtain a precise description of the tetrahedral core including rounding of the vertices promoted by high chemical potential of undercoordinated surface atoms. For this, the edge length of the larger tetrahedra (Figure 1.1c,d; Figure 4.2b) was measured manually using high-resolution TEM images. By collecting ~200 such measurements, an average estimated edge length of 9.32 nm was obtained (Figure 4.14a). Using $a_1 \approx 9.32$ nm and estimated vertex radius of curvature $r \approx 0.5$ nm (Figure 4.14b) the equivalent perfect tetrahedron edge length a_2 (Figure 4.14c) was estimated:

$$a_2 = a_1 + \frac{2}{3} r \cdot \left(1 + \sqrt{3}\right) \approx 10.14\, nm$$

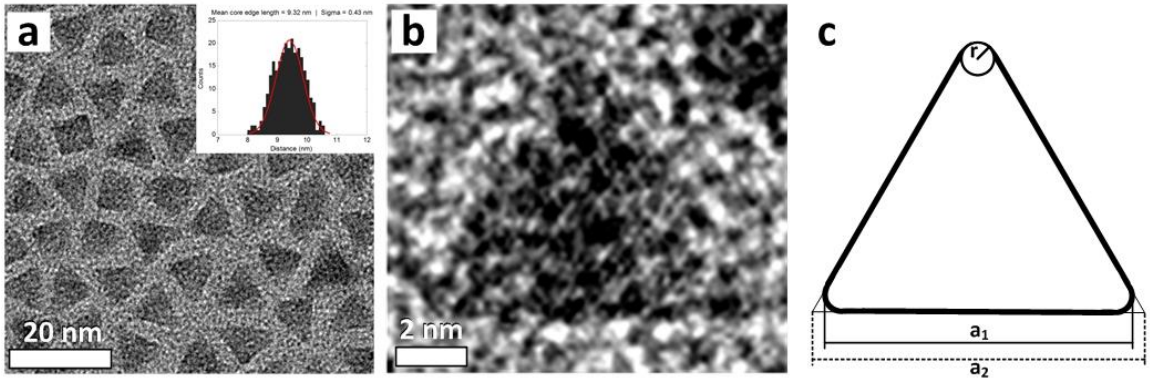

Figure 4.14. Measuring tetrahedron edge lengths and vertex rounding. (a) TEM image of randomly-oriented, oleate-capped tetrahedral CdSe NCs. Inset: Gaussian profile fit of manually-collected core edge length measurements. (b) TEM image of single CdSe NC viewed down (111)-projection. From such images, vertex radius of curvature was estimated. (c) Sketch of triangle with rounded vertices. With measured average edge length (a_1) and some assumption for vertex radius of curvature (r), the edge length of the equivalent perfect tetrahedron (a_2) can be estimated.

4.6.2. Software extraction of interparticle separations

The first step to estimate experimental packing density is to establish the distance between inorganic cores in the superlattice. Interparticle separations were estimated from by application of MATLAB code written to analyze bright-field TEM images based on pixel contrast between particles (dark) and background (light). In brief, particle centroids are assigned, and, using the set of points, a pair distribution function is plotted to extract in-plane separations. For full details of particle tracking analysis, see the dedicated section in Chapter 5. Such measurements were applied to two projections of the superlattice comprised of oleate-capped, 10-nm CdSe tetrahedra, yielding line segment distances d_1, d_2, d_3 (Figure 4.15a) and d_4 (Figure 4.15b). These values are also tabulated in Table 4.1.

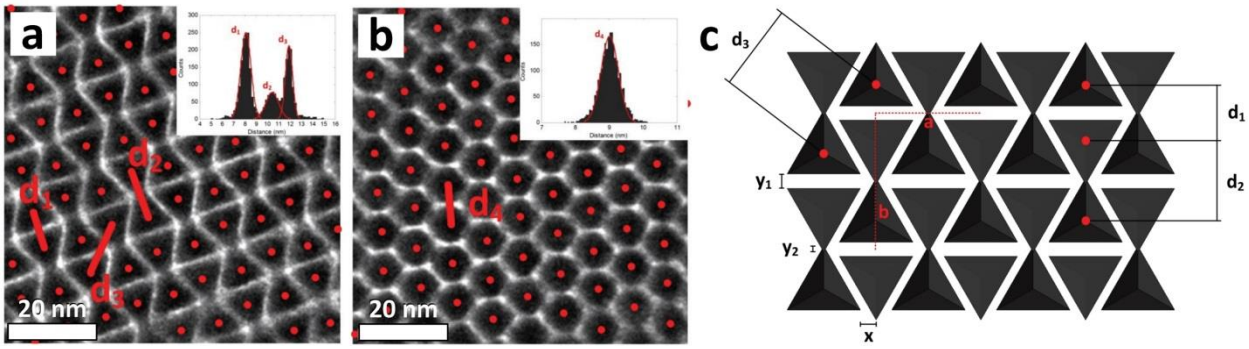

Figure 4.15. Software measurement of experimental interparticle separations and lattice parameters. (a) TEM image of (001)-projection of the superlattice showing particle centers and measured distances (red dots and lines). Inset: Gaussian profile fits of measurements. (b) TEM image of similar measurement carried out on the (011) superlattice projection. Inset: fit of measured separation. (c) Modeled (001) superlattice projection and measured separations.

Table 4.1. In-plane interparticle distances measured by particle tracking analysis shown in Figure 4.15.

Distance	Measurement (nm)
d_1	8.10
d_2	10.43
d_3	11.92
d_4	9.02

The measured in-plane distances $d_1 – d_4$ were then used in conjunction with tetrahedron edge length a_2 (Figure 4.14c) and tip curvature radius r to obtain physically meaningful edge separations (x, y_1) and tip overlap (y_2; see also Figure 4.15c):

$$y_1 = d_1 - 2 \cdot \frac{\sqrt{3}}{6} \cdot a_2 \approx 2.19\, nm$$

$$y_2 = 2 \cdot \left(\frac{\sqrt{3}}{3} \cdot a_2 - r \right) - d_2 \approx 0.38\, nm$$

$$x = \sqrt{d_3^2 - \left(\frac{d_1 + d_2}{2} \right)^2} - \frac{a_2}{2} \approx 2.39\, nm$$

These calculated values (x, y_1, y_2) were then used together with the measured values (d_1, d_2, d_3, d_4) to estimate the unit cell lattice parameters:

$$a = 2 \cdot \sqrt{d_3^2 - \left(\frac{d_1 + d_2}{2}\right)^2} \approx 15.00\ nm$$

$$b = d_1 + d_2 \approx 18.43\ nm$$

$$c = d_4 \cdot \left\{ cos\left[arctan\left(\frac{\sqrt{\frac{2}{3}}a_2 - r}{\sqrt{3}a_2 + y_1} \right) \right] \right\}^{-1} \approx 9.70\ nm$$

This analysis naturally lends itself to estimating surface-to-surface separations between different structural elements of tetrahedra within this superlattice: (*1*) the distance between faces, (*2*,*3*) between edges, (*4*) between face and vertex, and (*5*) between vertices:

(1) $$d_{ff} = a_2 \cdot \sqrt{\frac{2}{3}} \cdot tan\left\{90° - \arccos\left(\frac{1}{3}\right)\right\} + y_1 \approx 5.14\ nm$$

(2) $$d_{ee1} = sin\{90° - \arctan(\sqrt{2})\} \cdot \left(a_2 \cdot \frac{\sqrt{3}}{3} - y_2\right) \approx 2.61\ nm$$

(3) $$d_{ee2} = \sqrt{y_1^2 + d_{fv}^2} \approx 2.86\ nm$$

(4) $$d_{fv} = c - \left(\sqrt{\frac{2}{3}} \cdot a_2 - r\right) \approx 1.84\ nm$$

(5) $$d_{vv} = \sqrt{x^2 + \left\{\frac{1}{2}(y_1 - y_2)\right\}^2} \approx 2.56\ nm$$

4.6.3. Estimation of experimental superlattice density

Ignoring ligands, the density can be approximated according to the picture presented in Figure 4.8c, where hard tetrahedra are in contact with one another and each enjoy a trigonal prismatic available volume, V_{prism}:

$$\varphi = \frac{V_{tetrahedron}}{V_{prism}} = \frac{a^3/6\sqrt{2}}{\frac{\sqrt{3}}{4}a^2 \cdot \sqrt{\frac{2}{3}}a} = \frac{1}{3} \approx 0.333$$

The inorganic mass per NC was calculated as:

$$V_{NC} = \frac{a_2^3}{6\sqrt{2}} = \frac{(1.014 \cdot 10^{-6} cm)^3}{6\sqrt{2}} \approx 1.229 \cdot 10^{-19} cm^3/NC$$

$$m_{NC} = V_{NC} \cdot \rho_{CdSe} = 1.295 \cdot 10^{-19} cm^3/NC \cdot 5.816\ g/cm^3 \approx 7.146 \cdot 10^{-19} g/NC$$

Organic mass fraction (27.5%) obtained from TGA measurement (Figure 4.3c) can be used to estimate number of ligands per NC and ligand surface grafting density. The mass of the ligand shell of one NC was calculated as:

$$m_{NC+ligand} = \frac{7.146 \cdot 10^{-19} g/NC}{1 - 0.275} \approx 9.857 \cdot 10^{-19} g/NC$$

$$m_{OA} = m_{NC+ligand} - m_{NC} \approx 2.711 \cdot 10^{-19} g/NC$$

This, in turn, was correlated to number of ligands per NC and corresponding grafting density:

$$N_{OA} = \frac{m_{OA}}{MW_{OA}} = \frac{2.711 \cdot 10^{-19} g/NC}{4.690 \cdot 10^{-22} g/ligand} \approx 578.0\ ligands/NC$$

$$\sigma_{OA} = \frac{N_{OA}}{SA_{NC}} = \frac{578.0\ ligands/NC}{\sqrt{3} \cdot a_2^2} \approx 3.245\ ligands/nm^2$$

For simplicity, nanocrystal inorganic core volume and surface area were calculated using equivalent perfect tetrahedron edge length a_2. Oleic acid molecules likely pack more densely when tethered to the NC surface than they do in bulk liquid form. An estimate of ligand shell volume might be made using frozen oleic acid density ($\rho_{OA,solid} \approx 0.99$ g/cm^3):

$$V_{shell} = \frac{m_{OA}}{\rho_{OA,solid}} = \frac{2.711 \cdot 10^{-19} g/NC}{0.99\ g/cm^3} = 273.8\ nm^3/NC$$

With estimates for core and ligand components of NC volume and measured unit cell dimensions, the space-filling fraction of the CdSe-OA was estimated:

$$\varphi = \frac{V_{tetrahedra}}{V_{unit\ cell}} = \frac{2 \cdot (V_{NC} + V_{shell})}{\frac{1}{2} \cdot a \cdot b \cdot c} \approx \frac{2 \cdot (122.9\ nm^3 + 273.8\ nm^3)}{\frac{1}{2} \cdot 15.0\ nm \cdot 18.5\ nm \cdot 9.7\ nm} \approx 0.590$$

4.6.4. Effective radius of curvature of tetrahedron face

For flat tetrahedron faces, the radius of curvature of the equivalent sphere was estimated by drawing a circle through three points whose positions are determined by the end of the ligand alkyl tail radiating outwards from the NC surface (Figure 4.16).

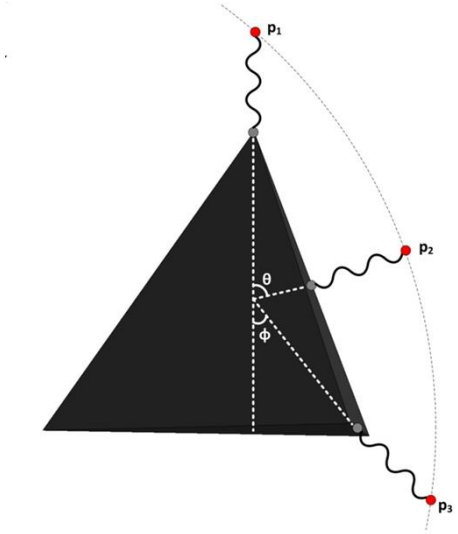

Figure 4.16. Fitting the perimeter of a circle through three points of ligand chain ends enables estimate of effective radius of curvature of "flat" tetrahedron faces. See text for details.

The geometry of the illustration in Figure 4.16 sets

$$p_1 = (0, R_{out} + L)$$

$$p_2 = \{(R_{in} + L) \cdot \sin\theta\,, (R_{in} + L) \cdot \cos\theta\}$$

$$p_3 = \{(R_{mid} + L) \cdot \sin\varphi\,, (R_{mid} + L) \cdot \cos\varphi\}$$

Where R_{in} is the tetrahedron insphere radius (sphere surface is tangent to faces), R_{out} is the circumsphere radius (tangent to vertices), and R_{mid} is the midsphere radius (tangent to edges).

Using simple geometric arguments for a perfect tetrahedron it can be shown that

$$R_{in} = \frac{a}{\sqrt{24}} \qquad R_{mid} = \frac{a}{\sqrt{8}} \qquad R_{out} = \sqrt{\frac{3}{8}}a$$

$$\theta = \arccos\left(\frac{1}{3}\right) \qquad \varphi = \arctan(\sqrt{2})$$

With the experimental tetrahedron edge length obtained from measurements (a ≈ 10 nm), we find the tetrahedron face has an equivalent radius of 17.4 nm. Subtraction of 2-nm extended ligand length gives $R_{face} \approx 15.4$ nm.

4.6.5. Calculation of ligand repulsion in good solvent.

According to Flory-Krigbaum theory,[34] the free energy of interpenetration of two chains brought from infinite separation together in volume *dV* may be expressed as

$$\Delta G = 2k_B T \cdot \frac{v_s^2}{v_i} \cdot \left(\frac{1}{2} - \chi\right) \cdot \int_V \varphi_1 \varphi_2 \, dV$$

Where v_s is Kuhn segment volume (for polyethylene, $v_s \sim 0.2$ nm^3), v_i is solvent molecular volume (for TCE, $v_i \sim 0.1$ nm^3), and χ is the Flory-Huggins chain-solvent interaction parameter (for polyethylene-TCE, $\chi \sim 0$). Assuming uniform segment density parallel to the tethering surface, the free energy of mixing may be rewritten for one-dimensional mixing

$$\Delta G = 2k_B T \cdot \frac{v_s^2}{v_i} \cdot \frac{1}{b^2} \cdot \left(\frac{1}{2} - \chi\right) \cdot \int_{d-L}^{L} \hat{\varphi}_1 \hat{\varphi}_2 \, dh$$

Where *b* is length of the Kuhn segment. The one-dimensional segment density distribution function φ is derived from the geometry of the cone-shaped volume available to a ligand of alkyl chain cross-sectional area A_{chain} and headgroup area A_{head}, tethered to a sphere of radius *R*

$$\varphi(h) = \frac{A_{chain}}{A_{head}} \cdot \left(\frac{R}{R+h}\right)^2$$

Normalization of the segment density distribution function such that $\int_0^L \hat{\varphi}(h) \, dh = 1$ gives

$$\hat{\varphi}(h) = \frac{R}{L} \cdot \frac{R+L}{(R+h)^2}$$

We set $\hat{\varphi}_1 = \hat{\varphi}$. We create $\hat{\varphi}_2$ by reflection of $\hat{\varphi}$ across the y-axis and translation by D in the +x-direction

$$\hat{\varphi}_2(h) = \frac{R}{L} \cdot \frac{R+L}{(R-(h-d))^2}$$

The overlap integral S_{12} was evaluated analytically using Mathematica

$$S_{12} = \int_{d-L}^{L} \hat{\varphi}_1 \hat{\varphi}_2 \, dh$$

$$= \frac{2R^2 \cdot (L+R)^2}{L^2 \cdot (D+2R)^3} \cdot \left\{ \frac{D+2R}{D+R-L} - \frac{D+2R}{L+R} + 2 \cdot \ln(L+R) - 2 \cdot \ln(D+R-L) \right\}$$

Using parameters relevant to our experiments (v_s ~ 0.2 nm^3, v_i ~ 0.1 nm^3, χ ~ 0, L = 2 nm), the osmotic repulsion for two ligands brought from infinite separation to moderate interpenetration (L $\leq$ D< 2L) was plotted for several grafting surface radii.

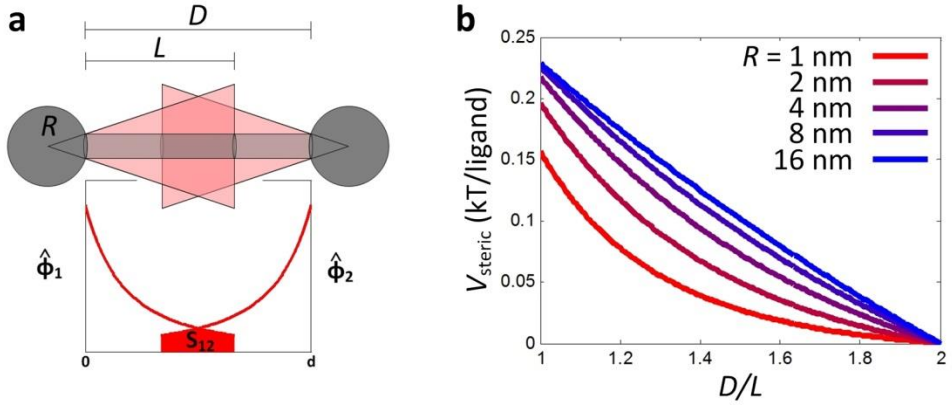

Figure 4.17. Calculation of ligand-ligand repulsion energy in good solvent. (a) Overlapping segment density distribution functions contribute to osmotic repulsion. (b) Repulsive energy per ligand for selected grafting surface radii.

4.6.6. Calculation of ligand potential in poor solvent or vacuum.

The van der Waals-dispersion energy of attraction between two hydrocarbon chains in vacuum is given by Salem:[37]

$$E = A \cdot \frac{3\pi}{8\lambda^2} \cdot \frac{L}{D^5}$$

Where energy (E) depends on hydrocarbon Hamaker coefficient (-0.1 kcal/mol of methylene units), basic unit length (0.127 nm), close-packing separation distance (0.49 nm), and length of molecular overlap, L.

With Salem's conclusion that E ~ L, and with the attractive energy for stearic acid (given as -8.4 kcal/mol, or -14.2 k_BT/molecule), we may relate interaction length and interaction strength:

$$V_{vdW}(d\,) \approx -7.1 \cdot k_B T \cdot (2L - D)$$

Where length of molecular overlap L is replaced with our measure of overlap, $2L_{OA}$-d, in nanometers. The reported $E_{\text{stearic acid}}$ is recovered for full overlap of C_{18} molecules (2L-d = 2 nm).

To estimate elastic repulsion energy between oleic acid ligands bound to CdSe tetrahedron faces, we referenced experimental measurement of Young moduli of hydrocarbon SAMs on gold given by Del Rio et al.,[38] reported to be on the order of 1 GPa for C_{18}-length alkanethiol molecules.

The elastic modulus (E) can be related to elastic repulsion energy:

$$V_{el} = \frac{1}{2} \cdot \frac{E \cdot A_o}{L_o} \cdot (\Delta L)^2$$

Where A_o is the original cross-sectional area through which the force is applied, L_o is the original length of the object, and ΔL is the amount by which the length of the object changes.

Using $E = 10^9$ N/m^2, $A_o = 0.25$ nm^2, $L_o = 2$ nm, and $\Delta L = 2L - D$, we obtain an expression for the elastic energy:

$$V_{el} \approx 15.2 \cdot k_B T \cdot (4\,nm - d)^2$$

The full potential (vdW + elastic) for two (2-nm length) face-bound ligands can therefore be represented as

$$V_{vdW+el} \approx 15.2 \cdot k_B T \cdot (4\,nm - d)^2 - 7.1 \cdot k_B T \cdot (4\,nm - d)$$

This potential features a shallow minimum of -0.75 k_BT at small surface separation distance $D_{face\text{-}face} \approx 3.75$ nm (Figure 4.18).

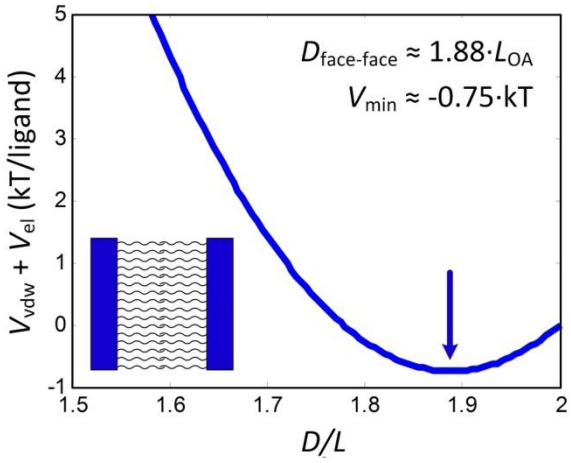

Figure 4.18. The sum of van der Waals and elastic potentials between two ligands tethered to a flat surface produces an estimate for equilibrium face-face separation distance of 1.88LOA or ~3.76 nm.

4.7. Acknowledgements

I wish to thank Prof. Tom Witten in the Physics Department at the University of Chicago for inviting me to present this work at the Physics Bag Lunch seminar series during which he and Prof. Heinrich Jaeger (Chicago) offered insightful thoughts on nanotetrahedron assembly. Additionally, I would like to thank Prof. Philippe Guyot-Sionnest (Chicago) and Prof. Kwang Seob Jeong (now at Korea University) for the invitation to present on this topic at the University of Chicago 2014 Nano Talks symposium.

4.8. References

1 Conway, J. H. & Torquato, S. Packing, Tiling, and Covering with Tetrahedra. *Proceedings of the National Academy of Sciences of the United States of America* **103**, 10612-10617, (2006).

2 Chen, E. A Dense Packing of Regular Tetrahedra. *Discrete & Computational Geometry* **40**, 214-240, (2008).

3 Haji-Akbari, A. *et al.* Disordered, quasicrystalline and crystalline phases of densely packed tetrahedra. *Nature* **462**, 773-777, (2009).

4 Chen, E. R., Engel, M. & Glotzer, S. C. Dense Crystalline Dimer Packings of Regular Tetrahedra. *Discrete & Computational Geometry* **44**, 253-280, (2010).

5 Damasceno, P. F., Engel, M. & Glotzer, S. C. Crystalline Assemblies and Densest Packings of a Family of Truncated Tetrahedra and the Role of Directional Entropic Forces. *ACS Nano* **6**, 609-614, (2011).

6 van Anders, G., Ahmed, N. K., Smith, R., Engel, M. & Glotzer, S. C. Entropically Patchy Particles: Engineering Valence through Shape Entropy. *ACS Nano* **8**, 931-940, (2013).

7 Kallus, Y. & Elser, V. Dense-packing crystal structures of physical tetrahedra. *Physical Review E* **83**, 036703 (2011).

8 G. van Anders, N. K. A., D. Klotsa, M. Engel, S. C. Glotzer. *arXiv:1309.1187* (2013).

9 Chen, Q., Bae, S. C. & Granick, S. Directed self-assembly of a colloidal kagome lattice. *Nature* **469**, 381-384, (2011).

10 Wang, Y. *et al.* Colloids with valence and specific directional bonding. *Nature* **491**, 51-55, (2012).

11 Jaoshvili, A., Esakia, A., Porrati, M. & Chaikin, P. M. Experiments on the Random Packing of Tetrahedral Dice. *Physical Review Letters* **104**, 185501 (2010).

12 Baker, J. & Kudrolli, A. Maximum and minimum stable random packings of Platonic solids. *Physical Review E* **82**, 061304 (2010).

13 Evers, W. H. *et al.* Entropy-Driven Formation of Binary Semiconductor-Nanocrystal Superlattices. *Nano Letters* **10**, 4235-4241, (2010).

14 Talapin, D. V. LEGO Materials. *ACS Nano* **2**, 1097-1100, (2008).

15 Liu, L. *et al.* Shape Control of CdSe Nanocrystals with Zinc Blende Structure. *Journal of the American Chemical Society* **131**, 16423-16429, (2009).

16 Houtepen, A. J., Koole, R., Vanmaekelbergh, D., Meeldijk, J. & Hickey, S. G. The Hidden Role of Acetate in the PbSe Nanocrystal Synthesis. *Journal of the American Chemical Society* **128**, 6792-6793, (2006).

17 Hostetler, M. J., Stokes, J. J. & Murray, R. W. Infrared Spectroscopy of Three-Dimensional Self-Assembled Monolayers: N-Alkanethiolate Monolayers on Gold Cluster Compounds. *Langmuir* **12**, 3604-3612, (1996).

18 Rupich, S. M., Shevchenko, E. V., Bodnarchuk, M. I., Lee, B. & Talapin, D. V. Size-Dependent Multiple Twinning in Nanocrystal Superlattices. *Journal of the American Chemical Society* **132**, 289-296, (2009).

19 Bodnarchuk, M. I., Shevchenko, E. V. & Talapin, D. V. Structural Defects in Periodic and Quasicrystalline Binary Nanocrystal Superlattices. *Journal of the American Chemical Society* **133**, 20837-20849, (2011).

20 Zhang, J. *et al.* Low Packing Density Self-Assembled Superstructure of Octahedral Pt3Ni Nanocrystals. *Nano Letters* **11**, 2912-2918, (2011).

21 M. Gruenwald, P. G. *arXiv:1310.0652* (2013).

22 Keys, A. S. & Glotzer, S. C. How do Quasicrystals Grow? *Physical Review Letters* **99**, 235503 (2007).

23 Schapotschnikow, P., Pool, R. & Vlugt, T. J. H. Molecular Simulations of Interacting Nanocrystals. *Nano Letters* **8**, 2930-2934, (2008).

24 Mourdikoudis, S. & Liz-Marzán, L. M. Oleylamine in Nanoparticle Synthesis. *Chemistry of Materials* **25**, 1465-1476, (2013).

25 Widmer-Cooper, A. & Geissler, P. Orientational Ordering of Passivating Ligands on CdS Nanorods in Solution Generates Strong Rod–Rod Interactions. *Nano Letters* **14**, 57-65, (2013).

26 Wang, Z. L., Harfenist, S. A., Whetten, R. L., Bentley, J. & Evans, N. D. Bundling and Interdigitation of Adsorbed Thiolate Groups in Self-Assembled Nanocrystal Superlattices. *The Journal of Physical Chemistry B* **102**, 3068-3072, (1998).

27 Mao, X., Chen, Q. & Granick, S. Entropy favours open colloidal lattices. *Nat Mater* **12**, 217-222, (2013).

28 Zhao, K., Bruinsma, R. & Mason, T. G. Entropic crystal–crystal transitions of Brownian squares. *Proceedings of the National Academy of Sciences* **108**, 2684–2687, (2011).

29 Zhang & Glotzer, S. C. Self-Assembly of Patchy Particles. *Nano Letters* **4**, 1407-1413, (2004).

30 Walker, D. A., Leitsch, E. K., Nap, R. J., Szleifer, I. & Grzybowski, B. A. Geometric curvature controls the chemical patchiness and self-assembly of nanoparticles. *Nat Nano* **8**, 676-681, (2013).

31 Vincent, B., Edwards, J., Emmett, S. & Jones, A. Depletion flocculation in dispersions of sterically-stabilised particles ("soft spheres"). *Colloids and Surfaces* **18**, 261-281, (1986).

32 Saunders, A. E. & Korgel, B. A. Second Virial Coefficient Measurements of Dilute Gold Nanocrystal Dispersions Using Small-Angle X-ray Scattering. *The Journal of Physical Chemistry B* **108**, 16732-16738, (2004).

33 Kim, J. U. & Matsen, M. W. Interaction between Polymer-Grafted Particles. *Macromolecules* **41**, 4435-4443, (2008).

34 Napper, D. H. Steric stabilization. *Journal of Colloid and Interface Science* **58**, 390-407, (1977).

36 Matsen, M. W. Effect of Chain Tilt on the Interaction between Brush-Coated Colloids. *Macromolecules* **38**, 4525-4530, (2005).

37 Salem, L. Attractive Forces between Long Saturated Chains at Short Distances. *J. Chem. Phys.* **37**, 2100, (1962).

38 W., D. F., Cherno, J., A., F. D. & F., C. R. Elastic and adhesive properties of alkanethiol self-assembled monolayers on gold. *Appl. Phys. Lett.* **94**, (2009).

5. Structural characterization of nanocrystal superlattices

5.1. Single-component superlattices

This section provides a selection of transmission electron microscopy (TEM) images of superlattices self-assembled from one size of approximately spherical NCs.

5.1.1. Thin film superlattices

The air-liquid interfacial evaporation technique (Section 1.4.1) allows assembly of hexagonally close-packed superlattice monolayers and few-layer-thick superlattices (Figure 1.4).

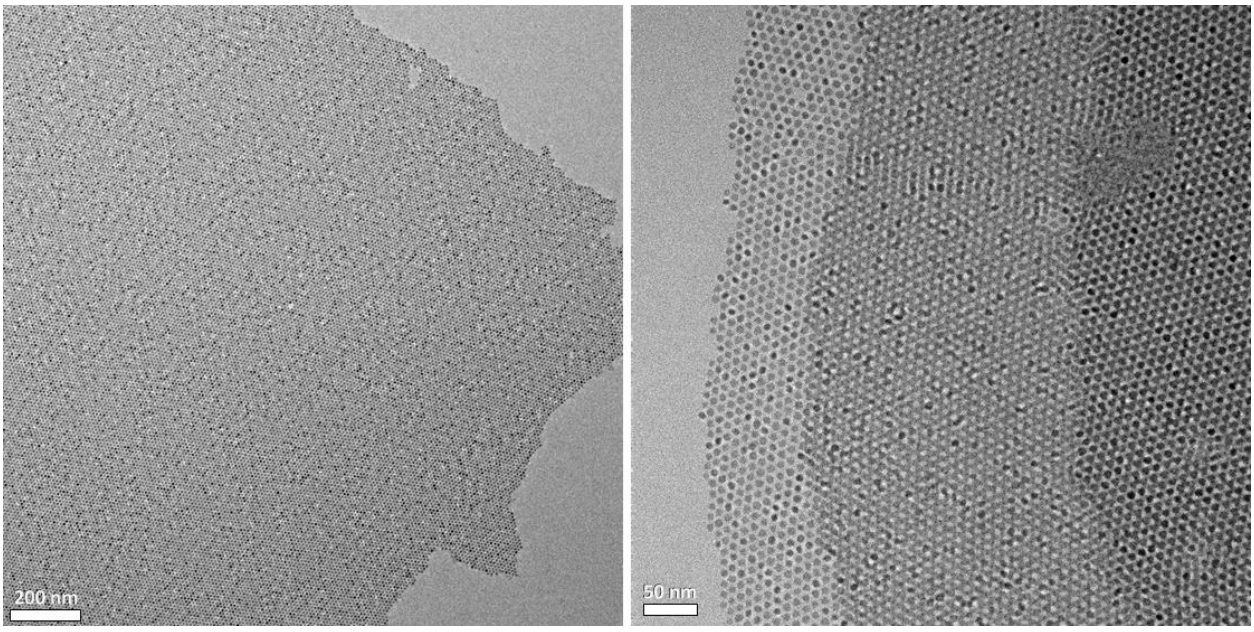

Figure 5.1. TEM images of PbS nanocrystals assembled into hexagonal monolayer (left) and multilayer (right) sheets.

5.1.2. Three-dimensional nanocrystal superlattices

Three or more layers of hexagonally-close packed NC sheets may be stacked in A-B-A fashion to produce hexagonally close-packed *hcp* superlattices (Figure 5.2, left side of left image; right image). On the other hand, A-B-C-A stacking produces the face-centered cubic (*fcc*)

arrangement (Figure 5.2, right side of left image). Both *hcp* and *fcc* structures represent the densest possible packing (74%) of spheres (Section 3.3.2).

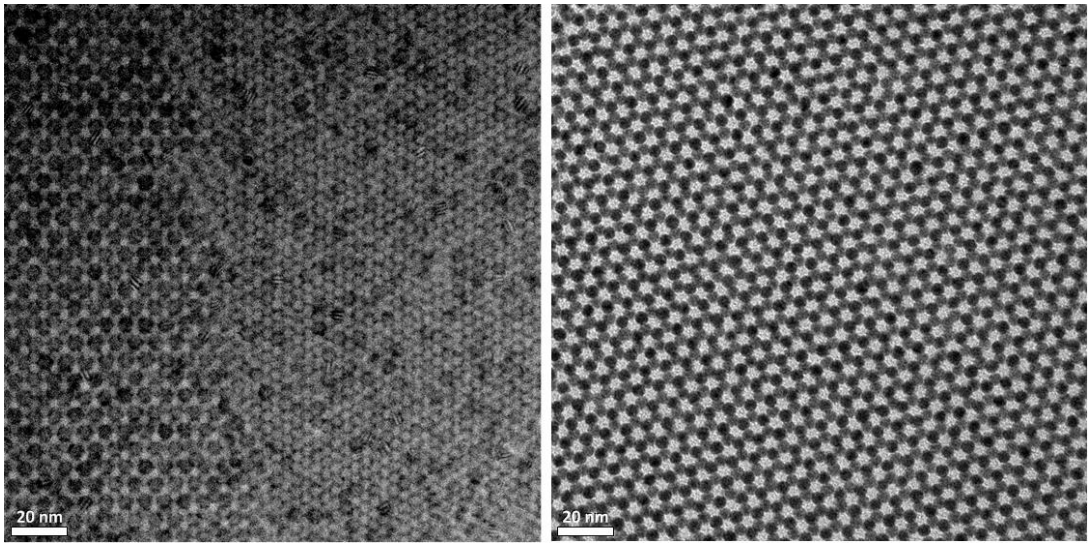

Figure 5.2. TEM images of close-packed superlattices of approximately spherical PbS (left) and Au (right) nanocrystals capped with hydrocarbon surface ligands.

Body-centered cubic (*bcc*) superlattices, with slightly lower sphere packing fraction (68%), are also commonly observed packings of nearly spherical NCs (Figure 5.3).

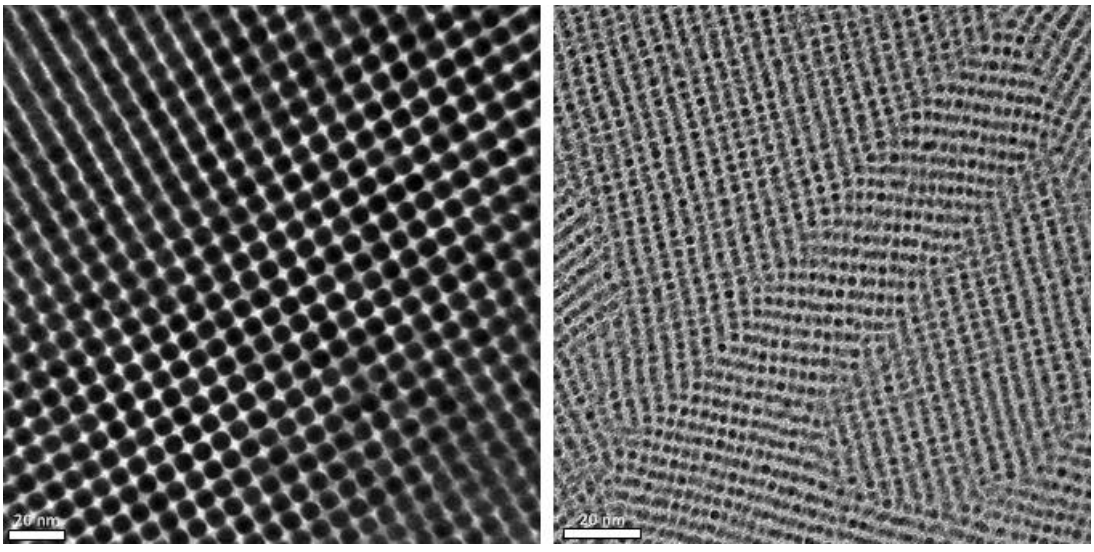

Figure 5.3. TEM images of body-centered cubic superlattices of approximately spherical PbS (left) and Au (right) nanocrystals capped with hydrocarbon surface ligands.

Body-centered cubic (*bcc*) superlattices, with slightly lower sphere packing fraction (68%), are also commonly observed packings of nearly spherical NCs (Figure 5.4).

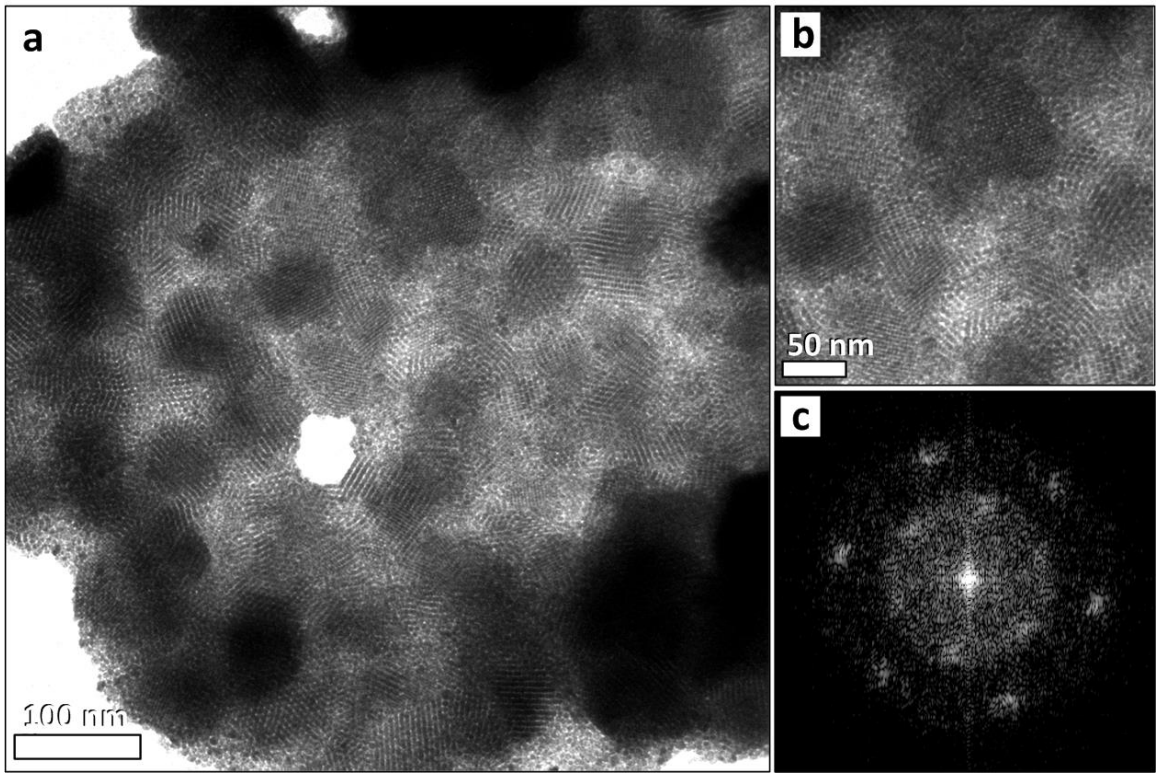

Figure 5.4. Close-packed superlattices of approximately spherical Au nanocrystals capped with inorganic ligands. (a) TEM overview of precipitate obtained upon evaporation of hydrazine solution of thiostannate-capped Au nanocrystals. (b) Zoom of local structure and (c) Fourier transform of corresponding region revealing hexagonal superlattice symmetry.

5.2. Binary nanocrystal superlattices

This section provides a selection of TEM images of binary nanocrystal superlattice (BNSL) structures, many of which were first reported in 2006 by Shevchenko and coworkers.[1]

5.2.1. Binary phases with AB stoichiometry

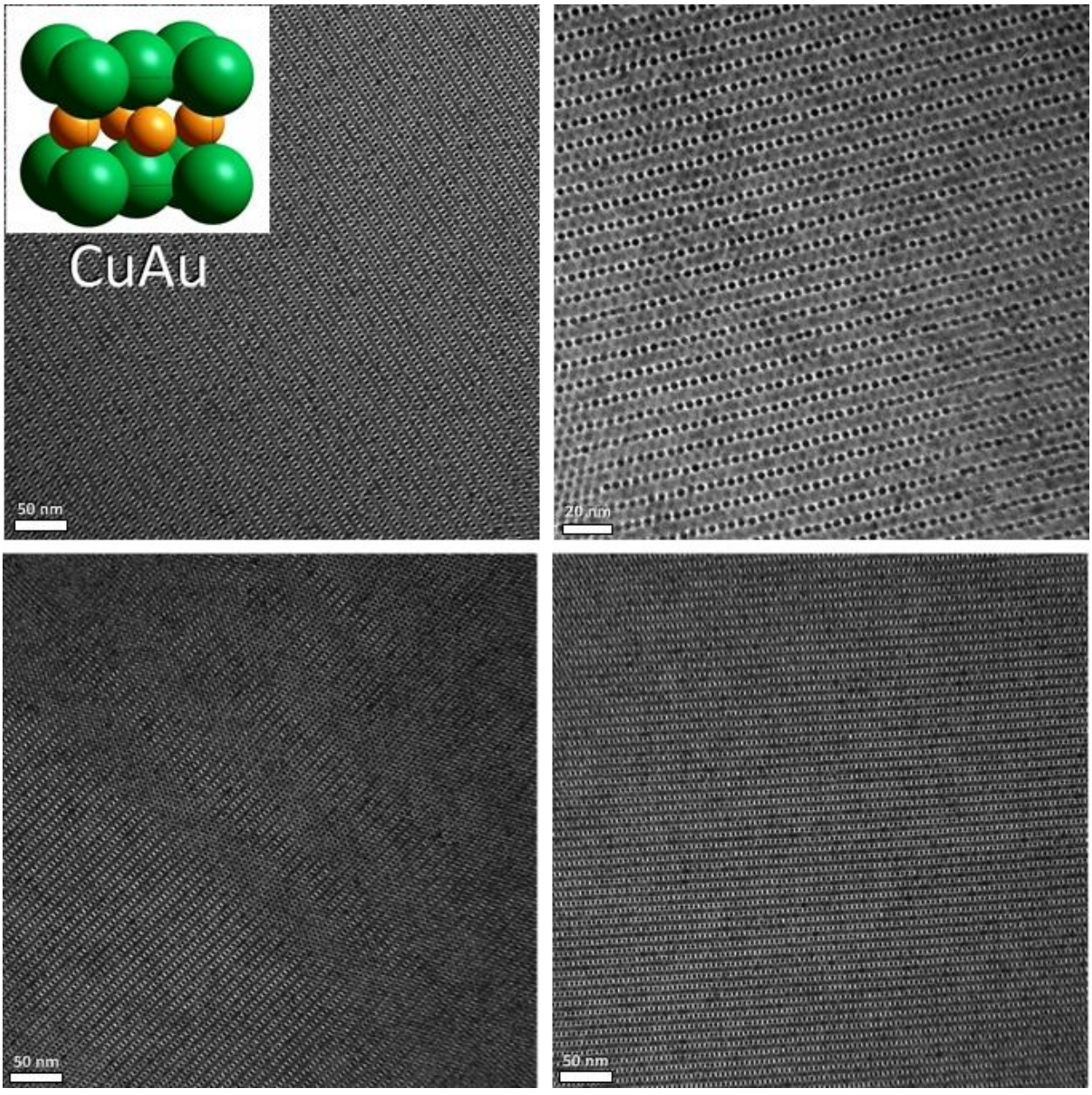

Figure 5.5. TEM images of (100)-projections of CuAu-type binary superlattices assembled from Au and PbS nanocrystals.

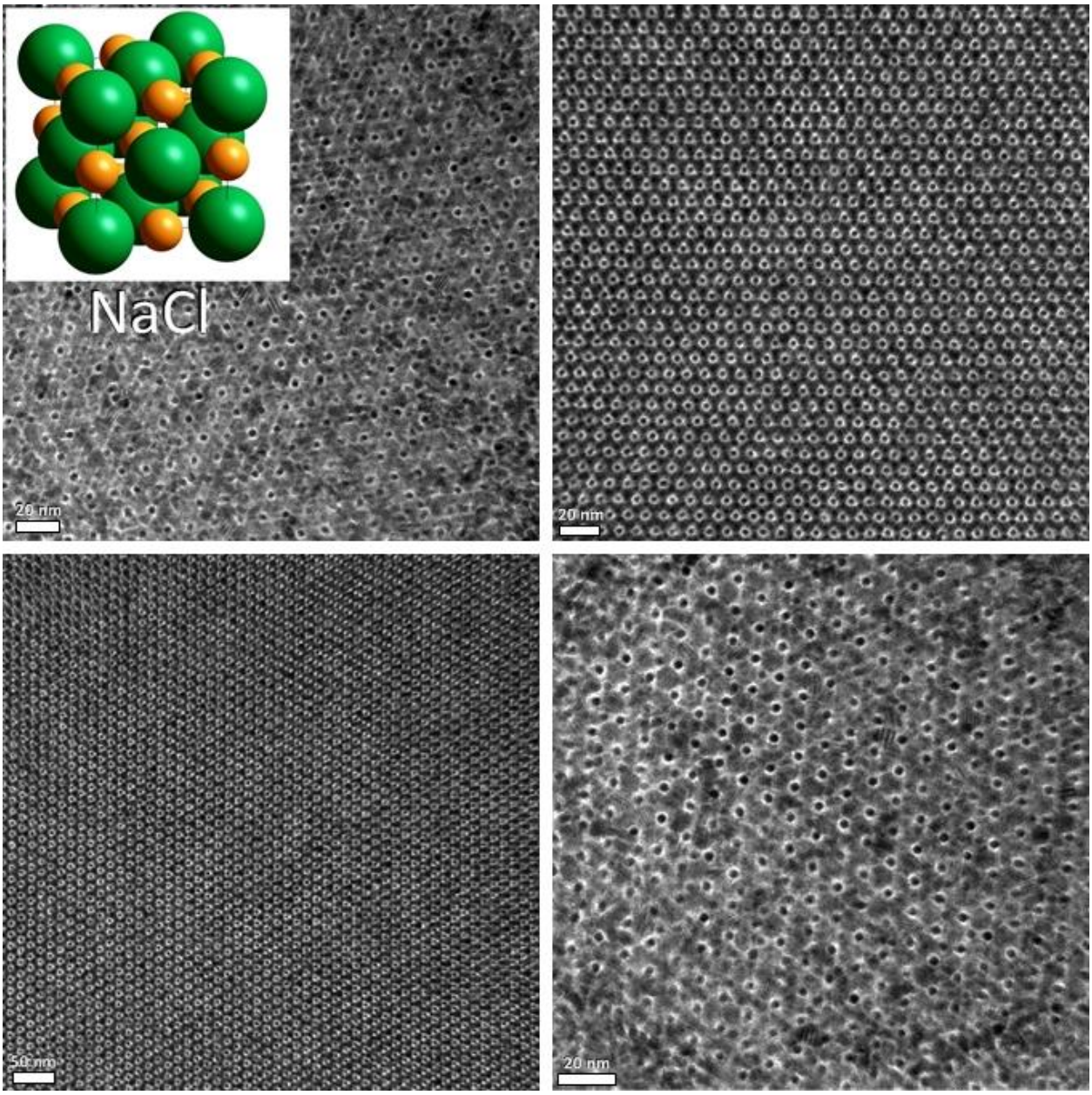

Figure 5.6. TEM images of (001)-projections of NaCl-type binary superlattices assembled from Au with Fe_2O_3 or PbS nanocrystals.

5.2.2. Binary phases with AB_2 stoichiometry

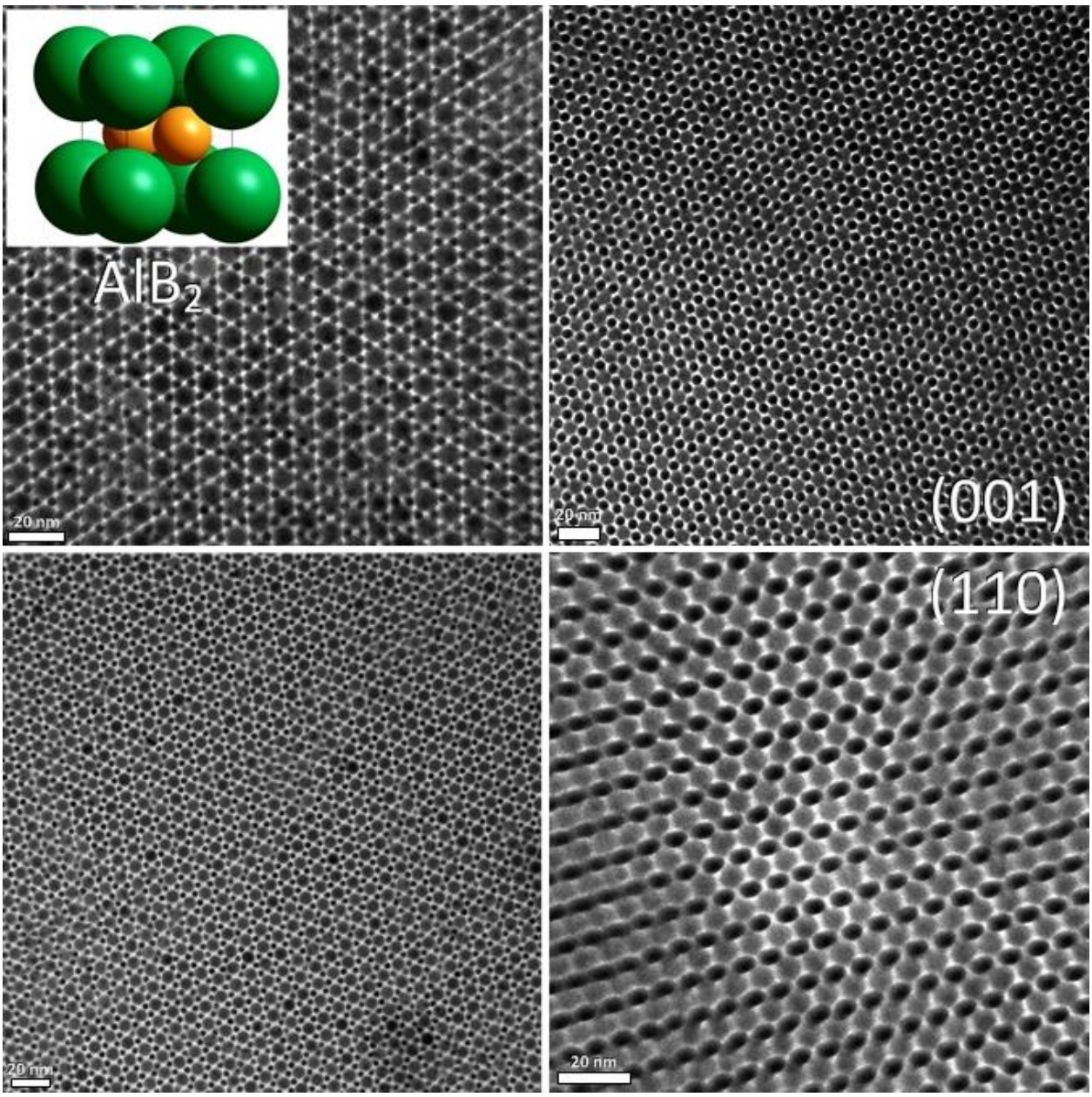

Figure 5.7. TEM images of AlB_2-type binary superlattices assembled from Au and PbS nanocrystals.

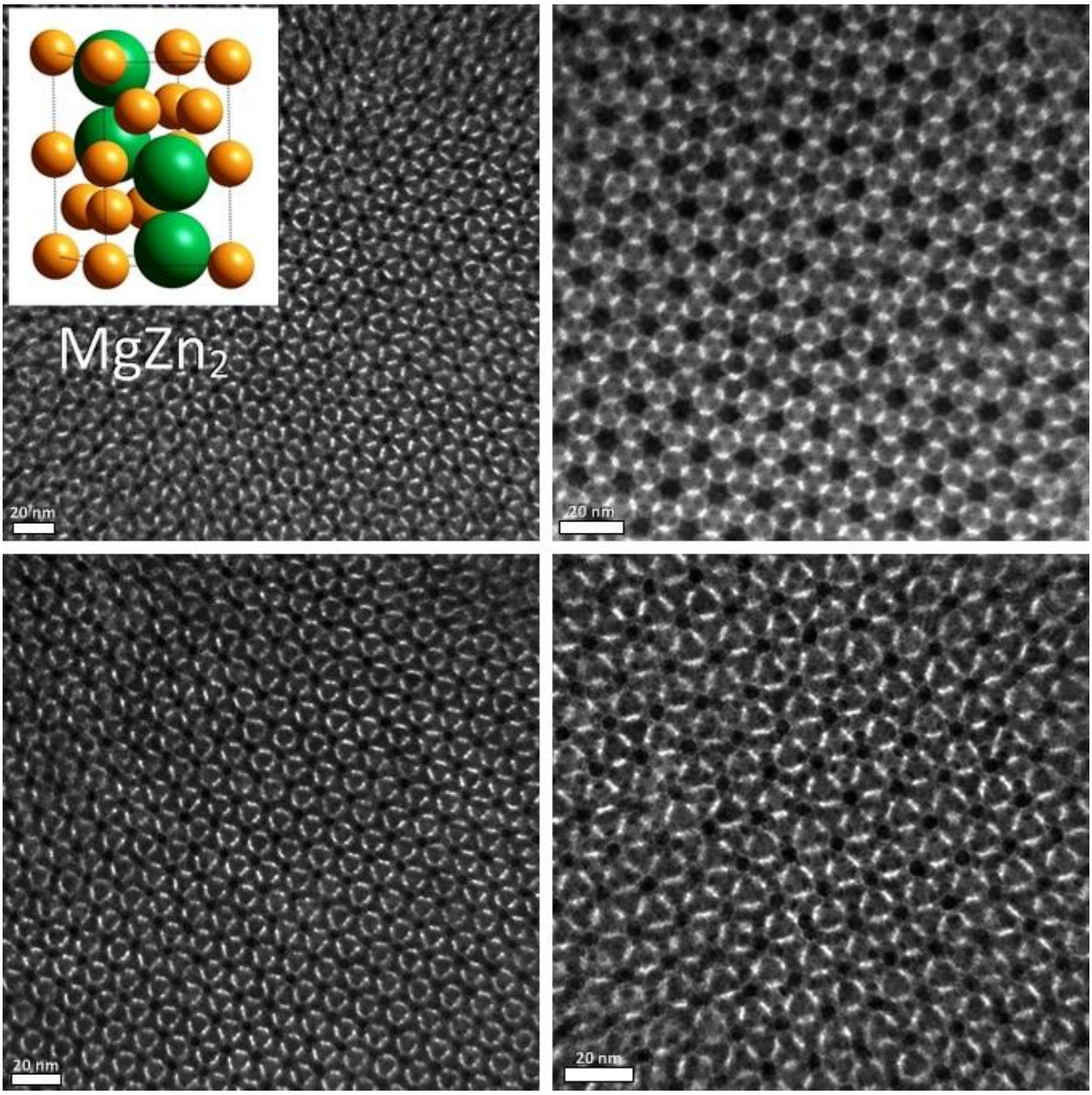

Figure 5.8. TEM images of (001)-projections of $MgZn_2$-type binary superlattices assembled from Au and PbS nanocrystals.

5.2.3. Binary phases with AB_3 stoichiometry

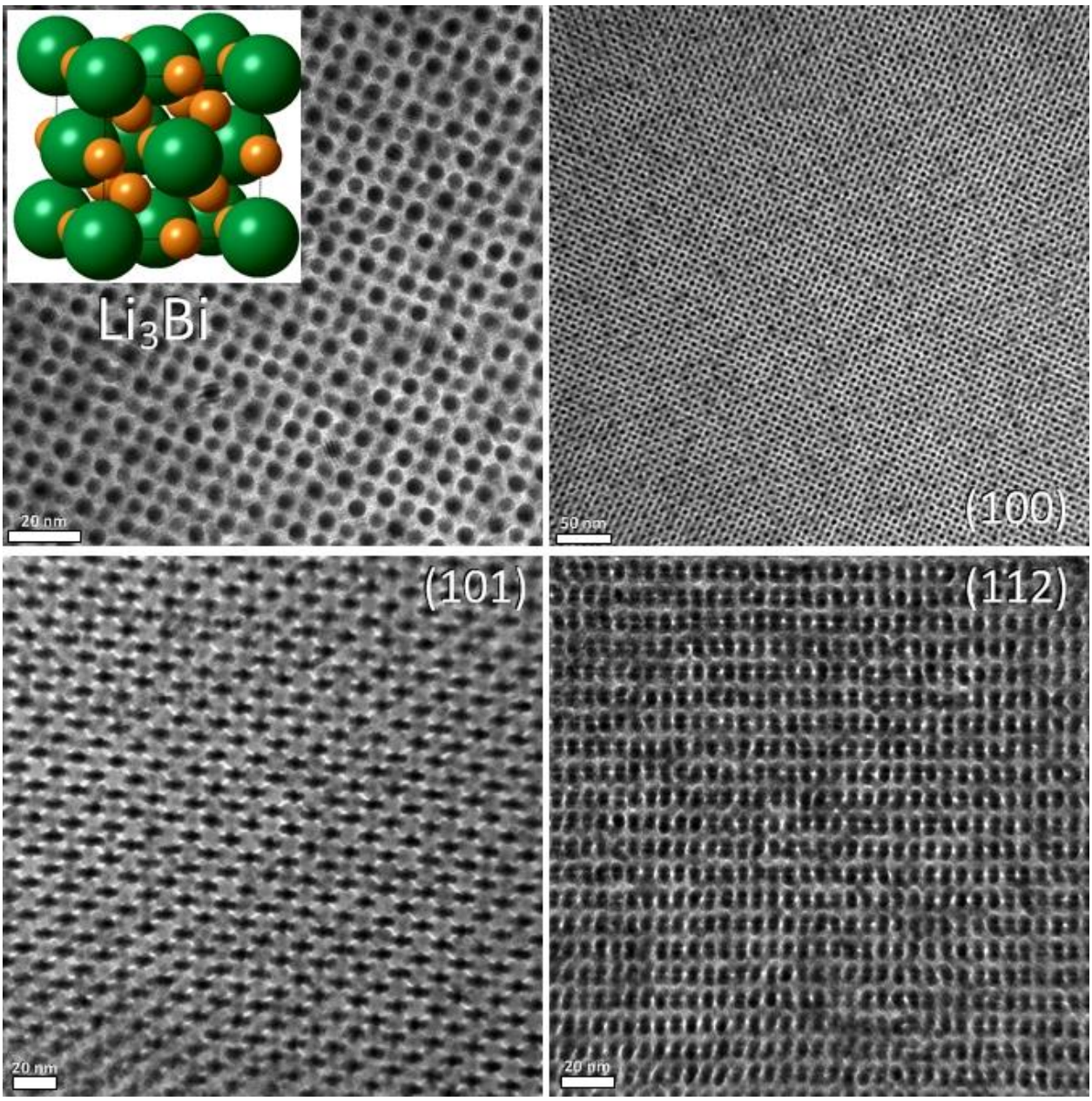

Figure 5.9. TEM images of Li_3Bi-type binary superlattices assembled from Au with Fe_2O_3 or PbS nanocrystals.

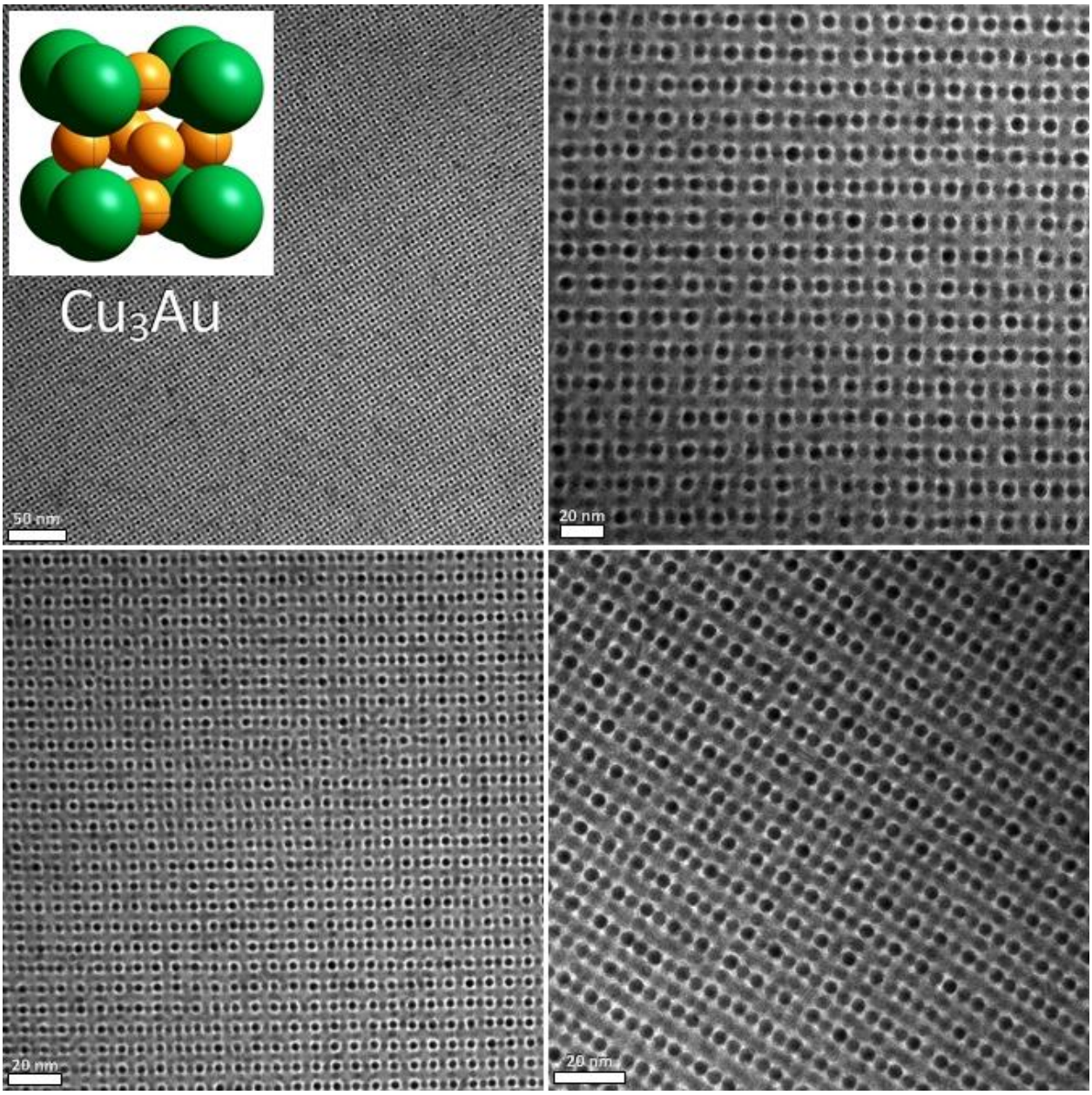

Figure 5.10. TEM images of (001)-projections of Cu_3Au-type binary superlattices assembled from Au and PbS nanocrystals

5.2.4. Binary phases with irrational (~$AB_{3.8}$) stoichiometry

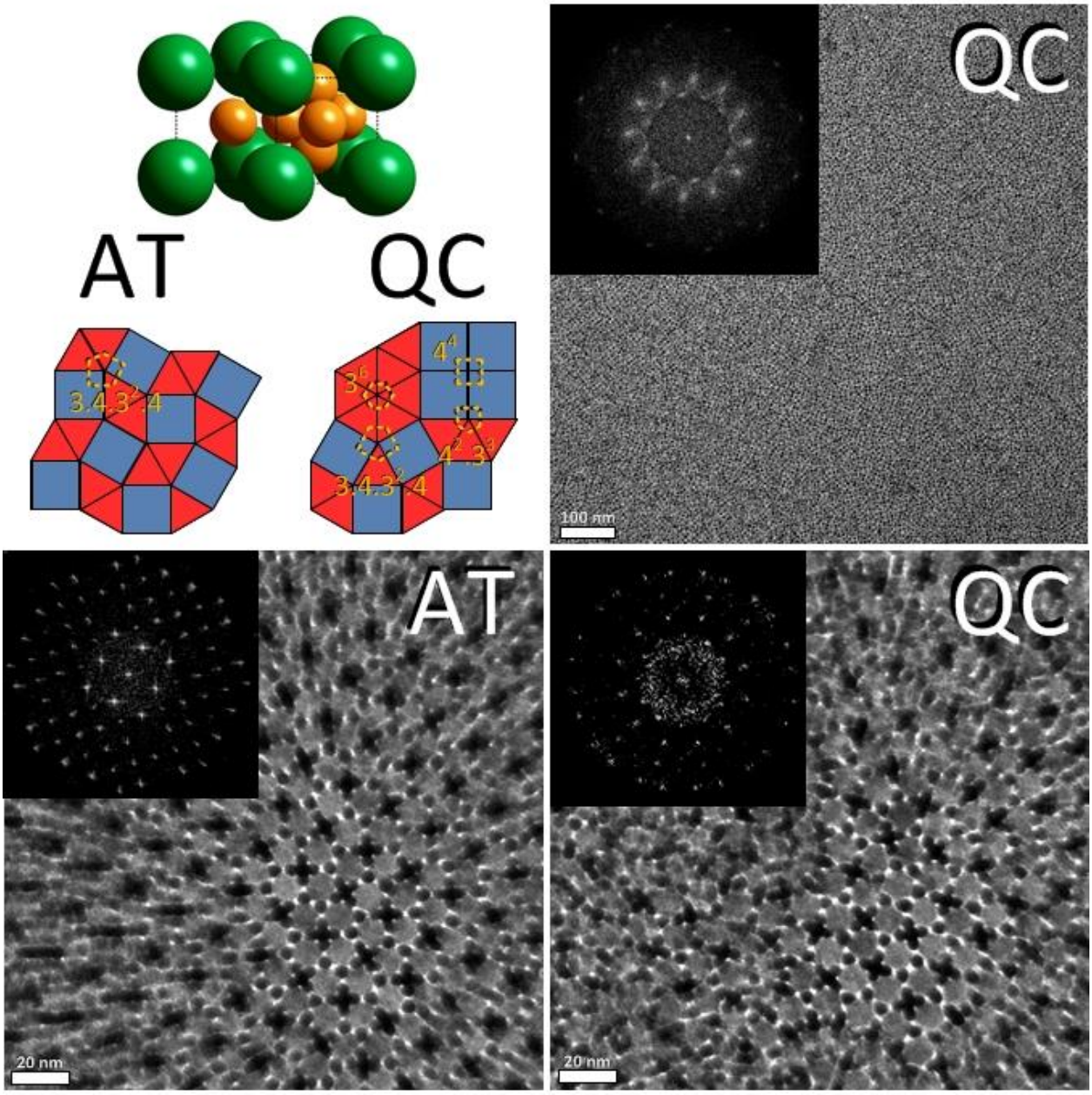

Figure 5.11. TEM images of Archimedean tiling and quasicrystalline binary superlattices assembled from Au with Fe_2O_3 or PbS nanocrystals. Upper left box shows structural motif of face-sharing CaB_6-type unit cell and AlB_2-type half unit cell (top) and the square and triangle tilings that give rise to periodic and aperiodic arrangements. Insets: Fourier transforms.

5.2.5. Binary phases with AB_5 stoichiometry

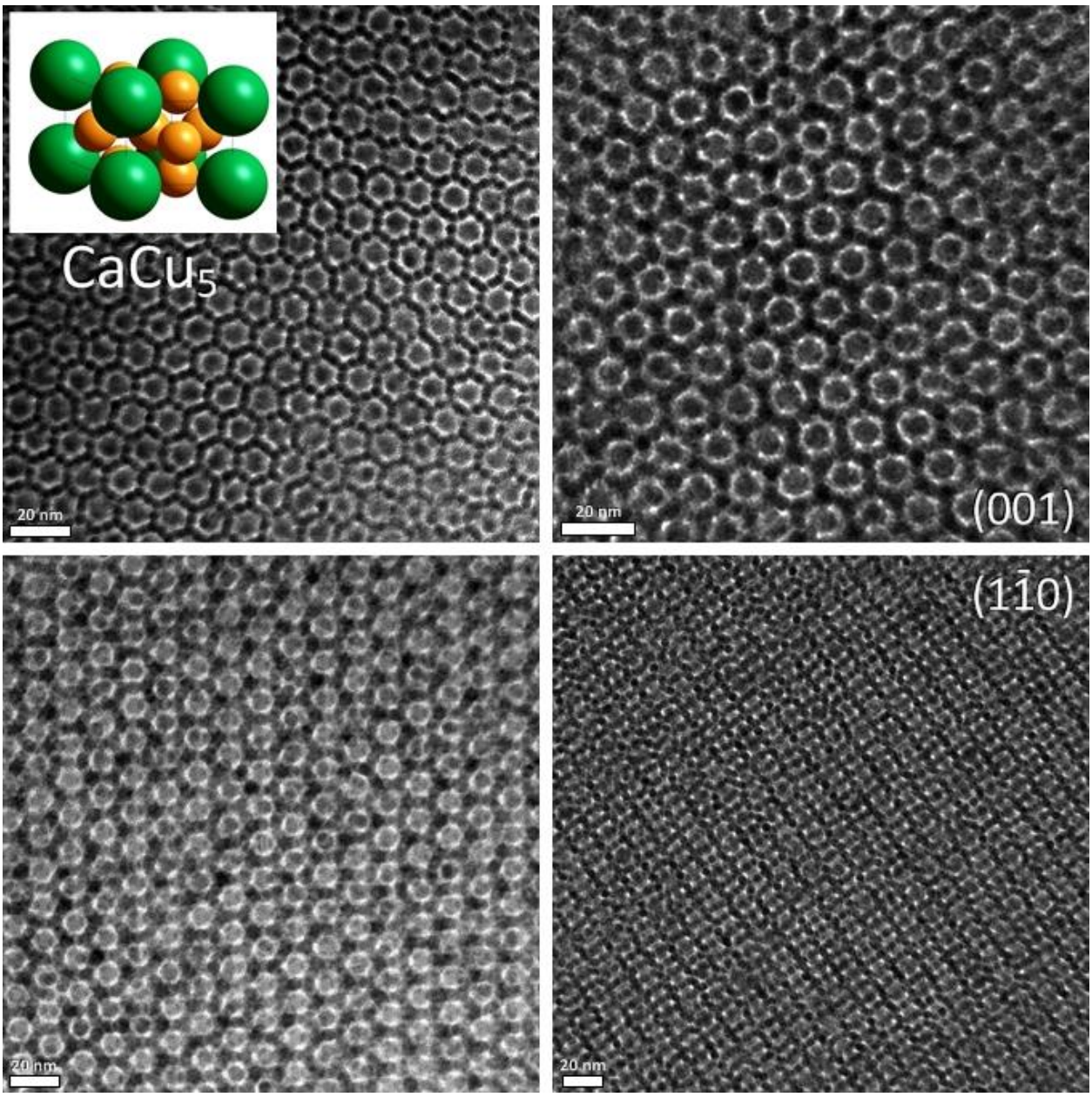

Figure 5.12. TEM images of $CaCu_5$ type binary superlattices assembled from Au and PbS nanocrystals.

5.2.6. Binary phases with AB_6 stoichiometry

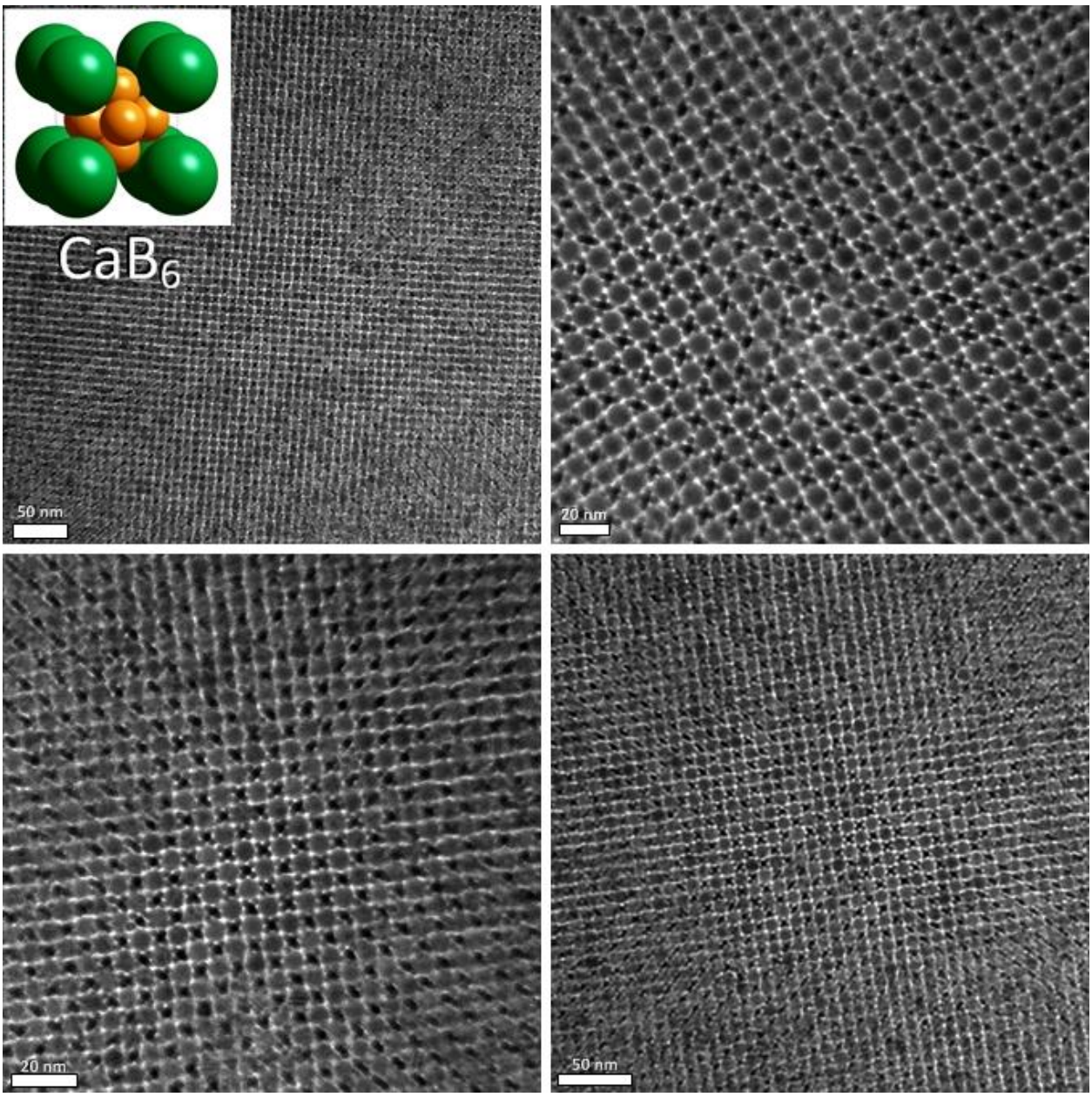

Figure 5.13. TEM images of (001)-projections of CaB_6 type binary superlattices assembled from Au and PbS nanocrystals.

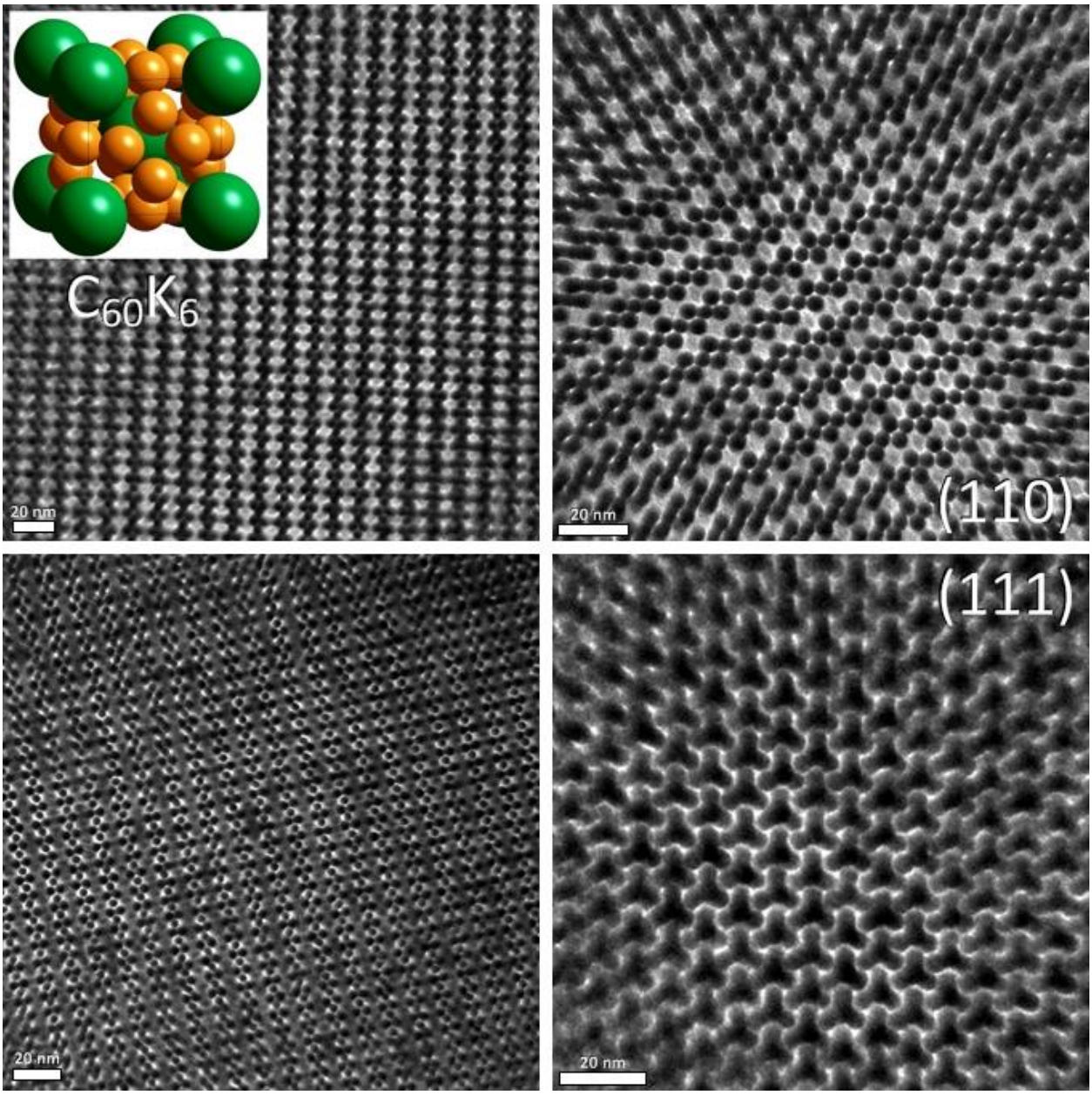

Figure 5.14. TEM images of $C_{60}K_6$ type binary superlattices assembled from Au with Fe_2O_3 or PbS nanocrystals.

5.2.7. Binary phases with AB_{13} stoichiometry

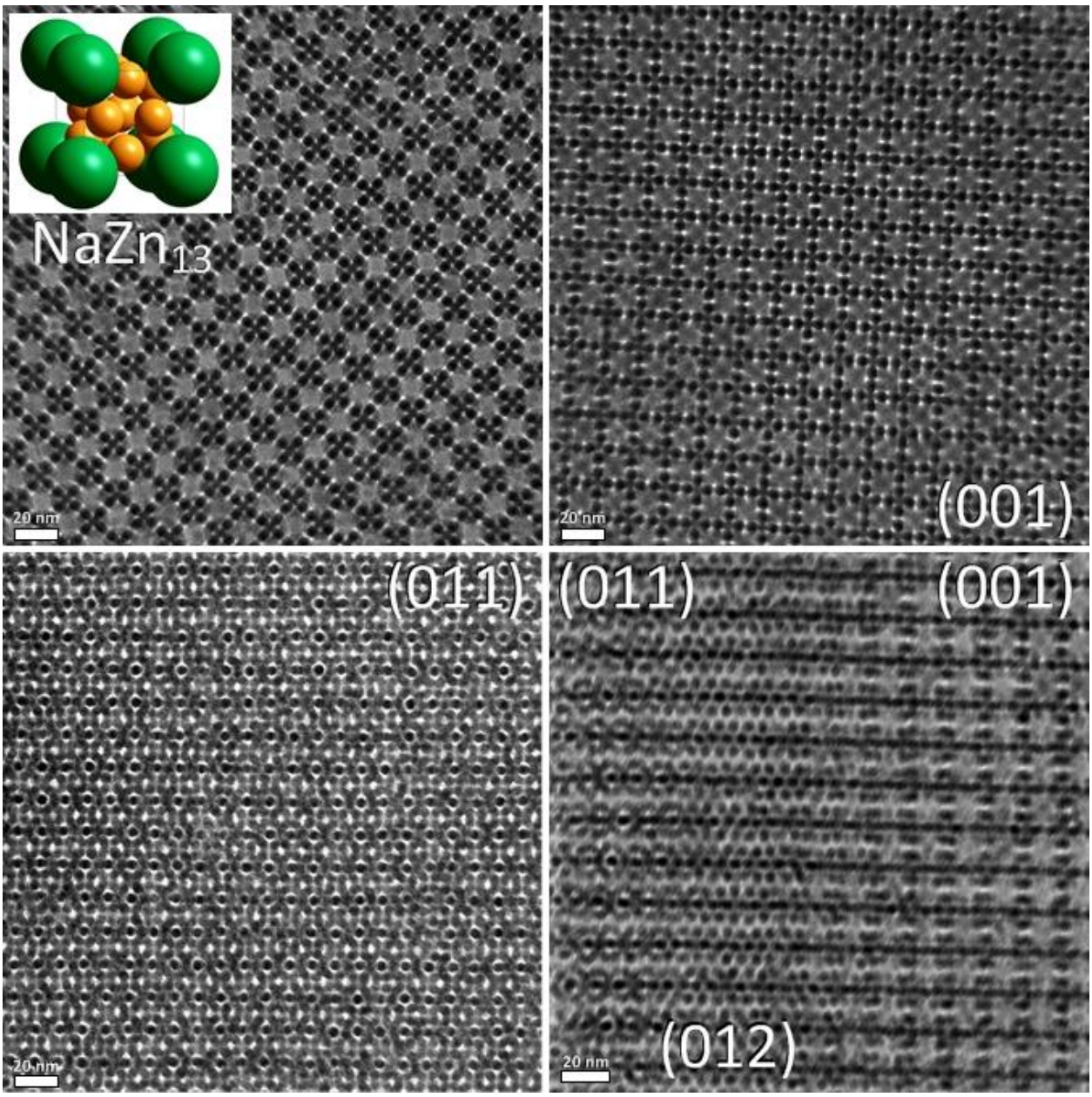

Figure 5.15. TEM images of $NaZn_{13}$ type binary superlattices assembled from Au with Fe_2O_3 or PbS nanocrystals.

5.3. Unknown binary structures

Not all observed binary phases were able to be identified. A few examples of such structures are shown below.

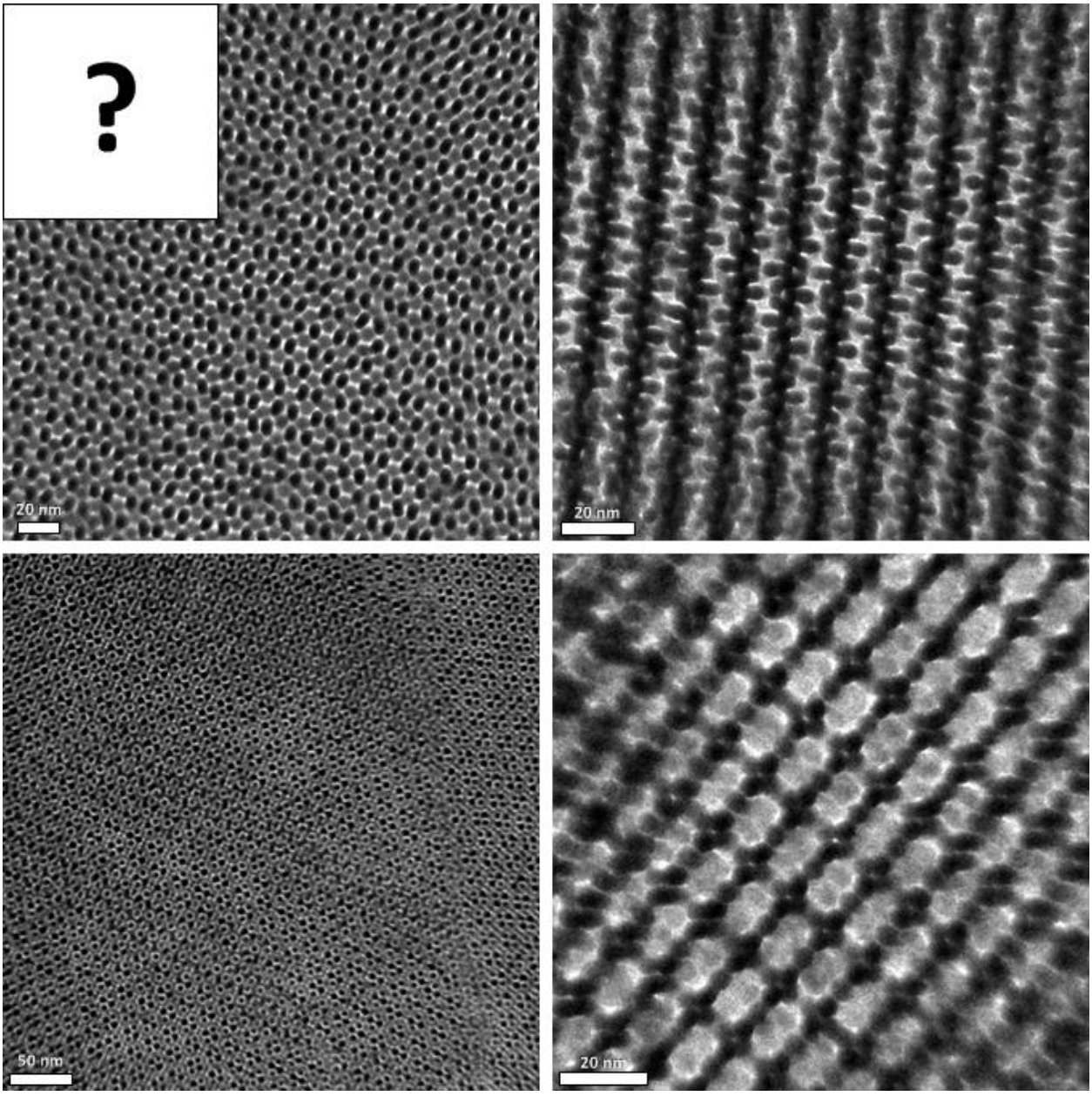

Figure 5.16. TEM images of unknown binary structures assembled from Au with Fe_2O_3 or PbS nanocrystals.

5.4. Structural defects in binary nanocrystal superlattices

Binary superlattices are a convenient system for real-space imaging of crystallographic defects.[2] A few examples are shown below.

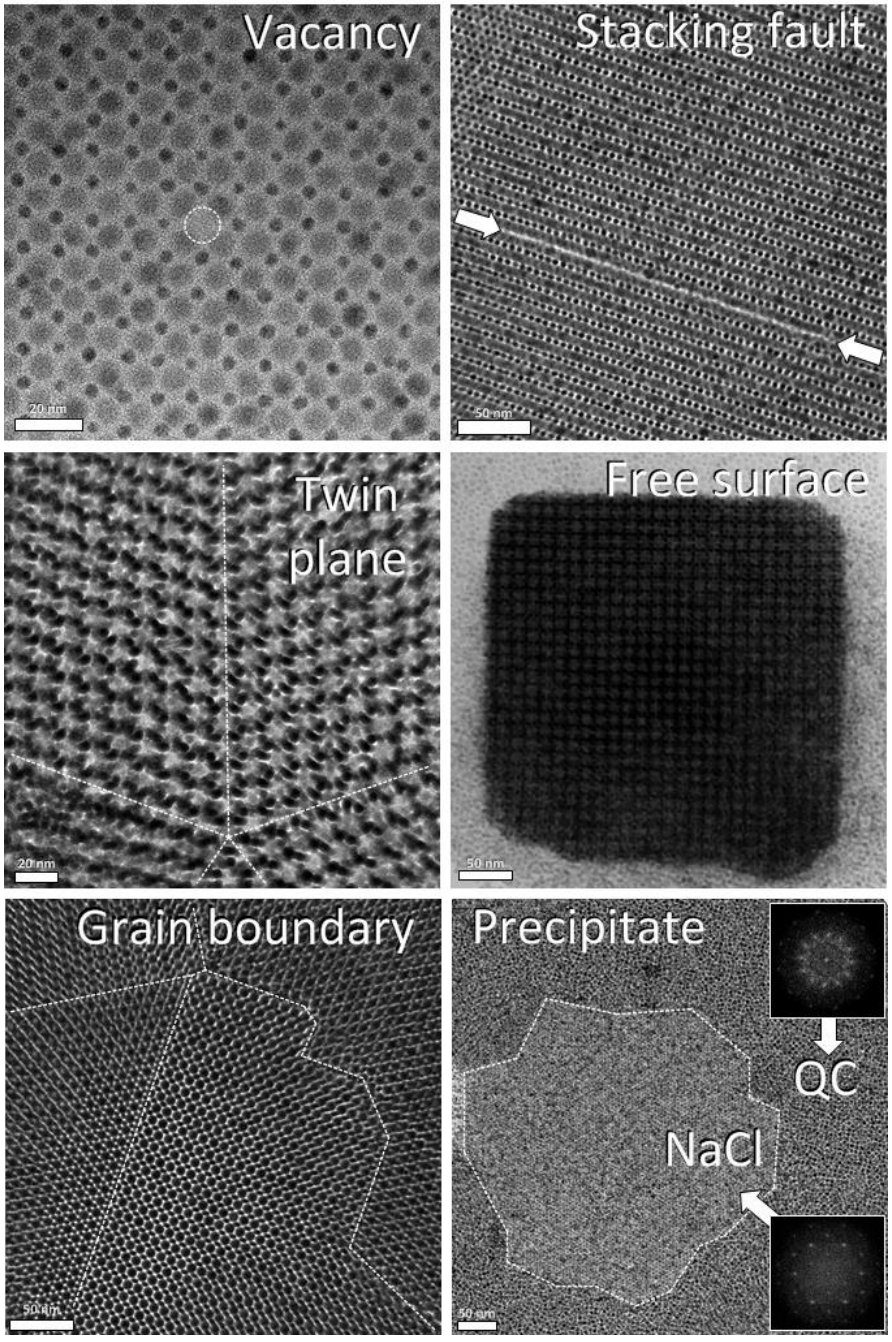

Figure 5.17. TEM images of structural defects identified in binary superlattices assembled from Au with Fe_2O_3 or PbS nanocrystals. Insets: Fourier transforms.

5.5. Acknowledgements

I wish to thank Dr. Joe Austin, Prof. Robert Josephs, and Dr, Yimei Chen for their help using the University of Chicago TEM facilities.

5.6. References

1 Shevchenko, E. V., Talapin, D. V., Murray, C. B. & O'Brien, S. Structural Characterization of Self-Assembled Multifunctional Binary Nanoparticle Superlattices. *Journal of the American Chemical Society* **128**, 3620-3637, (2006).

2 Bodnarchuk, M. I., Shevchenko, E. V. & Talapin, D. V. Structural Defects in Periodic and Quasicrystalline Binary Nanocrystal Superlattices. *Journal of the American Chemical Society* **133**, 20837-20849, (2011).

6. Many-body effects in nanocrystal superlattices: departure from sphere packing explains stability of binary phases

This work analyzes the role of hydrocarbon ligands in the self-assembly of nanocrystal (NC) superlattices. Typical NCs, comprised of an inorganic core of radius *R* and layer of capping ligands with length *L*, can be described as soft spheres with softness parameter *L*/*R*. Using particle tracking measurements of transmission electron microscopy images, we find that close-packed NCs, like their hard-sphere counterparts, fill space at approximately 74% density, independent of softness. We uncover deformability of the ligand capping layer that leads to variable effective NC size in response to coordination environment. This effect plays an important role in the packing of particles in binary nanocrystal superlattices (BNSLs). Measurement of BNSLs comprised of NCs of varying softness in several coordination geometries indicates NCs deform to produce dense BNSLs that would otherwise be low-density arrangements if particles remained spherical. Consequently, rationalizing the mixing of two NC species during BNSL self-assembly need not employ complex energetic interactions. We summarize our analysis in a set of rules for packing of soft objects. These findings contribute to a general understanding of entropic effects during crystallization of deformable objects (e.g., micelles, vesicles, globular proteins) that can adapt their shape to local coordination environment.

6.1. Colloidal crystallization: hard and soft sphere phase behavior

6.1.1. Entropy-driven crystallization of micron-sized colloidal beads

Self-organization of monodisperse colloidal particles has been a topic of interest since the iridescence of gem opals was attributed to diffraction of light from regularly packed silica spheres.[1] Micron-sized silica or polymer beads crystallize into close-packed structures, either cubic (*fcc*) or hexagonal (*hcp*), which may be rationalized by simple sphere packing arguments.[2] This ordering transition is driven by entropy: with negligible energetic interactions between beads, the preferred structure of the solvated colloidal crystal is one that maximizes free volume available to individual spheres. While a disordered collection of monodisperse spheres jams at particle volume fraction $\varphi \approx 0.64$, adoption of a close-packed arrangement allows for local translations of individual particles at volume fractions as high as $\varphi \approx 0.74$.

Cocrystallization of two sizes of micron-diameter spheres[3,4] has produced binary arrangements isostructural with NaCl, AlB_2, and $NaZn_{13}$ (Figure 6.1a). In parallel, much effort has been made to evaluate the relative stability of binary phases of hard[5-7] and soft-sphere[8,9] colloids. In the latter case, soft interactions have been treated using pair potentials. Packing geometry considerations reveal that, for certain sphere radius ratios ($\gamma = R_B/R_A$, where R_B is the radius of the smaller B sphere and R_A is the radius of the larger A sphere), binary structures of micron-sized beads fill space with density approaching or exceeding single-component *fcc* and *hcp* arrangements (Figure 6.1a). For these particles, size ratio has excellent predictive power over binary phase stability, confirming that efficient packing of spheres drives the system towards ordered two-component assemblies.

6.1.2. Complex phase diagram of binary nanocrystal superlattices

A new class of colloids emerged with the development of synthesis of monodisperse semiconductor,[10] metal,[11] and metal oxide[12] nanocrystals (NCs). These nanometer-sized, solution-grown particles consist of an inorganic core and a surface-tethered surfactant shell that prevents flocculation of NCs. Monodisperse NCs can be coaxed into adoption of ordered arrangements,[13,14] including cocrystallization of two types of particles into binary NC superlattices, BNSLs.[15,16] BNSL phases have been reported with AB, AB_2, AB_3, A_6B_{19}, AB_4, AB_5, AB_6, and AB_{13} stoichiometry and cubic, hexagonal, tetragonal, orthorhombic,[17] and dodecagonal quasicrystalline[18] (DDQC) symmetries (Figure 6.1a).

These structures have been modeled as sphere packings with effective sphere radius R_{eff} given as core radius plus measured effective ligand shell thickness.[13,16] In contrast to assemblies of micron-sized particles, attempts to rationalize BNSLs as efficient sphere packings using the assigned effective NC sizes and size ratio have been less fruitful. Of the twenty or so BNSL phases reported to date, most (~85%) are predicted to fill space less densely than close-packed arrangements of monodisperse hard spheres (Figure 6.1b). Stability of these BNSLs against phase separation into dense packings of large and small particles has remained an open question. It was suggested that a confluence of energetic forces (electrostatic, dipolar, van der Waals) may be responsible for BNSL formation.[8,19,20] However, the growing body of literature showing the diversity of binary NC arrangements, as well as the similarity of BNSLs self-assembled from chemically-different NCs, motivates our search for yet-unknown general principles that promote structural complexity of BNSLs far beyond the simple phase diagram of micron-sized spherical colloidal particles.

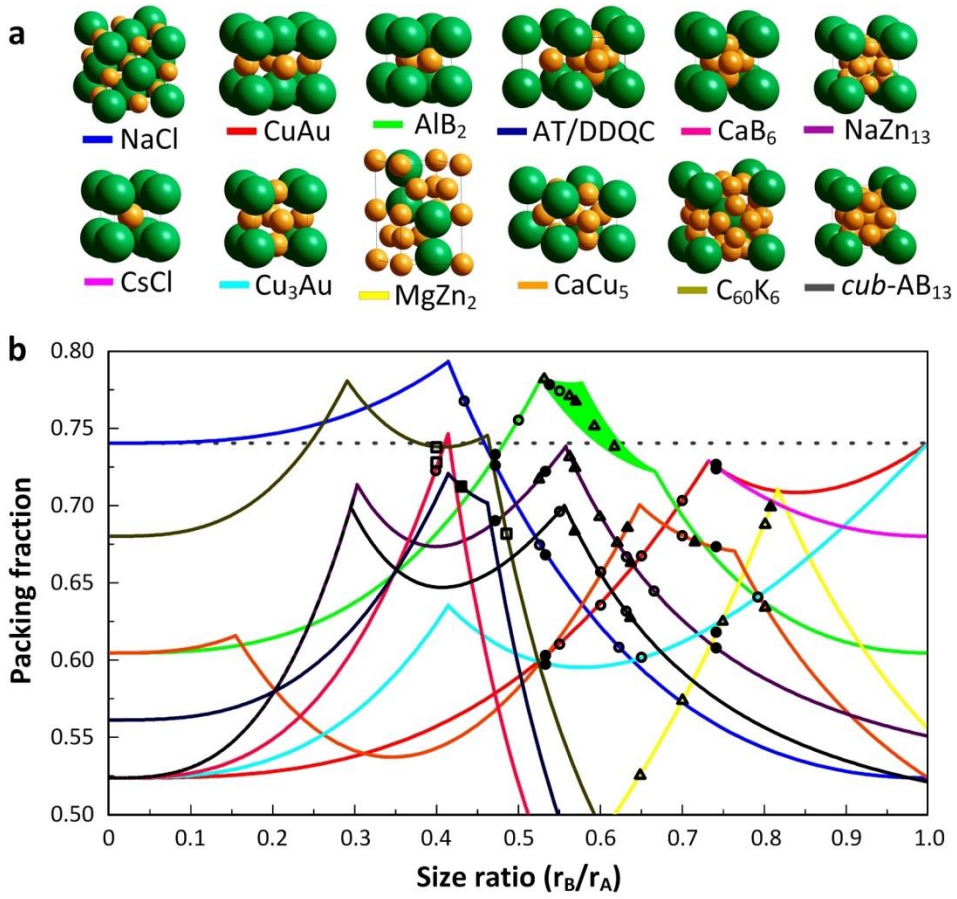

Figure 6.1. Structural diversity of binary nanocrystal superlattices and low packing density predictions for most observed phases. (a) Models of twelve commonly-observed binary arrangements showing larger A-spheres in green and smaller B-spheres in orange. Unit cells with AB, AB_2, AB_3, AB_5, AB_6, and AB_{13} stoichiometry, as well as the structural motif of Archimedean tiling (AT) and dodecagonal quasicrystal (DDQC) configurations, are shown. (b) Plot of density versus size ratio for spheres packed in these arrangements. Overlay: data points showing phases observed in several BNSL studies using reported effective size ratio and predicted density using sphere packing models. Most observed BNSLs appear to be open arrangements when compared to close-packed monodisperse hard spheres (dotted line). Works cited: ❍ ref.[16] ● ref.[21] . ☐ ref.[22] . ■ ref.[18] . △ ref.[23] . ▲ ref.[24] .

6.2. Microscopy investigation of ligand packing in monodisperse nanocrystal superlattices

Here we investigate the structure of surface ligands within single-component and binary NC arrays and analyze their role in directing the unique phase behavior observed for such particles. Surface ligands, typically hydrocarbon chains tethered to the NC surface through a headgroup linker, collectively form a soft corona around the particle. The ratio of extended chain length (L) to core radius (R) can be used as a measure of particle softness and means of differentiation between colloidal NCs ($L/R \sim 1$) and typical micron-sized colloidal beads ($L/R \sim 0.01$). Interaction between surface ligands is repulsive in good solvent (e.g., hexane) but attractive in vacuum (e.g., a dry superlattice). During self-assembly, solvent evaporation acts to densify the NC solution, forcing solvated particles into contact with one another. Complete removal of solvent freezes the collection of NCs into a superlattice with dimensions set by the balance between ligand elastic repulsion and van der Waals attraction forces.

We chose software analysis of transmission electron microscopy (TEM) images to collect information on NC surface ligand structure. While infrared (IR) spectroscopy can be used for detailed reconstruction of hydrocarbon structure in highly-ordered systems (e.g., crystalline self-assembled monolayers, SAMs[25]), disorder of capping ligands in NC SLs hides such microscopic details in ensemble averages.[26] Similarly, small-angle x-ray scattering (SAXS) can be used to evaluate the ligand contribution to overall particle size[27] but is unable to gather information on local structure of NC superlattices. TEM, on the other hand, allows for real-space imaging of individual superlattice domains and single particles with sub-nanometer resolution. While ligand molecules are not visible against the amorphous carbon support, their structure can be indirectly probed by measuring the separation between NC surfaces. Electron beam transmission through the entire sample ensures that measurements collected on multilayer superlattices are

representative of bulk dimensions. In addition, tilting of the TEM sample holder allows for three-dimensional reconstruction of the superlattice unit cell. We used software analysis of hundreds of images to collect large data sets (~10^6 individual NCs) and confirm statistical significance of our results.

6.2.1. Theoretical models of contacts between hydrocarbon-capped nanocrystals

To date, two models have been proposed to evaluate the contribution of soft ligand corona to the effective size of a hydrocarbon-capped NC. In simple analytical form, ligand packing has been reduced to geometric shapes, with sphere, cylinder, and cone representing the NC core, ligand chain, and explorable space, respectively (Figure 6.2a). The optimal packing model[28] (OPM) is built on the assumption that ligands pack densely only within a narrow volume along the contact axis between nearest neighbors (Figure 6.2b) and predicts interparticle separation to be $R_{eff}/R = (1+3L/R)^{1/3}$. An alternative overlap cone model[29] (OCM) assumes ligands fill space at bulk hydrocarbon density within the entire overlap volume (Figure 6.2b, bottom). For sufficiently soft ($L/R \gtrsim 0.5$) core-ligand combinations, this model predicts alkane chains completely fill the volume between NC cores, and that assemblies of such particles are perfectly space-filling. The OCM dense ligand packing assumption suggests a shorter separation between NC cores than OPM and predicts the existence of many-body effects, or non-pairwise interaction between ligand capping layers. Some experiments[28] support the accuracy of OPM while other data and molecular simulations[29] agree with the OCM predictions.

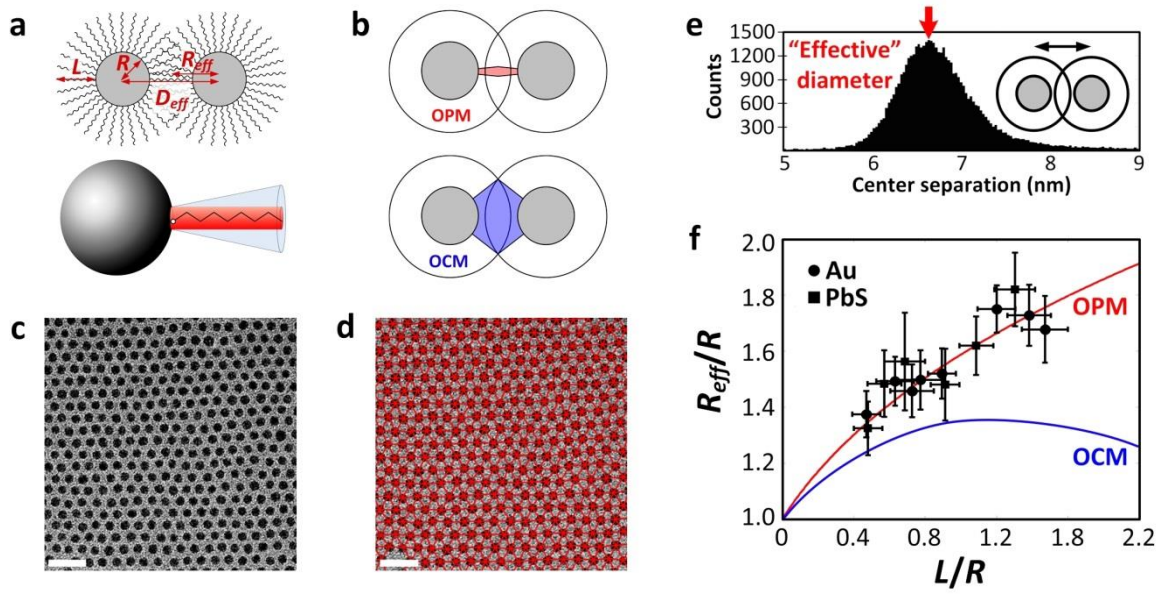

Figure 6.2. Geometric models for soft particle contact and measurement of separations in Au and PbS monolayer arrays. (a) Sketch of NC contact with labeled core radius, ligand length, effective NC radius, diameter (top) and geometric reduction of NC, ligand, and excess volume to sphere, cylinder, and cone (bottom). (b) Sketch of hydrocarbon space-filling assumptions made by two models of ligand packing in NC arrays. See main text for explanation. (c,d) Particle tracking analysis of TEM images allows for collection of experimental interparticle separation statistics. Sample area of monolayer of 4.1-nm Au NCs capped with octadecanethiol ligands is shown. Scale bars, 20 nm. (e) Effective NC diameter, including core and ligand contributions to particle size, is extracted from histogram plot of center separations. (f) Plot of effective radius versus ligand length predictions by OPM (red curve) and three-body OCM (blue curve) with experimental data collected from hexagonal monolayers of PbS and Au NCs of 3- to 5-nm core diameter and C_9- or C_{18}-length ligands. Full width at half maximum of effective size and core diameter distributions are denoted by vertical and horizontal error bars, respectively.

6.2.2. Experimental interparticle separation in Au and PbS nanocrystal arrays

We began our study by establishing how deeply ligand coronas interpenetrate after solvent evaporation and the associated implications for space-filling efficiency of close-packed NCs. Using several batches of PbS and Au NCs with core diameter varying from 3 to 5 nm, we carried out ligand exchange (Appendix I, Figure 6.7 and Figure 6.8Figure 6.8) to replace original capping ligands with C_9- and C_{18}-length hydrocarbon chains with carboxylic acid and thiol

anchoring group for PbS and Au NCs, respectively. This allowed us to obtain sets of capped NCs with softness parameter spanning $0.5 < L/R < 1.75$. Tetrachloroethylene solutions of these NCs were drop cast on carbon support and many (~25) TEM images of hexagonally-arranged NCs at sub-monolayer coverage were collected for each set (Appendix I, Figure 6.10). TEM images were analyzed using MATLAB particle tracking code. Identification of NC cores in the image and connecting their centers produced a hexagonal network of line segments (Figure 6.2c,d) with length corresponding to the effective NC diameter, including core and ligand contributions to the particle size. Plotting a histogram of measured separations yields a distribution centered on the effective NC diameter and broadened by some variation in core size and depth of corona overlap (Figure 6.2e).

For all values of softness, the measured average effective NC size was found to fall within 10% of the OPM prediction (Figure 6.2f). The three-body OCM solution, on the other hand, systematically underestimated effective size, most notably for the softest core-ligand combinations ($L/R > 1$). From this observation we conclude that hydrocarbon chains do not completely fill space between NC cores but instead, jam at a separation that leaves ~1/3 of this volume open (Appendix II, Section 6.7.1). The attraction between hydrocarbon chains (~4 meV per methylene unit in vacuum[30]) favoring dense packing of segments is opposed by the finite compressibility of entangled, interdigitating chains tethered at one end to a spherical surface. Indeed, with molecular lengths ($C_9 - C_{18}$, 1.2 to 2.3 nm) on the order of the Kuhn segment (for polyethylene, 1.4 nm, ref.[31]), organic capping ligands may best be described as semi-flexible rods with elastic response that precludes liquid-like molecular packing of alkane chains.

6.2.3. Interparticle separation changes with nanocrystal coordination number

Figure 6.2f shows the measured effective particle size averaged over all contacts in NC films deposited at sub-monolayer coverage. While most particles we imaged are embedded within the array interior, some sit at island edges and have comparatively fewer nearest neighbors (Appendix I, Figure 6.13). To get a deeper insight to the local structure of NC packings, we used particle tracking to assign each NC a coordination number and categorize center separations based on the coordination state of the two NC endpoints (Figure 6.3a). We found that coordination number plays an important role in setting effective NC size: measured separations are greater between fully-coordinated particles as compared with those having open coordination sites. Using 4.1-nm Au-C_{18} NCs as an example, we demonstrate expansion of effective NC size with increasing coordination number, plotting interparticle separations for coordination series 6-*n*, where one NC is fully-coordinated in two dimensions and the other has coordination number $3 \leq n \leq 6$ (Figure 6.3b). We also collect separations for the same Au NCs embedded in *hcp* trilayers ($n = 12$), which appear as hexagonal arrays of alternating dark and light NCs (Appendix I, Figure 6.11).

Taking the distribution maximum to be the true separation, effective NC size increases with number of overlaps. To exclude the possibility of size selection on the grid, whereby small NCs are pushed to the superlattice periphery, we measured core diameter using edge detection code (Appendix I, Figure 6.14). We found no change in core size with coordination number, confirming variation in effective NC size is a capping ligand effect. We tested the statistical significance of our measurements by calculating the probability that these observed shifts in effective NC size might be attributed to random fluctuations around the typical separation of

fully-coordinated particles (the *p*-value). This analysis confirmed that the largest shifts are significant to a 95% confidence level (Appendix IV, Section 6.9.1).

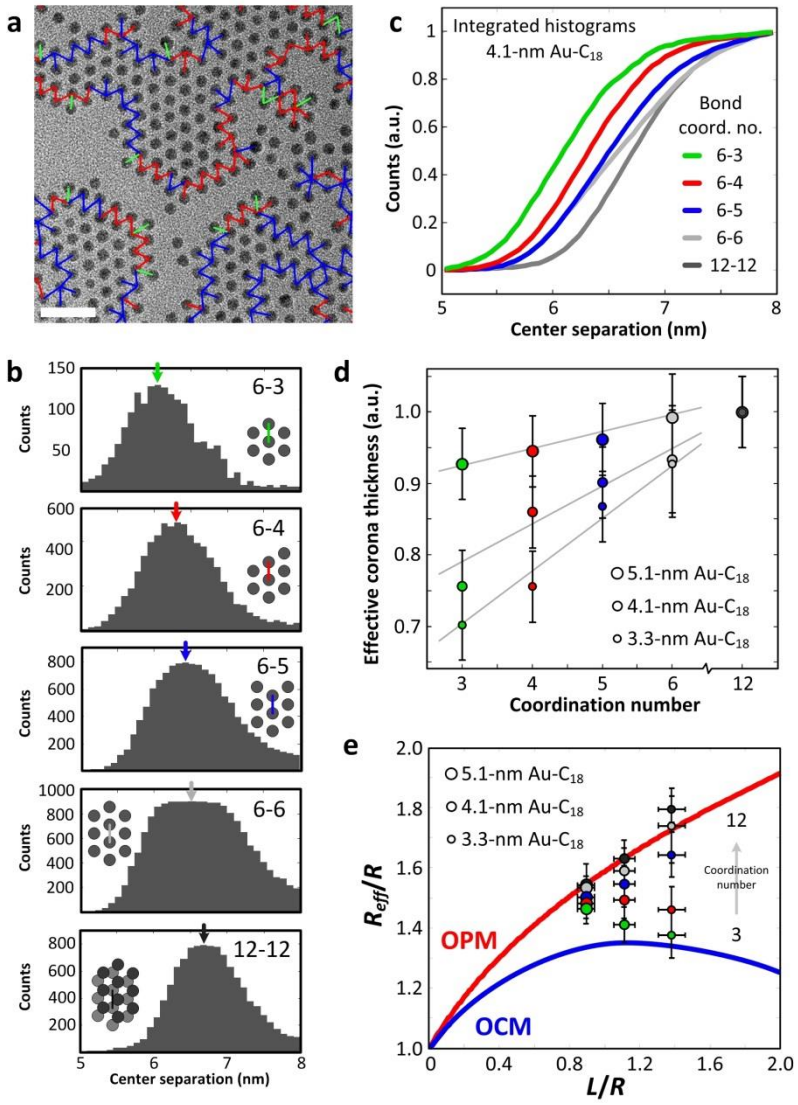

Figure 6.3. Measurement of coordination-dependent effective nanocrystal size. (a) Sample area of TEM image of 4.1-nm Au-C_{18} NCs with 6-3 bonds shown in green, 6-4 bonds in red, 6-5 bonds in blue, and 6-6 bonds omitted for clarity. Scale bar, 20 nm. (b) Extracted interparticle separation statistics for 6-3, 6-4, 6-5, and 6-6 monolayer bonds as well as 12-12 trilayer bonds. Distribution modes marked with arrows. (c) Integration of histogram plots allows for comparison of the left edge of the distributions, containing bonds between NCs in closest association. (d) Effective corona thickness versus coordination number for three sizes of Au-C_{18} NCs normalized with respect to surface separation in multilayer superlattice. Error bars correspond to distribution fwhm. Grey lines serve to guide the eye. (e) Plotting measured effective NC sizes in R_{eff}-L space allows for comparison against ligand packing theories..

Bond length distributions have positive skew (a long right-side tail) attributed to a population of loosely-overlapping NCs. Examining those in close contact on the left side of the distribution enables meaningful comparison of relaxed interparticle spacings. Integrating the histograms reveals closest approach for coordinatively-unsaturated NCs (Figure 6.3c). The non-Gaussian shape of the 6-6 distribution may be a consequence of local relaxation of tensile stress by roughening of separations within the interior of islands (Appendix IV, Figure 6.21). We also measure interparticle separation versus coordination number for 3.3-nm and 5.1-nm Au-C_{18} NCs (Appendix I, Figure 6.10) and plot the results for all three sets of NCs in the same window (Figure 6.3d). Separations were normalized with respect to *hcp* trilayer distance. For 3.3-nm Au-C_{18} NCs ($L/R \approx 1.4$), we found that removing nearest neighbors resulted in considerable (~30%) reduction of corona contribution to effective NC size, while the same effect was much smaller (~6%) for 5.1-nm Au-C_{18} NCs ($L/R \approx 0.9$). Since van der Waals interaction energy between NC cores scales with particle volume (i.e., should be significantly larger for 5.1nm Au NCs compared to 3.3nm NCs), this observation allowed us to exclude core-core attraction as the primary cause of variation in effective NC size. Plotting separations on top of the predictions made by OPM and OCM theories (Figure 3e) reveals that, although measured separations of coordinatively-saturated NCs are close to the OPM prediction, much shorter separations are measured for NCs with large L/R and few nearest neighbors. The observed influence of surrounding particles on the state of two contacting particles indicates that the hydrocarbon capping layer supports many-body interactions between NCs not anticipated by the pairwise considerations of OPM.

6.2.4. Many-body effects: deformation of hydrocarbon corona

We attribute the many-body effect to deformation of the ligand corona. As particles are brought into contact during solvent evaporation, hydrocarbon chains are concentrated along the central axis between nearest neighbors (Figure 6.4a, top). This accumulation of ligand segments is accompanied by osmotic pressure pushing solvated chains outwards (Figure 6.4a, bottom). While the corona of a particle embedded within the bulk of a close-packed array experiences nearly uniform pressure from all sides (Figure 6.4b), the corona of a low-coordination particle does not. As a result, the entropic drive to distribute ligand segments uniformly throughout the space between NC cores forces coordinatively-unsaturated particles to shift chains away from contacts and allows them to sit closer to their neighbors (Figure 6.4c). Indeed, this effect has been anticipated by molecular dynamics (MD) simulations of pairwise interactions between alkanethiol-capped Au NCs[32] and self-consistent field theory calculations of overlapping spherical brushes.[33]

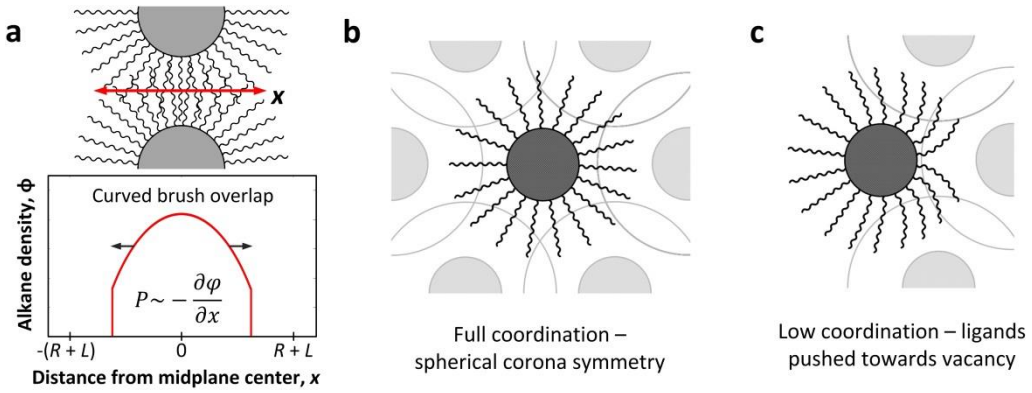

Figure 6.4. Geometric model of ligand overlap and deformation of corona for low-coordination nanocrystals. (a) Overlap of spherical brushes (e.g., nanocrystal coronas) results in accumulation of segments in the center of the midplane. Osmotic pressure at the contact pushes ligands toward the periphery. (b) Corona of nanocrystal fully surrounded by neighbors (top) experiences nearly uniform pressure from neighboring segments and features isotropic ligand chain distribution. Corona of coordinatively-unsaturated nanocrystal (bottom) is shifted away from contact and towards solvent-rich void space as a result of osmotic pressure gradient across the sphere surface.

Capping ligand structure may also be influenced by the amorphous carbon film that supports NCs resting on the TEM grid. MD simulations of Au NCs passivated with dodecanethiol and adsorbed to graphite surface predict that ligand chains are tilted away from the graphite surface normal,[34] creating some solid angle of the NC surface in which no chain ends are found. This effect should apply to all NCs in contact with the carbon support (Figure 6.2c, Figure 6.3a) and substrate can be viewed as an additional "neighbor" acting on all NCs in the monolayer. We expect that the effect of coordination environment on effective NC size shown in Figure 6.3, should be even stronger for NC assemblies suspended in solution.

To conclude, with simple geometry and chain packing assumptions, OPM and OCM are appealing models for considering "hairy" sphere packings. OPM correctly predicts the dimensions of extended NC arrays. On the other hand, this model treats only pairwise interactions between nearest neighbors and thus provides no means to understand the observed many-body interaction. OCM correctly anticipates the many-body effect, however it results from the assumed tendency for alkanes to pack between cores in extended space-filling domains, an assumption that leads to predicted separations much shorter than our experimental measurements (Figure 6.2f). Importantly, the ability of a spherical NC corona to be deformed in response to its surroundings appears to be missing from this analysis to date.

6.3. Self-assembly of binary arrays with similar and contrasting nanocrystal softness

6.3.1. Case one: 7.0-nm PbS and 4.1-nm Au

Next, we investigate the role of ligands in binary nanocrystal superlattices (BNSLs). We used ligand exchange to tune the softness of NC building blocks and effective radius ratio ($\gamma_{eff} = R_{eff,B}/R_{eff,A}$, with R_{eff} values measured from single-component arrays[16]) for nominally identical NC cores. For example, we assembled BNSLs from 4.1-nm Au and 7.0-nm PbS NCs in two capping ligand combinations: PbS-C_{18} ($L/R \approx 0.65$) and Au-C_9 ($L/R \approx 0.58$) with both components having similar soft character, and PbS-C_9 ($L/R \approx 0.34$) and Au-C_{18} ($L/R \approx 1.1$) with Au-C_{18} much softer than PbS-C_9. Evaporation of a solution containing Au-C_9 and PbS-C_{18} NCs ($\gamma_{eff} \approx 0.62$) in various concentration ratios reproducibly generated three binary phases: CuAu, AlB_2, and $NaZn_{13}$ (Figure 6.5a). On the other hand, doing the same with Au-C_{18} and PbS-C_9 ($\gamma_{eff} \approx 0.76$) produced two phases: $MgZn_2$ and $CaCu_5$ (Figure 6.5b). If we model the observed BNSLs as rigid sphere packings, we find that only AlB_2 has density comparable to close-packed monodisperse spheres, $\rho_{fcc/hcp} \approx 0.74$ (Figure 6.5c). This is in line with previous works[17] and highlights the apparent conflict between the entropic preference for dense NC packings and the frequent observation of supposedly-open BNSL arrangements.

6.3.2. Case two: 10.2-nm Fe_2O_3 and 4.1-nm Au

Similar results were observed for assembly of a second set of BNSLs from 4.1-nm Au and 10.2-nm γ-Fe_2O_3 building blocks. Cocrystallization of Fe_2O_3-C_{18} ($L/R \approx 0.45$) and Au-C_9 ($L/R \approx 0.58$) NCs ($\gamma_{eff} \approx 0.45$) yielded 3^2.4.3.4 Archimedean tilting (AT), dodecagonal quasicrystal (DDQC[13]) and body-centered cubic (*bcc*) AB_6-type[22] BNSLs isostructural with K_6C_{60} (Figure 6.5d), while the Au-C_{18} ($L/R \approx 1.1$) and Fe_2O_3-C_9 ($L/R \approx 0.24$) combination ($\gamma_{eff} \approx 0.56$) produced Li_3Bi and $NaZn_{13}$ phases (Figure 6.5e). We note that the Li_3Bi BNSL,

constructed by *fcc* arrangement of large spheres with small spheres occupying all tetrahedral and octahedral sites, was not reported in earlier work on BNSLs. Li_3Bi structure assignment was made with the assistance of TEM tilting experiments (Appendix I, Figure 6.9). Modeling these structures as binary arrangements of hard spheres suggests AT, DDQC, *bcc*-AB_6, and $NaZn_{13}$ phases pack with efficiency close to *fcc*/*hcp*, while Li_3Bi appears to be a low-density outlier with predicted space-filling fraction $\rho \approx 0.55$ at this size ratio (Figure 6.5f).

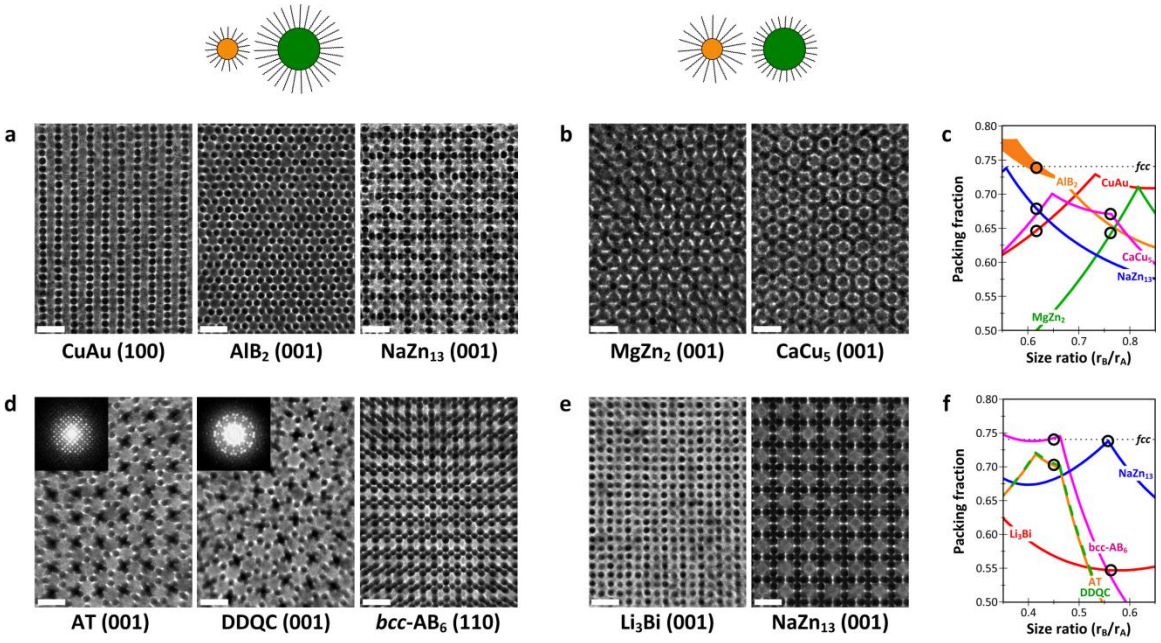

Figure 6.5. Self-assembly of binary nanocrystal superlattices with different ligand combinations. (a) TEM images of CuAu, AlB_2, and $NaZn_{13}$-type BNSL phases formed from evaporation of solution containing 7.0-nm PbS-C_{18} and 4.1-nm Au-C_9 NCs. (b) TEM images of $MgZn_2$ and $CaCu_5$-type BNSLs formed from PbS-C_9 and Au-C_{18} with same cores as (a). Schematic of tailoring ligand corona thickness shown above BNSL images. (c) Space-filling curves calculated for hard-sphere arrangements of observed binary structures of PbS and Au NCs. (d) TEM images of $3^2.4.3.4$ Archimedean tiling (AT), dodecagonal quasicrystal (DDQC), and body-centered cubic (*bcc*) AB_6-type BNSL phases formed from 10.2-nm Fe_2O_3-C_{18} and 4.1-nm Au-C_9 NCs. (e) TEM images of Li_3Bi and $NaZn_{13}$-type BNSLs at formed from 10.2-nm Fe_2O_3-C_9 and 4.1-nm Au-C_{18} NCs with same cores as (d). (f) Space-filling curves calculated for hard-sphere arrangements of observed binary structures of Fe_2O_3 and Au NCs. Scale bars, 20 nm.

6.4. Microscopy investigation of ligand packing in binary nanocrystal superlattices

For each observed BNSL structure, we collected images of many domains and systematically tilted samples with respect to electron beam to obtain several crystallographic projections of the same superlattice. We subjected our library of BNSL images to MATLAB particle tracking analysis (Appendix III, Figure 6.17 and Figure 6.18) similar to measurements shown in Figure 2d. This approach enabled three-dimensional reconstruction of the BNSL unit cell and extraction of experimental interparticle separations (Appendix III, Figure 6.19).

6.4.1. Average coordination number of contacting nanocrystals in binary superlattices

To quantify the crowding of NC contacts we introduce a BNSL coordination number: for BNSLs supported by contacts between A-spheres (e.g., PbS-PbS contacts in $MgZn_2$- and CuAu-type structures), the BNSL coordination number is simply the coordination state of A-spheres (e.g., 4 for diamond-type A-sphere sublattice of $MgZn_2$ and 6 for octahedral A-sphere coordination of CuAu). For BNSLs supported by contacts between B-spheres (e.g., Au-Au contacts in $CaCu_5$- and $NaZn_{13}$-type structures), the average coordination number of non-equivalent B_1- and B_2-spheres was calculated, weighted by abundance of each within the BNSL structure (Section 6.8.2). We assign average coordination number of 7.2 for $CaCu_5$ and 8.3 for $NaZn_{13}$-type BNSLs. For BNSLs supported by A-B contacts (e.g., PbS-Au contacts in AlB_2 and Fe_2O_3-Au contacts in Li_3Bi and *bcc*-AB_6 BNSLs), the same weighted average BNSL coordination number used A- and B-sphere coordination states. We gave Li_3Bi, *bcc*-AB_6, and AlB_2 BNSLs average coordination numbers of 5, 6.9, and 8, respectively.

6.4.2. Many-body effects: evidence for corona deformation in binary superlattices

We then calculated a normalized separation by dividing the experimental surface-to-surface separation by the separation expected for extended arrays of single-component close-packed NCs (the OPM prediction). This analysis revealed that the NC corona, while nearly spherical when particles are embedded in extended close-packed arrays, can be significantly deformed for particles packed in low-coordination sites. For example, BNSLs supported by A-sphere framework ($MgZn_2$, CuAu, AT, DDQC) feature PbS or Fe_2O_3 NCs in sites with fewer nearest neighbors (just 4 to 7) than the 12-coordinated *fcc*/*hcp* arrangement. BNSL measurements suggest these NCs are able to pack more closely together in binary structures, with surface separations ~65-80% that of the same particles packed in monodisperse arrays (Figure 6a, left three data points). BNSLs supported by contacting B-spheres ($CaCu_5$, $NaZn_{13}$) incorporate Au NCs with fewer nearest neighbors than *fcc/hcp* arrangement (~7-8 versus 12), and these particles also appear to be compressed slightly as compared with monodisperse close-packing predictions (Figure 6.6a, right three data points). BNSLs with A-B contacts (Li_3Bi, *bcc*-AB_6, AlB_2) show the same structure densification resulting from compression of particles with low coordination number (Figure 6.6b). Most notably, the Li_3Bi BNSL, incorporating soft Au-C_{18} NCs packed into the tetrahedral voids between hard Fe_2O_3-C_9 NCs, appears to squeeze the soft particle corona such that surface separation between the two is less than half that predicted based on OPM predictions and monodisperse array measurements. Analysis of statistical significance of this measurement allowed us to reject the null hypothesis with 96% confidence (Section 6.9.1).

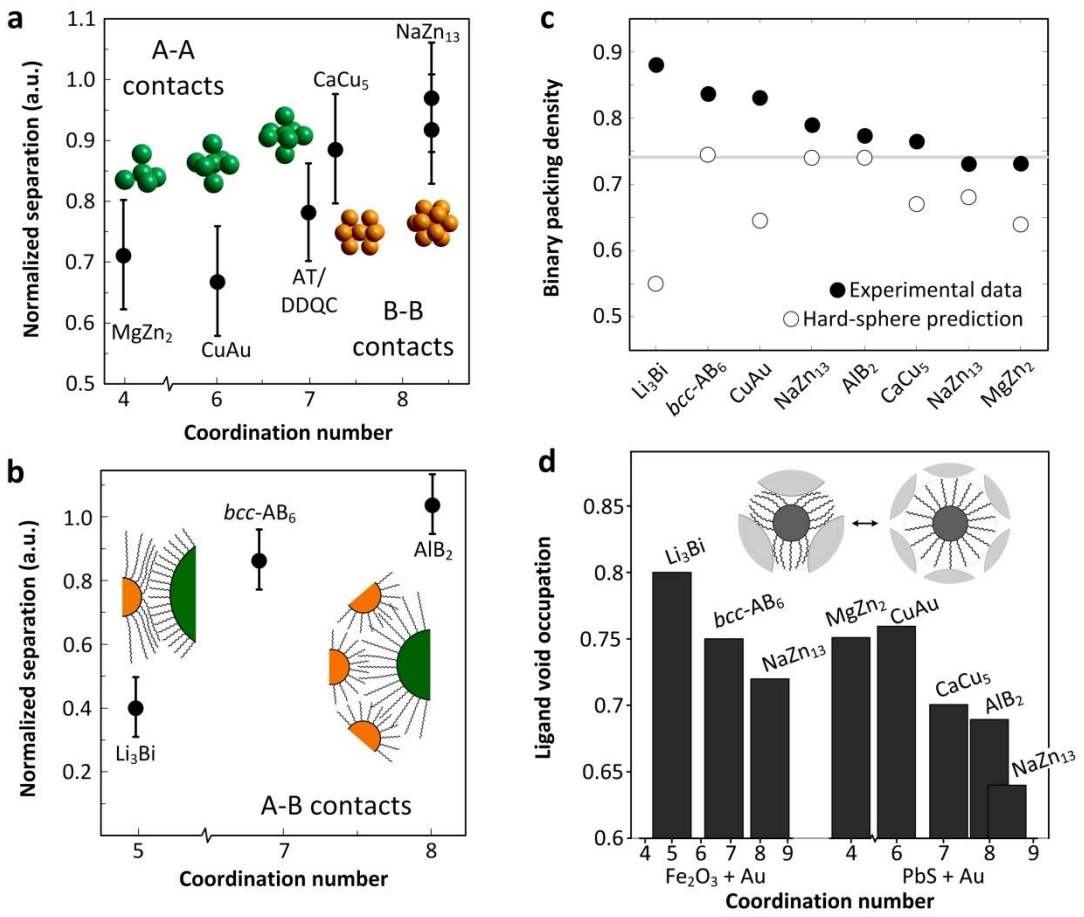

Figure 6.6. Estimation of experimental interparticle separation, packing density, and ligand void filling in BNSLs. (a) Measurement of NC surface separation in BNSLs with A-A or B-B contacts plotted against coordination number. Each BNSL contact separation is normalized with respect to separation measured for close-packed monodisperse arrays of the same NCs. Error bars represent full width at half maximum of surface separation distribution. Inset, illustration of jamming contact geometry for each BNSL structure. (b) Measurement of NC surface separation in BNSLs with A-B contacts versus BNSL coordination number. Inset, illustration of proposed collapse of diffuse corona at contact with dense corona for Li_3Bi (left) and spherical symmetry of corona engaged in crowded contacts (right). (c) Experimental density (filled circles) and density predictions based on hard sphere models (open circles) for observed BNSL structures. Grey line marks density of monodisperse close-packed spheres. (d) Experimental estimation of ligand void occupation for BNSLs ordered by average coordination number. Inset: sketch of low-coordination NC with deformed ligand corona and high-coordination NC with spherical effective shape.

6.5. Packing rules for hydrocarbon-capped, spherical nanocrystals

Variable effective particle size resulting from deformability of the hydrocarbon capping layer brings up an unanticipated connection between NCs and metal ions whose radii similarly depend on coordination environment. The Na^+ ion serves as a textbook example: its ionic radius is defined as 0.99, 1.02, 1.18 and 1.39Å for structures with coordination number of 4, 6, 8 and 12, respectively.[35] We extend this analogy between ionic compounds and NC solids by proposing a set of principles for predicting the relative stability of BNSL structures in the style of the Pauling rules[36] for simple salts. These rules expand upon the concepts of sphere packing[6] and complement a different set of rules[37] devised for the unique case where particles feature strong attraction of complementary DNA ligands during assembly.

6.5.1. Rule one: hydrocarbon ligands impart softness

In addition to effective size, a hydrocarbon-capped NC has "softness" (L/R) that determines its ability to adopt the shape of a particular coordination environment. The fraction of total particle volume contributed by ligands can be approximated (Section 6.8.1) as

$$V_{lig} \div \left(V_{lig} + V_{core}\right) \approx (L/R) \div (L/R + 1/3)$$

Accordingly, for core-ligand combinations $L/R \gtrsim 0.33$, hydrocarbons represent most of the NC footprint in space. Self-assembly of NCs with minimal softness generally follows the rules of sphere packing. On the other hand, for sufficiently soft NCs, the tendency for ligands to be redistributed away from contacts during colloidal crystallization should be taken into account.

6.5.2. Rule two: soft nanocrystals can deform in response to environment

In a low-coordination site, a soft NC fills space more efficiently than a hard NC because it may adjust its shape to the available space as determined by local coordination geometry. Perturbation of spherical corona symmetry via deformation of capping layer always acts to densify the structure by allowing a particle to adopt an effective shape that resembles the Voronoi cell of the lattice site. This geometric distortion changes poorly-packing units (for packing in three dimensions, spheres are the least-efficient convex solid known[38]) into a softened version of perfectly-packing Voronoi polyhedra.

6.5.3. Rule three: softness stabilizes cocrystallization

Although not stated in the original work, it can be easily shown[32] that the OPM interparticle separation results in the packing density of close-packed (*fcc*) spheres $\pi/3\sqrt{2} \approx 0.74$ for all *L*/*R* values. The agreement between our measurements of extended arrays of close-packed monodisperse NCs and the OPM result (Figure 6.2f) leads us to the satisfyingly simple conclusion that hydrocarbon-capped spheres, like their hard-sphere counterparts, close pack at 74% density for all values of softness.

We also estimated an experimental packing fraction for the observed binary structures and compared it to the predictions made by rigid sphere packings (Figure 6.6c). We found some BNSLs are in fact much denser than sphere-packing models predict, with estimated space-filling fractions $0.73 < \rho < 0.88$, indicating that cocrystallization does not lead to anomalously open arrangements. As such, while hard and soft particles only fill 74% of space as separately close-packed arrangements of spheres, they can mix together into a dense, low-coordination binary structure that uses deformable spheres to "glue" together the rigid ones. Indeed, simulations of soft repulsive disc mixtures[39] reveal formation of low-coordination binary phases when repulsion

between dissimilar discs is lower than between identical discs (e.g., when a soft NC corona is "dented" upon collision with a hard NC, see sketch in Figure 6.6b, left inset).

Structure densification resulting from deformability of soft particle surfaces offers important insight into thermodynamics of BNSL formation. If BNSL self-assembly is driven by free-volume entropy, two NC species should not mix unless it increases their density. Our observation that cocrystallization does not produce anomalously low-density BNSLs indicates no complex set of distance-dependent energetic interactions need be invoked to explain the formation of BNSLs, though we do not suggest they cannot play some part in the free energy of BNSL formation. Some binary phases, however, appear to contain slightly more open space than close-packed monodisperse spheres (Figure 6.6c, $NaZn_{13}$, $MgZn_2$). This allows for the possibility that second-order effects may play a role in favoring mixing of two NC components. Indeed, for binary hard-sphere mixtures, simulations[5] and experiments[40] suggest that the configurational entropy gain associated with formation of $NaZn_{13}$ arrangement is sufficient to stabilize the structure against phase separation for densities as low as ~0.69 within size ratio range $0.52 < \gamma < 0.60$. With the additional degrees of freedom offered by reduced spatial ordering of binary crystals as compared to phase-separated arrangements, configurational entropy should be sufficient to stabilize the observed BNSLs with estimated density ~0.73.

6.5.4. Rule four: soft particles prefer low-coordination sites

In stark contrast to ionic solids, soft NC packings prefer low-coordination arrangements, as this geometry allows for densest packing of ligands between cores. We used the measured BNSL dimensions to estimate space-filling efficiency of ligands between NC cores and found densest packing of hydrocarbons in low-coordination structures (Figure 6.6d). This observation can be applied to rationalize the relative stability of plausible BNSL candidate structures at a

particular effective size ratio. For example, AlB_2 at $\gamma = 0.56$ has optimal sixfold-coordinated B-spheres and the densest packing of all possible binary hard-sphere arrangements. Instead of forming AlB_2-type arrangement, NCs mixed at $\gamma_{eff} \approx 0.56$ in this work self-assembled into Li_3Bi structure with a fourfold-coordinated Au-C_{18} NCs. Similarly, NaCl at $\gamma = 0.45$ maximally coordinates the B-sphere with six nearest neighbors and is the densest binary phase for hard-sphere packings. Instead of forming NaCl, NCs mixed at $\gamma_{eff} \approx 0.45$ yielded *bcc*-AB_6, with fourfold B-sphere coordination. Once more, instead of CuAu-type BNSLs, the densest binary sphere arrangement at $\gamma = 0.76$, $MgZn_2$ and $CaCu_5$ are found. In these structures, B-spheres form a network of vertex-sharing trigonal bipyramids with fewer nearest-neighbor contacts than the optimal eightfold-coordinated B-spheres of CuAu. Dense packing of soft NCs in low-coordination lattice sites might also naturally explain the observed complexity of other soft-particle phase diagrams like the *fcc*-to-*bcc* transition for alkanethiolate-capped Au NC SLs when $L/R > 0.7$.[14]

6.5.5. Conclusion: entropy-driven crystallization of soft objects

This work characterizes the contribution of surface ligands to self-assembly of NC superlattices. We laid the conceptual foundation for describing dense arrangements of deformable spheres and used it to rationalize the complex zoo of BNSL phases as entropy-driven crystallization of soft objects. We anticipate that these findings should apply to other deformable objects (e.g., micelles, vesicles, globular proteins).

6.6. Appendix I: experimental details

Decomposition of precursors in hot organic surfactant solutions was used to prepare monodisperse Au, PbS, and Fe_2O_3 NCs.

6.6.1. Nanocrystal synthesis and ligand exchange

Au NCs were made by reduction of gold (III) chloride with *t*-butylamine-borane complex in tetrahydronaphthalene and oleylamine.[41] Au NC core diameter was varied between ~2.5 and ~5.1-nm by adjusting the injection temperature between 40°C and 2°C, respectively. PbS NCs were made by injection of bis(trimethylsilyl)sulfide into lead (II) oleate in octadecene (ODE) and oleic acid (OA) at 150°C.[42] PbS NC core diameter was adjusted between ~3.0 and ~7.0 nm by varying the OA:ODE ratio. γ-Fe_2O_3 NCs were made by oxidative decomposition of iron pentacarbonyl with trimethylamine oxide in the presence of oleic acid and dioctylether at 120°C.[12] All NCs were precipitated twice from hexane/ethanol and redispersed in hexane for storage.

Ligand exchange was carried out by stirring NCs with excess displacing ligand at 1:1 mass ratio in hexane for 2 hours at room temperature. Ligand-exchanged NCs were separated from excess unbound ligands by washing twice with hexane/ethanol and then stored in tetrachloroethylene (TCE). Octadecanethiol-capped Au and stearic acid capped PbS NCs typically precipitate partially from TCE storage solution over several days. Warming the NC solution to ~50°C for a couple minutes allows for complete redissolution of precipitated NCs. TEM and FTIR measurements corroborated exchange of native ligands (Figure 6.7).

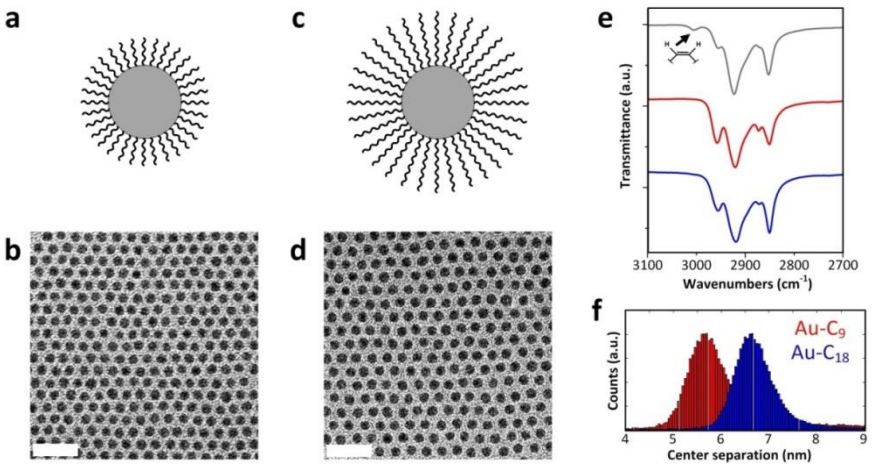

Figure 6.7. Tuning ligand shell thickness by ligand exchange. (a) sketch of spherical NC capped with short (C_9-length) hydrocarbon ligands. (b) TEM image of monolayer array of nonanethiol-capped Au NCs of core diameter 4.1 nm. (c) sketch of spherical NC capped with long (C_{18}-length) hydrocarbon ligands. (d) TEM image of monolayer array of the same Au NC cores with octadecanethiol capping ligands. Scale bars, 20 nm. (e) confirmation of completion of ligand exchange by FTIR: vinyl resonance at 3005 cm^{-1} (sketch inset) present in oleylamine-capped Au NC sample (grey trace) is absent in saturated alkanethiol-exchanged NC samples of nonanethiol and octadecanethiol (red and blue traces, respectively). (f) measurement of TEM images of Au NC monolayers reveals difference between interparticle separation of Au-C_9 (red) and Au-C_{18} (blue) NCs.

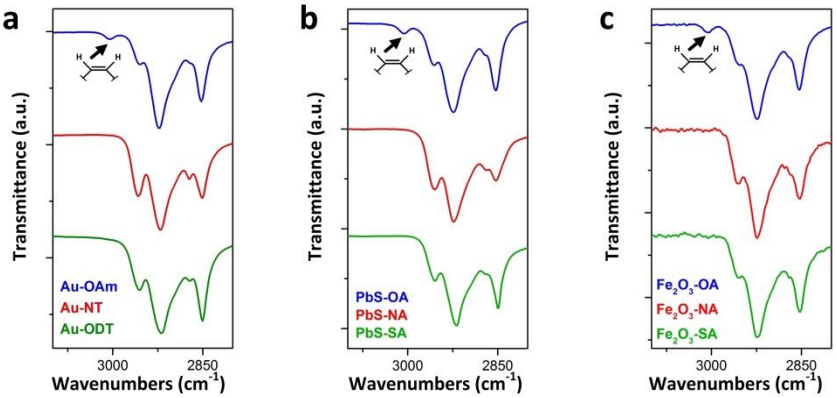

Figure 6.8. FTIR characterization of NCs used in BNSL self-assembly. FTIR confirmation of ligand exchange using disappearance of vinyl C-H stretch at ~3005 cm^{-1} for (a) Exchange of oleylamine (OAm) ligands at the surface of 4.1-nm Au NCs for nonanethiol (NT) and octadecanethiol (ODT) ligands. (b) Exchange of oleic acid (OA) ligands at the surface of 7.0-nm PbS NCs for nonanoic acid (NA) and stearic acid (SA) ligands. (c) Exchange of OA ligands at the surface of 10.2-nm Fe_2O_3 NCs for NA and SA ligands.

6.6.2. Nanocrystal self-assembly

Single-component arrays of Au, PbS, and Fe_2O_3 NCs were prepared by drop casting 10 μL NC solution in tetrachloroethylene (TCE) onto TEM carbon support resting on filter paper placed upon a hotplate set to 50°C. NC array thickness was tuned from sub-monolayer to multilayer coverage by adjusting drop cast solution concentration within the range 0.2 – 2 mg/mL. Drop casting at room temperature reduced the degree of ordering of NC arrays as compared with drop casting at 50°C. Binary nanocrystal superlattices were assembled by evaporation of a two-component NC solution at 50°C and ~0.5 atm over TEM grid tilted ~25° from horizontal.[11] Assembly solutions contained on the order of 0.1 mg of each NC component in 20 μL TCE. Variation of concentration ratio of NC components was found to influence the relative abundance of BNSL structures with different stoichiometry (e.g., AB versus AB_{13}).

Tilting experiments were used to elucidate the structure of the previously unreported Li_3Bi binary structure, which features all tetrahedral and octahedral sites of the *fcc* sublattice occupied by smaller B-particles (Figure 6.9).

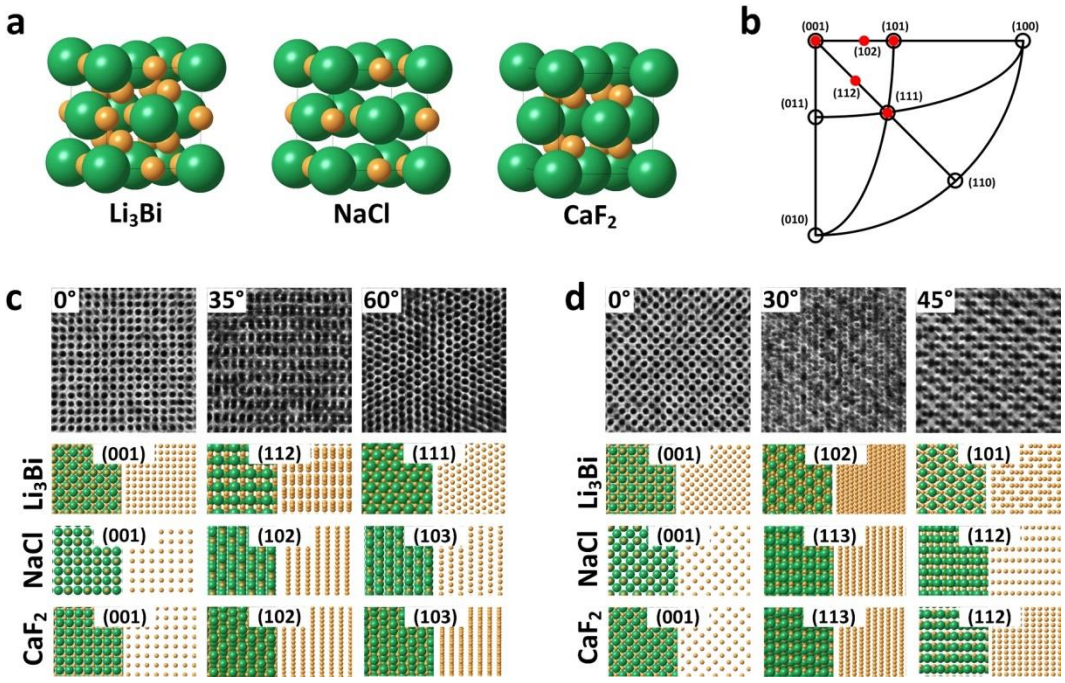

Figure 6.9. TEM tilting of Li_3Bi-type BNSL assembled from 10.2-nm Fe_2O_3-C_9 and 4.1-nm Au-C_{18}. (a) Unit cells of Li_3Bi, NaCl, and CaF_2-type sphere arrangements. Li_3Bi has B-spheres occupying both the octahedral sites, like NaCl, and the tetrahedral sites, like CaF_2. (b) Stereograph showing in red the crystallographic projections of Li_3Bi visited in TEM tilting. (c) Tilt series 1: (001) – (112) – (111). TEM images (top) and modeled projections of Li_3Bi, NaCl, and CaF_2 sphere arrangements. Left panes show both A (green) and B (gold) spheres, right pane shows only high-contrast B spheres for clarity. (d) Tilt series 2: (001) – (102) – (101).

6.6.3. Particle tracking measurement of effective nanocrystal size

Single-component and binary NC arrays were imaged on an FEI Technai F30 transmission electron microscope (TEM) operating at 300 kV accelerating voltage. Tilting experiments with dual-axis sample holder allowed for clear assignment of BNSL structure and extraction of the lattice parameter lying perpendicular to the carbon support. Extreme curvature of AT, DDQC BNSL domains prevented measurement of c-axis. Small- and wide-angle electron diffraction (SAED, WAED) patterns were collected from ~0.1 μm^2-sized BNSL areas.

TEM images of NC arrays were analyzed using MATLAB particle tracking code. Images are filtered to reduce noise and particle centers are assigned based on a weighted average of pixel intensity within a NC core. Delaunay triangulation of NC centers produces a set of bonds whose lengths were used for estimation of effective NC size. Comparison of core diameters for various coordination numbers was made by using edge detection to trace the NC core perimeter, filling the interior of the trace to create a blob, and extracting an equivalent diameter from the blob area. Batch measurement of 25 TEM images of single-component arrays allowed for analysis of a large ($10^4 – 10^5$ bond counts) data set (Figure 6.10). Statistical significance of variations in effective particle size was evaluated by assigning *p*-values to measured separations in single-component and binary arrays (Section 6.9.1).

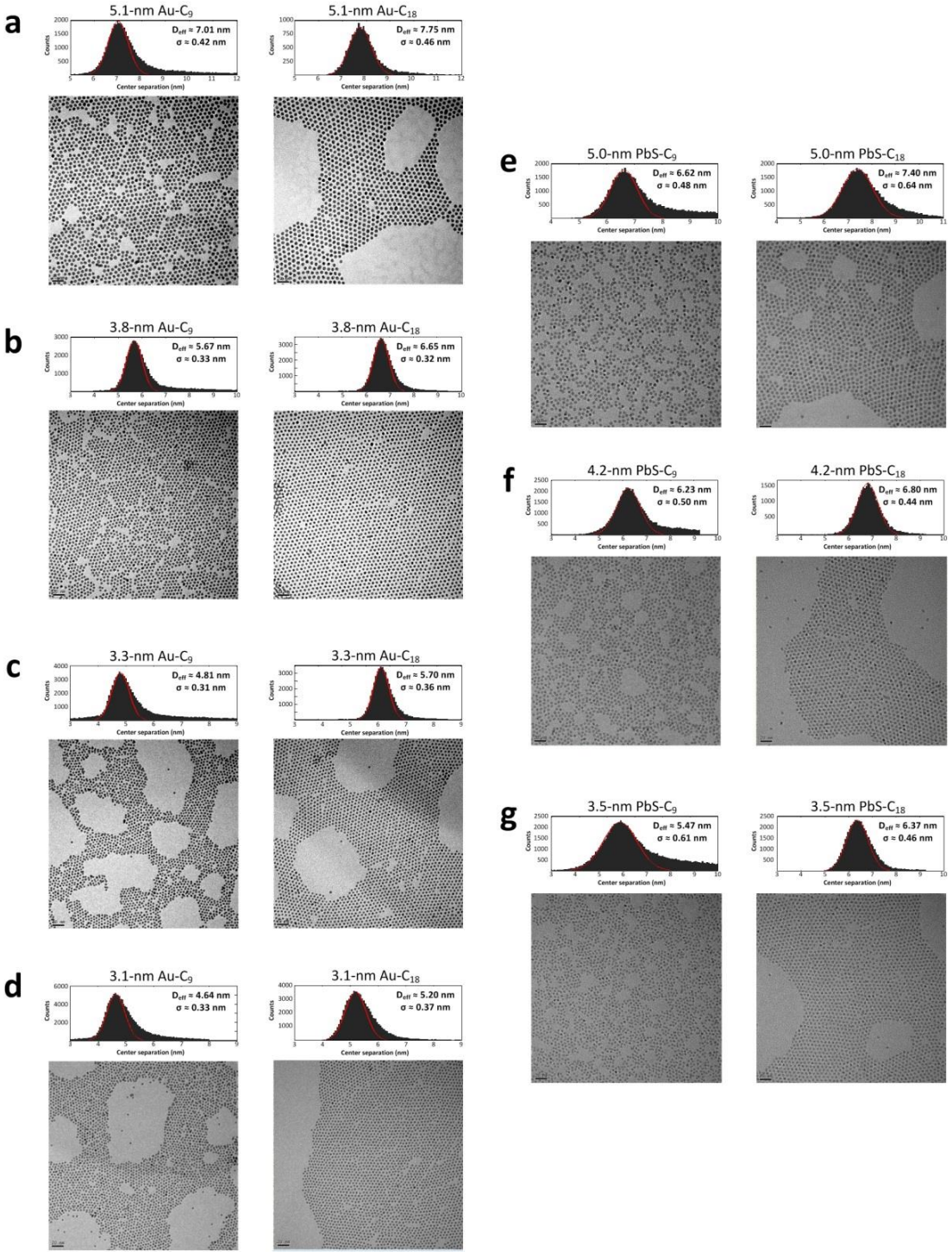

Figure 6.10. Particle tracking analysis of TEM images of monolayer arrays. Collection of experimental effective NC size for several combinations of *L*, *R*. (a-d) Bond length histograms (top) and sample TEM images (bottom) for four sizes of Au NCs with either nonanethiol (C_9) or octadecanethiol (C_{18}) capping ligands. (e-g) Bond length histograms and sample TEM images for three sizes of PbS NCs with either nonanoic acid (C_9) or stearic acid (C_{18}) capping ligands. Measured effective diameter (D_{eff}) and standard deviation are used in constructing Figure 6.2f.

Interparticle separations were also collected for *hcp* trilayers of Au-C_{18} NCs, which showed characteristic alternating darker and lighter NC cores (Figure 6.11).

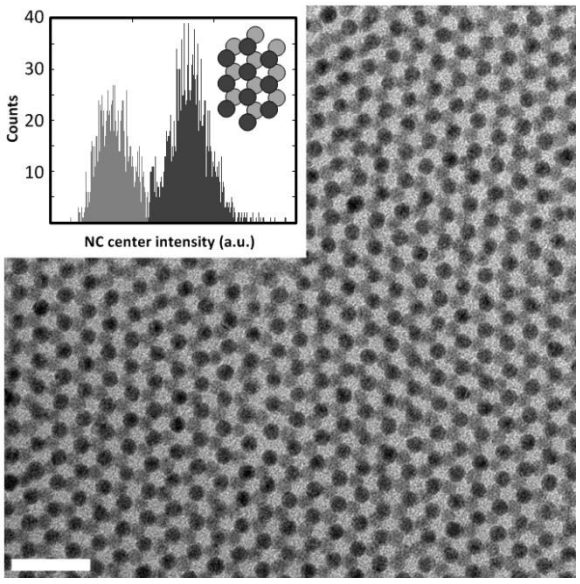

Figure 6.11. Measurement of effective NC size for Au-C_{18} NCs with twelve neighbors. Trilayer arrays are identified by alternating intensity of NC centers. Overlay of layers one and three gives rise to darker NCs; lighter NCs comprise the second layer. The distance separating light NCs is taken to be effective size of NCs with coordination number of 12. Scale bar, 20 nm. Inset: histogram of NC center intensities shows bimodal distribution with layer two contributing the left (lighter) set of counts.

6.6.4. Measurement of nanocrystal coordination numbers

Coordination number was calculated for a NC by counting the number of centroids falling within two standard deviations of the interparticle separation distribution maximum. This analysis revealed the relative numbers of undercoordinated (peripheral) NCs for arrays drop cast at sub-monolayer coverage (Figure 6.12).

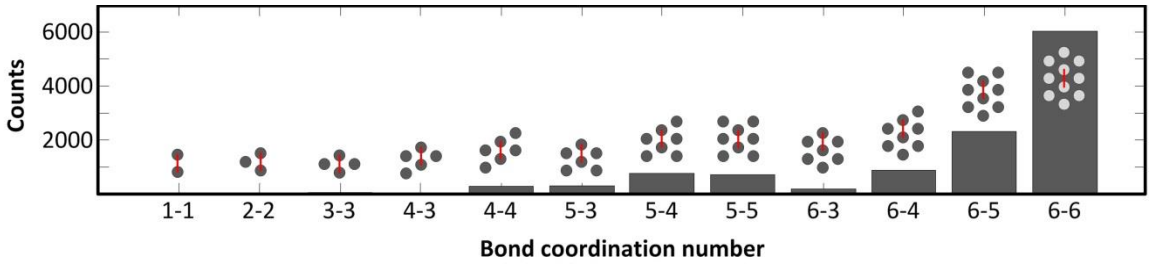

Figure 6.12. Bond coordination number frequency for 4.1-nm Au-C_{18} drop cast on carbon support at sub-monolayer coverage. Bonds containing at least one sixfold-coordinated NC endpoint comprise ~82% of bonds imaged.

Variation in effective particle size with coordination number was confirmed using three sets of NCs: 3.3-nm Au-C_{18}, 4.1-nm Au-C_{18}, and 5.1-nm Au-C_{18} NCs (Figure 6.13). The results are summarized in Figure 6.3d,e.

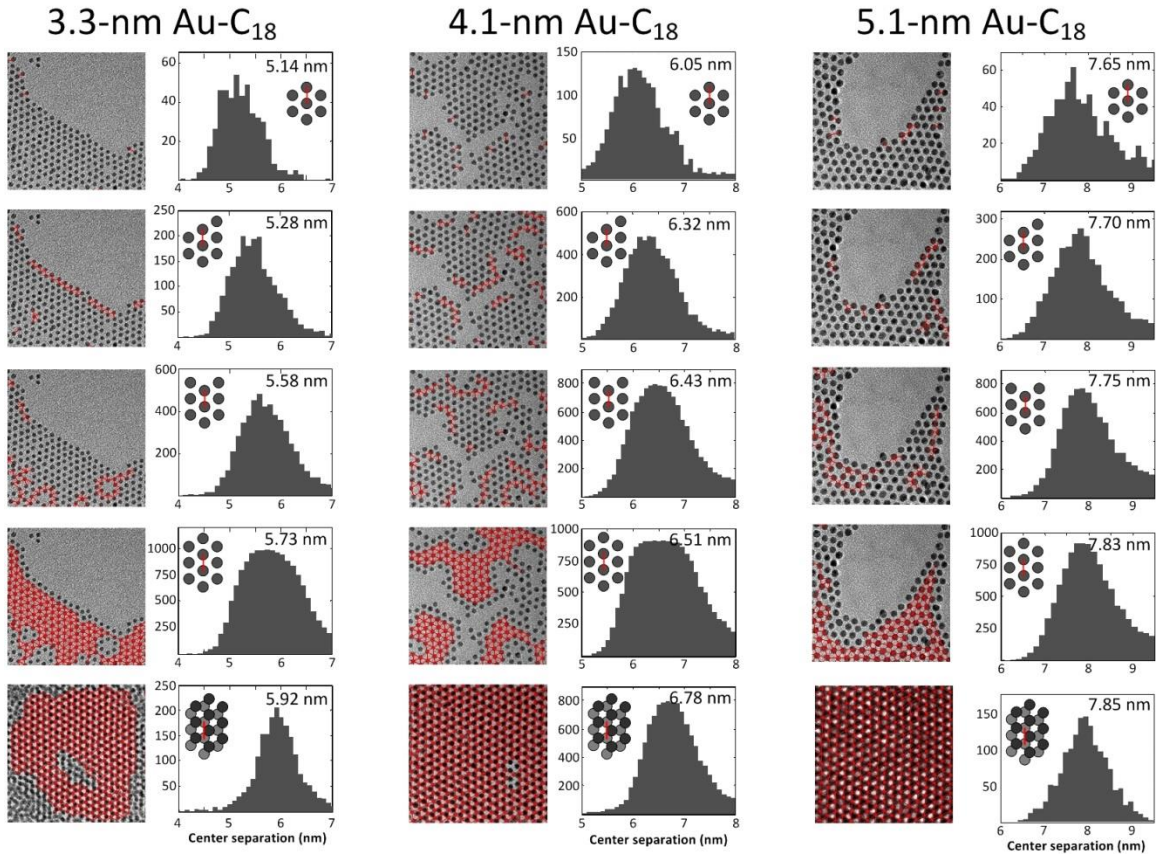

Figure 6.13. Coordination-dependent center separation measurement for three sizes of Au-C_{18}. Example areas of TEM images of octadecanethiol-capped Au NCs with superimposed 6-3, 6-4, 6-5, 6-6, 12-12 (top to bottom) bonds drawn in red. Bond length distributions for each are shown next to sample TEM images. Distribution modes are indicated in upper right of each histogram.

6.6.5. Edge detection measurement of inorganic core diameter

Edge detection (Roberts technique) was used to estimate the diameter of the inorganic core. This method likely results in slight underestimation of core size due to negligible contrast from the few atoms contributing to signal from the core perimeter. Even so, this analysis allowed us to exclude the possibility that peripheral NCs have different average core size than NCs within the interior of island arrays (size selection across the grid surface) as a primary factor contributing to coordination dependence of effective nanocrystal size (Figure 6.14).

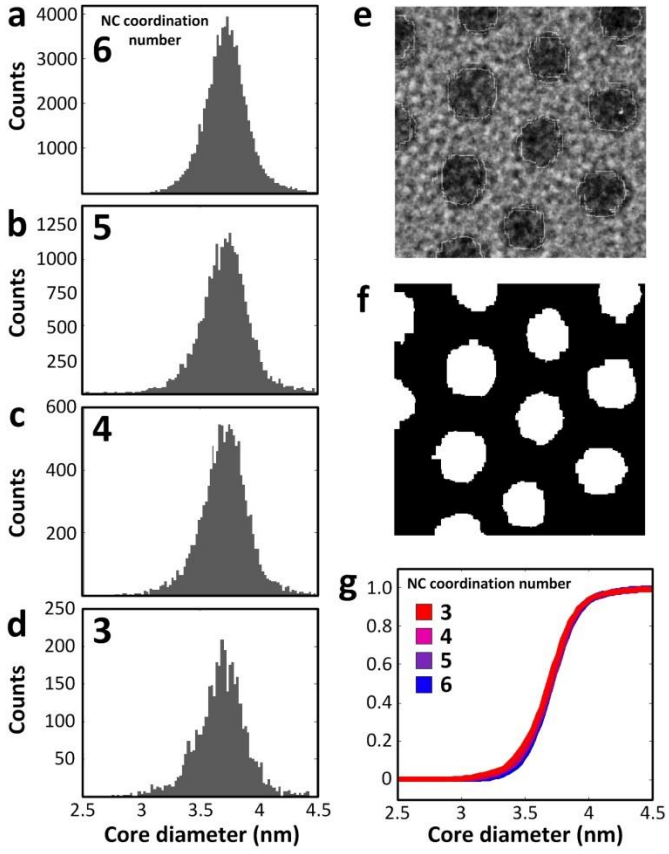

Figure 6.14. Core diameter is constant for NCs of varying coordination number. Core diameter statistics for Au-C_{18} NCs of coordination number 6 (a), 5 (b), 4 (c), 3 (d) collected from TEM images discussed in Figure 6.3. Manual measurements suggest core diameter is ~4.1 nm. (e) TEM image with superimposed edges (white lines around core periphery) reveal edge detection algorithm systematically underestimates size of Au core. (f) Area of blobs created from edges is used to calculate approximate NC core diameter. (g) integration of histograms shown in (a-d) reveal core diameter distributions nearly coincide across coordination numbers.

6.7. Appendix II: incorporating ligands in superlattice density calculations

6.7.1. Experimental space-filling fraction of close-packed nanocrystal arrays

The density of a packing is the fraction of space occupied by particles. This can be calculated experimentally by obtaining a unit cell volume from measured dimensions of the packing and comparing this with the space occupied by NC cores and ligands packed into this volume.

For example, inter-NC separation within *hcp* trilayers of 4.1-nm Au-C_{18} was measured to be D_{eff} ~6.78 nm (Figure 6.11). Using *n*-carbon ligand chain length L = 0.12 nm·(*n*+1), polyethylene cross-sectional area A_o ~ 0.2 nm^2, and TGA-estimated σ ~ 5.5 ligands/nm^2 (Figure 6.16b), the experimental *hcp* space-filling fraction is calculated as follows:

$$\rho_{hcp} = \frac{V_{NCs}}{V_{unit\ cell}^{hcp}} = \frac{V_{cores} + V_{ligands}}{\frac{3}{2}\sqrt{2} \cdot D_{eff}^3} = \frac{N_{NCs}^{hcp}\left(\frac{4}{3}\pi R^3 + 4\pi R^2 \cdot \sigma \cdot A_o \cdot L\right)}{\frac{3}{2}\sqrt{2} \cdot D_{eff}^3}$$

$$= \frac{3 \cdot \left(\frac{4}{3}\pi\left(\frac{4.1\ nm}{2}\right)^3 + 4\pi\left(\frac{4.1\ nm}{2}\right)^2 \cdot 5.5\ nm^{-2} \cdot 0.2\ nm^2 \cdot 2.28\ nm\right)}{\frac{3}{2}\sqrt{2} \cdot (6.78\ nm)^3}$$

$$\approx \frac{3 \cdot (36.1\ nm^3 + 132.4\ nm^3)}{661.1\ nm^3} \approx 0.765$$

The space-filling fraction of ligands within superlattice void space can be calculated too:

$$\rho_{ligands} = \frac{V_{ligands}}{V_{unit\ cell} - V_{cores}} = \frac{N_{NCs}^{hcp} \cdot SA_{NC} \cdot \sigma \cdot A_o \cdot L}{\frac{3}{2}\sqrt{2} \cdot D_{eff}^3 - N_{NCs}^{hcp} \cdot \frac{4}{3}\pi R_{NC}^3}$$

$$= \frac{3 \cdot 4\pi \left(\frac{3.3\ nm}{2}\right)^2 \cdot 5.5\ nm^{-2} \cdot 0.2\ nm^2 \cdot 0.12\ nm \cdot (18+1)}{\frac{3}{2}\sqrt{2} \cdot (5.92\ nm)^3 - 3 \cdot \frac{4}{3}\pi \left(\frac{3.3\ nm}{2}\right)^3} \approx 0.671$$

6.7.2. Theoretical (OPM) space-filling fraction of close-packed nanocrystal arrays

The center separation prediction made by the optimal packing model (OPM) provides unit cell dimensions for a NC of any values of *L* and *R*. With this information, we can calculate a theoretical space-filling efficiency for close-packed soft spheres:

$$\rho_{ss} = \frac{N_{NCs}^{hcp} \cdot V_{NC}}{V_{unit\ cell}^{hcp}} = \frac{3 \cdot \left(V_{core} + V_{ligands}\right)}{\frac{3}{2}\sqrt{2} \cdot 8R_{eff}^3}$$

Plugging the OPM solution

$$R_{eff}^{OPM}(L,R) = R\left(1 + 3 \cdot \sigma A_o \cdot \frac{L}{R}\right)^{1/3}$$

into the expression for soft-sphere packing efficiency ρ_{ss} yields

$$\rho_{ss}^{OPM}(L,R) = \frac{3 \cdot \left(\frac{4}{3}\pi R^3 + 4\pi R^2 \cdot \sigma A_o \cdot L\right)}{\frac{3}{2}\sqrt{2} \cdot 8 \cdot \left\{R\left(1 + 3 \cdot \sigma A_o \cdot \frac{L}{R}\right)^{1/3}\right\}^3}$$

which reduces to the hard-sphere packing density limit independent of *L* and *R*.

$$\rho_{ss}^{OPM}(L,R) = \frac{\pi}{3\sqrt{2}} \approx 0.7405$$

6.7.3. Theoretical (OPM) efficiency of hydrocarbon packing within interparticle matrix

The OPM prediction also naturally lends itself to calculating space-filling efficiency of ligands in superlattice void space:

$$\rho_{ligands} = \frac{N_{NCs}^{hcp} \cdot V_{ligands}}{V_{unit\ cell}^{hcp} - N_{NCs}^{hcp} \cdot V_{core}} = \frac{3 \cdot 4\pi R^2 \cdot \sigma A_o \cdot L}{\frac{3}{2}\sqrt{2} \cdot 8R_{eff}^3 - 3 \cdot \frac{4}{3}\pi R^3}$$

$$= \frac{3 \cdot 4\pi R^2 \cdot \sigma A_o \cdot L}{\frac{3}{2}\sqrt{2} \cdot 8 \cdot \left\{R\left(1 + 3 \cdot \rho A_o \cdot \frac{L}{R}\right)^{1/3}\right\}^3 - 3 \cdot \frac{4}{3}\pi R^3}$$

$$= \frac{\frac{\pi}{3\sqrt{2}} \cdot 3 \cdot \sigma A_o \cdot \frac{L}{R}}{1 - \frac{\pi}{3\sqrt{2}} + 3 \cdot \sigma A_o \cdot \frac{L}{R}}$$

This curve approaches $\frac{\pi}{3\sqrt{2}}$ in the limit of large *L*/*R*.

6.7.4. Superlattice density depends on ligand packing assumptions

We can also examine how our choice of ligand packing efficiency influences the density of close-packed arrangements of soft spheres. For this we add a term λ to the optimal packing model (OPM) expression to represent the extent to which hydrocarbons can pack densely between NC surfaces:

$$\frac{R_{eff}}{R} = \left(1 + 3 \cdot \lambda \cdot \sigma A_o \cdot \frac{L}{R}\right)^{1/3}$$

Increasing the value of λ increases the separation between sphere surfaces for a given choice of *L* and *R*, creating a "sub-optimal" packing case. Similarly, decreasing λ reduces separation and allows for "super-optimal" ligand packing. For λ = 1, the OPM solution is recovered (Figure 6.15).

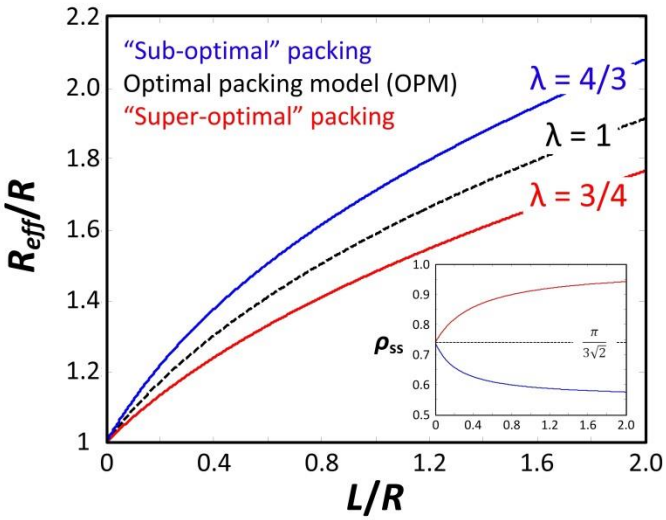

Figure 6.15. Influence of ligand packing efficiency on density of close-packed arrangements of soft spheres. Effective size versus softness plotted for three choices of ligand packing efficiency parameter, λ. Inset: plot of density versus softness for the same three values of λ. .

Incorporating this term λ into the soft-sphere packing density expression yields

$$\rho_{ss}^{OPM}(L,R) = \frac{3 \cdot \left(\frac{4}{3}\pi R^3 + 4\pi R^2 \cdot \sigma A_o \cdot L\right)}{\frac{3}{2}\sqrt{2} \cdot 8 \cdot \left\{R\left(1 + 3 \cdot \lambda \cdot \sigma A_o \cdot \frac{L}{R}\right)^{\frac{1}{3}}\right\}^3} = \frac{\pi}{3\sqrt{2}} \cdot \frac{1 + 3\frac{L}{R}}{1 + 3\lambda \cdot \frac{L}{R}}$$

With this we calculate the softness dependence of packing efficiency for each of these three cases ($\lambda < 1$, $\lambda = 1$, $\lambda > 1$), finding that with increasing L/R, the assumed ligand packing efficiency parameter λ may significantly alter the overall soft-sphere packing density ρ_{ss} (Figure 6.15, inset).

6.7.5. Experimental space-filling fraction of binary nanocrystal arrays

The Au, PbS, and Fe_2O_3 NCs used in binary assembly experiments were characterized by a suite of techniques (Figure 6.16). Particle tracking measurements of hexagonal monolayers provided effective NC sizes to assign size ratio for space-filling curves (Figure 6.5c,f). Thermogravimetric analysis (TGA) enabled estimation of ligand grafting density to calculate experimental space-filling fractions of single-component and binary arrays.

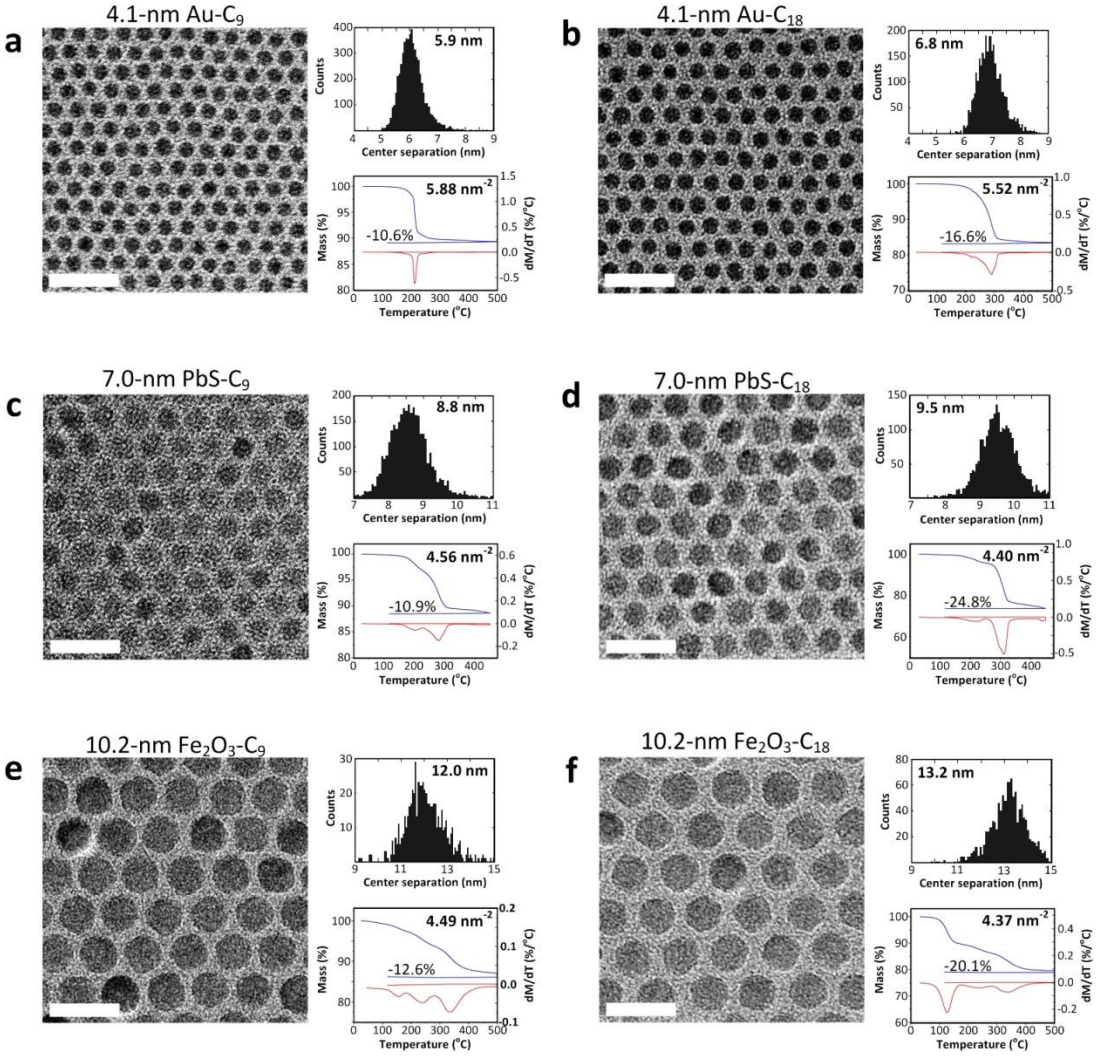

Figure 6.16. TEM and TGA characterization of NCs used in BNSL self-assembly. Sample TEM area (left), effective diameter measurement (upper right), and TGA mass loss data with estimated ligand grafting density (lower right) for (a) 4.1-nm Au-C_9, (b) 4.1-nm Au-C_{18}, (c) 7.0-nm PbS-C_9, (d) 7.0-nm PbS-C_{18}, (e) 10.2-nm Fe_2O_3-C_9, (f) 10.2-nm Fe_2O_3-C_{18}.

TEM images of several projections of the BNSLs shown in Figure 6.1a-d were subjected to particle tracking analysis, enabling estimation of experimental BNSL lattice parameters (Figure 6.17, Figure 6.18).

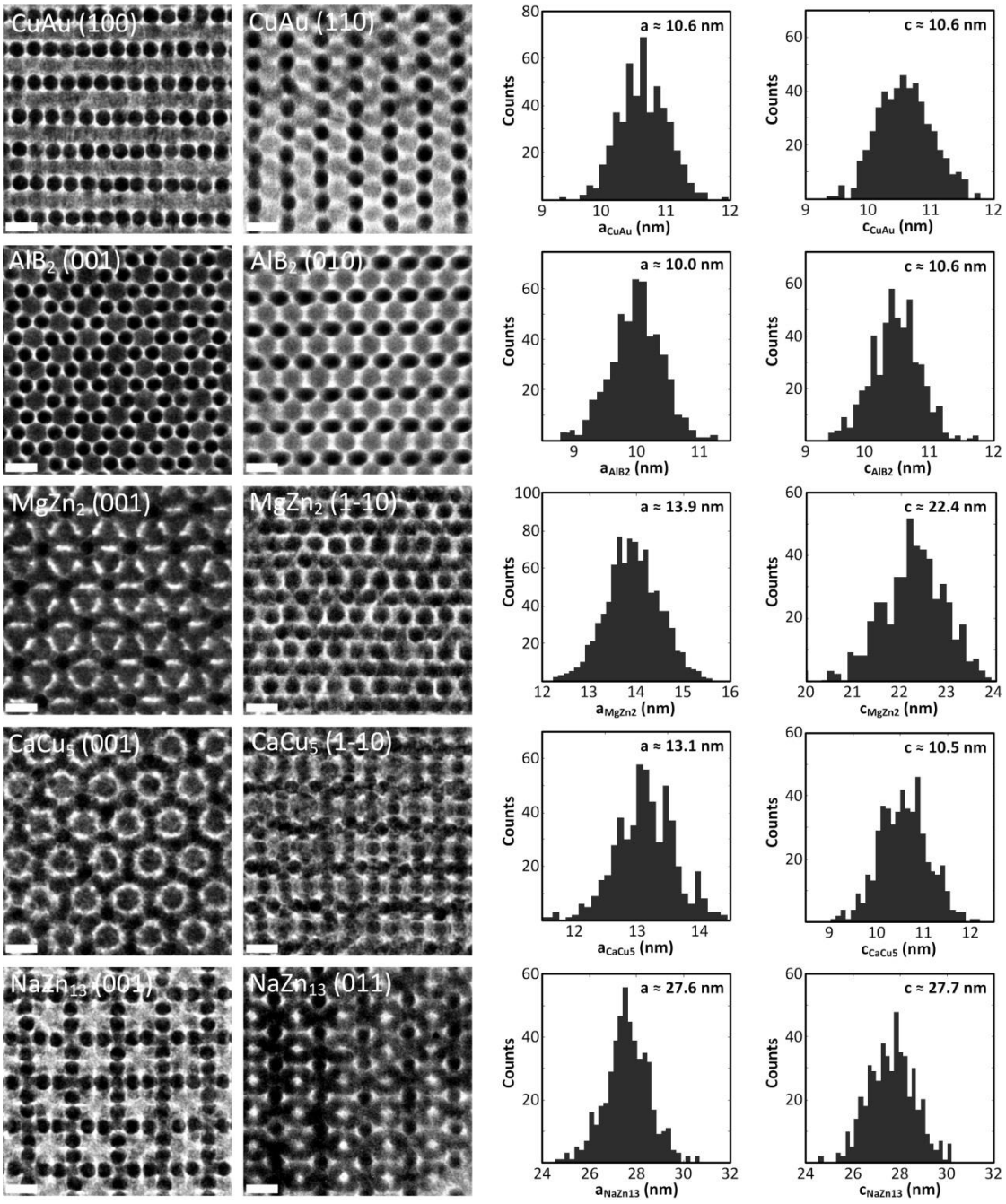

Figure 6.17. Measurement of experimental unit cell size for BNSLs containing PbS and Au NCs. Sample TEM areas (left) and extracted lattice parameters (right). Scale bars, 10 nm.

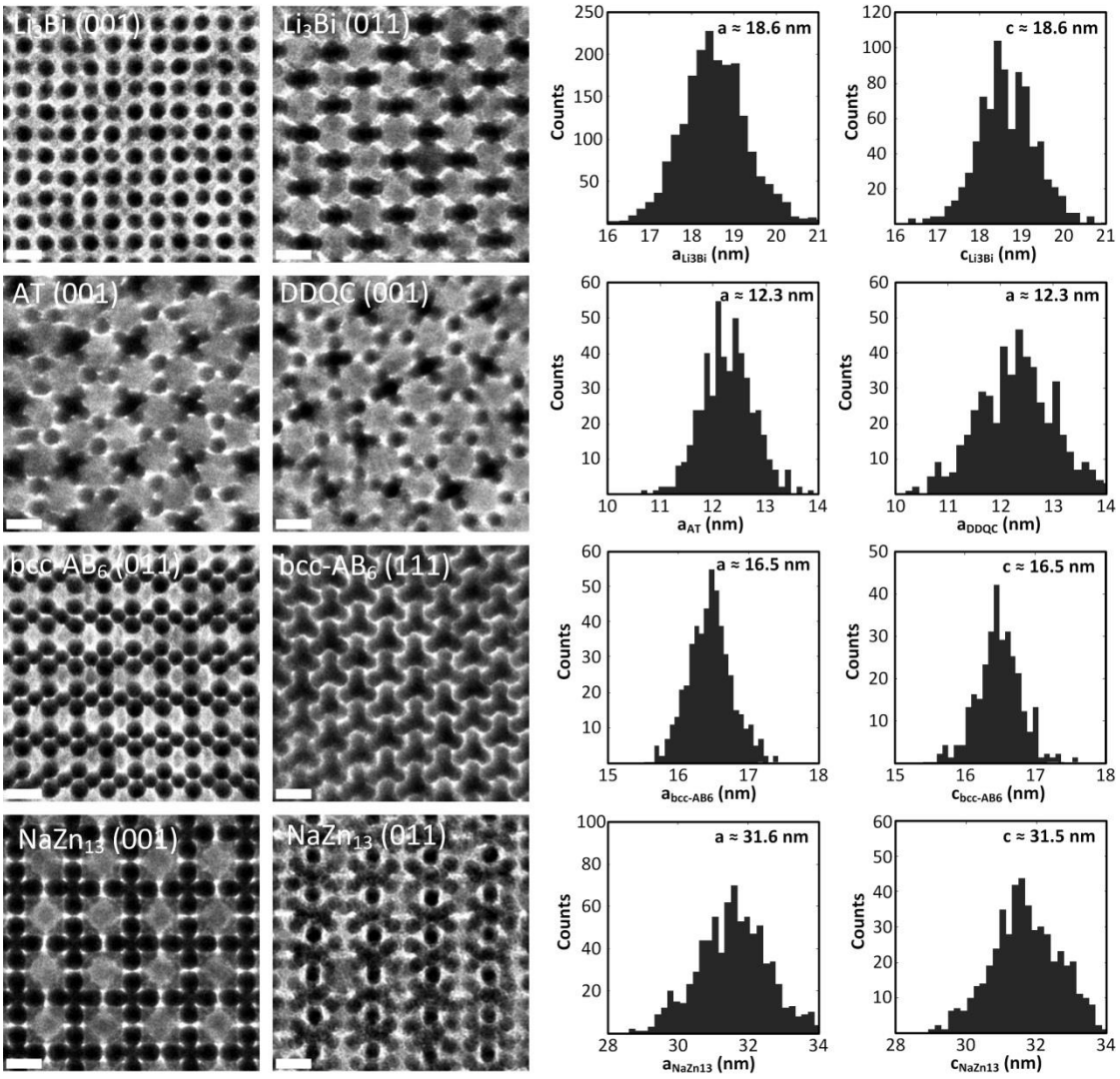

Figure 6.18. Measurement of experimental unit cell size for BNSLs containing Fe_2O_3 and Au NCs. Sample TEM areas (left) and extracted lattice parameters (right). Scale bars, 10 nm.

The results of these measurements are recorded in Tables 6.1 and 6.2.

Table 6.1. Extracted interparticle separations for BNSLs with A-A or B-B contacts.

Structure	Component A	Component B	Size ratio	Contacts	Coordination	Comparison of surface separations		
						d_{SCSL} (nm)	d_{BNSL} (nm)	d_{BNSL} / d_{SCSL}
CuAu	PbS-C_{18}	Au-C_9	0.62	A-A	A: 6A	2.50	1.67	0.67
$MgZn_2$	PbS-C_9	Au-C_{18}	0.76	A-A	A : 4A	1.80	1.30	0.72
AT/DDQC	Fe_2O_3-C_{18}	Au-C_9	0.45	A-A	A: 7A	2.80	2.16	0.77
$CaCu_5$	PbS-C_9	Au-C_{18}	0.76	B-B	B_1: 8B B_2: 6B	2.70	2.40	0.89
$NaZn_{13}$	PbS-C_{18}	Au-C_9	0.56	B-B	B_1: 12B B_2: 8B	1.80	1.75	0.97
$NaZn_{13}$	Fe_2O_3-C_9	Au-C_{18}	0.62	B-B	B_1: 12B B_2: 8B	2.70	2.48	0.92

Table 6.2. Extracted interparticle separations for BNSLs with A-B contacts.

Structure	Component A	Component B	Size ratio	Contacts	Coordination	Comparison of interparticle separations		
						$(d_{A,SCSL} + d_{B,SCSL})/2$ (nm)	$d_{A\text{-}B,BNSL}$ (nm)	d_{BNSL} / d_{SCSL}
AlB_2	PbS-C_{18}	Au-C_9	0.62	A-B	A: 12B B: 6A	2.15	2.29	1.06
Li_3Bi	Fe_2O_3-C_9	Au-C_{18}	0.56	A-B	A: 8B B_1: 4A B_2: 6A	2.25	0.90	0.40
bcc-AB_6	Fe_2O_3-C_{18}	Au-C_9	0.45	A-B	A: 24B B: 4A	2.30	1.96	0.85

Geometric considerations (Figure 6.19) allowed estimation of interparticle separations of contacting NCs in binary arrays. These values can be quite different from those obtained using sphere packing treatment of BNSLs with effective radii measured from hexagonal monolayer arrays, as was routinely done in previous BNSL structure analyses.[16,43]

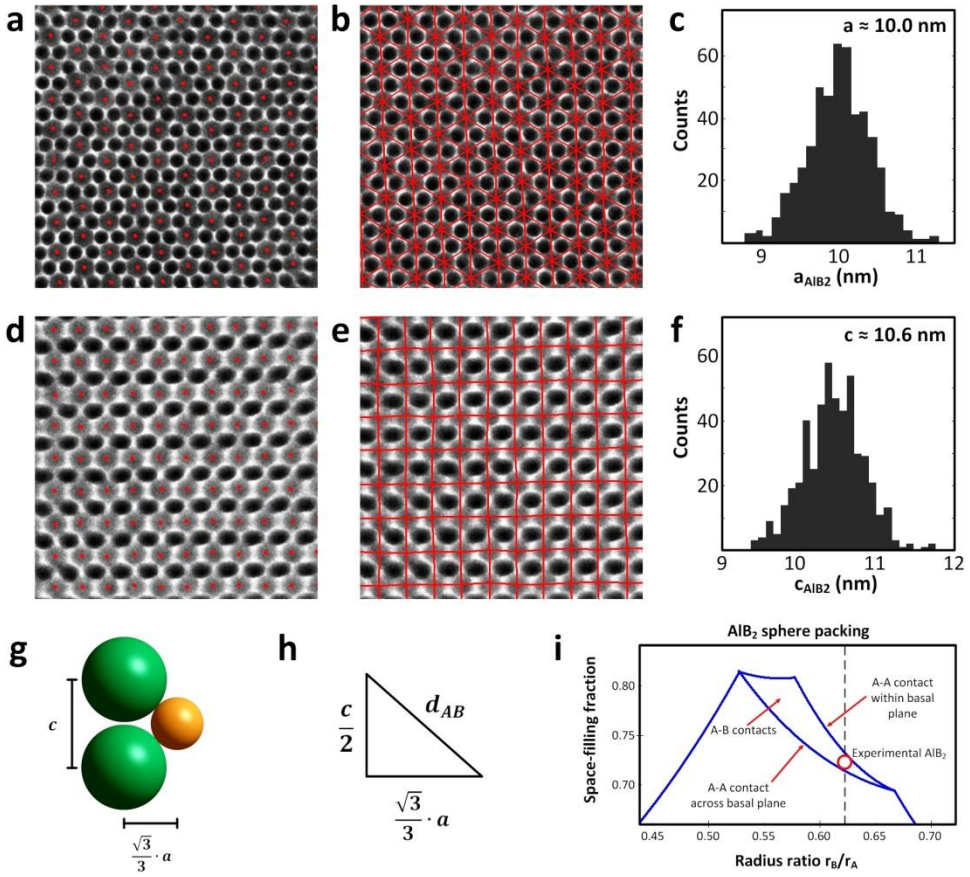

Figure 6.19. Geometric extraction of effective sizes of NCs packed in binary arrays demonstrated for the AlB_2-type BNSL.

Extraction of inter-NC separation within BNSLs is demonstrated here using the example of AlB_2-type structure formed from 4.1-nm Au-C_9 and 7.0-nm PbS-C_{18}. Measured separations in monolayer arrays are: $d_{eff,Au\text{-}C9} \approx 5.9$ nm and $d_{eff,PbSC18} \approx 9.5$ nm (Figure 6.16a,d). Measured separation between PbS-C_{18} NCs in basal plane of AlB_2-type BNSL is 10.0 nm (Figure 6.19a-c), suggesting loose overlap of A-sphere coronas. Measurement of (010)-projection of AlB_2 shows 10.6-nm separation between PbS-C_{18} NCs along the c-axis (Figure 6.19d-f), suggesting loose A-A overlap across basal plane. A-B contacts are thus jamming contacts supporting BNSL structure. Extraction of interparticle separation between 4.1-nm Au-C_9 and 7.0-nm PbS-C_{18} is possible using measured lattice dimensions *a* and *c* (Figure 6.19g-i):

$$d_{AB} = \left\{\left(\frac{1}{2}c\right)^2 + \left(\frac{\sqrt{3}}{3}a\right)^2\right\}^{\frac{1}{2}} - (r_A + r_B)$$

$$= \left\{\left(\frac{1}{2}\cdot 10.6\ nm\right)^2 + \left(\frac{\sqrt{3}}{3}\cdot 10.0\ nm\right)^2\right\}^{\frac{1}{2}} - (3.5\ nm + 2.05\ nm)$$

$$\approx 2.29\ nm$$

Experimental BNSL packing density ρ_{BNSL} was calculated using measured dimensions of BNSL unit cell (Figure 6.17, Figure 6.18) and measured core radius and ligand grafting density (Figure 6.16).

$$\rho_{BNSL} = \frac{V_{cores}}{V_{unit\ cell}} + \frac{V_{ligands}}{V_{unit\ cell}}$$

$$V_{cores} = n_A \cdot \frac{4}{3}\pi R_A^3 + n_B \cdot \frac{4}{3}\pi R_B^3$$

$$V_{ligands} = n_A \cdot SA_{NC,A} \cdot \sigma_A \cdot A_o \cdot L_A + n_B \cdot SA_{NC,B} \cdot \sigma_A \cdot A_o \cdot L_B$$

$$V_{unit\ cell} = \frac{\sqrt{3}}{2} \cdot a^2 \cdot c$$

Where n_A, n_B is number of A, B spheres per unit cell; *a*, *b*, *c* are BNSL lattice parameters measured from TEM images. Estimation BNSL density is demonstrated for AlB_2-type structure formed from 4.1-nm Au-C_9 and 7.0-nm PbS-C_{18}.

$$\frac{V_{cores}}{V_{unit\ cell}} = \frac{1 \cdot \frac{4}{3}\pi(3.5\ nm)^3 + 2 \cdot \frac{4}{3}\pi(2.05\ nm)^3}{\frac{\sqrt{3}}{2} \cdot (10.0\ nm)^2 \cdot 10.6\ nm} \approx 0.27$$

$$\frac{V_{ligands}}{V_{unit\ cell}} = 1 \cdot \left(\frac{4\pi(3.50\ nm)^2 \cdot 4.4\ nm^{-2} \cdot 0.2\ nm^2 \cdot (18+1) \cdot 0.12\ nm}{\frac{\sqrt{3}}{2} \cdot (10.0\ nm)^2 \cdot 10.6\ nm} \right)$$

$$+2 \cdot \left(\frac{4\pi(2.05\ nm)^2 \cdot 5.9\ nm^{-2} \cdot 0.2\ nm^2 \cdot (9+1) \cdot 0.12\ nm}{\frac{\sqrt{3}}{2} \cdot (10.0\ nm)^2 \cdot 10.6\ nm} \right) \approx 0.50$$

$$\rho_{AlB2} = 0.27 + 0.50 \approx 0.77$$

6.8. Appendix III: additional calculations

6.8.1. Organic volume fraction of hydrocarbon-capped nanocrystals

We calculated the fraction of total particle volume contributed by surface ligands:

$$\frac{V_{ligands}}{V_{ligands} + V_{core}} = \frac{4\pi R^2 \cdot \sigma \cdot A_o \cdot L}{4\pi R^2 \cdot \sigma \cdot A_o \cdot L + \frac{4}{3}\pi R^3}$$

Where σ is ligand grafting density, A_o is cross-sectional area of polyethylene, L is extended ligand length, and R is NC core radius. Using a simple assumption of complete ligand coverage of the sphere surface ($\sigma \cdot A_o = 1$) we obtain:

$$\frac{4\pi R^2 \cdot L}{4\pi R^2 \cdot L + \frac{4}{3}\pi R^3} = \frac{L/R}{L/R + \frac{1}{3}}$$

Here it is immediately clear that, for $L/R > 1/3$, most of the total particle volume is contributed by hydrocarbon ligands. This work explored NC packings with softness parameter spanning the range $0.24 < L/R < 1.75$, with 10.2-nm Fe_2O_3-C_9 the hardest NCs and 3.0-nm Au-C_{18} the softest. For these particles, fraction of total particle volume contributed by surface ligands is approximately 42% and 84%, respectively.

6.8.2. Average coordination number in binary nanocrystal superlattices

Coordination number plays an important role in determining the effective size and shape of soft particles packed in an ordered arrangement. Here we define coordination number using contacting NCs which set dimensions of the BNSL (e.g. A-A, B-B, or A-B contacts).

A-A contacts. For BNSLs supported by jammed contacts within the A-sphere framework, we take the coordination state of A-spheres to be the BNSL coordination number. For example,

$MgZn_2$ at $\gamma_{eff} \approx 0.76$ has A-A contacts in a diamond-type arrangement, with each A-sphere making contact with four other A-spheres in a tetrahedral arrangement. The $MgZn_2$-type BNSL is assigned coordination number 4. Similarly, CuAu at $\gamma_{eff} \approx 0.62$ has A-A contacts in an octahedral rock salt arrangement, and CuAu BNSL is assigned coordination number 6.

B-B contacts. For BNSLs supported by jammed contacts within the B-sphere framework, the existence of two types of B-spheres complicates the assignment of BNSL coordination number. In this case, we take an average of the coordination numbers of non-equivalent B_1 and B_2 spheres, weighted by the abundance of each within the BNSL. For example, $NaZn_{13}$ at $\gamma_{eff} \approx 0.62$ has B-B contacts within and across icosahedral B-sphere clusters, involving both B_1 (in center of icosahedron, with coordination number 12) and B_2 (one of twelve particles at the icosahedron vertices, with coordination number 8) spheres. The average coordination number of $NaZn_{13}$-type BNSL in B-B contact regime ($\gamma_{eff} \geq 0.56$) is calculated as:

$$CN_{NaZn13} = \frac{n_A}{n_A + n_B} \cdot CN_A + \frac{n_B}{n_A + n_B} \cdot CN_B = \frac{1}{1+12} \cdot 12 + \frac{12}{1+12} \cdot 8 \approx 8.31$$

Similarly, average coordination number of the $CaCu_5$-type BNSL is calculated using coordination number of B_1 (in basal plane of pure B-spheres, with coordination number 8) and B_2 (in basal plane of mixed A and B spheres, with coordination number 6)

$$CN_{CaCu5} = \frac{3}{2+3} \cdot 8 + \frac{2}{2+3} \cdot 6 = 7.20$$

A-B contacts. For BNSLs with A-B contacts setting lattice dimensions, the same average coordination number calculation is applied. For example, *bcc*-AB_6 at $\gamma_{eff} \approx 0.45$ has A-B

contacts, with A-spheres surrounded by 24 contacting B-spheres and B-spheres each touching four A-spheres:

$$CN_{bcc-AB6} = \frac{1}{1+6} \cdot 24 + \frac{6}{1+6} \cdot 4 \approx 6.86$$

Similarly, the AlB_2-type BNSL at $\gamma_{eff} \approx 0.62$ has A-B contacts (TEM measurement suggests no A-A contacts within or across basal planes, see Figure 6.19) setting the dimensions of the packing. In this structure, A-spheres are coordinated by 12 B-spheres, and B-spheres each have 6 A-sphere neighbors:

$$CN_{AlB2} = \frac{1}{1+2} \cdot 12 + \frac{2}{1+2} \cdot 6 = 8$$

The dimensions of the Li_3Bi-type BNSL at $\gamma_{eff} \approx 0.56$ are set by A-B_1 contacts between the *fcc* A-sphere sublattice and the B_1 spheres occupying tetrahedral sites. In this structure, A-spheres are coordinated by 8 B-spheres, and B-spheres each have 4 A-sphere neighbors:

$$CN_{Li3Bi} = \frac{1}{1+3} \cdot 8 + \frac{3}{1+3} \cdot 4 = 5$$

6.8.3. Space-filling curves for quasicrystal and Archimedean tiling binary structures

3^2.4.3.4 Archimedean tiling (AT) and dodecagonal quasicrystal (DDQC) arrangements are comprised of subcells based on AlB_2- and CaB_6-type structures. The CaB_6 component sets the dimensions of AT and DDQC BNSLs by establishing B-B contacts between octahedral B-sphere clusters across the basal plane at $\gamma \approx 0.414$ (Figure 6.20a) and between a B_6-cluster and an AlB_2 B-sphere within the basal plane at $\gamma \approx 0.462$ (Figure 6.20b). Space-filling curves were calculated for AlB_2 and CaB_6 components in AT, DDQC structures (Figure 6.20c) and a weighted sum of these produces space-filling curves for AT, DDQC structures (Figure 6.20d). The weighting prefactors correspond to volumetric abundance of CaB_6 and AlB_2 units within DDQC (equal areas of squares and triangles, or 50% of each AlB_2 and CaB_6) and AT (twice as many triangles as squares, or $2\sqrt{3} - 3 \approx 0.464$ AlB_2 and 0.536 CaB_6.

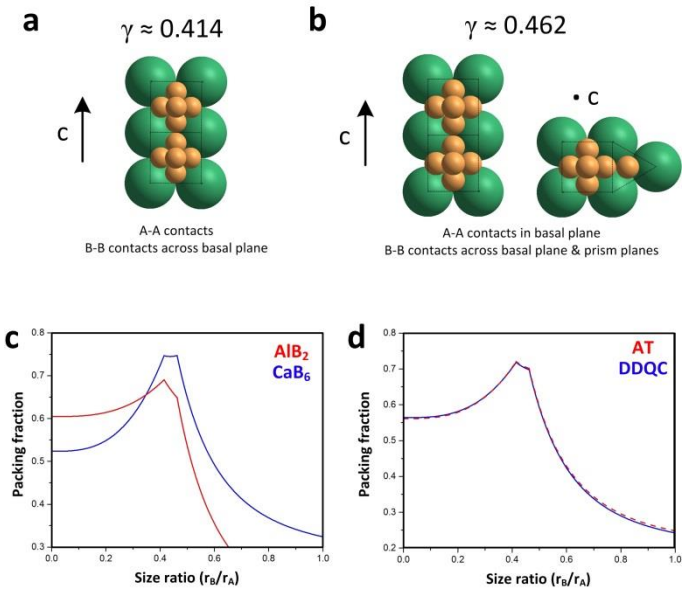

Figure 6.20. Space filling of hard spheres in AT, DDQC-type BNSLs. (a) B-B contacts are established between B-sphere clusters across the basal plane at γ ≈ 0.414. (b) B-sphere clusters of CaB_6 expand into adjacent AlB_2-type half-cells until B-B contact occurs within the basal plane at γ ≈ 0.462. (c) Space-filling curves for CaB_6 unit cell and AlB_2-type half-cell in AT, DDQC. (d) AT, DDQC space-filling curves obtained by summing AlB_2 and CaB_6 components weighted by abundance in each arrangement. .

6.9. Appendix IV: other considerations

6.9.1. Statistical significance of particle tracking measurements

We calculated the statistical significance of measured variations in effective particle size using the *p*-test. The *p*-value was defined as the probability, under the assumption that a soft particle maintains its effective size in all coordination environments, of obtaining a measurement equal to or more extreme than the one actually observed. For example, the measured center separation between 4.1-nm Au-C_{18} NCs is 6.8 nm in *hcp* superlattice (12-12 bonds) and 6.05 nm when one particle has six neighbors and the second has three (6-3 bonds) (Figure 6.13). The fraction of 12-12 counts falling to the left of the 6-3 measurement was taken to be the *p*-value, in this case 0.05, providing 95% confidence that the observed variation in effective size is meaningful (Table 6.3). *p*-values were calculated in a similar manner for extracted contact distances in BNSLs (Table 6.4). For example, the A-B contact separation between Au-C_{18} and Fe_2O_3-C_9 NCs in Li_3Bi BNSLs was measured to be 8.1 nm. Under the assumption of invariant effective size, we added the effective radii for each particle measured from hexagonal monolayers and obtained a distribution centered at 9.4 nm. The fraction of counts within this distribution that fall to the left of 8.1 nm was calculated to be 0.04, indicating with 96% confidence that the measured variation in effective size was statistically significant.

Table 6.3. Statistical significance (*p*-values) of measured deviations from hard-sphere behavior for Au-C_{18} NCs in various coordination environments.

NC core / ligand	*P*-value for bond measurement			
	6-6	6-5	6-4	6-3
3.3-nm Au-C_{18}	0.18	0.14	0.09	0.04
4.1-nm Au-C_{18}	0.13	0.11	0.08	0.05
5.1-nm Au-C_{18}	0.30	0.24	0.23	0.19

Table 6.4. Statistical significance (*p*-values) of measured deviations from hard-sphere behavior for contacting NCs in BNSLs.

BNSL	*P*-value
CuAu	0.16
$MgZn_2$	0.25
AT	0.11
DDQC	0.11
$CaCu_5$	0.14
$NaZn_{13}$*	0.34
$NaZn_{13}$**	0.32
AlB_2	0.42
Li_3Bi	0.04
bcc-AB_6	0.16

*PbS & Au, **Fe_2O_3 & Au

6.9.2. Bending of ligand chains away from contacts

The position of nanocrystals and spatial distribution of ligands within a superlattice is established in the late stages of solvent evaporation when NCs are forced into contact with one another. At the moment of self-assembly, when enough solvent remains to allow for translation and rotation of individual particles, osmotic and elastic contributions to NC pair potential oppose the densification of ligands accompanying corona overlap. Osmotic pressure arises at the contact due to unfavorable exclusion of solvent molecules from the overlap region and an elastic penalty arises from perturbation of the chain backbone conformation associated with interdigitation and densification of ligand chains.

Grafting surface curvature imparts a non-uniform segment concentration within the lens-shaped overlap volume: chain density (and chemical potential of segments) is highest in the center of this region, along the contact axis (see Figure 6.4a of main text). The geometry-imposed density gradient within the overlap region suggests that diffusion of segments away from the contact should be spontaneous, provided that peripheral open space is available to receive bending ligands. In this way, the structure of surface ligands for a particle embedded in a NC solid depends on the particle's surroundings: chains may bend away from contacts if there is sufficient open space (low coordination) but are prevented from doing so if the NC is uniformly surrounded by many segments (high coordination). Measurements of interparticle separations in single-component and binary arrays reveal that effective NC size increases with coordination number, consistent with the chain bending argument proposed here.

6.9.3. Non-Gaussian shape of Au-C_{18} 6-6 distribution.

The platykurtic (flat) distribution of bond lengths connecting two NCs within island interior required additional attention. It may be a convolution of two Gaussian distributions arising from two populations of Au NCs with different core sizes, each phase-separated on the grid. We tested this hypothesis by separating the distribution into two halves (Figure 6.21a) and plotting spatial location of long and short bonds from a sample TEM image of Au-C_{18} NCs (Figure 6.21b). We see no evidence for phase separation, however, as long and short 6-6 bonds appear to be intermixed.

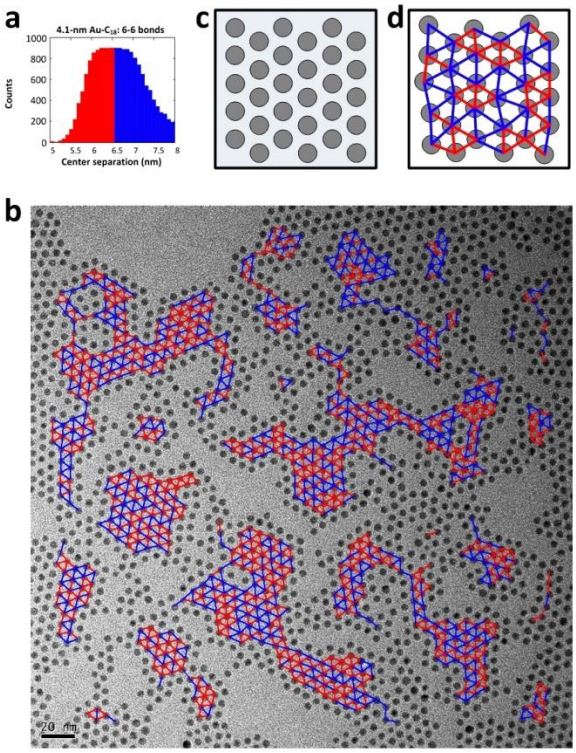

Figure 6.21. Ruling out size selection as the origin of non-Gaussian shape of 4.1-nm Au-C_{18} 6-6 bond distribution. Plotting the shorter half of fully-coordinated NC effective sizes (red) and longer half (blue) shows particles are intermixed. Separate domains resulting from core diameter size selection is not observed.

Instead, we propose that local relaxation of tensile stress results in roughening of interior bond lengths. During late stages of drying, inter-NC separations are set by ligand chains still swollen with solvent, embedded in an array with hexagonal symmetry (Figure 6.21c). Removal of residual solvent from corona overlaps reduces the equilibrium interparticle separation, giving rise to a tensile stress pulling inward on the sheet of NCs. Interaction between carbon substrate and NC corona (pinning) prevents large-scale movement of NCs and uniform contraction of the entire sheet. Instead, a short-range roughening of separations takes place: contraction of one interior bond results in elongation of another, distorting hexagonal symmetry (Figure 6.21d) and giving rise to the broad distribution observed for 6-6 bonds.

6.9.4. Orientational registry of inorganic cores in some binary superlattices

Strong orientational registry of PbS inorganic cores is routinely observed in CuAu-type BNSLs (Figure 6.22a) and somewhat more weakly in AlB_2- and Li_3Bi-type BNSLs (Figure 6.22b). Such effects cannot be accounted for by modeling inorganic cores as perfect spheres and may indicate the existence of flat-surface interactions between NCs with weakly-passivated (100)-type surfaces (Chapter 6). Most BNSLs, however, are plastic crystals with randomly-rotated inorganic cores of both A- and B-components (Figure 6.22c-j).

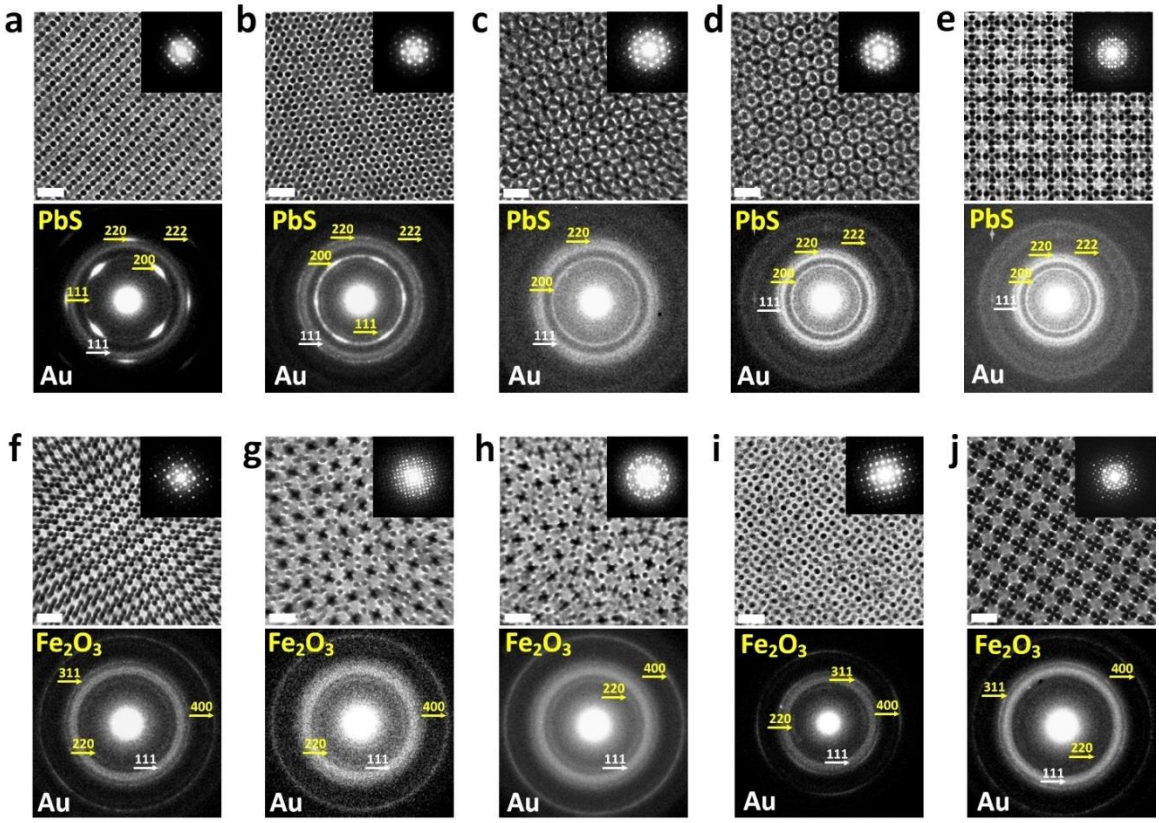

Figure 6.22. Electron diffractograms of observed BNSLs. Top, TEM image of BNSL domain. Inset: Small-angle electron diffractograms (SAED). Bottom, wide-angle electron diffractograms (WAED) with labeled atomic reflections for (a) CuAu, (b) AlB_2, (c) $MgZn_2$, (d) $CaCu_5$, (e) $NaZn_{13}$, (f) $C_{60}K_6$, (g) AT, (h) DDQC, (i) Li_3Bi, (j) $NaZn_{13}$.

6.10. Acknowledgements

I wish to express my gratitude to Prof. William Irvine in the Physics Department at the University of Chicago for providing me with a kernel of MATLAB particle tracking code (originally written by Prof. Eric Dufresne, Yale University) to get me started with this analysis. He also took time to explain to me the basics of writing software code, for which I am grateful. In addition, I would like to thank Prof. Tom Witten in the Physics Department at the University of Chicago for inviting me to present this work at the Physics Bag Lunch seminar series. Finally, I wish to thank Prof. Alex Travesset (Iowa State Physics Department) for his interest in this work and his calculations exploring phase behavior of soft repulsive spheres as well as topological defects within the shell of hydrocarbon surface ligand s.

6.11. References

1 Sanders, J. V. Colour of Precious Opal. *Nature* **204**, 1151-1153 (1964).

2 Pusey, P. N. & Megen, W. v. Phase behaviour of concentrated suspensions of nearly hard colloidal spheres. *Nature* **320**, 340-342, doi:10.1038/320340a0 (1986).

3 Hunt, N., Jardine, R. & Bartlett, P. Superlattice formation in mixtures of hard-sphere colloids. *Physical Review E* **62**, 900-913 (2000).

4 Sanders, J. V. Close-packed structures of spheres of two different sizes I. Observations on natural opal. *Philosophical Magazine A* **42**, 705-720, (1980).

5 Eldredge, M. D. Entropy-driven formation of a superlattice in a hard-sphere binary mixture. **365**, 35-37 (1993).

6 Murray, M. J. & Sanders, J. V. Close-packed structures of spheres of two different sizes II. The packing densities of likely arrangements. *Philosophical Magazine A* **42**, 721-740, (1980).

7 Bartlett, P., Ottewill, R. H. & Pusey, P. N. Superlattice formation in binary mixtures of hard-sphere colloids. *Physical Review Letters* **68**, 3801-3804 (1992).

8 Ben-Simon, A., Eshet, H. & Rabani, E. On the Phase Behavior of Binary Mixtures of Nanoparticles. *ACS Nano* **7**, 978-986, (2013).

9 Leunissen, M. E. *et al.* Ionic colloidal crystals of oppositely charged particles. *Nature* **437**, 235-240, (2005).

10 Murray, C. B., Norris, D. J. & Bawendi, M. G. Synthesis and characterization of nearly monodisperse CdE (E = sulfur, selenium, tellurium) semiconductor nanocrystallites. *Journal of the American Chemical Society* **115**, 8706-8715, (1993).

11 Leff, D. V., Brandt, L. & Heath, J. R. Synthesis and Characterization of Hydrophobic, Organically-Soluble Gold Nanocrystals Functionalized with Primary Amines. *Langmuir* **12**, 4723-4730, (1996).

12 Hyeon, T., Lee, S. S., Park, J., Chung, Y. & Na, H. B. Synthesis of Highly Crystalline and Monodisperse Maghemite Nanocrystallites without a Size-Selection Process. *Journal of the American Chemical Society* **123**, 12798-12801, (2001).

13 Murray, C. B., Kagan, C. R. & Bawendi, M. G. Self-Organization of CdSe Nanocrystallites into Three-Dimensional Quantum Dot Superlattices. *Science* **270**, 1335-1338, (1995).

14 Whetten, R. L. *et al.* Crystal Structures of Molecular Gold Nanocrystal Arrays. *Accounts of Chemical Research* **32**, 397-406, (1999).

15 Kiely, C. J., Fink, J., Brust, M., Bethell, D. & Schiffrin, D. J. Spontaneous ordering of bimodal ensembles of nanoscopic gold clusters. *Nature* **396**, 444-446 (1998).

16 Shevchenko, E. V., Talapin, D. V., Murray, C. B. & O'Brien, S. Structural Characterization of Self-Assembled Multifunctional Binary Nanoparticle Superlattices. *Journal of the American Chemical Society* **128**, 3620-3637, (2006).

17 Shevchenko, E. V., Talapin, D. V., Kotov, N. A., O'Brien, S. & Murray, C. B. Structural diversity in binary nanoparticle superlattices. *Nature* **439**, 55-59, (2006).

18 Talapin, D. V. *et al.* Quasicrystalline order in self-assembled binary nanoparticle superlattices. *Nature* **461**, 964-967, (2009).

19 Talapin, D. V. LEGO Materials. *ACS Nano* **2**, 1097-1100, (2008).

20 Talapin, D. V., Shevchenko, E. V., Murray, C. B., Titov, A. V. & Král, P. Dipole−Dipole Interactions in Nanoparticle Superlattices. *Nano Letters* **7**, 1213-1219, (2007).

21 Bodnarchuk, M. I., Kovalenko, M. V., Heiss, W. & Talapin, D. V. Energetic and Entropic Contributions to Self-Assembly of Binary Nanocrystal Superlattices: Temperature as the Structure-Directing Factor. *Journal of the American Chemical Society* **132**, 11967-11977, (2010).

22 Ye, X., Chen, J. & Murray, C. B. Polymorphism in Self-Assembled AB6 Binary Nanocrystal Superlattices. *Journal of the American Chemical Society* **133**, 2613-2620, (2011).

23 Evers, W. H. *et al.* Entropy-Driven Formation of Binary Semiconductor-Nanocrystal Superlattices. *Nano Letters* **10**, 4235-4241, (2010).

24 Chen, Z. & O'Brien, S. Structure Direction of II−VI Semiconductor Quantum Dot Binary Nanoparticle Superlattices by Tuning Radius Ratio. *ACS Nano* **2**, 1219-1229, (2008).

25 Laibinis, P. E. *et al.* Comparison of the structures and wetting properties of self-assembled monolayers of n-alkanethiols on the coinage metal surfaces, copper, silver, and gold. *J. Am. Chem. Soc.* **113**, 7152-7167 (1991).

26 Badia, A., Cuccia, L., Demers, L., Morin, F. & Lennox, R. B. Structure and Dynamics in Alkanethiolate Monolayers Self-Assembled on Gold Nanoparticles: A DSC, FT-IR, and Deuterium NMR Study. *Journal of the American Chemical Society* **119**, 2682-2692, (1997).

27 Korgel, B. A., Fullam, S., Connolly, S. & Fitzmaurice, D. Assembly and Self-Organization of Silver Nanocrystal Superlattices: Ordered "Soft Spheres". *The Journal of Physical Chemistry B* **102**, 8379-8388, (1998).

28 Landman, U. & Luedtke, W. D. Small is different: energetic, structural, thermal, and mechanical properties of passivated nanocluster assemblies. *Faraday Discussions* **125**, 1-22, (2004).

29 Schapotschnikow, P. & Vlugt, T. J. H. Understanding interactions between capped nanocrystals: Three-body and chain packing effects. *The Journal of Chemical Physics* **131**, 124705-124713 (2009).

30 Salem, L. Attractive Forces between Long Saturated Chains at Short Distances. *J. Chem. Phys.* **37**, 2100, (1962).

31 Rubinstein, M. & Colby, R. *Polymer Physics*. (Oxford University Press, 2003).

32 Schapotschnikow, P., Pool, R. & Vlugt, T. J. H. Molecular Simulations of Interacting Nanocrystals. *Nano Letters* **8**, 2930-2934, (2008).

33 Matsen, M. W. Effect of Chain Tilt on the Interaction between Brush-Coated Colloids. *Macromolecules* **38**, 4525-4530, (2005).

34 Luedtke, W. D. & Landman, U. Structure, Dynamics, and Thermodynamics of Passivated Gold Nanocrystallites and Their Assemblies. *The Journal of Physical Chemistry* **100**, 13323-13329, (1996).

35 Shannon, R. Revised effective ionic radii and systematic studies of interatomic distances in halides and chalcogenides. *Acta Crystallographica Section A* **32**, 751-767, (1976).

36 Pauling, L. THE PRINCIPLES DETERMINING THE STRUCTURE OF COMPLEX IONIC CRYSTALS. *Journal of the American Chemical Society* **51**, 1010-1026, (1929).

37 Macfarlane, R. J. *et al.* Nanoparticle Superlattice Engineering with DNA. *Science* **334**, 204-208, (2011).

38 Kallus, Y. The 3-ball is a local pessimum for packing. *Advances in Mathematics* **264**, 355-370, (2014).

39 Widmer-Cooper, A. & Harrowell, P. Structural phases in non-additive soft-disk mixtures: Glasses, substitutional order, and random tilings. *The Journal of Chemical Physics* **135**, -, (2011).

40 Eldridge, M. D., Madden, P. A., Pusey, P. N. & Bartlett, P. Binary hard-sphere mixtures: a comparison between computer simulation and experiment. *Molecular Physics* **84**, 395-420, (1995).

41 Peng, S. *et al.* A facile synthesis of monodisperse Au nanoparticles and their catalysis of CO oxidation. *Nano Research* **1**, 229-234, (2008).

42 Hines, M. A. & Scholes, G. D. Colloidal PbS Nanocrystals with Size-Tunable Near-Infrared Emission: Observation of Post-Synthesis Self-Narrowing of the Particle Size Distribution. *Advanced Materials* **15**, 1844-1849, (2003).

43 Chen, Z., Moore, J., Radtke, G., Sirringhaus, H. & O'Brien, S. Binary Nanoparticle Superlattices in the Semiconductor−Semiconductor System: CdTe and CdSe. *Journal of the American Chemical Society* **129**, 15702-15709, (2007).

7. PbS nanocrystal surface passivation drives binary phase behavior

Evaporation of two-component nanocrystal (NC) solutions has produced more than twenty phases of binary nanocrystal superlattices (BNSLs). Here we show with proton- and diffusion-ordered nuclear magnetic resonance spectroscopy (^{1}H- and DOSY-NMR) that a weakly-bound subset of oleic acid (OA) ligands readily desorbs from the PbS NC surface, significantly altering the binary phase behavior of such particles. In this process, washing-induced removal of labile OA ligand from PbS(100) surfaces alters the effective NC shape from approximately spherical to cubic by development of flat surfaces along NC (+/-) x-, y-, and z-directions. Such desorption favors self-assembly of structures that incorporate face-face registry and thus dense packing of the faceted particles. This effect was found to result in essentially complete structural conversion from AlB_2-type to CuAu-type BNSLs when 7-nm PbS NCs are mixed with 3.5-nm Au NCs. These observations provide yet another example of capping ligands contributing to NC superlattice structural diversity and offer a potential strategy to target particular binary arrangements.

7.1. Colloidal crystallization and binary nanocrystal phase behavior

Colloidal NCs are nanometer-sized inorganic crystals stabilized by a layer of surfactant molecules attached to their surface.[1] Preparation of sufficiently size- and shape uniform NCs allows for self-assembly of such units into ordered arrays, or NC superlattices.[2] Evaporation of two sizes of NCs can result in formation of two-component superlattices, or BNSLs.[3] In stark contrast to two-component crystals of micron-sized silica or polymer beads, a rich set of BNSL structures has been observed, including Frank-Kasper phases[4] and quasicrystals.[5] In addition, two different NC shapes can cocrystallize into “shape alloys” such as rods and spheres[6] and

different-shaped platelets.[7] These examples serve to highlight the wide-ranging compositional space accessible to ordered arrangements of NCs.

The simplest approach to predicting phase behavior of NCs is to make an assumption about effective particle shape and then find the arrangement that maximizes packing density, φ. The densest structure is favored by free volume entropy in solution and by cohesive interactions between particles after solvent evaporation. Accordingly, approximately spherical NCs should assemble into face-centered cubic (*fcc*) packing ($\varphi_{fcc} \approx 0.74$). Similarly, a mixture of spherical NCs with different radii R should cocrystallize if the size ratio ($\gamma = R_B/R_A$) allows the system to access denser binary packings ($\varphi_{BNSL} > \varphi_{fcc}$). This logic predicts formation of BNSLs isostructural with $C_{60}K_6$ at $\gamma \sim 0.3$, NaCl at $\gamma \sim 0.4$, and AlB_2 at $\gamma \sim 0.6$. However, the diversity of BNSLs observed, including over 20 arrangements, several of which have yet to be identified, highlights the limitations of such sphere packing models.

Recent work has shown that the ligand capping layer may contribute to complex phase behavior of BNSLs. For example, the deformability of the soft corona allows for departure from sphere packing, enabling BNSL density to exceed the hard sphere prediction.[8] In addition, density functional theory (DFT) calculations indicate large difference in binding energy of oleic acid ligands on the PbS (100) and (111) surface, opening up the possibility of variable ligand coverage on such particles during assembly.[9] Here, we combine evaporation-based assembly of PbS and Au NCs with NMR measurements of PbS NC surface ligands to correlate the observed binary phase behavior with PbS ligand capping layer coverage.

7.2. Ligand surface coverage during nanocrystal synthesis and purification

Colloidal nanocrystals (NCs) are routinely prepared by decomposition of molecular precursors in the presence of organic surfactants.[1] Characterization and application of NCs typically requires separation of NCs from high-boiling organics present in the synthetic mixture. These include surface-binding species such as oleic acid (OA) as well as non-binding liquids which act as high-temperature solvent during synthesis such as 1-octadecene (ODE). The most common technique to separate NCs from the crude reaction mixture is size-selective precipitation. In this approach, successive flocculation and redispersal ('washing") steps are used to obtain NCs as solid sediment and remove organics in the supernatant. For example, addition of ethanol to a hexane solution of hydrocarbon-capped NCs induces aggregation of the particles. The density difference between such aggregates and the surrounding solvent causes them to sediment to the bottom of the container, particularly when used in conjunction with centrifugation. Subsequent decanting of the supernatant and exposure of the pellet (compressed solid) to fresh solvent enables redispersal of the colloid with lower concentration of residual organics.

Diminished NC solubility after successive washing steps is a commonly observed during post-preparative NC purification.[10] Indeed, while some NCs can be precipitated and redispersed many times (e.g., phosphonate-capped CdSe, ref.[11]), most colloidal nanomaterials tolerate only three or fewer cycles before solubility is compromised (e.g., amine-capped Au, ref.[12] and oleate-capped PbS, ref.[13]). This results from loss of stabilizer ligands from the NC surface (Figure 6.1).

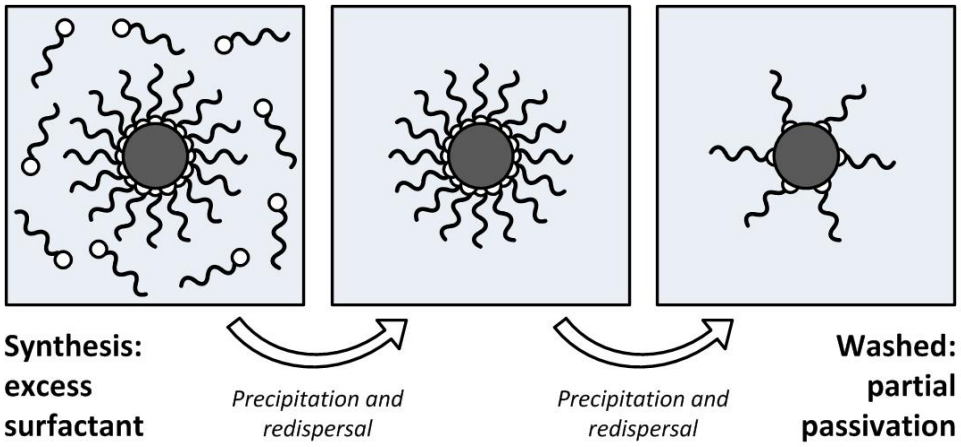

Figure 7.1. Simple illustration of abundance of surface ligands during NC synthesis and subsequent purification steps. In the presence of excess surfactant molecules, the particle is well-passivated (left). On the other hand, precipitation and redispersal steps intended to remove excess high-boiling organics often result in stripping of ligands from the NC surface (right).

Two mechanisms may be invoked to explain such observations: (*1*) ligand dissolution and (*2*) ligand exchange. The first case involves neutral (*L*-type) ligands, which dynamically bind to the NC surface.[14] A free ligand (*L*) binds to a free site on the NC surface, becoming a bound ligand (*NC*-*L*):

$$NC \quad + \quad L \quad \overset{K_a}{\rightarrow} \quad NC - L$$

Here, the adsorption constant (K_a) denotes the strength of NC-ligand affinity. Addition of excess ligand to the NC solution will increase the population of bound ligands (rightward shift of the equilibrium, according to the Le Chatelier principle). Conversely, and important to the aforementioned washing procedure, removal of free ligands from solution by precipitation and redispersal will induce desorption of bound ligands.

A second mechanism for ligand removal involves exchange with competing surface binding species ("ligand stripping"). For example, common nonsolvents (e.g., alcohols such as methanol, ethanol, isopropanol) displace ligands in a proton-coupled *X*-for-*X'*-type exchange[15] (see also Section 2.2):

$$NC - X \; + \; HX' \; \overset{K}{\rightarrow} \; NC - X' \; + \; HX$$

Here, *K* is the equilibrium constant of the *X*-for-*X'* exchange. Use of aprotic nonsolvents, on the other hand, prevents such process from taking place and minimizes loss of NC capping ligands during purification and size-selection procedures.

For moderate reduction in grafting density of surface ligands, NCs can be dispersed in the colloidal state. Extending the exploration of surface ligands in driving the phase behavior of colloidal NCs, this chapter seeks to highlight the role of labile ligands at the surface of PbS NCs and their influence on the cocrystallization of such particles with Au NCs. Though a combination of self-assembly experiments with TEM and SAXS characterization, and ^{1}H- and DOSY-NMR titration experiments, it was found that a significant fraction of PbS NC surface is left unpassivated after typical washing steps, favoring CuAu-type binary nanocrystal superlattice (BNSL) structures. With the addition of excess oleic acid to the PbS solution, evaporating the same binary solution results in near complete conversion of CuAu- to AlB_2-type BNSLs. The orientational registry of inorganic cores observed in CuAu-type BNSLs, and its absence in AlB_2-type BNSLs, leads us to conclude that capping ligand surface saturation plays an important role in establishing the effective shape of PbS NCs which determines binary phase behavior.

7.3. Oleic acid capped PbS nanocrystals: anisotropic ligand binding energy

The discussion of nanocrystal surfaces provided in Chapter 2 examines the chemistry of ligand binding. Nearly-spherical NCs, presenting at least two or three distinct inorganic surface patterns (e.g., (100)-, (110)-, (111)-type crystallographic facets) can have surprisingly complex surface chemistry. Even with just one ligand species, both *L*- and *X*-type binding motifs may be present at the NC surface.[16] The difference in adsorption energy across these motifs can be significant, leading to facet-specific ligand release. For example, density functional theory (DFT) calculations indicate that, while oleic acid binds in protonated form (OAH) to stoichiometric (001)-type facets of PbS NCs with -0.16 eV/ligand, the oleate anion (OA^-) binds to Pb-covered (111)-type facets with -0.52 eV/ligand.[9] Simple Boltzmann factor calculations predict that desorption of OAH from PbS(001) is thus more than one million times more likely than desorption of OA^- from PbS(111) surface.

As a result, even with use of aprotic nonsolvent for purification of PbS crude synthetic mixture, the tendency of OAH to establish equilibrium solution population upon each redispersal step can be expected to lead to variations in ligand surface grafting density between (001)- and (111)-type facets on PbS NCs.

7.4. Preparation and characterization of 7.5-nm PbS nanocrystals

Oleic acid capped PbS NCs were prepared by reacting $Pb(CH_3COO)_2$ and $((CH_3)_3Si)_2S$ in a mixture of oleic acid and 1-octadecene at 150°C. The NCs were separated from crude reaction mixture by washing three times with hexane/ethanol, size-selecting on the third cycle. These NCs were redispersed in concentrated (~100 mg/mL) octane solutions for storage.

Microscopy (TEM), absorption/emission spectroscopy (UV-Vis-NIR), and thermal analysis (TGA) were used to characterize the PbS NCs. TEM revealed single-crystalline PbS NC cores with approximately spherical shape (Figure 7.2a). When the NC solution is evaporated atop a water droplet, large-area hexagonal superlattice sheets are obtained with some presence of vacancy defects (Figure 7.2b). Several absorbance peaks in the near infrared (NIR) confirmed uniform size and shape distribution of the NC solution (Figure 7.2c).

Mass loss data indicate oleic acid surface ligands decompose into volatile organic products between 250 and 350°C (Figure 7.2d). This measurement enables estimation of the organic mass fraction of as-prepared PbS NCs (16%) and, in turn, the grafting density of ligands at the surface of PbS NCs. Such calculations indicate that approximately 2.5 ligands are present per nm^2 of NC surface. Taking the carboxylic acid footprint area to be 0.28 nm,[17] the predicted grafting density at full surface coverage is ~3.5 nm^{-2}. From this analysis, we conclude that the PbS NCs washed three times with hexane / ethanol and stored in concentrated octane solution have approximate ligand coverage of 70% of the surface saturation limit.

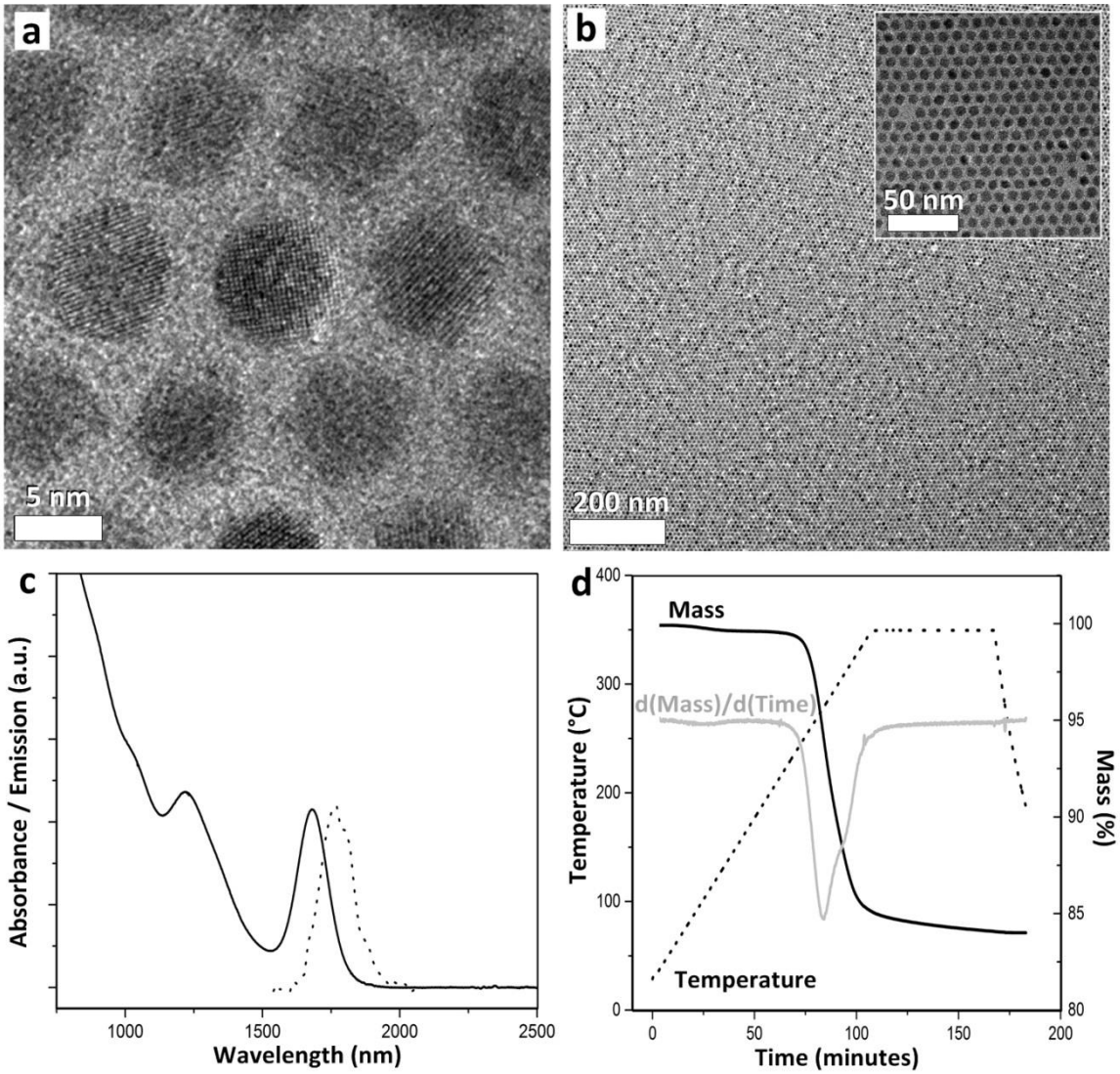

Figure 7.2. (a) High-resolution TEM of individual oleic acid capped PbS NCs packed in hexagonal monolayer. (b) TEM overview of sheet of PbS NCs with zoom (inset) of local structure. (c) UV-Vis-NIR absorbance (solid) and emission (dashed trace) of PbS NCs dispersed in tetrachloroethylene solution. (d) TGA showing 16% mass loss corresponding to thermal decomposition of organic ligands at ~300°C.

7.5. Binary phase behavior: switching from CuAu to AlB_2 with excess ligand

Binary assembly experiments were carried out by evaporating an octane solution of above-described oleic acid capped 7.5-nm PbS NCs with dodecanethiol-capped 3.1-nm Au NCs in a tilted 2-mL scintillation vial containing carbon TEM grid at 50°C. Such experiments routinely yielded large-area CuAu-type BNSLs covering nearly the entire grid surface (Figure 7.3a), with small presence of excess Au NCs deposited as close-packed solid alongside the BNSLs. On the other hand, self-assembly of the same NCs with the addition of oleic acid resulted in dramatically different binary phase behavior, with nearly exclusive formation of AlB_2-type BNSLs (Figure 7.3b). Electron diffractograms (ED) were also obtained by collecting transmitted electrons in the diffraction plane (Figure 7.3c-f). Small-angle ED patterns revealed off-center spots corresponding to reflections off lattice planes of the superlattice (Figure 7.3c,e). Intriguingly, wide-angle ED revealed a significant difference between the two phases: while both Au and PbS NC cores are packed in orientationally random arrangements in the AlB_2-type BNSL (Figure 7.3f), wide-angle reflections of the PbS core lattice planes indicate strong orientational registry of PbS cores within the CuAu-type BNSL (Figure 7.3d).

While TEM is a useful tool for probing local structure of NC arrays, small-angle x-ray scattering (SAXS) enables information collection representative of the entire sample. Both samples were subjected to transmission SAXS measurement taken in raster fashion across the TEM grid surface. Such measurement points comprised an 8-by-8 grid, with 64 measurements collected in total. These two-dimensional raw data (pixel intensities) were added together to create a composite scattering pattern and subsequently subjected to radial averaging (Figure 7.3g,h). The SAXS features were compared with theoretical scattering pattern of CuAu and AlB_2 structures obtained using CrystalDiffract software with appropriate lattice parameter fitting.

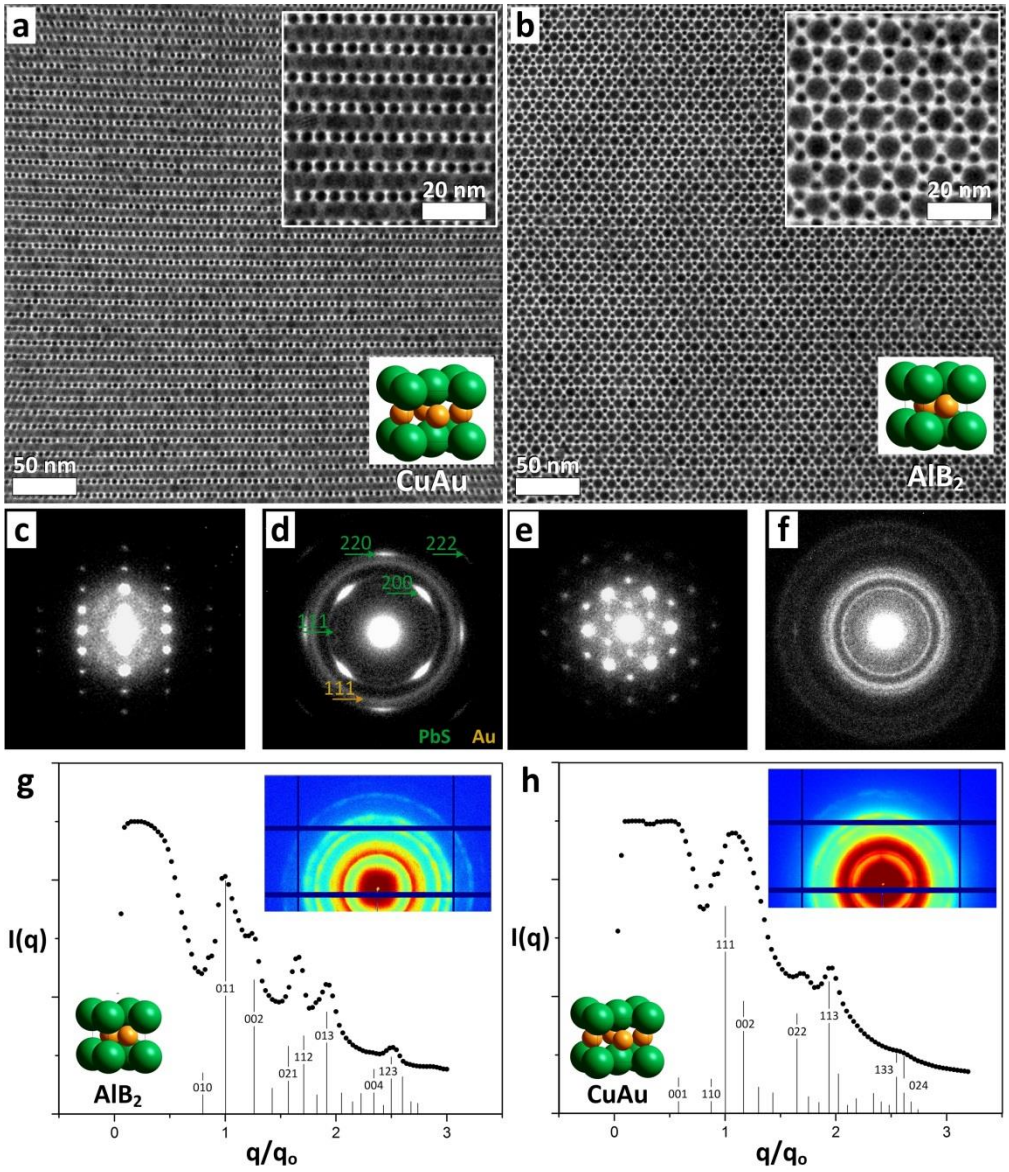

Figure 7.3. Cocrystallization of PbS with Au NCs in the case of as-prepared PbS (left column) and with addition of excess oleic acid ligand (right column). (a) TEM image of CuAu-type BNSL obtained by evaporation of Au NCs with as-prepared PbS NCs. Insets: zoom of structure (top) and unit cell (bottom). (b) TEM image of AlB_2-type BNSL obtained by evaporation of Au NCs with as-prepared PbS NCs. Insets: zoom of structure (top) and unit cell (bottom). (c,d) Small- and wide-angle electron diffractograms of the CuAu-type BNSLs. (e,f) Small- and wide-angle electron diffractograms of the AlB_2-type BNSLs. (g) Radially-averaged SAXS pattern collected by summing 64 measurements scanned in raster fashion across the surface of the grid containing CuAu BNSLs. Delta functions shown underneath indicate expected position of lattice reflections of CuAu structure. Inset: 2D SAXS pattern. (h) Radially-averaged SAXS pattern collected by summing 64 measurements scanned in raster fashion across the surface of the grid containing AlB_2 BNSLs. Inset: 2D SAXS pattern. Delta functions shown underneath indicate expected position of lattice reflections of AlB_2 structure.

7.6. NMR investigation of oleic acid binding to PbS in solution

Nuclear magnetic resonance (NMR) is a routine analytical tool for organic chemists and has recently begun to be used by the nanocrystal research community to probe the binding of surfactant species to NCs in solution.[18] Here, proton (^{1}H-) and diffusion-ordered (DOSY-) NMR spectroscopy was used to examine the existence of PbS NC surface sites left bare after washing and size selection procedures typically carried out after synthesis (Figure 7.4).

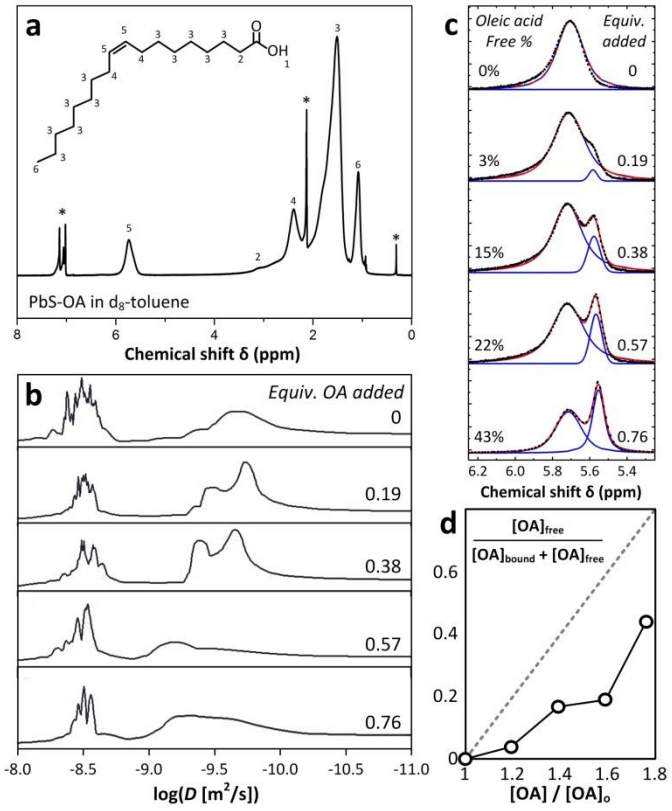

Figure 7.4. (a) ^{1}H-NMR spectrum of as-prepared, oleic acid capped PbS NCs dissolved in deuterated toluene. Solvent resonances are marked with asterisks. Inset: ligand molecular structure and corresponding signal assignment. (b) Monitoring titration of PbS NC solution with excess oleic acid using DOSY-NMR. Signal comes from (left to right, fastest to slowest diffusing species) solvent protons, free ligands, and bound ligands. (c) Zoom of vinyl resonance in ^{1}H-NMR during titration with excess oleic acid. Bound (left, broad) and free (right, sharp) resonances are modeled with Lorentzian profiles (blue traces), the sum of which (red trace) is fitted to the experimental data (black dotted trace). (d) Summary of ^{1}H-NMR titration data: free oleic acid population is plotted as a function of added oleic acid. Dotted grey trace represents the hypothetical case of no surface interaction upon oleic acid addition.

A typical ^{1}H-NMR spectrum of as-prepared oleic acid capped PbS NCs reveals sharp resonances contributed by residual protons in the deuterated solvent (here: d_8-toluene, 99.9%) and broadened resonances from bound surface ligands (Figure 7.4a). Aliphatic ligand resonances appear in the $1 < \delta < 3$ ppm chemical shift region, while significant deshielding of the vinyl proton leads to an isolated signal within the range of $5.5 < \delta < 6$ ppm. On the other hand, the DOSY-NMR spectrum plots diffusion coefficient for all protons in the sample (Figure 7.4b). In the as-prepared sample, solvent resonances appear at $D \sim 10^{-8.5}$ m^2/s, while oleic acid ligands fall between $10^{-9.25} < D < 10^{-10.25}$ m^2/s.

Titrating the NC solution with excess oleic acid ligands has been an effective approach to probe solution binding equilibria of ligands and NCs.[19] Such experiments were carried out by stepwise addition of oleic acid in 0.19 molar equivalents (moles of ligand added / moles of ligands bound to the NCs). At the end of four titrations, the amount of oleic acid in solution was increased by approximately 76%. During the titration, DOSY-NMR showed development of two peaks corresponding to ligand protons diffusing at two speeds, presumably free (left) and bound (right) species, which ultimately broaden or disappear after further ligand addition (Figure 7.4b). This observation may result from depletion flocculation of the colloid in the presence of oleic acid micelles in solution.[20]

Following titration experiments using the vinyl resonance in ^{1}H-NMR enables one to monitor the relative populations of bound and free oleic acid (Figure 7.4c). Deconvolution of bound (broadened downfield signal) and free (sharp upfield signal) ligand resonances reveals the extent to which added ligands remain solvated or bind to open sites at the NC surface. In the case of no interaction between added ligands and PbS NCs, the population of free ligands should increase in proportion with ligand addition (Figure 7.4d, dotted trace). However, the measured

intensity of the sharp vinyl signal is consistently below the zero-interaction case (Figure 7.4d, circles), suggesting a significant proportion of ligands added to solution bind to open sites at the surface of PbS NCs.

7.7. Unpassivated PbS(100) facets: flat-surface interactions during assembly

The shape of nearly-spherical (e.g., cuboctahedral[9] or rhombicuboctahedral[21]) PbS NCs is rounded by a full capping layer of oleic acid surface ligands. This is to say, the effective asphericity quotient (R_{out} / R_{in}) of the capped NC is lower than that of the bare cuboctahedron, due to effective softening of NC vertices and tips by weakly-repelling ligands in good solvent (Chapter 4). However, facet-selective ligand loss can lead to increase of effective asphericity over the bare cuboctahedron. The measured ligand grafting density of ~2.5 nm^{-2} indicates the significant presence of unbound sites, predicted to be located overwhelmingly on the (100)-type PbS surfaces. Such arguments indicate this process should lead to pronounced flat surfaces on the NC along Cartesian coordinates (i.e., +/- *x*-, *y*-, and *z*-directions).

Assembly behavior of particles with nearly-spherical and highly aspherical geometry has been established through Monte Carlo simulations on a catalog of polyhedra including Platonic, Archimedean, and Johnson solids.[22] Such investigations have led to conceptual development of directional entropic forces,[23] or "shape entropy", which acts upon anisotropic particles in crowded solution and favors mutual alignment of neighboring faces. Whereas nearly spherical particles tend to assemble into plastic crystals with solely translational ordering, those with large flat surfaces generally arrange themselves onto lattices which exhibit both translational and orientational ordering of particles.

The recent theoretical developments in understanding of phase behavior of polyhedral particles, and understanding of PbS NC surface chemistry, coupled with experimental data collected from thermal analysis (Section 7.4), binary self-assembly (Section 7.5) and solution NMR titration experiments (Section 7.6), allow for conclusions to be made concerning the role of oleic acid addition in determining binary phase behavior. As-prepared PbS NCs, with flat surfaces along Cartesian directions, assemble into layered binary structures with PbS – PbS core orientational registry promoted by shape entropy (Figure 7.5, top). On the other hand, addition of oleic acid to the assembly solution re-passivates the (100)-directions of PbS NCs, restoring the effective round shape and promoting rotationally random, hexagonal arrangement of NCs within the PbS layers (Figure 7.5, bottom).

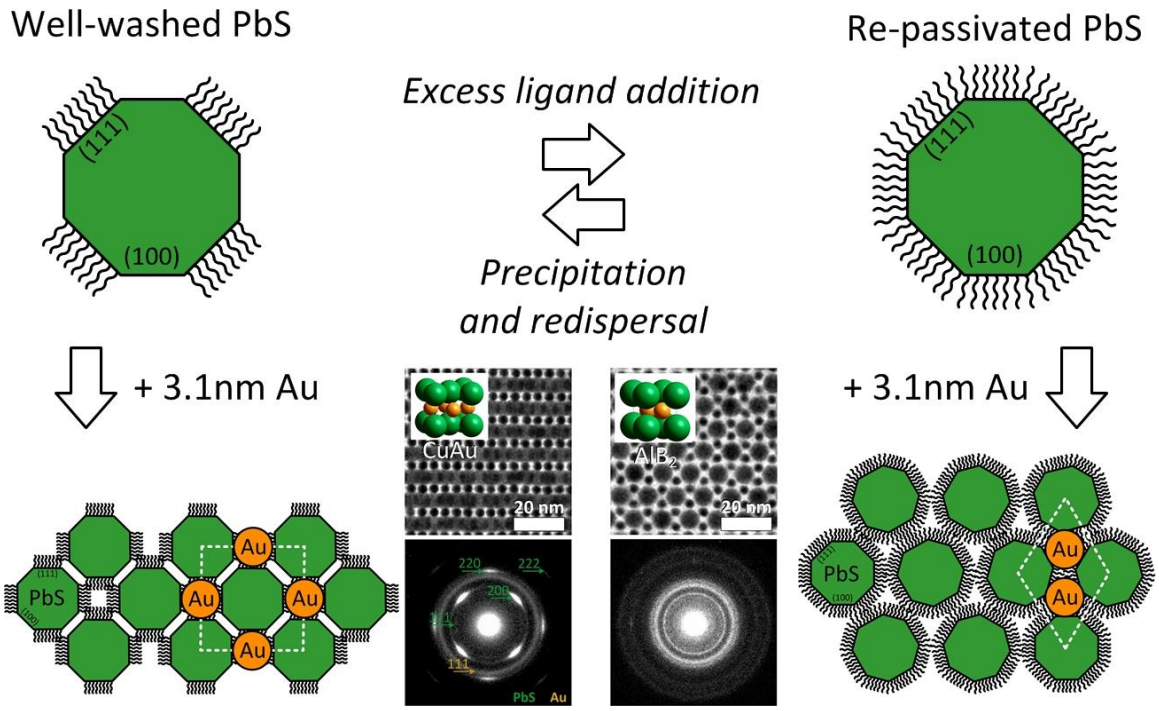

Figure 7.5. Schematic depiction of role of oleic acid addition in determining binary phase behavior of PbS and Au NCs. As-prepared PbS NCs feature flat surfaces and assemble into orientationally-registered CuAu BNSLs (top), while PbS NCs, re-passivated by added oleic acid, assemble into orientationally-random AlB_2-type BNSLs (bottom).

Further comment is required on a two aspects of the assembly mechanism proposed in Figure 7.5: (*1*) binary phase stoichiometry, and (*2*) oleic acid binding to Au NC surfaces. Clearly, the stoichiometry of AB_2-type BNSLs is richer in B-spheres than AB-type BNSLs. The question arises: if B-excess is available to form AB_2-type BNSLs, where do the extra B-spheres (Au NCs) go in the case of the sample covered in AB-type BNSLs? Indeed, local variations in stoichiometry are routinely observed across the grid. For example, AB- and AB_{13}-type BNSLs can coexist within the same sample.[8] In the case of CuAu-type BNSLs shown in Figure 7.3a, in between CuAu domains, close-packed superlattices of B-particles were found. On the other hand, alongside the AlB_2-type BNSLs shown in Figure 7.3b, close-packed superlattices of A-particles were found. Such observations indicate that the difference in stoichiometry between the stable BNSL phase and the experimental mixing ratio are compensated for by local phase segregation across the substrate.

In addition, the possibility of oleic acid interacting with Au NCs in the binary assembly solution must be discussed. The Au-S bond anchoring ligands to the Au NC surface is a classic example of robust association between soft acid and soft base.[24] This fact, coupled with the large electrostatic penalty for self-desorption of charged *X*-type (e.g., thiolate) anchor groups in nonpolar solvent, suggests that dodecanethiol-capped Au NCs should be less susceptible to ligand desorption than PbS(100) surfaces. Moreover, weak interaction between carboxylic acid oxygens (hard base) and Au NC surface (soft acid[25]) further disfavors such association. As a result, we conclude that the observed effect of oleic acid addition must result from adsorption to PbS NC surfaces and concomitant changes to effective PbS NC shape.

In conclusion, a combination of TEM, ED, NMR, and TGA experiments indicate that flat surfaces develop on PbS NCs due to loss of surface ligands along (100)-type NC directions, and

that such features favor orientationally-registered PbS NC packings within CuAu-type BNSLs. On the other hand, addition of oleic acid ligands re-passivates the bare surfaces, restoring effectively spherical PbS NC geometry, suppressing rotational registry of PbS NC cores and favoring binary phases representing a dense packing of two sizes of spheres.

7.8. Acknowledgements

I wish to acknowledge Dr. Antoni Jurkiewicz for his assistance with NMR experiments, including instrument calibration, setup of DOSY measurement protocol, and introduction to the Linux command line.

7.9. References

1 Yin, Y. & Alivisatos, A. P. Colloidal nanocrystal synthesis and the organic-inorganic interface. *Nature* **437**, 664-670 (2005).

2 Murray, C. B., Kagan, C. R. & Bawendi, M. G. Self-Organization of CdSe Nanocrystallites into Three-Dimensional Quantum Dot Superlattices. *Science* **270**, 1335-1338 (1995).

3 Shevchenko, E. V., Talapin, D. V., Kotov, N. A., O'Brien, S. & Murray, C. B. Structural diversity in binary nanoparticle superlattices. *Nature* **439**, 55-59 (2006).

4 Shevchenko, E. V., Talapin, D. V., Murray, C. B. & O'Brien, S. Structural Characterization of Self-Assembled Multifunctional Binary Nanoparticle Superlattices. *Journal of the American Chemical Society* **128**, 3620-3637 (2006).

5 Talapin, D. V. *et al.* Quasicrystalline order in self-assembled binary nanoparticle superlattices. *Nature* **461**, 964-967 (2009).

6 Ye, X. *et al.* Shape Alloys of Nanorods and Nanospheres from Self-Assembly. *Nano Letters* **13**, 4980-4988 (2013).

7 Paik, T. & Murray, C. B. Shape-Directed Binary Assembly of Anisotropic Nanoplates: A Nanocrystal Puzzle with Shape-Complementary Building Blocks. *Nano Letters* **13**, 2952-2956 (2013).

8 Boles, M. A. & Talapin, D. V. Many-Body Effects in Nanocrystal Superlattices: Departure from Sphere Packing Explains Stability of Binary Phases. *Journal of the American Chemical Society* **137**, 4494-4502 (2015).

9 Zherebetskyy, D. *et al.* Hydroxylation of the surface of PbS nanocrystals passivated with oleic acid. *Science* **344**, 1380-1384, (2014).

10 Murray, C. B., Norris, D. J. & Bawendi, M. G. Synthesis and characterization of nearly monodisperse CdE (E = sulfur, selenium, tellurium) semiconductor nanocrystallites. *Journal of the American Chemical Society* **115**, 8706-8715, (1993).

11 Gomes, R. *et al.* Binding of Phosphonic Acids to CdSe Quantum Dots: A Solution NMR Study. *The Journal of Physical Chemistry Letters* **2**, 145-152, (2011).

12 Peng, S. *et al.* A facile synthesis of monodisperse Au nanoparticles and their catalysis of CO oxidation. *Nano Research* **1**, 229-234, (2008).

13 Hines, M. A. & Scholes, G. D. Colloidal PbS Nanocrystals with Size-Tunable Near-Infrared Emission: Observation of Post-Synthesis Self-Narrowing of the Particle Size Distribution.

Advanced Materials **15**, 1844-1849, (2003).

14 Fritzinger, B. *et al.* In Situ Observation of Rapid Ligand Exchange in Colloidal Nanocrystal Suspensions Using Transfer NOE Nuclear Magnetic Resonance Spectroscopy. *Journal of the American Chemical Society* **131**, 3024-3032, (2009).

15 Hassinen, A. *et al.* Short-Chain Alcohols Strip X-Type Ligands and Quench the Luminescence of PbSe and CdSe Quantum Dots, Acetonitrile Does Not. *Journal of the American Chemical Society* **134**, 20705-20712, (2012).

16 Boles, M. A., Ling, D., Hyeon, T. & Talapin, D. V. The surface science of nanocrystals. *Nat Mater* **15**, 141-153, (2016).

17 Lide, D. R. *CRC Handbook of Chemistry and Physics*. 96 edn, (CRC Press, 2015).

18 Hens, Z. & Martins, J. C. A Solution NMR Toolbox for Characterizing the Surface Chemistry of Colloidal Nanocrystals. *Chemistry of Materials* **25**, 1211-1221 (2013).

19 Fritzinger, B., Capek, R. K., Lambert, K., Martins, J. C. & Hens, Z. Utilizing Self-Exchange To Address the Binding of Carboxylic Acid Ligands to CdSe Quantum Dots. *Journal of the American Chemical Society* **132**, 10195-10201, (2010).

20 Baranov, D. *et al.* Assembly of Colloidal Semiconductor Nanorods in Solution by Depletion Attraction. *Nano Letters* **10**, 743-749 (2010).

21 Boneschanscher, M. P. *et al.* Long-range orientation and atomic attachment of nanocrystals in 2D honeycomb superlattices. *Science* **344**, 1377-1380, (2014).

22 Damasceno, P. F., Engel, M. & Glotzer, S. C. Predictive Self-Assembly of Polyhedra into Complex Structures. *Science* **337**, 453-457 (2012).

23 van Anders, G., Klotsa, D., Ahmed, N. K., Engel, M. & Glotzer, S. C. Understanding shape entropy through local dense packing. *Proceedings of the National Academy of Sciences* **111**, E4812-E4821 (2014).

24 Hakkinen, H. The gold-sulfur interface at the nanoscale. *Nat Chem* **4**, 443-455 (2012).

25 Pearson, R. G. Hard and Soft Acids and Bases. *Journal of the American Chemical Society* **85**, 3533-3539 (1963).

8. Conclusion and outlook

The conceptual development of entropy-driven crystallization, inspired in part by the ordering of micron-sized, sterically-stabilized colloidal beads into superstructures (opals[1,2]), has provided an important foundation for considering self-assembly of nanometer-sized colloids. This line of reasoning anticipates that the densest packing of a given shape, offering the greatest free volume to particles in the concentrated assembly solution, is the stable phase (Section 3.3). Indeed, nanocrystal (NC) superlattices often adopt structures characteristic of hard-particle systems such as face-centered cubic (*fcc*) and hexagonal close-packed (*hcp*) arrays of monodisperse spheres,[3] arrangements isostructural with NaCl, AlB_2, $MgZn_2$, and $NaZn_{13}$ compounds in binary sphere mixtures,[4] and simple cubic packings of cube-shaped NCs.[5]

8.1. Nanocrystal self-assembly: puzzling superlattice phase behavior

This analysis, however, cannot fully explain NC self-assembly. Binary sphere mixtures (Chapters 5-7) represent perhaps the most striking example: while only four binary phases are predicted to be stable for hard spheres, more than fifteen distinct binary NC superlattice structures have been observed experimentally.[6] Similarly, polyhedral NCs (e.g., tetrahedra, Chapter 4) form ordered superlattices unable to be rationalized by entropy-driven crystallization into a dense packing of the shape.

These observations provide strong evidence that additional considerations must be invoked to understand the crystallization of nanoscale building blocks. Along these lines, electrostatic charging of NCs was offered as a preliminary explanation of the deviation of NC phase behavior from hard-shape packing expectations.[6] Indeed, charging of colloids can lead to stabilization of non-close-packed phases.[7,8] However, hydrocarbon-capped NCs with zero measured electrophoretic mobility routinely assemble into single-component and binary phases

outside of those predicted by the hard sphere model.[9] Furthermore, adjusting the A:B mixing ratio tunes binary superlattice stoichiometry across a wide range (e.g., from AB to AB_{13}).[10] Such observations indicate that Coulomb interactions are unlikely to be the primary driver of superlattice phase stability. Similarly, although dipole-dipole interactions between NC cores can also introduce complexity into the phase diagram,[11] the abundance of non-close-packed phases with randomly-oriented inorganic cores[10] indicates that dipolar interactions are unlikely to dominate formation of these structures.

8.2. Nanocrystal surface ligands: convergence of hard- and soft matter assembly

This logic, resulting in tentative elimination of core-core electrostatic interactions as the main driver of NC phase behavior, sets the stage for the body of research described in this thesis. By coupling self-assembly experiments with explicit treatment of surface ligand contributions to interparticle potential (Chapter 4) and effective NC shape (Chapters 5-7) during the ordering process, this thesis has shined a spotlight on the largely unrecognized connection between hydrocarbon-capped NCs and soft matter (e.g., block copolymers, Figure 8.).

The main findings of this work are:

(*1*) Surface curvature determines the spatial distribution of ligand density across the NC surface, yielding patches of weakly-repelling ligands at the vertices of polyhedral NCs. This effect favors spatial proximity of tips in dense assembly solution and thus promotes formation of open superlattices of anisotropic NCs (Chapter 4).

(*2*) Nearly-spherical NCs with significant organic volume fraction ("soft" NCs) can experience ligand corona deformation, particularly when occupying low-coordination lattice sites and in contact with NCs of lower organic volume fraction ("hard" NCs). The

implications of this departure from sphere packing on superlattice density can be anticipated using a set of rules for space filling of soft particles (Chapters 5,6).

(*3*) Large differences in the binding strength of ligands to distinct NC surface facets can lead to departure from sphere packing via desorption of hydrocarbon chains along particular crystallographic directions. In the case of PbS NCs, passivation of (001)-type NC facets influenced by washing or excess ligand addition enables tuning of effective NC shape, and as a result, control over binary phase behavior (Chapter 7).

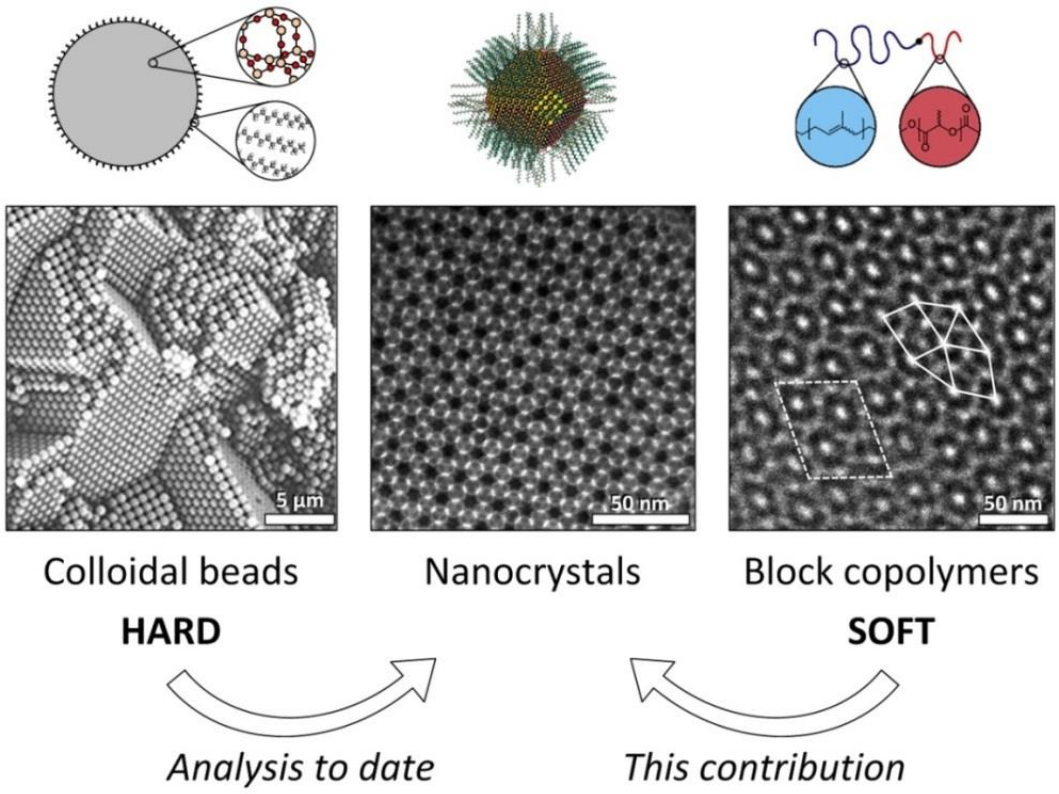

Figure 8.1. Systems capable of self-assembly include colloidal particles (a solid, left) and block copolymer melts (a liquid, right). Hydrocarbon-capped nanocrystals (center) feature both a solid core and a liquid-like corona, and display complex phase behavior resulting from the confluence of hard and soft elements. The ideas contained within this thesis serve to more fully establish the connection between nanocrystal superlattices and soft matter assemblies, and thereby rationalize heretofore unexplained nanocrystal phase behavior. Adapted from refs.[12-14]

Beyond the work outlined in this thesis, important contributions by other researchers in the field have furthered understanding of NC self-assembly. For instance, the Korgel group recently reported that binary superlattices (including non-close-packed phases such as $CaCu_5$) can form in the solid state when monodisperse Au NC films are heated to initiate coalescence of NC cores.[15] This observation revealed that, although colloidal assembly is assumed to take place from a mixture of particles and solvent in roughly equal abundance,[12] the ordering transition may occur in the absence of solvent entirely. As a result, one might conclude that NC superlattices, including those formed by solvent evaporation, may in fact represent the optimal structure vis-à-vis core and ligand packing in the solid state, analogous to assembly of block copolymers from the melt.

In addition, development of new theoretical analyses of ligand packing has shed light on the potential role of NC surfaces in driving phase behavior. For example, the Korgel group also recently elaborated upon the interfacial area minimization principle[16] to explain the stability of *bcc* superlattices over *fcc* phase when the NC "softness" value (L/R) exceeds ~0.7.[17] Such arguments represent important progress in extending the discussion of NC assembly beyond simple sphere packing analysis. However, the proposed preference of soft particles for the structure providing the most spherical partitioning of space must be reconciled with the fact that the same soft particles also frequently occupy low-coordination sites (i.e., lattice positions with highly aspherical Voronoi polyhedra) when cocrystallized with larger NCs into binary structures.[10]

8.3. Directions for future research

Perhaps unsurprisingly, the dominant role of the surface in governing many properties of colloidal NCs (Chapter 2) also applies to their phase behavior. The availability of atomistic details of capping layer structure will be a crucial enabler of (or roadblock to) progress in understanding NC self-assembly. Towards this aim, PbS NC atomic structure calculations[13] reported by the Alivisatos group have offered important insight into ligand chemistry and resulting spatial allocation of surface-bound hydrocarbon chains. This study also anticipated labile surface ligands on nonpolar facets (i.e., (001)- and (011)-type crystallographic directions). Such predictions offer important insight into self-assembly processes resulting in oriented attachment of inorganic cores investigated most recently by the Vanmaekelbergh group.[18-20]

Furthermore, the departure from sphere packing enabled by the soft ligand shell (Chapter 7) can be rigorously treated by considering topological defect configurations possible for chains grafted across the surface of a sphere, as recently described by Travesset.[21] This work found that the presence of vortices or disclinations within the ligand shell can stabilize many of the non-close-packed binary phases observed in experiments. Such analysis requires some assumption concerning the free energy associated with hydrocarbon chains bent away from surface normal (analogous to the Frank constant of a liquid crystal[22]), either at the anchor point or through the backbone. This is not a trivial task: the length of a polyethylene Kuhn segment is 1.4 nm,[23] suggesting that C_{18}-length hydrocarbon chains (i.e., 2-nm contour length) are already at the lower limit of the scale addressable by statistical arguments routinely employed in polymer physics.

Extending topological analysis of the ligand capping layer beyond perfectly spherical NCs to more pertinent NC shapes (e.g., the zoo of polyhedra recently explored by the Glotzer group[24]) may represent a logical next step. A preview of the potential influence of discrete facets

on collective hydrocarbon chain orientation was offered by the Geissler group using atomistic simulations of *n*-alkane molecules bound to the surface of hexagonal prismatic nanorods.[25] These theoretical models of capped NCs may be pushed further towards experimental relevance by considering ligand grafting density below full coverage and surface saturation varying with crystallographic facet type.

Beyond the theoretical push to understand the complex phase behavior of NC superlattices, experimental scientists will continue to exploit self-assembly to make unprecedented structures and open up new applications for superlattices. For instance, the liquid interfacial assembly technique (Figures 1.4, 1.5) developed by the Jaeger[26] and Murray[27] groups is being used to produce long-range-ordered single- and multicomponent superlattice thin films. Monolayer superlattices are mechanically robust,[28-30] can be controllably shaped,[31] and show tremendous promise for next-generation membrane filtration applications.[32]

Furthermore, new NC building blocks and combinations thereof offer possibilities for chemical design of solids with intriguing physical properties. Superlattices comprised of highly anisotropic nanostructures (e.g., nanorods[33,34] or plates[35,36]) represent two classic examples. In addition, the preparation of highly-uniform branched nanostructures pioneered by the Manna group has introduced hierarchical self-assembly and a route to porous metamaterials design.[37] Moreover, cocrystallization of shape mixtures (e.g., rods and spheres[38] or rods and plates[39]) promises new properties resulting from collective interactions across distinct functional units packed together in a common structure.

The self-assembly field will also capitalize on continued development of synthetic methods offering access to new colloidal nanomaterial compositions (e.g., III-V compounds[40])

and surface chemistries (e.g., compact, electronically-transparent surface ligands[41-44]). In the latter case, the structure-dependent collective properties that may emerge within superlattices comprised of strongly-coupled NCs presents a particularly exciting opportunity to demonstrate the utility of NC self-assembly. Along these lines, preliminary investigations by the Talapin and Kovalenko groups[41] show encouraging results (see also Figure 5.4), though experimental conditions enabling reliable self-assembly of electrostatically-stabilized NCs across several core compositions have yet to be established.

8.4. Final remarks

The astonishingly beautiful patterns resulting from self-assembly of NCs, nascent understanding of the mechanism underpinning superlattice formation, and the opportunity to design matter at an otherwise inaccessible length scale have captured my imagination over the past several years. It has been my privilege to work on this dynamic, challenging, and immensely important topic. I look forward to the resolution of outstanding mysteries and the arrival of new questions sure to come as the field matures.

8.5. References

1 Bartlett, P., Ottewill, R. H. & Pusey, P. N. Superlattice formation in binary mixtures of hard-sphere colloids. *Physical Review Letters* **68**, 3801-3804 (1992).

2 Eldridge, M. D., Madden, P. A., Pusey, P. N. & Bartlett, P. Binary hard-sphere mixtures: a comparison between computer simulation and experiment. *Molecular Physics* **84**, 395-420 (1995).

3 Murray, C. B., Kagan, C. R. & Bawendi, M. G. Self-Organization of CdSe Nanocrystallites into Three-Dimensional Quantum Dot Superlattices. *Science* **270**, 1335-1338 (1995).

4 Shevchenko, E. V., Talapin, D. V., Murray, C. B. & O'Brien, S. Structural Characterization of Self-Assembled Multifunctional Binary Nanoparticle Superlattices. *Journal of the American Chemical Society* **128**, 3620-3637 (2006).

5 Dumestre, F., Chaudret, B., Amiens, C., Renaud, P. & Fejes, P. Superlattices of Iron Nanocubes Synthesized from Fe[N(SiMe3)2]2. *Science* **303**, 821-823 (2004).

6 Shevchenko, E. V., Talapin, D. V., Kotov, N. A., O'Brien, S. & Murray, C. B. Structural diversity in binary nanoparticle superlattices. *Nature* **439**, 55-59 (2006).

7 Leunissen, M. E. *et al.* Ionic colloidal crystals of oppositely charged particles. *Nature* **437**, 235-240 (2005).

8 Ben-Simon, A., Eshet, H. & Rabani, E. On the Phase Behavior of Binary Mixtures of Nanoparticles. *ACS Nano* **7**, 978-986 (2013).

9 Bodnarchuk, M. I., Kovalenko, M. V., Heiss, W. & Talapin, D. V. Energetic and Entropic Contributions to Self-Assembly of Binary Nanocrystal Superlattices: Temperature as the Structure-Directing Factor. *Journal of the American Chemical Society* **132**, 11967-11977 (2010).

10 Boles, M. A. & Talapin, D. V. Many-Body Effects in Nanocrystal Superlattices: Departure from Sphere Packing Explains Stability of Binary Phases. *Journal of the American Chemical Society* **137**, 4494-4502 (2015).

11 Talapin, D. V., Shevchenko, E. V., Murray, C. B., Titov, A. V. & Král, P. Dipole−Dipole Interactions in Nanoparticle Superlattices. *Nano Letters* **7**, 1213-1219 (2007).

12 Pusey, P. N. & Megen, W. v. Phase behaviour of concentrated suspensions of nearly hard colloidal spheres. *Nature* **320**, 340-342 (1986).

13 Zherebetskyy, D. *et al.* Hydroxylation of the surface of PbS nanocrystals passivated with oleic acid. *Science* **344**, 1380-1384 (2014).

14 Lee, S., Bluemle, M. J. & Bates, F. S. Discovery of a Frank-Kasper σ Phase in Sphere-Forming Block Copolymer Melts. *Science* **330**, 349-353 (2010).

15 Goodfellow, B. W. *et al.* Ordered Structure Rearrangements in Heated Gold Nanocrystal Superlattices. *Nano Letters* **13**, 5710-5714 (2013).

16 Ziherl, P. & Kamien, R. D. Maximizing Entropy by Minimizing Area: Towards a New Principle of Self-Organization. *The Journal of Physical Chemistry B* **105**, 10147-10158 (2001).

17 Goodfellow, B. W., Yu, Y., Bosoy, C. A., Smilgies, D.-M. & Korgel, B. A. The Role of Ligand Packing Frustration in Body-Centered Cubic (bcc) Superlattices of Colloidal Nanocrystals. *The Journal of Physical Chemistry Letters* **6**, 2406-2412 (2015).

18 Cho, K.-S., Talapin, D. V., Gaschler, W. & Murray, C. B. Designing PbSe Nanowires and Nanorings through Oriented Attachment of Nanoparticles. *Journal of the American Chemical Society* **127**, 7140-7147, (2005).

19 Evers, W. H. *et al.* Low-Dimensional Semiconductor Superlattices Formed by Geometric Control over Nanocrystal Attachment. *Nano Letters* **13**, 2317-2323 (2013).

20 Boneschanscher, M. P. *et al.* Long-range orientation and atomic attachment of nanocrystals in 2D honeycomb superlattices. *Science* **344**, 1377-1380 (2014).

21 Travesset, A. Topological Structure Prediction in Binary Nanoparticle Superlattices. *Soft Matter* (2016).

22 Randall, D. K. a. J. V. S. Order and frustration in chiral liquid crystals. *Journal of Physics: Condensed Matter* **13**, R1 (2001).

23 Rubinstein, M. & Colby, R. *Polymer Physics*. (Oxford University Press, 2003).

24 Damasceno, P. F., Engel, M. & Glotzer, S. C. Predictive Self-Assembly of Polyhedra into Complex Structures. *Science* **337**, 453-457 (2012).

25 Widmer-Cooper, A. & Geissler, P. Orientational Ordering of Passivating Ligands on CdS Nanorods in Solution Generates Strong Rod–Rod Interactions. *Nano Letters* **14**, 57-65 (2013).

26 Bigioni, T. P. *et al.* Kinetically driven self assembly of highly ordered nanoparticle monolayers. *Nat Mater* **5**, 265-270 (2006).

27 Dong, A., Chen, J., Vora, P. M., Kikkawa, J. M. & Murray, C. B. Binary nanocrystal superlattice membranes self-assembled at the liquid-air interface. *Nature* **466**, 474-477 (2010).

28 Mueggenburg, K. E., Lin, X.-M., Goldsmith, R. H. & Jaeger, H. M. Elastic membranes of close-packed nanoparticle arrays. *Nat Mater* **6**, 656-660 (2007).

29 Kanjanaboos, P. *et al.* Self-Assembled Nanoparticle Drumhead Resonators. *Nano Letters* **13**, 2158-2162 (2013).

30 Wang, Y. *et al.* Strong Resistance to Bending Observed for Nanoparticle Membranes. *Nano Letters* **15**, 6732-6737, doi:10.1021/acs.nanolett.5b02587 (2015).

31 Jiang, Z. *et al.* Subnanometre ligand-shell asymmetry leads to Janus-like nanoparticle membranes. *Nat Mater* **14**, 912-917 (2015).

32 Barry, E., McBride, S. P., Jaeger, H. M. & Lin, X.-M. Ion transport controlled by nanoparticle-functionalized membranes. *Nat Commun* **5** (2014).

33 Ye, X. *et al.* Seeded Growth of Monodisperse Gold Nanorods Using Bromide-Free Surfactant Mixtures. *Nano Letters* **13**, 2163-2171 (2013).

34 Diroll, B. T., Greybush, N. J., Kagan, C. R. & Murray, C. B. Smectic Nanorod Superlattices Assembled on Liquid Subphases: Structure, Orientation, Defects, and Optical Polarization. *Chemistry of Materials* **27**, 2998-3008 (2015).

35 Paik, T., Ko, D.-K., Gordon, T. R., Doan-Nguyen, V. & Murray, C. B. Studies of Liquid Crystalline Self-Assembly of GdF3 Nanoplates by In-Plane, Out-of-Plane SAXS. *ACS Nano* **5**, 8322-8330 (2011).

36 Abécassis, B., Tessier, M. D., Davidson, P. & Dubertret, B. Self-Assembly of CdSe Nanoplatelets into Giant Micrometer-Scale Needles Emitting Polarized Light. *Nano Letters* **14**, 710-715 (2014).

37 Miszta, K. *et al.* Hierarchical self-assembly of suspended branched colloidal nanocrystals into superlattice structures. *Nat Mater* **10**, 872-876 (2011).

38 Ye, X. *et al.* Shape Alloys of Nanorods and Nanospheres from Self-Assembly. *Nano Letters* **13**, 4980-4988 (2013).

39 Paik, T., Diroll, B. T., Kagan, C. R. & Murray, C. B. Binary and Ternary Superlattices Self-Assembled from Colloidal Nanodisks and Nanorods. *Journal of the American Chemical Society* **137**, 6662-6669 (2015).

40 Liu, W., Chang, A. Y., Schaller, R. D. & Talapin, D. V. Colloidal InSb Nanocrystals. *Journal of the American Chemical Society* **134**, 20258-20261 (2012).

41 Kovalenko, M. V., Scheele, M. & Talapin, D. V. Colloidal Nanocrystals with Molecular Metal Chalcogenide Surface Ligands. *Science* **324**, 1417-1420 (2009).

42 Nag, A. *et al.* Metal-free Inorganic Ligands for Colloidal Nanocrystals: S^{2-}, HS^{-}, Se^{2-}, HSe^{-}, Te^{2-}, HTe^{-}, TeS_3^{2-}, OH^{-}, and NH_2^{-} as Surface Ligands. *J. Am. Chem. Soc.* **133**, 10612-10620 (2011).

43 Zhang, H., Jang, J., Liu, W. & Talapin, D. V. Colloidal Nanocrystals with Inorganic Halide, Pseudohalide, and Halometallate Ligands. *ACS Nano* (2014).

44 Dolzhnikov, D. S. *et al.* Composition-matched molecular “solders” for semiconductors. *Science* **347**, 425-428 (2015).